Numerical study of multi-scale flow-sediment-structure interactions using a multiphase approach.

Tim Nagel

▶ **To cite this version:**

Tim Nagel. Numerical study of multi-scale flow-sediment-structure interactions using a multiphase approach.. Fluid mechanics [physics.class-ph]. Université Grenoble Alpes, 2018. English. NNT : 2018GREAI050 . tel-01920495

HAL Id: tel-01920495
https://theses.hal.science/tel-01920495

Submitted on 13 Nov 2018

HAL is a multi-disciplinary open access archive for the deposit and dissemination of scientific research documents, whether they are published or not. The documents may come from teaching and research institutions in France or abroad, or from public or private research centers.

L'archive ouverte pluridisciplinaire **HAL**, est destinée au dépôt et à la diffusion de documents scientifiques de niveau recherche, publiés ou non, émanant des établissements d'enseignement et de recherche français ou étrangers, des laboratoires publics ou privés.

Communauté
UNIVERSITÉ Grenoble Alpes

THÈSE

Pour obtenir le grade de

DOCTEUR DE LA COMMUNAUTE UNIVERSITE GRENOBLE ALPES

Spécialité : **Mécanique des fluides, Énergétique, Procédés**

Arrêté ministériel : 25 mai 2016

Présentée par

Tim NAGEL

Thèse dirigée par **Achim WIRTH, Directeur de Recherche, LEGI, CNRS,**
co-encadrée par **Julien CHAUCHAT, Maître de Conférence, LEGI, Grenoble-INP**
et co-encadrée par **Cyrille BONAMY, Ingénieur de Recherche, LEGI, CRNS**

préparée au sein du **Laboratoire des Écoulements Géophysiques et Industriels (LEGI)**
dans **l'École Doctorale I-MEP2 – Ingénierie – Matériaux, Mécanique, Environnement, Énergétique, Procédés, Production**

Étude numérique des interactions multi-échelles écoulement-sédiment-structure par une approche multiphasique

Numerical study of multi-scale flow-sediment-structure interactions using a multiphase approach

Thèse soutenue publiquement le **17 Juillet 2018**
devant le jury composé de :

Membres du Jury de Thèse :

Monsieur Sylvain GUILLOU
Professeur des Universités, Universités de Caen Normandie, Rapporteur
Monsieur Ming LI
Senior Lecturer, University of Liverpool, Rapporteur
Monsieur Philippe GONDRET
Professeur des Université, Université Pierre et Marie Curie, Président
Monsieur Xiaofeng LIU
Assistant Professor, Pennsylvania State University, Examinateur
Monsieur Tian-Jian HSU
Professeur, University of Delaware
Monsieur Achim WIRTH
Directeur de Recherche, LEGI, CNRS, Directeur de Thèse
Monsieur Julien CHAUCHAT
Maître de Conférence, LEGI, Grenoble-INP, Co-encadrant de Thèse
Monsieur Cyrille BONAMY
Ingénieur de Recherche, LEGI, CNRS, Co-encadrant de Thèse

Communauté
UNIVERSITÉ Grenoble Alpes

Plan

Nomenclature

Greek symbols

α_s	upstream bed angle in the scour at an apron case (degrees)
α_s^∞	upstream bed angle at equilibrium in the scour at an apron case (degrees)
β	Sediment bed angle (degrees)
β_s	Static friction angle (angle of repose) for the sediment. (degrees)
$1-\phi$	fluid phase volume fraction (-)
δ	transport layer thickness (m)
δ^*	dimensionless transport layer thickness (-)
δ_s	scour depth (m)
δ_s^{max}	maximum scour depth (m)
Δ_r	ripples height (m)
Δt	time step (s)
ε	turbulent kinetic energy dissipation rate ($m^2.s^{-3}$)
γ	energy dissipation rate due to inelastic collision ($kg.m^{-1}.s^{-3}$)
κ	Von Karmann constant (-)
λ	bulk viscosity (kg $m^{-1}.s^{-1}$)
λ_r	ripples wavelength (m)
μ	friction coefficient
μ_c^s	particle shear viscosity (kg $m^{-1}.s^{-1}$)
μ_s	static friction coefficient for the rheology (-)
μ_2	dynamic friction coefficient for the rheology (-)
ν_{Fr}^s	frictional viscosity ($m^2.s^{-1}$)
ν_{Eff}^k	phase k effective viscosity ($m^2.s^{-1}$)
ν_t^f	turbulent viscosity ($m^2.s^{-1}$)
ν^f	fluid viscosity ($m^2.s^{-1}$)
ν^{mix}	mixture viscosity ($m^2.s^{-1}$)
ω	turbulent kinetic energy specific dissipation rate (s^{-1})
$\tilde{\omega}$	turbulent kinetic energy specific dissipation rate incorporating a stress-limiting term (s^{-1})
Ω_{ij}	vorticity (s^{-1})
Φ	Parameter in for sediment diffusivity in classical hydrosedimentary models. (-)
ϕ	solid phase volume fraction (-)
ϕ^0	initial solid volume fraction (-)
π	sediment flux ($m.s^{-1}$)
σ_d	turbulent coefficient (-)

σ_{d0}	turbulent coefficient (-)
σ_k	turbulent coefficients (-)
σ_ε	turbulent coefficients (-)
σ_ω	turbulent coefficients (-)
θ	Shields number (-)
θ_c	Critical Shields number (-)
Θ	granular temperature ($m^2.s^{-2}$)
τ_{ij}^f	total fluid stress (Pa)
τ_{ij}^s	particle shear stress (Pa)
τ_{ij}^{sc}	collisional stress (Pa)
τ_{ij}^{sf}	frictional stress (Pa)
χ_ω	Parameter for Pope Correction in k-ω2006 model (-)

Latin symbols

A	smoothing term for k-ω2006 turbulence model (-)
$C_{2\omega 0}$	turbulent coefficient in k-ω2006 model (-)
C_{lim}	turbulent coefficient in k-ω2006 model (-)
C_d	drag coefficient (-)
C_t	coefficient for the Reynolds stress like contribution for the solid phase (-)
d_{eff}	effective particle diameter (m)
D	Sediment deposition flux in classical hydrosedimentary models ($m.s^{-1}$)
D_{small}	regularization parameter for the rheology (s^{-1})
D_Θ	conductivity of granular temperature ($kg.m^{-1}.s^{-1}$)
E	Sediment erosion flux in classical hydrosedimentary models ($m.s^{-1}$)
$f_{C2\omega}$	turbulent coefficient in kω2006 model (-)
f_i	external force that drives the flow ($kg.m^{-2}.s^{-2}$)
g_i	gravitational acceleration ($m.s^{-2}$)
g_{s0}	radial distribution function for dense rigid spherical particles gases (-)
h^s	seabed height (m)
h_0^s	initial seabed height (m)
h^f	water column height (m)
$\mathcal{H}(.)$	Heaviside step function (-)
I	inertial number (-)
I_0	empirical parameter of the granular rheology (-)
J_{int}	energy dissipation (or production) due to the interaction with the carrier fluid phase(-)
K_ϕ	Sediment diffusivity coefficient in classical hydrosedimentary models ($m^2.s^{-1}$)
k	turbulent kinetic energy ($m^2.s^{-2}$)
k_s	Nikuradse roughness length (m)
K	drag parameter (kg $m^{-3}.s^{-1}$)
n	characteristic exponent (-)
n_s	characteristic exponent for the speed of the scour development (-)
p	fluid pressure (Pa)
p^s	collisional component of the particle pressure (Pa)
p^{ff}	permanent contact component of the particle pressure (Pa)
q^*	dimensionless sediment transport rate (-)
q^*_{creep}	dimensionless sediment transport rate due to creep flow (-)
q_j	flux of granular temperature ($kg.s^{-1}$)
$\tilde{p}^s$	particle normal stress (Pa)

Re_p	Particulate Reynolds number (-)
r_{ij}^f	viscous stress (Pa)
r_{ij}^s	granular stress contribution to the particle shear stress (Pa)
S_f	energy slope (%)
S_c	Schmidt number (-)
S_u	Suspension number (-)
$\underline{S_{ij}^k}$	deviatoric part of the phase k strain rate tensor (Pa)
$\overline{S_{ij}^k}$	Favre averaged strain rate tensor of the phase k (Pa)
S_t	Stokes number (-)
t	time (s)
T_s	scour characteristic timescale (s)
T_{α_s}	equilibrium timescale for upstream bed angle (s)
tmf	turbulent drag parameter (-)
t_l	characteristic time scale of energetic eddies (s)
t_p	particle response time (s)
u_i^k	phase k velocity, $i = 1; 2; 3$ represents streamwise, spanwise and vertical component, respectively (m.s^{-1})
u_*	bed friction velocity (m.s^{-1})
U	mixture velocity (m.s^{-1})
$\bar{U}$	mean velocity (m.s^{-1})
w_{fall}	settling velocity (m.s^{-1})
w_{fall0}	settling velocity of an isolated particle (m.s^{-1})
z_{bed}	bed interface vertical position (m)

List of Abbreviations

CW	Clear-Water regime of sediment transport.
HSV	Horseshoe Vortex.
KT	Kinetic Theory.
LB	Live-Bed regime of sediment transport.
LES	Large Eddy Simulations.
RANS	Reynolds Averaged Navier-Stokes equations.
RB	Rigid-Bed : flow case with a wall at the bottom.
RHS	Right Hand Side
SF	Sheet Flow regime of sediment transport.
SW	Shallow Water.
URANS	Unsteady Reynolds Averaged Navier-Stokes equations.
VS	Vortex shedding.

Chapitre 1

Introduction

Foreword

The complete translation of this chapter is availaible in Appendix C.

1.1 Contexte et enjeux de la thèse

La croissance démographique mondiale s'accompagne d'une très forte littoralisation. On estime qu'environ 60% de la population mondiale, soit près de 4 Milliards d'humains, vit à moins de 60 kilomètres des côtes. Il y a une pression démographique croissante sur les littoraux mondiaux. A titre d'exemple, en 2010, la densité de population des communes métropolitaines françaises situées sur le littoral était deux fois et demi supérieure à la densité moyenne en métropole selon le Ministère de l'Ecologie du Développement Durable et de l'Energie [1].
En parallèle d'une forte urbanisation du littoral, la zone côtière subit une autre transformation majeure depuis une trentaine d'années : l'utilisation de ce milieu naturel pour la production d'énergie renouvelable afin de satisfaire la demande d'énergie croissante de nos sociétés. Pour extraire de l'énergie du milieu marin plusieurs méthodes sont possibles : on peut extraire l'énergie des vagues (énergie houlomotrice), des courants (aussi bien marins que fluviaux) via des hydroliennes ou extraire l'énergie cinétique du vent à l'aide d'éoliennes offshore. Parmi ces méthodes, c'est l'extraction de l'énergie du vent qui dispose des technologies les plus efficaces et les moins coûteuses mais également du plus important potentiel énergétique. Ce dernier étant plus important en mer que sur le continent, de nombreux pays planifient ou multiplient la construction de fermes éoliennes offshore le long de leurs côtes. Ainsi, d'après le rapport annuel de 2013 de l'European Wind Energy Association (*EWEA*, 2013), la capacité éolienne offshore européenne était de 5GW en 2012. A l'horizon 2030, ce rapport estime que cette capacité pourrait atteindre 150 GW, ce qui correspondrait alors à 14% de la consommation d'électricité européenne actuelle.

Cette croissance de l'éolien offshore ne se limite pas à l'Europe ; la Chine et les Etats-Unis veulent également développer ce moyen de production d'énergie (*Archer et al.*, 2014). Cependant, à l'heure actuelle, plusieurs verrous majeurs (écologiques, techniques et scientifiques) limitent les capacités de l'énergie éolienne offshore.

1. http: //www.geolittoral.developpement−durable.gouv.fr/IMG/pdf/etat_des_lieux_mer_et_littoral.pdf

Le premier est l'impact écologique de la construction et de l'exploitation de fermes éoliennes offshore sur les écosystèmes côtiers et maritimes. Ainsi, les pales des éoliennes peuvent constituer une source de surmortalité pour l'avifaune et la présence de fermes peut modifier les routes migratoires de certains oiseaux si elles sont mal situées (*Gove et al.*, 2013). En milieu marin, les impacts sur la faune sont nombreux, allant de l'augmentation locale de la turbidité lors de la construction des piles d'éoliennes aux perturbations électromagnétiques des cables sous-marin. A ce sujet, un résumé non-exhaustif peut être trouvé dans *Dai et al.* (2015).
Dans l'atmosphère, le premier effet de la présence d'une turbine est la génération d'un sillage turbulent. A cause de ce sillage, l'augmentation du mélange turbulent atmosphérique proche de la surface peut conduire à l'augmentation locale de la température, au moins dans le cas de fermes onshore (*Zhou et al.*, 2012). A plus large échelle, l'impact des fermes éoliennes sur le climat régional (*Vautard et al.*, 2014) ou la possible réduction de la puissance des ouragans par la présence massive de fermes éoliennes (*Jacobson et al.*, 2014) sont des thèmes de recherche en cours.
La circulation océanique à l'échelle régionale peut, elle aussi, être perturbée par la présence de larges fermes éoliennes. Les travaux de *Broström* (2008) montrent qu'il peut y avoir une génération d'upwelling (remontée d'eau dans la couche supérieure de l'océan) en aval des fermes. Ces upwelling seraient une réponse de la dynamique océanique aux perturbations atmosphériques générées par les fermes éoliennes.

Les écoulements atmosphériques et océaniques ne sont pas les seuls à être perturbés par la présence de structures comme les éoliennes offshore. Si les perturbations atmosphériques sont contrôlées par les turbines, ce sont les fondations des éoliennes qui ont un impact sur la morphodynamique et le transport de sédiment. Les fondations possibles pour les éoliennes offshore peuvent être de différents types (comme montré sur la figure 1.1) mais disposent toutes d'un important ancrage dans le fond marin. Fin 2012, en Europe, sur un parc de 1662 machines, seules deux éoliennes expérimentales étaient "flottantes", c'est à dire sans fixations conséquentes dans le fond marin (*EWEA*, 2013). Parmi les éoliennes offshore construites sur le littoral européen, 74% ont une fondation de type monopile (*EWEA*, 2013).

On peut différencier les impacts de ces fondations sur le sédiment selon deux échelles spatiales : à l'échelle d'une ferme et à l'échelle de la pile. A l'échelle d'une ferme, il a été observé que l'élévation du fond marin pouvait être rehaussée localement au niveau de la ferme, la densité des piles perturbant l'écoulement et provoquant une accumulation locale de sédiment (*Van der Veen et al.*, 2007). A l'échelle de la pile, celle-ci perturbe l'écoulement de plusieurs manières : contraction des lignes de courant, accélération de l'écoulement, écoulement plongeant au front de la structure, génération d'un tourbillon dit "fer à cheval" devant et autour de la structure à l'interface eau/sédiment et lâché tourbillonnaire en aval de la structure. Toutes ces perturbations contribuent à l'augmentation locale du transport sédimentaire et à l'érosion autour de la structure : un phénomène que l'on appelle affouillement (voir section 1.2.4 pour une description complète du phénomène). Si l'affouillement est important, les fondations peuvent être mises à nues et il y a alors un risque d'effondrement de la structure. Des solutions existent pour réduire cet affouillement dans le cas de monopiles d'éoliennes offshore, mais elles ne sont pas sans coût ni inconvénients. Ainsi, le phénomène d'affouillement a également lieu au niveau des enrochements de protection pouvant être placés autour des piles et ne fait qu'éloigner spatialement le problème de la pile sans totalement le résoudre (*Petersen et al.*, 2015). Une autre solution pour éviter que l'affouillement soit critique est d'augmenter la profondeur des fondations ou le diamètre de la pile (*Matutano et al.*, 2013) ; là encore cela implique des surcoûts importants.

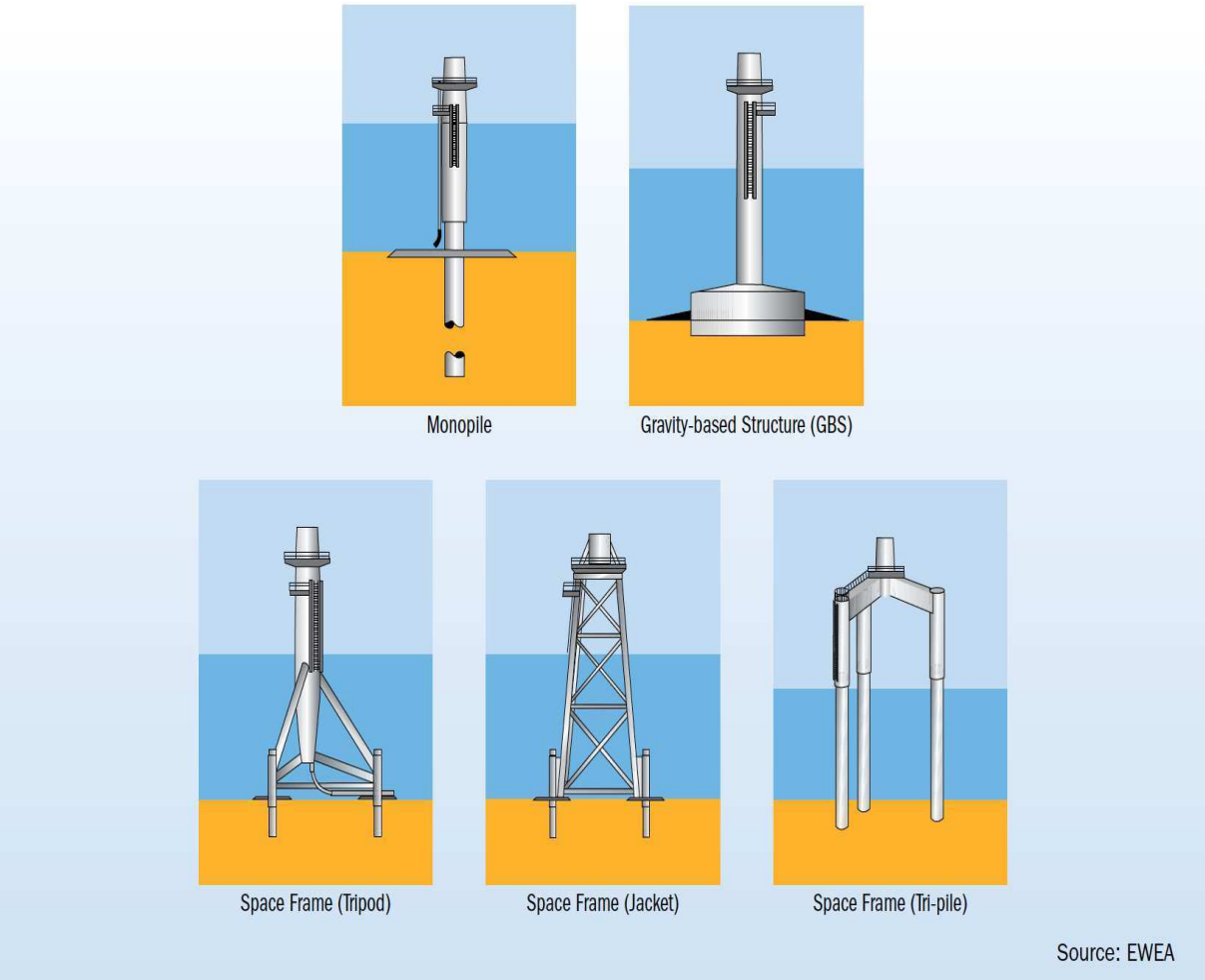

FIGURE 1.1: Sketch of the different offshore wind turbine foundations with a seabed anchorage. Source : EWEA 2013 annual report (*EWEA*, 2013)

L'affouillement participe également à la mise en suspension des sédiments autour et en aval de la pile. Les courants marins (principalement la marée) advectent les particules mises en suspensions formant ainsi des sillages de forte turbidité pouvant mesurer entre 30 et 150 mètres de large pour plusieurs kilomètres de long (*Vanhellemont and Ruddick*, 2014). Ces sillages sont orientés dans la direction du courant comme le montre la figure 1.2, représentant une image satellite de la ferme éolienne de Thanet dans l'estuaire de la Tamise. On y voit très clairement que le point de génération du sillage turbide est la pile de l'éolienne. Ces sillages ne sont pas sans nuisances potentielles pour l'environnement, une forte turbidité pouvant affecter la vie marine.

Le développement de l'éolien offshore doit s'accompagner d'avancées concrètes dans plusieurs domaines pour améliorer la production, réduire les coûts et prévenir les impacts. D'après *Archer et al.* (2014), les modèles numériques prédictifs utilisés pour déterminer le potentiel d'un site nécessitent l'amélioration et la multiplication de mesures in-situ pour leur calibration mais également l'amélioration de la prise en compte des effets de sillages turbulents et de leurs impacts sur la production d'énergie. En parallèle, les risques aussi bien environnementaux que

FIGURE 1.2: NASA Earth Observatory images of sediment plume generated by offshore wind turbine pile in Thanet wind farm, Thames River estuary. Image by Jesse Allen, using Landsat-8 data from the U.S. Geological Survey. Source : *earthobservatory.nasa.gov*

structurels engendrés par le phénomène d'affouillement doivent être mieux compris et maitrisés. Une meilleure compréhension des intéractions complexes entre l'écoulement, la structure et le lit sédimentaire est absolument nécessaire (*Sumer*, 2014). Elle permettra sans doute à terme de baisser les coûts liés aux fondations qui s'élèvent actuellement au tiers du coût total d'une turbine éolienne offshore (*Sumer*, 2014). A titre de comparaison, sur terre, où l'affouillement n'est pas présent et où les conditions d'installations sont moins difficiles, le coût associé aux fondations d'une éolienne ne représente qu'environ 10% du coût total (*Petersen*, 2014).
Plus généralement, le phénomène d'affouillement pour les éoliennes offshore est similaire à celui rencontré autour des piles de pont en régime fluvial (*Breusers and Raudkivi*, 1991; *Breusers et al.*, 1977), la majeure partie de la littérature étant d'ailleurs axée sur cette composante (voir section 1.2.4). Ainsi, une amélioration de la compréhension et des prédictions du phénomène d'affouillement permettra également des avancées dans le domaine du Génie Civil fluvial ou estuarien. Ces avancées sont attendues par les acteurs majeurs du domaine (ingénieurs, exploitants, collectivités locales ou agence gouvernementale) car du fait de l'urbanisation croissante du littoral, le nombre de structures interagissant avec les dynamiques fluviales/côtières et sédimentaires est en constante hausse et le prix de réparation des ouvrages endommagés est important. En effet, basé sur des exemples passés (*Lillycrop and Hughes*, 1993), on peut estimer que le prix de réparation pour des structures endommagées par l'affouillement varie entre 2 millions de Dollars US pour des piles de pont et jusqu'à plus de 10 millions de Dollars US pour des digues. Aux Etats-Unis,

le coût moyen de réparation des ouvrages autoroutiers impactés par les crues était de l'ordre de 50 millions de dollars US en 1995 (*Lagasse et al.*, 1995). Ce coût important s'explique aussi par le nombre important d'ouvrages de génie civil impactés par le phénomène d'affouillement. Ainsi, on estime que sur la période 1970-2000, parmi les 600 000 ponts existants aux USA, 600 se sont effondrés à cause du phénomène d'affouillement (*Briaud et al.*, 1999), ce qui représente 60% des causes de destruction des ponts sur cette période. Pour les ingénieurs, il n'existe pas à l'heure actuelle de modèle mathématique et numérique capable de prédire avec une précision suffisante le phénomène d'affouillement pour le dimensionnement d'ouvrage de génie civil. Le recours à des modèles réduits en laboratoire afin de dimensionner correctement ces ouvrages (*Harris et al.*, 2016) est encore généralisé dans de nombreux bureaux d'études. L'utilisation de ces modèles réduits a par ailleurs un coût non négligeable car il est nécessaire de construire une maquette pour chaque configuration étudiée. Une meilleure compréhension du phénomène d'affouillement mais surtout de meilleures prédictions de ce phénomène pour le dimensionnement d'ouvrages ou de leurs protections permettraient sans doute de réduire les coûts liés au dimensionnement mais également aux éventuelles réparations.
Ce travail de thèse s'articule autour de deux axes afin de mieux comprendre les interactions multi-échelles entre une éolienne offshore et son environnement : l'impact environmental du sillage éolien offshore sur la dynamique océanique et sédimentaire d'une part et la simulation diphasique de l'affouillement autour d'une pile cylindrique verticale d'autre part.

1.2 Etat de l'art

Cette partie du manuscript s'attache à dresser un état de l'art des connaissances du transport sédimentaire et de sa modélisation. Les principes de base de ce phénomène physique et les différents modes de transport de sédiments seront détaillés dans un premier temps. Ensuite on s'intéressera plus particulièrement à la façon dont le transport sédimentaire est habituellement décrit lorsque l'on cherche à le modéliser numériquement. Par la suite, une description de l'approche diphasique du transport sédimentaire permettra de présenter l'historique de l'approche choisie pour la majeure partie des travaux présentés dans ce manuscript. Enfin, une description physique et une revue historique des travaux de modélisation numérique du phénomène d'affouillement sera proposée.

1.2.1 Le transport sédimentaire - description physique

a) Définitions des sédiments

Les sédiments sont un ensemble de particules provenant de l'altération de formations géologiques continentales et dont l'érosion, le transport et le dépôt sont contrôlés par des processus physiques comme le vent, l'eau ou la glace. De composition chimique très variée car liée à la nature des roches dont ils sont originaires, les sédiments possèdent une grand diversité granulométrique (taille, forme, densité). Dans la littérature, de nombreuses classifications granulométriques on été proposées. Généralement, les limites entre les différentes catégories répertoriées correspondent à des changements de propriétés mécaniques ou physiques des grains.
Les sédiments ayant un comportement, une dynamique et des réactions différentes aux sollicitations du milieu en fonction de leur taille, on ne retrouvera pas les mêmes tailles de sédiments proches où loin de la zone d'érosion (zone d'arrachement au substrat rocheux). Les sédiments les plus grossiers seront ceux qui se déplaceront sur le moins de distance entre la zone d'érosion

et celle de dépôt. En milieu estuarien ou côtier, les sédiments ont des tailles inférieures à l'ordre de quelques millimètres et sont principalement des sables et des argiles. En milieu fluvial, on retrouve également des sédiments plus grossiers comme des graviers (de l'ordre de la dizaine de millimètres) ou des gros cailloux (plusieurs dizaines de millimètres).

La granulométrie n'est pas le seul paramètre influent sur le comportement des sédiments. Plus les sédiments sont fins et plus la connaissance de leur teneur en argile et en matière organique est nécessaire. Cela permet de faire la distinction en sédiments non-cohésifs et sédiments cohésifs. Les particules constituant les premiers sont indépendantes les unes des autres et leurs déplacements se font de façon individuelle, c'est le cas des graviers ou des sables grossiers à moyens. Une faible quantité d'argile (5 à 10%) est suffisante pour rendre un sédiment cohésif ; les particules vont avoir tendance à s'agglomérer sous l'effet de forces attractives moléculaires pour former des agrégats : c'est la floculation (*Chauchat*, 2007). Cette dernière est renforcée par la présence de matière organique. Les sédiments cohésifs répondent de manières différentes de ceux non-cohésifs aux sollicitations du milieu (courant, vagues...), c'est le cas des vases par exemple. Dans ce travail de thèse, on s'intéressera uniquement aux sédiments non-cohésifs de type sable.

b) Les différents modes de transport sédimentaire

Un fluide génère une contrainte de cisaillement τ lorsqu'il s'écoule sur un lit sédimentaire composé de particules. Lorsque, pour une particule donnée, cette contrainte dépasse une valeur seuil, alors la particule est déstabilisée, mise en mouvement et le transport sédimentaire commence. La force déstabilisatrice, générée par l'écoulement sur la particule est proportionnelle à τd^2, où d est le diamètre médian des particules déposée sur le lit. On la compare aux forces stabilisatrices s'exerçant sur la particule et correspondant au poids déjaugé des grains ($\propto (\rho^s - \rho^f) g d^3$) pour construire le nombre de Shields (*Shields*, 1936) :

$$\theta = \frac{\tau}{(\rho^s - \rho^f) g d}, \tag{1.1}$$

où ρ^s et ρ^f correspondent respectivement aux masses volumiques des particules de sédiments et du fluide et g à l'accélération de la gravité. Le nombre de Shields est donc le rapport entre les forces déstabilisatrices et stabilisatrices s'exerçant sur une particule. La contrainte de cisaillement τ peut être déterminer à partir de la vitesse de friction du fluide à la paroi u_* suivant la relation :

$$\tau = \rho^f {u_*}^2 \tag{1.2}$$

Pour un type de particule donné, son seuil de mise en mouvement est donné par le nombre de Shields critique, usuellement noté θ_c. Ce seuil de mise en mouvement dépend du nombre de Reynolds particulaire Re_p (*Shields*, 1936; *Van Rijn*, 1984a). Ce dernier dépend du diamètre médian des particules et s'écrit comme :

$$Re_p = \frac{\mid u^s - u^f \mid d}{\nu}, \tag{1.3}$$

avec u^s et u^f la vitesse des particules et du fluide, respectivement et ν la viscosité cinématique. Dans la pratique, pour des sables sur un fond horizontal, la dépendance du nombre de Shields critique au nombre de Reynolds particulaire est assez faible et l'on peut considérer que $\theta_c \approx 0.05$ (*Fredsøe and Deigaard*, 1992).

La mise en mouvement des grains sera facilitée si ceux ci sont placés sur un fond incliné. On peut distinguer deux cas où le Shields critique est modifié par la pente (*Fredsøe and Deigaard*, 1992) :

- Si la pente est transverse par rapport à la direction de l'écoulement :

$$\theta_c = \theta_{c0} \ \cos\beta \sqrt{1 - \frac{\tan^2\beta}{\tan^2(\beta_s)}} \tag{1.4}$$

- Si la pente est dans la direction de l'écoulement :

$$\theta_c = \theta_{c0} \ \cos\beta \left(1 - \frac{\tan\beta}{\tan(\beta_s)}\right), \tag{1.5}$$

avec θ_{c0} la valeur du Shields sur fond plat, β l'angle entre l'horizontale et le lit sédimentaire et β_s l'angle de friction statique (aussi appelé angle de repos) du sédiment. Ce dernier est l'angle avec l'horizontale au delà duquel un empilement de grains n'est plus stable. Pour $\beta > \beta_s$, une avalanche de surface mettant en mouvement quelques couches de grains se déclenche. Le phénomène d'avalanche se poursuit jusqu'à ce que l'angle β de la pente soit de nouveau égal à β_s.

La valeur du nombre de Shields contrôle la façon dont sont transportés les sédiments. On peut distinguer trois modes de transport de particules, le charriage, la saltation et la suspension.
Le charriage (bedload transport en anglais) correspond au mouvement des grains de la couche supérieure du lit sédimentaire roulant de façon discontinue sur le fond dans le sens de l'écoulement. Selon la definition de *Fredsøe and Deigaard* (1992), pendant le charriage, les particules sont toujours plus ou moins en contact avec le fond. Ce mode de transport a généralement lieu quand la contrainte de cisaillement sur le lit est proche de la contrainte critique de mise en mouvement τ_c.
Pour **la saltation**, le mouvement de la particule est fait de bonds successif dans le sens de l'écoulement. Le contact avec le fond n'est donc pas continu comme pour le charriage mais ponctuel. Lors d'un bond, le hauteur atteinte par les grains ne dépasse généralement pas l'ordre de grandeur de son diamètre. Ce mode de transport se met en place lorsque le seuil de mise en mouvement est dépassé.
La suspension (suspended load en anglais) correspond au transport des particules par la turbulence dans la colonne d'eau sans que celles-ci ne se déposent à nouveau sur le fond. Cela se produit lorsque l'écoulement est suffisamment intense pour maintenir ces particules en suspension. Ce phénomène ne concerne que les particules les plus petites, suffisamment légères pour être transportées par les fluctuations de vitesse turbulente de l'écoulement. De manière générale, on peut décrire ce phénomène à l'aide d'un nombre de suspension adimensionnel décrivant le rapport entre les forces gravitationnelles et les forces fluides turbulentes soulevant les particules dans la direction verticale (*Van Rijn*, 1984b) :

$$S_u = \frac{w_{fall0}}{u_*}, \tag{1.6}$$

où w_s est la vitesse de chute des particules. Ainsi, lorsque les vitesses verticales générées par fluctuations turbulentes de l'écoulement proches du lit sont plus grandes que la vitesse de chute des particules, les particules restent en suspension.
Il est assez commun de considérer le charriage et la saltation comme un seul type de mouvement des particules et de distinguer uniquement le charriage au sens global de la suspension

(roulement des grains et saltation). En effet, pour le charriage, la force du fluide met les grains en mouvement horizontalement alors que la mise en suspension des particules se fait suivant la direction verticale.
Comme les milieux naturels sont polydisperses en terme de granulométrie, on rencontre souvent plusieurs types de transport à la fois. Ainsi, pour un même écoulement, les sediments les plus fins seront transportés en suspension alors que ceux de taille plus importante seront transportés par charriage.

En considérant le cas particulier du transport par charriage, le taux de transport des particules change en fonction de la valeur du nombre de Shields. En effet, pour des valeurs de nombre de Shields inférieures au Shields critique θ_c (≈ 0.05 pour des sables sur fond plat), il n'y a pas de mise en mouvement des particules et donc pas de transport solide associé. Lorsque le nombre de Shields augmente, pour $0.05 \leq \theta \leq 0.3$, le transport solide est non nul mais reste assez faible, l'épaisseur de la couche de transport est de l'ordre du diamètre des grains et des formes de fond comme des rides ou des dunes peuvent se former. Quand $\theta \geq 0.3$, la couche de transport par charriage atteint plusieurs diamètres de particule d'épaisseur ; elle est dense en terme de grains, et l'intensité de l'écoulement ne laisse alors plus apparaître de formes de fond. Dans ce dernier cas, le transport solide est dans un régime de charriage intense ou sheet-flow en anglais (*Graf*, 1984). Le terme "upper stage plane bed" peut aussi être trouvé dans la littérature pour décrire ce régime.
La figure 1.3 montre une vision schématique du phénomène de sheet-flow. Chacune des quatre couches identifiées sur la figure 1.3 représente une région verticale où un type d'interactions particulaires est dominant. La couche la plus basse est représentative du lit sédimentaire poreux et immobile. Au dessus, on trouve une région très concentrée en particules où le transport sédimentaire est dominé par des interactions de contact entre les particules. Plus haut sur la verticale, la concentration en particule est plus faible et les collisions entre particules ainsi que leur mise en suspension par la turbulence sont les principaux moteurs du transport sédimentaire. Tout en haut de la colonne d'eau, on retrouve une région où la concentration en particules est extrêmement faible et où le transport sédimentaire est contrôlé par la turbulence.
La transition entre ces quatre zones est plutôt progressive dans la réalité et ce cas particulier illustre que le transport sédimentaire le long de la verticale est un phénomène continu.

1.2.2 Etat de l'art de la modélisation classique du transport sédimentaire

L'approche couramment utilisée pour modéliser le transport sédimentaire consiste à diviser le domaine de calcul en deux-sous domaines, dans lesquels l'hydrodynamique et la morphodynamique sont résolues distinctement et peuvent être reliées par des termes de frictions (voir chapitre 2 et plus particulièrement les équations 2.7, 2.8).
Suivant le cas d'étude et le degré de complexité du modèle hydrodynamique, la dynamique du milieu fluide peut être résolue en utilisant les équations de Barré de Saint-Venant 1D ou 2D (*de Saint-Venant*, 1871; *Vallis*, 2006) ou les équations de Navier-Stokes (NS) 3D (eq. 1.7). Ces équations de la dynamique pour le fluide sont notamment basées sur un bilan de la quantité de mouvement :

$$\rho^f \left(\frac{\partial \boldsymbol{u^f}}{\partial t} + (\boldsymbol{u^f} \cdot \nabla)\boldsymbol{u^f} \right) = -\nabla p^f + \nabla \cdot \boldsymbol{\tau^f} + \boldsymbol{f} + \rho^f \boldsymbol{g}, \tag{1.7}$$

où ∇ est l'opérateur gradient tridimensionnel, ρ^f et $\boldsymbol{u^f}$ sont la masse volumique et le vecteur vitesse pour le fluide, p^f la pression, $\boldsymbol{\tau^f}$ les contraintes de Reynolds du fluide, $\boldsymbol{g}$ l'accélération

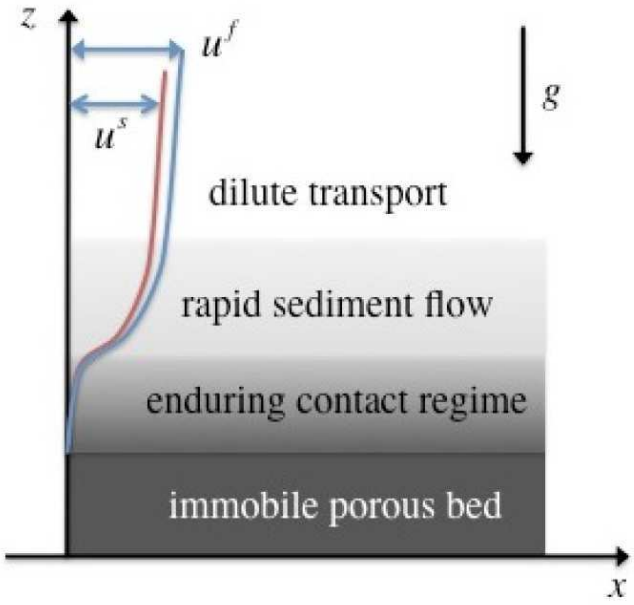

FIGURE 1.3: Sketch of the sheet-flow sediment transport regime. The different vertical layers highlight the main sediment transport mode along the vertical direction. u^s and u^f is the sediment and the fluid velocity, respectively. Source : *Cheng and Hsu* (2014).

liée à la gravité dans la direction $-\overrightarrow{z}$, $\boldsymbol{f}$ les forces volumiques autres que la gravité. Les termes de gauche de l'équation 1.7 représentent les variations temporelles et l'advection de la quantité de mouvement alors que les termes de droite sont les forces qui s'applique au fluide. On peut distinguer les forces de pressions (∇p^f), les efforts visqueux ($\nabla \cdot \boldsymbol{\tau^f}$) ou la pesanteur ($\rho^f \boldsymbol{g}$).

Suivant l'échelle spatiale de l'étude, le type de sédiment ou encore les conditions d'écoulement, la description complète de la morphodynamique passe par un système d'équations présentant plusieurs degrés de complexité. Dans cette description généraliste, on s'intéressera à l'évolution de la dynamique de sédiments non-cohésifs, à une échelle locale ou régionale. La couche de transport de sédiment, épaisse au maximum d'une dizaine de centimètres, ne peut donc pas être résolue explicitement (*Amoudry and Souza*, 2011).
La distinction du transport sédimentaire en suspension et charriage nécessite deux équations, l'une pour décrire l'évolution de la concentration en sédiment dans la phase fluide et l'autre pour décrire l'évolution de l'interface du lit sédimentaire. Ces deux équations sont basées sur le principe de conservation de la masse de sédiment.

a) Transport en suspension

L'application du principe de conservation de la masse de sédiment dans un volume élémentaire de fluide permet d'obtenir une équation pour la concentration de sédiment ϕ dans la colonne d'eau. Cette équation peut s'écrire comme une équation d'advection-diffusion pour la concentra-

tion comme suit (*Amoudry and Souza*, 2011) :

$$\frac{\partial \phi}{\partial t} + \nabla \cdot (\boldsymbol{u^f} \phi) = \frac{\partial w_{\text{fall}} \phi}{\partial z} + \nabla \cdot (K_\phi \nabla \phi). \tag{1.8}$$

La partie gauche de l'équation représente les variations temporelles et l'advection de la concentration en sédiment sous l'effet de l'écoulement du fluide porteur. Dans la partie droite de l'équation, le terme comprenant w_{fall}, la vitesse de chute des sédiments, représente leur déposition. Le deuxième terme dans la partie droite de l'équation représente la diffusion de la concentration sous l'effet des flux turbulents avec K_ϕ un terme de diffusivité pour le sédiment, qui, selon la définition de *Van Rijn* (1984b), peut-être relié à la viscosité turbulente par deux paramètres :

$$K_\phi = \frac{1}{S_c} \Phi {\nu_t}^f, \tag{1.9}$$

avec ${\nu_t}^f$ la viscosité turbulente. Le premier terme est fonction du rapport entre vitesse de chute des grains et vitesse de friction au fond. Il exprime l'importance des termes d'inertie de particules par rapport à la turbulence de l'écoulement, et peut être vu comme l'inverse du nombre de Schmidt S_c. Son expression, proposée par *Van Rijn* (1984b) est construite sur les données expérimentales de *Coleman* (1970) :

$$\frac{1}{S_c} = 1 + 2 \left(\frac{w_{fall}}{u_*} \right)^2. \tag{1.10}$$

Le deuxième paramètre dans l'équation 1.9 permet d'inclure les effets d'atténuation de la turbulence due à la présence de particules. Il s'exprime comme une fonction du rapport entre la concentration ϕ et la concentration maximale ϕ_{max} et augmente avec la concentration en particule (*Van Rijn*, 1984b) :

$$\Phi = 1 + \left(\frac{\phi}{\phi_{max}} \right)^{0.8} - 2 \left(\frac{\phi}{\phi_{max}} \right)^{0.2}. \tag{1.11}$$

La vitesse de chute des sédiments dans un colonne d'eau dépend de la concentration du milieu en particules. *Van Rijn* (1984b) propose une loi de type Richardson-Zaki :

$$w_{fall} = w_{fall0} (1 - \phi)^4, \tag{1.12}$$

où w_{fall0} est la vitesse de chute d'une particule isolée. On peut estimer cette dernière via de nombreuses relations, *Van Rijn* (1984b) recommande d'utiliser la formulation de *Zanke* (1977). Une des formulations les plus récente et complète est celle de *Jiménez and Madsen* (2003) :

$$w_{fall0} = \frac{1}{A + \frac{B}{S_*}} \sqrt{(s-1) g d}, \tag{1.13}$$

avec $S_* = \dfrac{d}{4\nu^f} \sqrt{(s-1) g d}$, $s = \dfrac{\rho^s}{\rho^f}$ et A et B des facteurs de forme pour les particules. Pour des particules naturelles (non-sphériques) les valeurs standards sont A=0.954 et B=5.12. Pour des particules sphériques, on prend A=0.79 et B=4.61.

Supposons un écoulement stationnaire et uniforme sans composante verticale pour la vitesse fluide. L'équation 1.8 se transforme pour décrire l'évolution de la concentration sur un profil vertical :

$$K_\phi \frac{\partial \phi}{\partial z} + w_{fall} \phi = 0 \tag{1.14}$$

On retrouve alors que l'expression du profil vertical de la concentration en sédiment résulte d'un équilibre entre le dépôt des particules sous l'effet de la gravité et un flux turbulent de mise en suspension (*Rouse*, 1939).

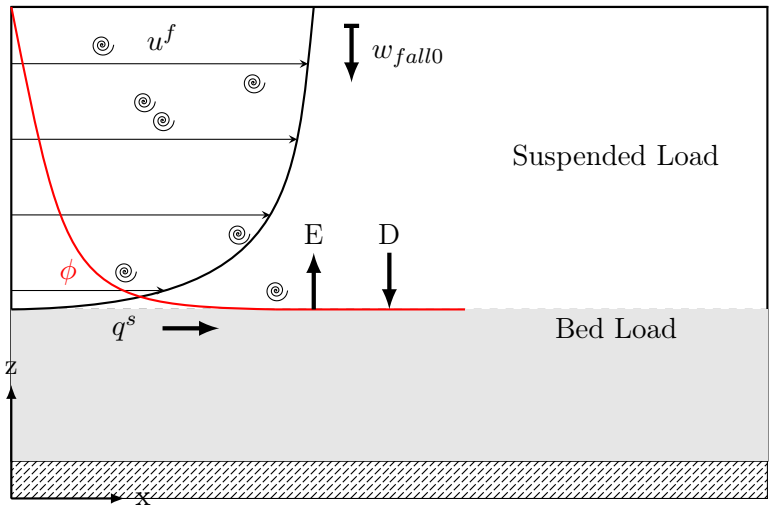

FIGURE 1.4: Sketch of the "classical" hydro-sedimentary models. Adapted from *Chauchat* (2007).

Il est nécessaire de déterminer les conditions aux limites sur le fond pour résoudre complètement l'équation 1.8 ou l'équation 1.14. De manière générale, le flux sédimentaire sur le fond est divisé en deux composantes verticales. La première composante est liée à l'érosion (E) et représente les échanges de sédiments entre le lit et le fluide. Elle est dirigée vers le haut comme le montre la figure 1.4. La deuxième composante D est dirigée vers le bas et liée à la déposition des sédiments sour l'effet de la gravité. La condition aux limites sur le fond pour l'équation 1.14 s'écrit donc :

$$\left(K_\phi \frac{\partial \phi}{\partial z} + w_{fall}\phi\right)\Big|_{z=z_{bed}} = E - D, \tag{1.15}$$

avec z_{bed} la position verticale de l'interface du lit sédimentaire. La déposition des sédiments sous l'effet de la gravité s'écrit simplement comme le flux de chute :

$$D = w_{fall}\phi_{bed}, \tag{1.16}$$

où ϕ_{bed} est la concentration locale en sédiment sur une couche très proche au-dessus de l'interface. Il est existe de nombreuses définitions pour le formulation du taux d'érosion E. Dans le cas de sédiments non-cohésifs, le plupart des formules sont dépendantes de la taille des particules et de la contrainte fluide sur le fond (*Van Rijn*, 1984c). La formulation proposée par *Van Rijn* (1984c) est celle présentant la plus faible variabilité avec la taille des particules pour d$\in [100 - 1000\mu m]$:

$$E = 0.00033\rho^s D^{*0.3} T^{1.5}((s-1)gd)^{0.5}, \tag{1.17}$$

où $T = \dfrac{u^{*2} - u_c^{*2}}{u_c^{*2}}$ est un paramètre décrivant le transport pour lequel u_c^* est la vitesse de friction au seuil de transport définit par *Shields* (1936). $D^* = d\left(\dfrac{(s-1)g}{\nu^2}\right)^{0.33}$ est le diamètre adimensionel des particules.

b) Transport sur le fond

L'application du principe de conservation de la masse de sédiment sur une surface élémentaire du lit permet d'écrire l'équation décrivant l'évolution de la morphodynamique, aussi connue sous le nom d'équation d'Exner (*Exner*, 1920, 1925). Ici, l'équation est présentée sous sa forme la plus simple, appliquée à une couche proche du lit sédimentaire :

$$\rho^s(1-p_b)\frac{\partial z_{bed}}{\partial t} + \nabla_{\mathbf{h}} \cdot \mathbf{q^s} = -E + D, \tag{1.18}$$

avec p_b la porosité du lit, ∇_h l'opérateur gradient horizontal, et $\boldsymbol{q^s}$ le flux de transport par charriage. L'équation d'Exner indique que l'augmentation ou la baisse du niveau du lit est proportionnelle à la déposition ou à l'érosion générée par le flux de sédiment.
Les équations 1.8 et 1.18 sont donc couplées via les termes représentant les flux d'érosion et de déposition avec l'aide de l'équation 1.15.

La résolution de l'équation 1.18 nécessite la détermination du flux de sédiment transporté par charriage $\mathbf{q^s}$. Dans la littérature, on trouve de nombreuses formules pour $\mathbf{q^s}$, la plupart étant empiriques ou semi-empiriques. Parmi les plus utilisées on peut citer les formules de transport de *Meyer-Peter and Müller* (1948), *Wilson* (1966) ou celle de *Engelund and Fredsøe* (1976). Malgré la diversité des formules permettant d'estimer le flux de transport par charriage, on peut exprimer la plupart comme une loi puissance entre le taux de transport adimensionné $q^* = q^s/\sqrt{(s-1)gd^3}$ et le nombre de Shields en excès par rapport au seuil de mise en mouvement des grains :

$$q^* = m\theta^j(\theta - \theta_c)^k, \tag{1.19}$$

où m, j et k sont des constantes différentes suivant les formules de transport. Quelque soit la formule choisie on retrouve généralement $j + k \approx 1.5$, alors que le préfacteur m varie de façon importante suivant les formules choisies. Pour *Meyer-Peter and Müller* (1948), m=8 et dans *Wilson* (1966) on retrouve m=12 par exemple. Une récente réanalyse des résultats de *Meyer-Peter and Müller* (1948) par *Wong and Parker* (2006) propose d'utiliser m=3.97. Ces travaux sont aujourd'hui considérés comme une référence.

La succincte présentation ci-dessus n'a pas vocation à dresser un état de l'art plus poussé de la modélisation "classique" du transport sédimentaire mais plutôt d'en montrer ses limites. On peut ainsi voir qu'avec cette approche, les processus à la petite échelle ne sont absolument pas pris en compte et la couche de transport n'est pas directement résolue. De plus, l'hypothèse de base d'un transport divisé en une composante liée au charriage et l'autre à la suspension est une vision assez simpliste, ne permettant pas de décrire de nombreux cas d'application concrets, comme celui du sheet-flow évoqué dans la section b). Les formulations empiriques permettent d'écrire la relation entre taux de transport et contraintes fluides sur le fond ont été obtenues dans des conditions uniformes idéalisées et sont pour la plupart utilisées en dehors de leur domaine de validité lorsque l'écoulement n'est plus uniforme ou que la pente du lit est importante, comme dans le cas de l'érosion autour d'une pile cylindrique par exemple.

1.2.3 Etat de l'art de la modélisation diphasique du transport sédimentaire

Les difficultés et les imprécisions liées à l'approche classique de la modélisation du transport sédimentaire nécessitent le développement d'autres approches de la modélisation transport, plus

complètes et intégrant la complexité des phénomènes de couplages entre les différents modes de transports sédimentaires et l'hydrodynamique, notamment à l'échelle des grains.

Depuis plus de vingt ans, le développement d'une approche diphasique du transport sédimentaire est un thème de recherche très actif. Dans l'approche diphasique, les équations de la dynamique sont résolues pour les deux phases constituant le milieu, le phase fluide (l'eau) mais également la phase particulaire. Pour cette dernière, le sédiment est vu comme une phase continue et dispersée dans le fluide. Contrairement à l'approche dite "classique", cette approche diphasique permet de tenir compte de la majorité des processus physiques du transport sédimentaire, à savoir les interactions entre particules et fluide, l'effet de la turbulence du fluide sur les particules mais également les interactions particules-particules qui sont dominantes près du lit sédimentaire.

La base de l'approche diphasique repose sur la résolution des équations de conservation de la masse et de la quantité de mouvement pour les deux phases (le fluide et le sédiment). On utilise toujours l'approche milieu continu pour la phase fluide, mais il y a plusieurs façon de décrire la dynamique de la phase particulaire. Il est possible de décrire le comportement de chaque particule et leurs intéractions. On parle alors d'approche lagrangienne. Cette approche est choisie dans les travaux de *Escauriaza and Sotiropoulos* (2011) par exemple. Décrire le sédiment de façon lagrangienne est très coûteux numériquement et donc restreint à un nombre limité de particules, de l'ordre de plusieurs dizaines de millions en 2012 (*Capecelatro and Desjardins*, 2013). Cette approche lagrangienne ne sera pas décrite plus en détail dans cet état de l'art. Dans la littérature, les modèles diphasiques utilisent plutôt une approche milieu continu (ou eulérienne) pour décrire le sédiment, on parle de modèles diphasiques Eulériens-Eulériens (pour la phase fluide et la phase sédimentaire). Dans ce cas, les équations permettant de résoudre la quantité de mouvement pour le fluide (eq. 1.20) et le sédiment (eq. 1.21) sont très similaires entre elles et inspirées des équations de Navier-Stokes (eq. 1.7) :

$$(1-\phi)\rho^f\left(\frac{\partial \boldsymbol{u^f}}{\partial t}+(\boldsymbol{u^f}\cdot\nabla)\boldsymbol{u^f}\right)=-(1-\phi)\nabla p^f+(1-\phi)\left(\boldsymbol{f}+\rho^f\boldsymbol{g}\right)+\nabla\cdot\boldsymbol{\tau^f}-n\boldsymbol{f_D}, \quad (1.20)$$

$$\phi\rho^s\left(\frac{\partial \boldsymbol{u^s}}{\partial t}+(\boldsymbol{u^s}\cdot\nabla)\boldsymbol{u^s}\right)=-\phi\nabla p^f-\nabla p^s+\nabla\cdot\boldsymbol{\tau^s}+\phi\left(\boldsymbol{f}+\rho^s\boldsymbol{g}\right)+n\boldsymbol{f_D}, \quad (1.21)$$

où ϕ est la fraction volumique de sédiment, ρ^k et $\boldsymbol{u^k}$ la masse volumique et le vecteur vitesse pour la phase k, p^k et $\boldsymbol{\tau^k}$ la pression et les contraintes de cisaillement de la phase k, $\boldsymbol{g}$ l'accélération liée à la gravité, $\boldsymbol{f}$ les forces volumiques autres que la gravité, $\boldsymbol{f_D}$ les forces exercées par le fluide sur une seule particule et n le nombre de particules par unités de volume.
Par rapport aux équations de Navier-Stokes utilisées pour l'approche monophasique (eq. 1.7), les équations de conservation de la quantité de mouvement pour les phases fluide (eq. 1.20) et solide (eq. 1.21) sont couplées par le terme $\boldsymbol{f_D}$, représentant les interactions entre le fluide et les particules. Comme détaillé dans le Chapitre 3, ces intéractions sont principalement régies par la trainée et sont proportionnelles au volume de la phase particulaire. Des modèles de fermeture sont nécessaires pour déterminer les contraintes granulaires pour le sédiment ($\boldsymbol{p^s}\overline{\overline{I}}+\boldsymbol{\tau^s}$) ainsi que les contraintes pour le fluide $\boldsymbol{p}\overline{\overline{I}}+\boldsymbol{\tau^f}$. On parlera respectivement de modèle de fermeture pour les contraintes granulaires (intéractions particules-particules) et de modèle de fermeture pour la turbulence. Les descriptions complètes des modèles de fermeture sont proposées dans le Chapitre 3.

Tableau 1.1: Summary of Eulerian-Eulerian two-phase flow models for sediment transport applications

Authors	Turbulence model	Particle stress	Application case
Jenkins and Hanes (1998)	mixing length	kinetic theory	1D Sheet-Flow (SF)
Revil-Baudard and Chauchat (2013)	mixing length	granular rheology	1D Sheet-Flow
Bakhtyar et al. (2009)	$k-\varepsilon$	Bagnold	2D oscillatory SF
Amoudry et al. (2008); *Chauchat and Guillou* (2008); *Cheng et al.* (2017); *Hsu et al.* (2004); *Yu et al.* (2010)	$k-\varepsilon$	kinetic theory	1D SF, 2D Scour
Amoudry (2014); *Jha and Bombardelli* (2009)	$k-\omega$	kinetic theory	1D oscillatory SF, 1D open channel
Lee et al. (2016)	$k-\varepsilon$	granular rheology	2D Scour
Cheng et al. (2018b)	LES	Kinetic theory	3D Sheet-FLow

Les différents modèles diphasiques pour le transport de sédiments présentés dans la littérature peuvent être différenciés par les choix faits par leur auteurs concernant les modèles de fermeture pour la turbulence ou les contraintes granulaires. Un résumé des différents modèles existants avec mention des cas sur lesquels ils ont été appliqués est proposé dans le tableau 1.1.

Concernant les modèles de fermeture pour les contraintes turbulentes, on recense plusieurs grandes familles : les modèles RANS (Reynolds Averaged Navier Stokes equations) dits à "zero-equation" comme l'approche longueur de mélange, les modèles RANS à deux équations (k-ε, k-ω) et les approches de simulations des grandes échelles (LES pour Large Eddy Simulation en anglais) (*Cheng et al.*, 2018b), très récentes et qui ne seront pas détaillées ici.
Parmi les approches RANS, la première développée pour le diphasique est une fermeture type longueur de mélange dans les travaux de *Jenkins and Hanes* (1998). Cette approche a été couramment utilisée par la suite en se limitant à des cas 1D, principalement de sheet-flow (*Chauchat*, 2018; *Dong and Zhang*, 1999; *Revil-Baudard and Chauchat*, 2013). Plus récemment, ce sont les modèles de fermeture à deux équations qui ont abondamment été utilisés dans la littérature, notamment le modèle k-ε (e.g. *Bakhtyar et al.*, 2009; *Hsu et al.*, 2004; *Longo*, 2005) et dans une moindre mesure le modèle k-ω (*Amoudry*, 2014; *Jha and Bombardelli*, 2009). Le modèle k-ε, originalement développé par *Hsu et al.* (2004), a été testé et validé dans de nombreuses configurations allant du sheet-flow unidimensionnel (*Chauchat*, 2018; *Hsu et al.*, 2004), ou oscillant (*Cheng et al.*, 2017) à des configurations 2D d'affouillement derrière une marche (*Amoudry and Liu*, 2009; *Cheng et al.*, 2017), de formation de plug-llow (*Cheng et al.*, 2017) ou d'affouillement 2D sous un pipeline (*Lee et al.*, 2016). Le phénomène de plug-flow (*Sleath*, 1999) est une perte de cohésion momentanée du lit sédimentaire sous l'effet d'un fort gradient de pression horizontal. Le transport de sédiment est alors très intense et ne peut pas être résolu uniquement en tenant compte de la contrainte de cisaillement fluide sur le lit comme dans les modèles classiques. Ce phénomène peut se produire sous l'effet des vagues en zone côtiere (*Foster et al.*, 2006).

Pour la fermeture sur les contraintes granulaires, une première approche basée sur la rhéologie de *Bagnold* (1954) a été proposée par *Hanes and Bowen* (1985) et utilisée dans le cas d'un sheet-flow oscillant par *Bakhtyar et al.* (2009). Néanmoins, ce modèle de fermeture reste assez peu utilisé dans la littérature et on lui préfère deux autres approches : la théorie cinétique des écoulements granulaires (*Jenkins and Savage*, 1983) ou la rhéologie des écoulements granulaires denses $\mu(I)$ (*Forterre and Pouliquen*, 2008; *GDRmidi*, 2004; *Jop et al.*, 2006).
Issue de la théorie cinétique des gaz, la théorie cinétique des écoulements granulaires a d'abord été écrite pour des écoulements granulaires secs (dans l'air) et la première adaptation pour le transport de sédiment a été réalisée par *Jenkins and Hanes* (1998). Cette approche repose sur l'idée que les interactions entre particules sont dominées par les collisions binaires. Dans ce système granulaire collisionnel, la contrainte granulaire peut être déterminée à partir des fluctuations de vitesses de la phase particulaire, la mesure de ces fluctuations est appelée température granulaire (voir Chapitre 3,). La détermination de température granulaire nécessite la résolution d'une équation de transport en plus de l'équation de quantité de mouvement pour la phase particulaire. Très utilisée, notamment pour l'étude du sheet-flow (e.g. *Hsu and Hanes*, 2004; *Hsu et al.*, 2004; *Jenkins and Hanes*, 1998), cette approche est connue pour être inadaptées dans les parties les plus denses de l'écoulement, c'est-à-dire dans les régions où les interactions particules-particules sont régies par des contacts quasi-permanents et non plus par des collisions binaires (*Jenkins*, 2006). Une amélioration, récemment proposée par *Jenkins* (2006) consiste à décomposer l'écoulement en une couche collisionnelle où la théorie cinétique est appliquée et une couche visqueuse décrivant la transition entre ce régime collisionnel et celui quasi-statique du lit sédimentaire fixe. La description de cette couche visqueuse peut se faire de façon analytique. Cette approche semi-analytique et ses améliorations successives (*Berzi*, 2011; *Berzi and Fraccarollo*, 2013, 2015, 2016) peuvent être trouvées dans la littérature sous le nom de théorie cinétique étendue (Extended Kinetic Theory) mais ne seront pas utilisées dans ce travail de thèse.

La seconde grande approche pour la détermination des contraintes granulaires est une approche phénoménologique, appelée rhéologie des écoulements granulaires denses (ou rhéologie $\mu(I)$) et issue des travaux initiés par le *GDRmidi* (2004) pour les écoulements granulaires secs. Cette approche est construite sur une analyse dimensionelle d'une configuration de cisaillement simple (*Forterre and Pouliquen*, 2008) et utilise le nombre inertiel I comme paramètre de contrôle. Ce dernier peut être interprété comme un rapport entre l'échelle de temps caractéristique pour un réarrangement vertical des grains et une échelle de temps de déformation horizontale. Le nombre inertiel I est le paramètre contrôlant le coefficient de friction $\mu(I)$ permettant de faire le lien entre la pression particulaire et les contraintes de cisaillement granulaires nécessaires pour fermer l'équation de quantité de mouvement de la phase particulaire (voir chapitre 3, section b) pour plus de détails). La rhéologie $\mu(I)$ a été appliquée avec succès pour la modélisation du transport sédimentaire dans des conditions laminaires (*Ouriemi et al.*, 2009) et turbulentes (*Chauchat*, 2018; *Lee et al.*, 2016; *Revil-Baudard and Chauchat*, 2013).

Comme indiqué dans le tableau 1.1 la plupart des cas d'application de l'approche diphasique sont monodimensionels et utilisent des modèles de fermeture RANS pour la turbulence. On retrouve quelques cas bidimensionnels (*Amoudry et al.*, 2008; *Bakhtyar et al.*, 2009; *Chauchat and Guillou*, 2008; *Cheng et al.*, 2017; *Lee et al.*, 2016) et un cas très récent 3D, utilisant une approche LES pour la turbulence (*Cheng et al.*, 2018b). Le peu de cas multidimensionnels s'explique par la complexité des modèles utilisés pour l'approche diphasique ainsi que par leur coût important, en terme de temps de calcul. Néanmoins, les configurations pour lesquelles les modèles classiques sont uti-

lisés en dehors de leurs domaines de validité sont souvent des cas complexes, multi-dimensionnels et instationnaires. L'application de l'approche diphasique à des cas d'études multidimensionnels variés passe donc par le développement d'un modèle diphasique multi-dimensionnel intégrant les différents choix de fermeture aussi bien pour la turbulence que pour les contraintes granulaires.

1.2.4 Le phénomène d'affouillement et l'état de l'art de sa modélisation

a) Le phénomène d'affouillement autour d'un obstacle cylindrique

Lorsqu'un objet comme une pile d'éolienne offshore ou une pile de pont est placé dans un écoulement constant (une rivière ou un courant marin en zone côtière), ce dernier va être modifié par la présence de l'objet. Plusieurs structures caractéristiques apparaissent (figure 1.5). Il y a une séparation tridimensionnelle de l'écoulement au niveau du corps solide, sous l'effet notamment d'un fort gradient de pression adverse. Cette séparation de l'écoulement génère une contraction des lignes de courant de chaque côté de l'objet considéré. Cela conduit à une accélération de l'écoulement autour du corps solide. Il y a formation d'une couche limite au niveau de la structure solide et génération d'un lâché tourbillonnaire dans le sillage de la structure à partir du point de décollement (on parlera de vortex-shedding en anglais). Devant la pile, au niveau du point d'arrêt, l'écoulement devient plongeant et vient impacter sous forme d'un jet le lit sédimentaire, générant ainsi la formation d'un tourbillon dit "en fer à cheval" (horseshoe vortex, HSV) près du fond, devant et autour de la structure solide. La présence du corps solide induit également une déflexion de la surface libre et une génération de tourbillons (surface roller). Moins importante que les autres structures tourbillonnaires de l'écoulement, cette déflexion peut être négligée quand le nombre de Froude ($F_r = u^f/\sqrt{gh}$, avec h la hauteur d'eau) est inférieur à 0.2 (*Roulund et al.*, 2005), c'est à dire quand les effets de pesanteur sont importants devant l'inertie du fluide.

Les structures tourbillonnaires comme le lâché tourbillonnaire à l'aval mais surtout le tourbillon fer à cheval (HSV) conduisent à une augmentation locale des contraintes fluides sur le fond. En milieu fluvial ou côtier, le fond étant généralement composé de sédiments, le transport solide local est alors plus important et une fosse d'érosion (scour hole) se met en place autour de l'ouvrage comme le montre la figure 1.5. C'est le phénomène d'affouillement. Ce phénomène est difficile à mesurer et quantifier sur le terrain. Sa compréhension s'est d'abord construite sur une approche empirique en laboratoire et sur des cas simples, notamment celui de l'affouillement autour d'une pile cylindrique dans un écoulement constant.

Selon *Chabert and Engeldinger* (1956), les conditions de l'écoulement loin de l'ouvrage permettent de distinguer deux types d'affouillement :

- Si l'écoulement amont n'induit pas de transport sédimentaire ($\theta < \theta_c$), alors on parle d'affouillement de type eau claire (clear-water). Dans ce cas le sédiment est érodé par l'écoulement et la fosse d'érosion n'est jamais réapprovisionnée en sédiment.
- Si l'écoulement amont induit un transport sédimentaire, alors on parle d'affouillement de type lit mobile (live-bed). Dans ce cas, le sédiment est érodé par l'écoulement pour former la fosse d'érosion, mais, dans le même temps, celui-ci réapprovisionne continuellement la fosse d'érosion en particules.

Dans le temps, le profondeur de la fosse d'érosion augmente et la capacité d'érosion du tourbillon fer à cheval diminue progressivement jusqu'à ce qu'un état d'équilibre soit atteint. Dans le cas d'affouillement de type clear-water, l'état d'équilibre est atteint lorsque la contrainte sur le fond

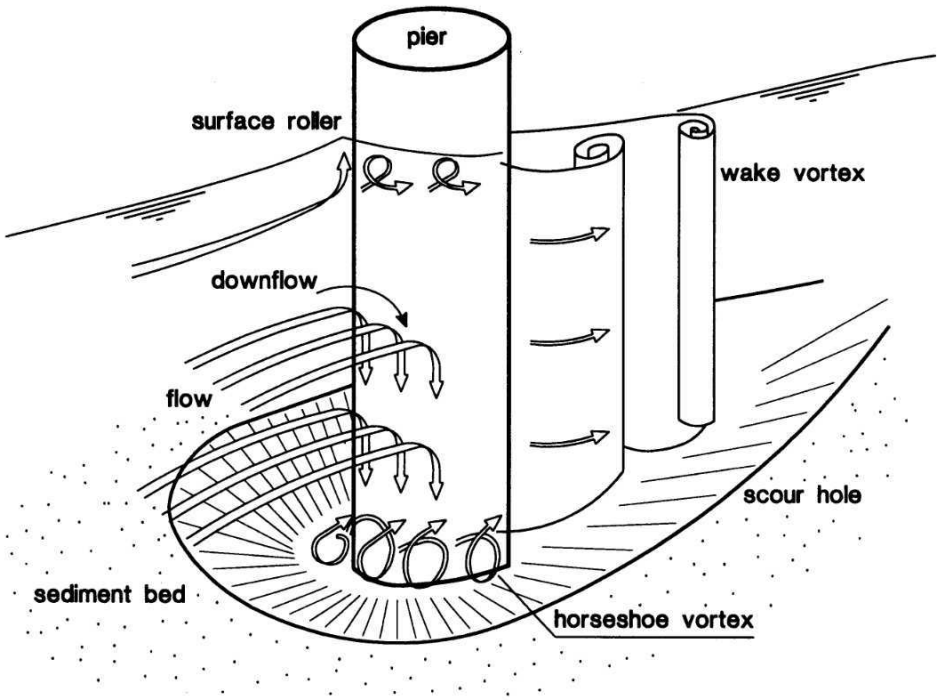

FIGURE 1.5: Sketch of the flow around a vertical cylinder mounted in a sediment bed. Source : *Melville and Sutherland* (1988).

de la fosse d'érosion est de l'ordre de la contrainte critique de mise en mouvement des grains ($\theta \approx \theta_c$). Dans le cas d'un affouillement de type live-bed, il est atteint lorsque sur une période donnée, la quantité moyenne de sédiment apportée à la fosse d'érosion et égale à celle extraite sous l'effet des structures tourbillonnaires (*Melville*, 1984). Dans les deux cas, la profondeur à l'équilibre correspond à l'écart d'élévation entre le point le plus profond de la fosse d'érosion et l'interface du lit sédimentaire non perturbé. Son ordre de grandeur est celui du diamètre de l'obstacle.
La dynamique d'affouillement est également différente suivant que celui-ci soit de type eau claire ou lit mobile. Ainsi, pour le cas lit mobile, l'équilibre est atteint rapidement et la profondeur d'équilibre évolue périodiquement autour d'une valeur moyenne à cause du passage des formes de fond dans la fosse d'érosion. La figure 1.6, issue de *Melville and Chiew* (1999) montre que le temps nécessaire pour atteindre le regime d'équilibre est plus long en configuration d'affouillement eau claire que lit mobile. On peut également y voir que le temps mis pour atteindre l'équilibre augmente rapidement avec la vitesse dans le cas d'un régime eau claire alors que c'est le contraire dans le cas d'un régime lit mobile.

Les premiers travaux présentés dans la littérature ont d'abord cherché à caractériser les structures tourbillonnaires autour de la pile et les profondeurs maximales d'affouillement en fonction de paramètres comme la vitesse, la profondeur de l'écoulement, le diamètre ou la forme de la pile ainsi que l'angle d'incidence de l'écoulement par rapport à celle-ci. Une revue de différents travaux sur le sujet peut être trouvée dans *Breusers et al.* (1977). Des travaux portant sur l'es-

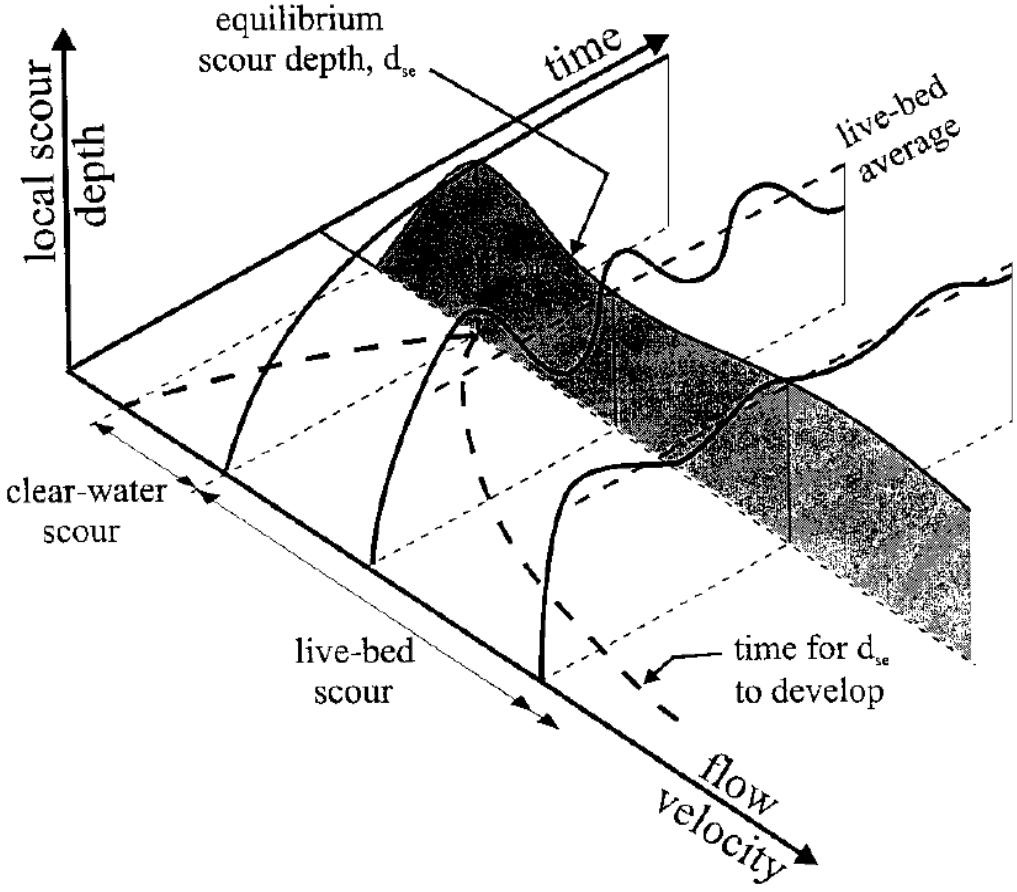

FIGURE 1.6: Erosion depth variations as a function of flow velocity and time. Source : *Melville and Chiew* (1999)

.

timation des sur-contraintes générées par les structures tourbillonnaires sur le lit sédimentaire peuvent être trouvés dans *Hjorth* (1975) ou *Melville et al.* (1975).

L'étude détaillée de l'interaction des structures tourbillonnaires, tel que le tourbillon fer à cheval avec le lit sédimentaire a été faite par *Dargahi* (1990) dans le cas d'un affouillement de type eau claire et pour un Reynolds de 39 000. Le nombre de Reynolds considéré ici est celui lié au diamètre de la pile et est défini comme :

$$Re_D = \frac{\overline{U^f} D}{\nu}, \tag{1.22}$$

avec $\overline{U^f}$ la vitesse moyenne de l'écoulement fluide et D le diamètre de la pile.
Initialement, l'affouillement généré par le HSV apparait non pas dans l'axe du cylindre mais à $\pm 45°$ par rapport à l'axe longitudinal. Il est généré par le vortex que *Dargahi* (1990) nomme V1, situé à la base de la pile (voir figure 1.7). Très rapidement l'affouillement apparait de façon

simultanée en dessous des quatre autres vortex composant le système et un processus d'érosion du sédiment sous l'effet de ces structures tourbillonnaires se met en place. Par la suite, les fosses d'érosion formées sous V2 et V4 se déplacent vers la face amont du cylindre. Le comportement du HSV est décrit par *Dargahi* (1990) comme suit : le sédiment est érodé sous l'effet de V2 et V4, et mis en suspension dans V3 et V5. Une partie du sédiment est piégée dans le système tourbillonnaire et évacuée vers l'aval tandis que l'autre va avoir tendance à se redéposer sous V3 et V5 (voir figure 1.7.c) formant deux bosses. Si la position de V1 n'évolue pas dans le temps, les tourbillons V2, V3, V4 et V5 possèdent une dynamique oscillante amont/aval dans le plan de symétrie. De ce fait, les fosses d'érosions générées par V2 et V3 et les zones de déposition varient spatialement dans le temps. C'est de cette dynamique que naît l'affouillement. A mesure que le temps augmente, les fosses d'érosions sont de plus en plus profondes et présentent de fortes pentes. L'ensemble du sédiment devient très instable ; ce qui a pour effet d'augmenter le transport. L'augmentation de la profondeur de la fosse liée à V2 a une influence sur l'hydrodynamique, les vortex V1 et V2 se rassemblent (figure 1.7.f et .g) et la pente de la fosse formée présente une forme concave près du cylindre. Le système tourbillonnaire présente alors deux tourbillons principaux et deux fosses d'érosion associées (figure 1.7.f et .g). Le sédiment érodé au sein de ces deux fosses provient partiellement de leur excavation et partiellement de l'évacuation du surplus apporté par les avalanches produites sur leurs pentes amont. Dans le temps, le système tend vers une seule fosse d'érosion présentant deux pentes différentes mais de longueur similaire (figure 1.7.k). Ces deux pentes résultent de la présence des deux vortex principaux du système pour les temps longs, V2 et V4. En effet, si V3 et V5 sont toujours présents, leur intensité et leur importance pour les temps longs sont fortement réduites.

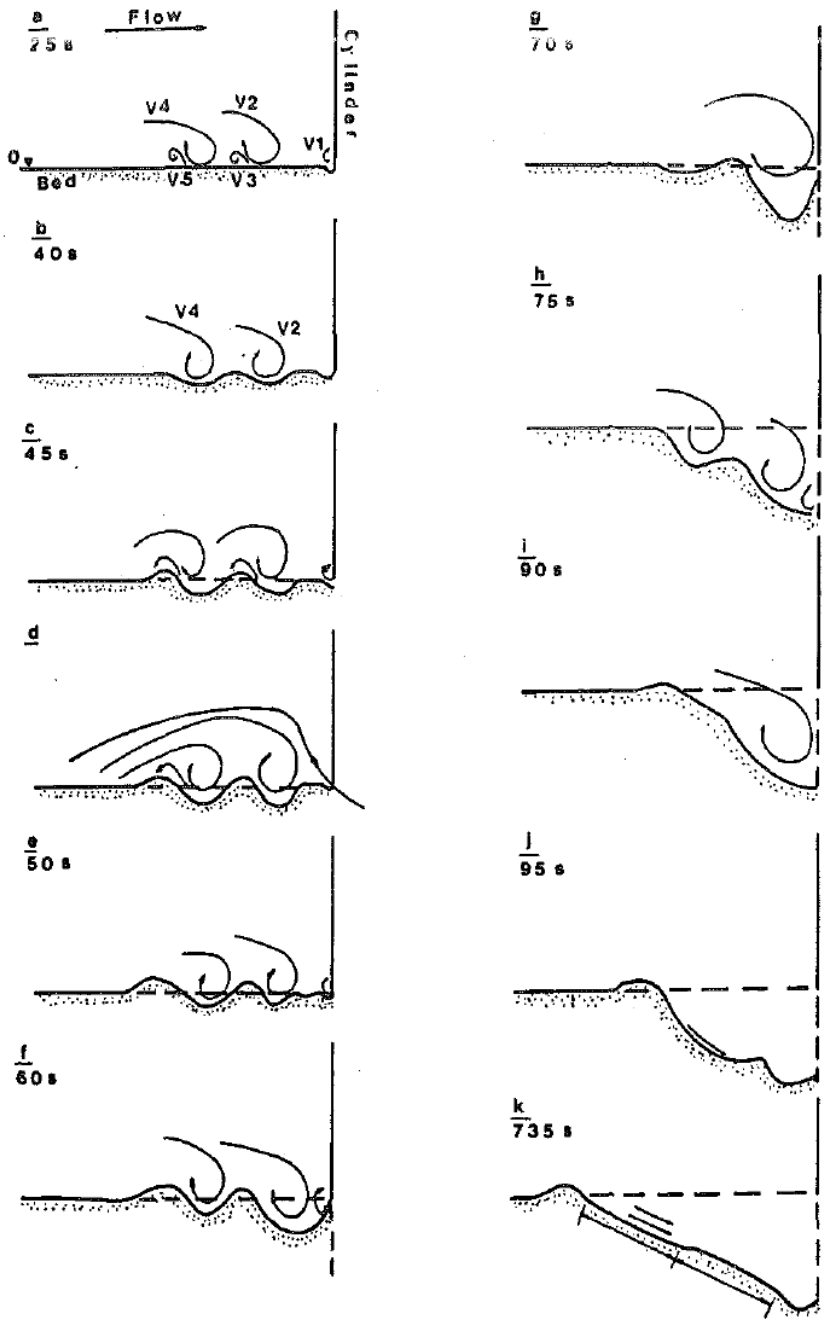

FIGURE 1.7: Schematic sketch of a clear-water scour hole formation under the effect of the horseshoe vortex. Source : *Dargahi* (1990).

La figure 1.8 montre le profil d'érosion observé par *Dargahi* (1990) le long du plan de symétrie pour un affouillement de type eau claire autour d'une pile cylindrique. On distingue une certaine symétrie entre la fosse amont générée par le HSV et celle avale, due au vortex shedding. Dans les deux cas on retrouve une rupture de pente entre une pente supérieure (entre les points 1 et 2)

et inférieure (entre 2 et 3). De plus, ces pentes sont à peu près d'égale longueur. Les différences notables sont la formation d'une dune en 1 à l'aval de la pile alors que le lit reste plat pour l'amont. Ensuite, la pente concave liée à l'intéraction de l'écoulement plongeant et du tourbillon fer à cheval est uniquement observable pour la fosse d'érosion amont.
Dans le cas eau claire, *Dargahi* (1990) décrit le mécanisme d'érosion amont comme le résultat de la combinaison de l'action des deux vortex principaux V2 et V4 et de l'écoulement plongeant au front du cylindre. A l'aval, la formation de la fosse d'érosion est due à l'action des tourbillons détachés du cylindre. Le transport à l'aval est périodique et gouverné par la fréquence de lâché des tourbillons. La formation de rides y a également été observée par *Dargahi* (1990). C'est le tourbillon fer à cheval dont la formation s'étend jusqu'à l'aval qui fait le lien entre les fosses d'érosion amont et avale.

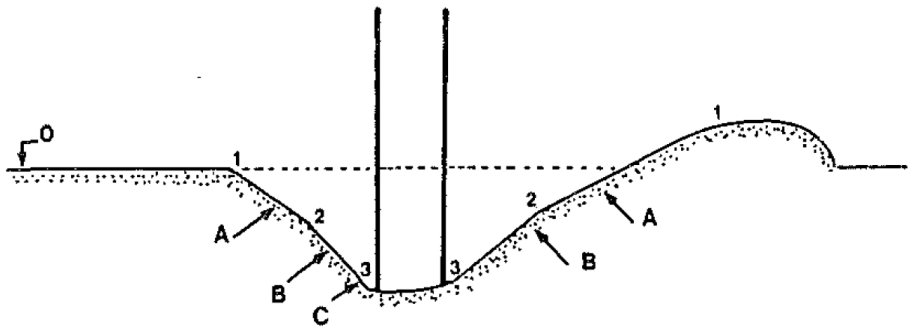

FIGURE 1.8: Erosion profile along the symmetry plane in the case of clear-water scour around a cylindrical pile. A and B are the upper and lower part of the scour slopes, C the concave slope upstream of the pile. The flow is coming from the left. Source : *Dargahi* (1990).

L'étude de l'affouillement et de l'évolution de la forme de la fosse d'érosion proposée par *Dargahi* (1990) est faite principalement dans le plan de symétrie. Des expériences plus récentes ont permis de montrer que dans le cas eau claire, l'érosion est maximum dans un premier temps sur les côtés du cylindre mais qu'à l'équilibre on retrouve toujours le maximum d'érosion devant l'obstacle, dans plan de symétrie. Ce résultat est vrai pour des sédiments allant des sables (*Link et al.*, 2008) aux graviers (*Diab et al.*, 2010).

Concernant le cas lit mobile, la dynamique d'affouillement est impactée par le transport de sédiment en dehors de la fosse d'érosion vers celle-ci. Les structures tourbillonnaires responsables de l'affouillement sont également le tourbillon fer à cheval et le lâché tourbillonaire à l'aval mais la littérature ne semble pas montrer une investigation poussée de l'interaction de ces structures avec la dynamique d'érosion comme celle de *Dargahi* (1990) pour le cas eau claire. Les dynamiques et les états d'équilibre de chaque type d'affouillement comportent des différences. Cependant leurs effets sur les ouvrages comme les éoliennes offshore ou les ponts sont similaires. En effet, si l'affouillement est trop important, les fondations de la pile peuvent être mises à nue, réduisant sa stabilité jusqu'à parfois conduire à son effondrement. Une conséquence connue mais pas si marginale avec des coûts associés important (voir section 1.1).

C'est pour réduire ces risques que parallèlement à l'amélioration des connaissances sur la physique de l'affouillement, la littérature a produit beaucoup de travaux portant sur le développement de formules permettant de déterminer la profondeur maximum d'érosion pour des configurations précises (forme de la pile, type d'affouillement). Parmi les plus utilisées, on peut citer celles de *Breusers et al.* (1977) ou *Melville and Sutherland* (1988). La plupart des ces formules sont obtenues de façon empirique et beaucoup présentent des biais importants lorsqu'elles sont comparées à des données de terrain (*Johnson*, 1995).

L'amélioration des connaissances du phénomène d'affouillement à principalement été construite sur le cas des piles de ponts en rivière, et donc soumises à un écoulement constant. Des ouvrages comme ceux de *Dargahi* (1982), *Breusers and Raudkivi* (1991) ou *Melville and Coleman* (2000) permettent d'avoir une vision claire de l'état de l'art à une époque et de son évolution dans le temps.
En zone côtière, le courant dans lequel sont placées les structures solides n'est plus constant mais oscillant (marées, vagues). La dynamique oscillante du courant peut être générée par la marée ou par les variations météorologiques locales. Ces perturbations vont alors complexifier la dynamique de l'affouillement. Un état de l'art complet de l'affouillement en zone côtière peut être trouvé dans des ouvrages comme ceux de *Whitehouse* (1998) ou *Sumer et al.* (2002).

La dynamique de l'affouillement est également complexifiée quand les objets solides autour desquels elle s'effectue sont très rapprochés. On évoquera uniquement ici le cas d'un groupe de piles cylindriques dans un écoulement constant. Dans ce cas, on distingue alors deux échelles spatiales pour l'affouillement, autour d'une pile et autour du groupe de pile. Les résultats expérimentaux de *Sumer et al.* (2005) ont montré que suivant l'agencement des piles constituant le groupe, l'affouillement autour de l'ensemble pouvait être bien plus important que celui autour de chaque pile.

La plupart des configurations expérimentales d'affouillement les plus récentes sont des configurations complexes portant sur l'étude de régimes d'affouillement particuliers. On peut citer ici plusieurs sujets de recherches actuels comme l'affouillement autour de piles possédant des enrochements de protections (*De Vos et al.*, 2011, 2012; *Petersen et al.*, 2015; *Whitehouse et al.*, 2011), l'affouillement autour de structures complexes comme des tripods (*Stahlmann et al.*, 2013) ou encore la meilleure détermination de la forme globale de la fosse d'érosion et de sa dynamique de formation (*Link et al.*, 2008, 2012).

Si la recherche expérimentale actuelle s'axe majoritairement sur les configurations complexes évoquées ci-dessus, le cas simple d'un affouillement autour d'une pile cylindrique dans un écoulement constant continue d'être étudié. Ainsi, il a été récemment observé que, dans le cas clear-water, la condition de déclenchement de l'érosion par le lâché tourbillonnaire à l'aval du cylindre est plus faible que celle du tourbillon fer à cheval. De ce fait, pour une petite gamme d'écoulements, l'érosion est principalement liée au lâché tourbillonnaire à l'aval et non au tourbillon fer à cheval (*Lachaussée et al.*, 2018).

b) Modélisation numérique du phénomène d'affouillement

La littérature est moins riche concernant la simulation numérique de l'affouillement. Cette approche fut longtemps impossible car les ressources informatiques n'étaient pas suffisantes pour permettre de résoudre des problèmes tri-dimensionnels complexes. On se limite ici à des cas

d'affouillement dans un courant constant et à des approches numériques utilisant un couplage entre un code pour l'hydrodynamique (résolution des équations de Navier-Stokes 3D) et un code pour la morphodynamique (résolution de l'équation d'Exner, voir section 1.2.2). Ces modèles sont à ce jour ceux qui traitent de la meilleure façon la simulation numérique de l'affouillement. La première simulation numérique 3D du phénomène d'affouillement autour d'une pile placée dans un écoulement constant date de 1993 (*Olsen and Melaaen*, 1993). Dans ce travail, la résolution de l'hydrodynamique repose sur les équations Navier-Stokes (NS) stationnaires avec un modèle de turbulence k-ε et une équation d'advection-diffusion permet de décrire l'évolution de la concentration en sédiments à partir des contraintes de cisaillement. L'affouillement n'est pas simulé jusqu'à l'équilibre, mais les comparaisons avec les mesures expérimentales montrent que le transitoire est bien reproduit au niveau du tourbillon fer à cheval. En revanche, le modèle de *Olsen and Melaaen* (1993) n'est pas à même de reproduire l'érosion à l'aval du cylindre, car le modèle k-ε ne prédit pas de lâché tourbillonnaire.
L'amélioration de la puissance de calcul permet à *Olsen and Kjellesvig* (1998) de poursuivre le cas eau claire reporté dans *Olsen and Melaaen* (1993) jusqu'à l'équilibre de l'affouillement et d'obtenir une profondeur de la fosse d'érosion amont (générée par le tourbillon fer à cheval) en accord avec plusieurs formules empiriques de la littérature.

Les travaux de *Roulund et al.* (2005) présentent une avancée majeure dans la simulation numérique du phénomène d'affouillement. Les équations de NS stationnaires sont résolues et le modèle RANS le plus performant pour les cas de fort gradient de pressions adverses, le k-ω SST (*Menter*, 1993) est utilisé pour déterminer les contraintes de Reynolds. Le transport sédimentaire (simplifié à un transport par charriage uniquement) est résolu grâce à la formulation de *Engelund and Fredsøe* (1976). Un modèle d'avalanche permettant d'éviter des angles de pentes supérieurs à l'angle de repos des sédiments dans la fosse d'érosion est également utilisé. Pour la première fois, c'est un cas de transport lit mobile qui est modélisé. Les contraintes sur le fond ainsi que les profondeurs d'erosion amont et avale sont comparées entre les prédictions numériques et les expériences réalisées. *Roulund et al.* (2005) montrent que l'accord entre prédictions numériques et observations expérimentales est concluant dans le transitoire et à l'équilibre pour la plupart des grandeurs observées. Les simulations présentées dans *Roulund et al.* (2005) sont souvent considérées comme un cas de référence dans de nombreuses simulations numériques postérieures (*Baykal et al.*, 2015; *Stahlmann et al.*, 2013).

Avec une approche de types RANS pour la turbulence, une amélioration significative des prédictions d'érosion par rapport à *Roulund et al.* (2005) passe par la prise en compte du transport par suspension en plus de celui par charriage. Ainsi, *Baykal et al.* (2015) obtiennent une amélioration très nette par rapport aux prédictions de *Roulund et al.* (2005) lorsqu'une équation d'advection diffusion pour la concentration en sédiment (*Fredsøe and Deigaard*, 1992) est ajoutée dans le modèle de transport, un résultat déjà obtenu par *Stahlmann et al.* (2013).
De plus, *Stahlmann et al.* (2013) et *Baykal et al.* (2015) montrent que la résolution des équations de NS instationnaires permet de prédire le vortex-shedding et donc d'améliorer les prédictions d'affouillement en aval du cylindre.

Il ressort des travaux précédents que l'amélioration de la prédiction des structures tourbillonnaires comme le tourbillon fer à cheval ou le lâché tourbillonnaire à l'aval de la pile permettrait d'améliorer l'accord entre les mesures et les prédictions numériques pour le phénomène d'affouillement. Cependant, les approches URANS couramment utilisées sont généralement trop diffusives

pour résoudre avec precision les structures cohérentes de l'écoulement (*Paik et al.*, 2004, 2007). ll vaut alors mieux recourir à des approches LES. Il n'existe pas à l'heure actuelle de travaux traitants de l'application d'une approche SGE pour la turbulence couplée avec un modèle de transport sédimentaire "classique" au cas d'affouillement tri-dimensionnel autour d'un cylindre. Cependant, les travaux de *Kirkil et al.* (2008) et *Link et al.* (2012) utilisant l'approche SGE pour l'hydrodynamique dans des fosses d'érosion "figées" (le fond du domaine de calcul a la forme d'une fosse d'érosion mais il n'y a pas de modèle de transport sédimentaire) montrent bien que cette approche permet de retrouver une dynamique tourbillonnaire complexe dans le HSV proche de celle décrite par *Dargahi* (1990) (oscillation bimodale, plusieurs vortex de tailles différentes).

L'étude de configurations d'affouillement complexes comme celui autour de structures de types treillis ou tripods (*Stahlmann et al.*, 2013) ou l'affouillement en présence d'enrochements de protections (*Nielsen et al.*, 2013) peut également se faire numériquement. Pour les tripods, les calculs sont très lourds et les interactions entre l'hydrodynamique et la structure solide sont assez mal maitrisées. Pour le moment, seule une preuve de concept de l'applicabilité des modèles numériques sur ce genre de configuration a été apportée par *Stahlmann et al.* (2013).

L'approche "classique" de modélisation de l'affouillement passe par l'utilisation de formules de transport sédimentaire empiriques (voir section 1.2.2) pour résoudre la dynamique du lit. Celles-ci sont majoritairement obtenues dans des configurations uniformes et idéalisées (*Engelund and Fredsøe*, 1976; *Meyer-Peter and Müller*, 1948). De ce fait, la plupart sont utilisées en dehors de leur domaine de validité lorsqu'on les applique dans le cas de l'affouillement tri-dimensionnel autour d'une pile cylindrique. Ainsi, dans la fosse d'érosion, les interactions complexes entre le tourbillon fer à cheval, les sédiments et la forte pente rendent l'environnement très éloigné des conditions d'obtention de ces lois de transport.
Dans un cas comme celui de l'affouillement autour d'une pile cylindrique les accords entre les prédictions des modèles et les observations sont concluantes du point de vue de la recherche (*Baykal et al.*, 2015). Cependant, pour dimensionner des ouvrages de génie civils, les modèles classiques de transport sédimentaire ne sont pas assez complets pour être utilisées par les ingénieurs sans avoir préalablement recours à des modèles physiques (*Harris et al.*, 2016) pour les paramétriser.
Dans le cas d'affouillements plus complexes (backfilling, vagues, protections, tripods) les études numériques sont aujourd'hui un moyen d'améliorer les connaissances scientifiques sur ces phénomènes complexes plutôt qu'un outil d'ingénierie.

Pour la simulation numérique du phénomène d'affouillement, s'affranchir des hypothèses classiquement utilisées comme la distinction du flux sédimentaire généré par le charriage et la suspension semble nécessaire pour améliorer les prédictions des modèles. Le développement de modèles diphasiques eulériens-lagrangiens comme celui de *Escauriaza and Sotiropoulos* (2011) peut être ici cité dans cet effort de recherche d'une autre approche pour la modélisation de l'affouillement. Cependant, les ressources de calcul demandées par une approche lagrangienne pour la description du milieu granulaire sont si importantes qu'on ne peut modéliser qu'un petit nombre de particules, moins que nécessaire pour une simulation complète d'un affouillement tridimensionnel. Ainsi, la configuration présentée dans le Chapitre 5 nécessiterait d'utiliser 6.5 Milliards de particules, beaucoup plus que ce qui est actuellement possible. L'utilisation de l'approche diphasique lagrangienne pour réaliser une simulation d'affouillement complète est donc impossible. On peut néanmoins étudier certains aspects de l'affouillement via une approche lagrangienne,

comme dans les travaux de *Link et al.* (2012) où 10 000 particules sont utilisées pour étudier le transport de sédiment dans une fosse d'érosion déjà formée.
Les temps de calculs associés à une approche diphasique eulérienne-eulérienne sont également très importants. Ils sont néanmoins plus compatibles avec une configuration 3D d'affouillement qu'une description lagrangienne des sédiments. Par le passé, seules des configurations 2D ont été réalisées avec cette approche (*Amoudry and Liu*, 2009; *Cheng et al.*, 2017; *Lee et al.*, 2016), et le passage à une configuration 3D représente un réel challenge en terme de calculs numériques à haute performance.

1.3 Objectifs et organisation de la thèse

Deux grands axes de recherche sont suivis dans ce manuscrit. Le premier porte sur les interactions entre le sillage éolien généré par la turbine et les dynamiques locales de l'océan et du sédiment à l'aide d'un modèle bi-dimensionnel suivant l'approche classique du transport sédimentaire. Le second traite de la modélisation du phénomène d'affouillement autour d'une pile cylindrique à l'aide d'un modèle diphasique eulérien tri-dimensionnel.
Les échelles spatiales d'étude mais également les approches de modélisation numérique choisies sont différentes entre les deux axes de ce travail. En revanche, l'objectif global est le même : il s'agit d'apporter des éléments de réponses contribuant à l'amélioration de la connaissance des interactions entre les différentes parties d'une éolienne offshore et son environnement.

Le chapitre 2 porte sur la modélisation numérique des interactions multi-échelles entre le système couplé atmosphère-ocean-sédiment et le sillage atmosphérique généré par une turbine éolienne offshore. Ce travail est motivé par les études de *Broström* (2008), *Rivier et al.* (2016) et *Van der Veen et al.* (2007) montrant les impacts d'une ferme éolienne offshore sur la dynamique locale de l'océan et du sédiment. Ici on cherche à savoir si des impacts similaires peuvent être trouvés à l' échelle d'un sillage. L'approche utilisée pour le transport de sédiment est l'approche "classique" présentée dans la section 1.2.2. Concernant la dynamique océanique, *Moulin and Wirth* (2014) ont récemment montré l'importance de la prise en compte de la vitesse de l'océan pour les intéractions atmophère-océan à la méso échelle (O (10km)). Or, la plupart des modèles de sillages éolien considèrent l'océan comme une frontière inerte, ce qui peut nuire à leur fiabilité.
Les travaux présentés dans ce chapitre 2 tentent de répondre aux questions suivantes : (i) Quel est l'impact d'un sillage éolien offshore sur la dynamique locale de l'océan et du sédiment en tenant compte de la vitesse de l'océan pour les intéractions atmophère-océan ? (ii) Est-il possible de les paramétriser pour de futurs calculs à l'échelle d'un parc ou d'une région ? (iii) Est ce que les dynamiques de l'océan et du sédiment peuvent avoir une rétro-action sur les bilans énergétiques autour d'une turbine ? Ces résultats ont été publiés dans *Nagel et al.* (2018).

L'étude de l'affouillement par une approche diphasique fait l'objet des chapitres suivants. Le chapitre 3 décrit le modèle diphasique eulérien pour le transport de sédiment (SedFoam). Le chapitre 4 porte sur la validation du modèle sur des cas de transport de sédiment 1D et 2D. Enfin le chapitre 5 traite de l'application à l'affouillement tridimensionnel autour d'une pile de forme cylindrique dans un écoulement constant. Les objectifs de cette partie du manuscrit sont les suivants : (i) apporter une preuve de concept que l'approche diphasique peut être utilisée dans le cas de simulations tri-dimensionnelles complexes, avec des interactions multiples entre l'écoulement, la structure solide et le lit sédimentaire. (ii) caractériser l'apport des processus à la

petite échelle dans la modélisation du phénomène d'affouillement. (iii) caractériser l'impact des hypothèses classiquement effectuée comme la corrélation locale entre le flux de sédiments et la contrainte de cisaillement fluide sur le fond pour le transport de sédiment dans la fosse d'érosion. Une partie des résultats présentés dans le chapitre 4 a été utilisée pour la rédaction d'une publication sur SedFoam (*Chauchat et al.*, 2017).
Enfin, une conclusion générale sur les deux grands axes de ce travail de thèse ainsi que les perpectives est proposées dans le chapitre 6.

Chapitre 2

Offshore wind turbine wake interaction with the ocean-sediment dynamics

2.1 Résumé

La première partie de cette thèse porte sur la modélisation numérique des interactions multi-échelles entre le système couplé atmosphère-ocean-sédiment et le sillage atmosphérique généré par une turbine éolienne offshore. Ici on veut modéliser ces interactions à l'échelle locale grâce à un modèle numérique idéalisé en deux dimensions. Ce dernier est composé de deux modules, le premier résout les équations de Shallow Water (SW) pour l'océan et le second résout l'équation de conservation de la masse du sédiment pour le transport sédimentaire. Les deux modules sont couplés par une loi de friction quadratique. La vitesse relative entre l'atmosphère et l'océan est prise en compte dans le forçage atmosphérique, ce qui est novateur par rapport à la littérature.

Les résultats obtenus montrent que le sillage généré par la turbine d'une éolienne offshore impacte la surface de l'océan et peut générer des instabilités ou des allées de tourbillons à cet interface. Pour des conditions de vent forts et pour des épaisseurs de colonne d'eau importantes (H>15m), des instabilités grandes échelles sont générées, conduisant à une dynamique turbulente dans l'océan. Cette turbulence océanique est contrôlée par le paramètre de sillage $S = C_D D/H$, où D est le diamètre du sillage au point d'impact sur la surface de l'océan et C_D est le coefficient de la loi de friction quadratique entre l'océan et le fond.
La dynamique turbulente océanique est intégrée numériquement à l'aide de simulations instationnaires fine échelle (1m). A partir de ces simulations, des coefficients de viscosité turbulente permettant la parametrisation des flux turbulents sont proposés pour être utilisés dans des modèles à plus grande échelle, notamment des modèles RANS. La dynamique océanique, donc les valeurs des coefficients de viscosité turbulente, dépendent principalement du paramètre S.

La dynamique océanique peut avoir (i) un comportement laminaire ($S>7.10^{-2}$), (ii) turbulent localement ($3.10^{-2}<S<7.10^{-2}$) ou (iii) complètement turbulent ($S<3.10^{-2}$). Dans les deux premiers cas, les variations de l'élévation du fond marin sont de l'ordre de quelque millimètres par mois. Pour le troisième cas, si l'on moyenne sur plusieurs jours, les variations d' élévation du fond marin diminuent jusqu'à atteindre quelques dixièmes de millimètres par mois alors que les variations instantanées (de l'ordre de la demi-heure) sont jusqu'à dix fois plus importantes. Ce

phénomène s'explique par la dynamique tourbillonnaire de chaque cas. Quand celle ci est importante (iii), l'alternance de vitesses positives et négatives en un point de l'espace conduit à un mouvement de va et vient des sédiments localement réduisant le transport sédimentaire global dans le temps.
Les résultats ont également permis de mettre en évidence que le fait de tenir compte de la vitesse de l'ocean dans le calcul du forçage atmosphérique à l'interface ocean-atmosphère permet de diminuer de 4% (dans la configuration étudiée) l'énergie perdue par friction à cet interface. Ce dernier résultat laisse penser que la dynamique océanique pourrait avoir un effet rétroactif non négligeable sur la puissance de vent disponible pour chaque turbine dans une ferme éolienne offshore.

Foreword

This part of the manuscript (together with the Appendix A) is the copy of the article entitled "On the multi-scale interactions between an offshore-wind-turbine wake and the ocean-sediment dynamics in an idealized framework - A numerical investigation" and published in the ***Renewable Energy*** *journal, (Nagel et al., 2018).*
All the work undertaken on this topic is reported in the article, including an appendix presenting the morphodynamic model (see Appendix A).
Please note that the physical variables naming convention in the article may varies from the ones used in other parts of this thesis.

2.2 Physical and Mathematical Model

The physical model consists in two superposed layers (figure 2.1.a), a homogeneous shallow water ocean layer above a sediment bed layer, composed of cohesion-less particles. The atmospheric layer is represented as an external forcing (F), which corresponds to the wake of wind turbines.

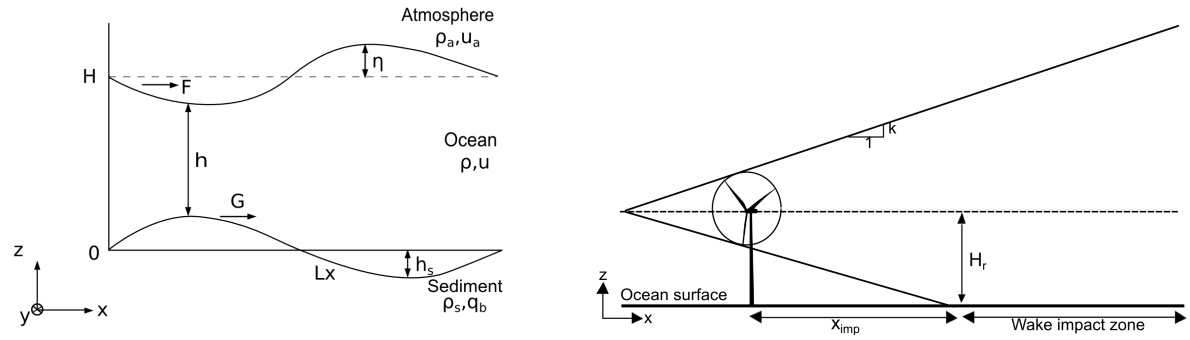

FIGURE 2.1: Sketch of the two layer physical model (a) and of the Jensen wake (b). All the variables are detailled in the text.

The domain length in the x-direction is denoted by L_x and by L_y in the y-direction. The average depth of the ocean layer is denoted as H and the bed load transport rate is denoted as q_b. The local thickness of the ocean layer and the seabed elevation, are denoted as $h(x, y, t)$ and

$h_s(x, y, t)$, respectively. The free surface elevation is :

$$\eta(x, y, t) = h(x, y, t) - H + h_s(x, y, t). \tag{2.1}$$

The dimensional variables are consigned in the table 2.1. Densities are denoted as ρ, ρ_s and ρ_a for the ocean, the sediment and the atmosphere, respectively, d_s is the diameter of a sand grain. The ocean layer is forced by the local wind stress at its upper surface. The spatial variation of this wind stress incorporates the wake-profile of a wind turbine.
The oceanic motion induces a shear stress τ_b on the sediment bed layer. This stress and the seabed elevation are responsible for the coupling between the ocean and the sediment bed layers.

2.2.1 Hydrodynamic model

Mathematically, the ocean dynamics is given by the two dimensional Shallow Water (SW) equations (*de Saint-Venant*, 1871; *Vallis*, 2006). Most of the wind farms are localized in coastal areas, in 2012 for example, the average water depth of offshore wind farms was of 22m (*EWEA*, 2013). These equations are therefore considered to be adequate to describe the problem :

$$\partial_t \mathbf{u} + (\mathbf{u} \cdot \nabla)\mathbf{u} + g\nabla\eta \;=\; \nu\nabla^2\mathbf{u} + \mathbf{F} - \mathbf{G} \tag{2.2}$$

$$\partial_t h + \nabla(h\mathbf{u}) \;=\; 0, \tag{2.3}$$

where g is the gravitational acceleration, $\mathbf{u}\begin{pmatrix} u \\ v \end{pmatrix}$ is the velocity vector and ν is the kinematic viscosity. Finally, $\mathbf{F}$ and $\mathbf{G}$ correspond to the frictionnal accelerations applied on the ocean layer by the atmosphere (wind stress) and the sediment (bottom shear stress), respectively. They are characterized by a quadratic friction law (*Schlichting and Gersten*, 2016) :

$$\mathbf{F} = \frac{1}{\rho h}\,\mathbf{f}, \tag{2.4}$$

where $\mathbf{f}$ is the shear stress applied to the ocean. It is calculated using the velocity difference between wind and ocean current as described by *Moulin and Wirth* (2014) :

$$\mathbf{f} = C_{Da}\;\rho_a \;||\; \mathbf{u}_{10} - \mathbf{u} \;||\; (\mathbf{u}_{10} - \mathbf{u}), \tag{2.5}$$

where $||\; \mathbf{u}_{10} - \mathbf{u} \;||$ is the magnitude of the velocity difference between the atmospheric velocity at 10m above the sea surface and the ocean current. In this work $u_{10} \in [10; 20]$ m/s and is directed in the positive x-direction. The drag coefficient C_{Da} follows *Wu* (1982) and *Smith* (1988) :

$$C_{Da} = (0.6 + 0.07u_{10})\;10^{-3} \quad \text{for } \mathrm{u}_{10} \in [6; 26]\mathrm{m/s}. \tag{2.6}$$

The validity range of this friction law corresponds to the good working conditions of wind turbines, from 4 $\mathrm{m.s^{-1}}$ to 25 $\mathrm{m.s^{-1}}$. A similar quadratic friction law is used to model the friction between the ocean and the sediment layers :

$$\mathbf{G} = \frac{1}{h}\,\tau_{\mathbf{b}}, \tag{2.7}$$

$$\tau_{\mathbf{b}} = C_D \;\; ||\; \mathbf{u} \;||\; \mathbf{u}, \tag{2.8}$$

with $|| \mathbf{u} ||= \sqrt{u^2 + v^2}$ and $C_D = 0.005$ the friction coefficient between the sediment bed and the ocean. This approach parametrizes the wave-current boundary layer and the effect of bed-form roughness, but does not take into account the local roughness variations in space and time (*Fredsøe and Deigaard*, 1992).

Under strong wind conditions, when the sea surface is rough, vertical turbulent density fluxes are high, especially near the surface. This reduces the vertical shear and the stratification in the surface-mixed-layer. It has a depth up to 50m in the ocean (*Mellor and Durbin*, 1975). In the dynamics of eddies, the pressure exerted by the free-surface has a governing role. In an unstratified ocean, under the hydrostatic approximation,the vertical penetration of the pressure is comparable to the horizontal extension of the eddy (*Vallis*, 2006). In the cases considered here, eddies extend over the total depth.

2.2.2 Morphodynamic model

For an oceanic bed composed of cohesionless grains (sand), the sediment starts to move when the drag force exerted by the flow is higher than the friction force between the grains. The dimensionless Shields parameter *Shields* (1936), gives the ratio between the drag force and the apparent submerged grains weight :

$$\theta = \frac{\tau_b}{(\rho_s - \rho) g d_s}, \tag{2.9}$$

The sediment starts to move as soon as the Shields parameter exceeds a critical value ($\theta > \theta_c$), which depends on the density and the grain size.
Variability of the bed motion results from a local flux balance described by the Exner (*Exner*, 1920) equation :

$$\partial_t h_s(x, y, t) + \nabla \cdot \mathbf{q}(x, y, t) = 0, \tag{2.10}$$

where h_s is the bed elevation and $\mathbf{q}$ is the total sediment flux.
Two modes of sediment transport exist, bedload transport and suspended load transport. In this work, only the bedload transport will be considered, this type of transport is generally dominating for rather low values of the bed shear stress, i.e when the Shields parameter of the flow is just above the critical value.
If only bedload transport is considered, the total sediment flux becomes :

$$\mathbf{q} = \frac{1}{1 - p}\, \mathbf{q}_b, \tag{2.11}$$

where p=0.5 is the bed porosity and $\mathbf{q}_b$ is the bed load transport rate.
In the present model, the *Meyer-Peter and Müller* (1948) transport formula is used to describe the bed load transport rate q_b. It relates the latter to the excess Shields parameter :

$$\frac{q_b}{d_s \sqrt{(\rho_s/\rho) g d_s}} = \begin{cases} 8(\theta - \theta_c)^{3/2} & \text{if } \theta > \theta_c \\ 0 & \text{otherwise} \end{cases}. \tag{2.12}$$

2.2.3 Turbine wake model

The turbine wake affects the ocean by modifying the surface shear in the region where the wake intersects the ocean surface (see figure 2.1.b). This perturbation is maximal at the impact

location, x_{imp} and then decreases downstream until vanishing. The wake model used in this work describes the velocity deficit induced by the rotor in the far wake region. The simplest model is given by *Jensen* (1983), assuming a linearly expanding or cone wake with a velocity deficit that only depends on the distance from the rotor.

$$u_{10} = U_\infty \left[1 - \frac{1 - \sqrt{1 - C_w}}{(1 + 2kx/D)^2} \right] , \tag{2.13}$$

where U_∞ is the wind velocity far from the turbine, C_w is the drag coefficient between the turbine and the air and k is the Wake Decay Constant. The standard Wake Decay Constant recommended in the WAsP help facility [1] is k=0.05 for offshore wind turbines. .

The wake impacts the ocean surface at a given distance downstream from the rotor position (figure 2.1.b). For the Jensen's model we have :

$$x_{\text{imp}} = \frac{H_r - D_r/2}{k} \tag{2.14}$$

This impact distance x_{imp} depends on the wind turbine height and on the rotor diameter and is increasing with the turbine size. For the turbines considered here ($H_r = 70$m and $D_r = 80$m, $k = 0.05$), the impact distance is 600 meters, several times the turbine height. Perturbations in the seabed induced by the turbine pile are localized in the pile vicinity. The pile diameter doesn't exceed 5 meters for the type of turbine considered. Furthermore, the perturbations due to the pile can extend up to 200m downstream in the oceanic layer (*Yin et al.*, 2014), which is still significantly less than the wake impact distance. The seabed perturbations induced by the pile and the wake presence are thus uncorrelated provided that the spacing between two consecutive turbine is larger than the impact distance. Finally, the order of magnitude of the drag forces deficit induced by the wake (≈100kN) on the flow is at least one order of magnitude larger than the one induced by the pile (≈5kN). The effect of the pile is therefore not considered in the present work.

The Jensen wake model boundaries are extremely sharp, indeed, the velocity difference between inside and outside the wake corresponds to a step function. Such sharp boundaries are unrealistic and are prone to generating artificial instabilities. To be more realistic without changing the large scale characteristic of the wake model, we used a gaussian mollifier (also known as approximation to the identity) function with a characteristic mollify length L_m.

2.2.4 Non-dimensional equations

The SW equations (2.2) and (2.3) can be made dimensionless by the length scale D (the wake diameter at the impact location) for the horizontal direction, H (the average ocean layer thickness) for the vertical one, by U (the unperturbed flow velocity) for the velocity scale and by D/U for the timescale.

1. *www.wasp.dk*

The SW equations can thus be rewritten as :

$$\partial_{t^*}\mathbf{u}^* + (\mathbf{u}^*\cdot\nabla^*)\mathbf{u}^* + \frac{H}{D}\frac{1}{{F_r}^2}g^*\nabla^*\eta^* \;=\; \frac{1}{R_e}\nabla^{*2}\mathbf{u}^* + \underbrace{\frac{S_a}{\rho\; h^*}\;\rho_a\;||\;\mathbf{u}^*_{10}-\mathbf{u}^*\;||\;(\mathbf{u}^*_{10}-\mathbf{u}^*)}_{\overline{F^*}} - \underbrace{\frac{S}{h^*}\;\;||\;\mathbf{u}^*\;||\;\mathbf{u}^*}_{\overline{G^*}} \tag{2.15}$$

$$\partial_{t^*}h^* + \nabla^*(h^*\mathbf{u}^*) \;=\; 0, \tag{2.16}$$

where $F_r = \dfrac{U}{\sqrt{gD}}$ and $R_e = \dfrac{UD}{\nu}$ are the Froude and the Reynolds numbers, respectively. Furthermore, in the non-dimensionnal bottom friction acceleration $\overline{G^*}$ an other dimensionless number appears, denoted as S. It is the so-called "wake stability parameter" introduced by *Ingram and Chu* (1987), or *Chen and Jirka* (1995, 1997) :

$$S = \frac{C_D D}{H} \tag{2.17}$$

The S parameter compares the bottom friction to the advection terms. S is a control parameter of the wake instabilities in shallow water flows, it has been used in the case of an island in a bay (*Ingram and Chu*, 1987) or in laboratory experiments (*Chen and Jirka*, 1995).
A similar parameter (S_a) appears in the non-dimensionnal atmospheric forcing but its effect on the eddy dynamic is small. Indeed, the wind shear mainly depends on the (imposed) wind velocity and only weakly on the ocean velocity. It will therefore not be discussed in the present paper.

2.3 Numerical model

2.3.1 Structure of the numerical model

Written in Fortran 90, the overall model can be divided in two coupled modules, the hydrodynamic and the morphodynamic modules. They are subject to input data, such as atmospheric forcing and bedform elevation. The hydrodynamic module solves the SW equations and is spatially discretized using the centered finite difference method and temporally discretized using a second order Runge-Kutta scheme (see *Moulin* (2015), chapter 4). Output from this module are the velocity fields u and v along with the free surface elevation η. These velocity fields are necessary to compute the Shields number. The morphodynamic module is only called if the Shields number exceeds the critical value in one or more of the grid points. The morphodynamic module solves the Exner equation using a NOCS (Non-Oscillatory Central Scheme) scheme as described by Jiang et al. (*Jiang and Tadmor* (1998), *Jiang et al.* (1998)) (see Appendix).
As the morphological timescale is large compared to the to hydrodynamic one, two time-steps are used, one for the hydrodynamic module (Δt) and the other for the morphodynamic module with $\Delta t_{morpho} = 1000 \times \Delta t$. The value of n_{morpho}=1000 has been determined based on a 1D benchmark consisting of the advection-diffusion calculation of a sand dune by a current. This test case has been inspired from *Marieu* (2007). Furthermore, having a large morphodynamics time-step allows to reduce the diffusion of the NOCS scheme and save computational time.
The organization chart of the code can be found in figure 2.2 and all the input parameters are given in table 2.1.

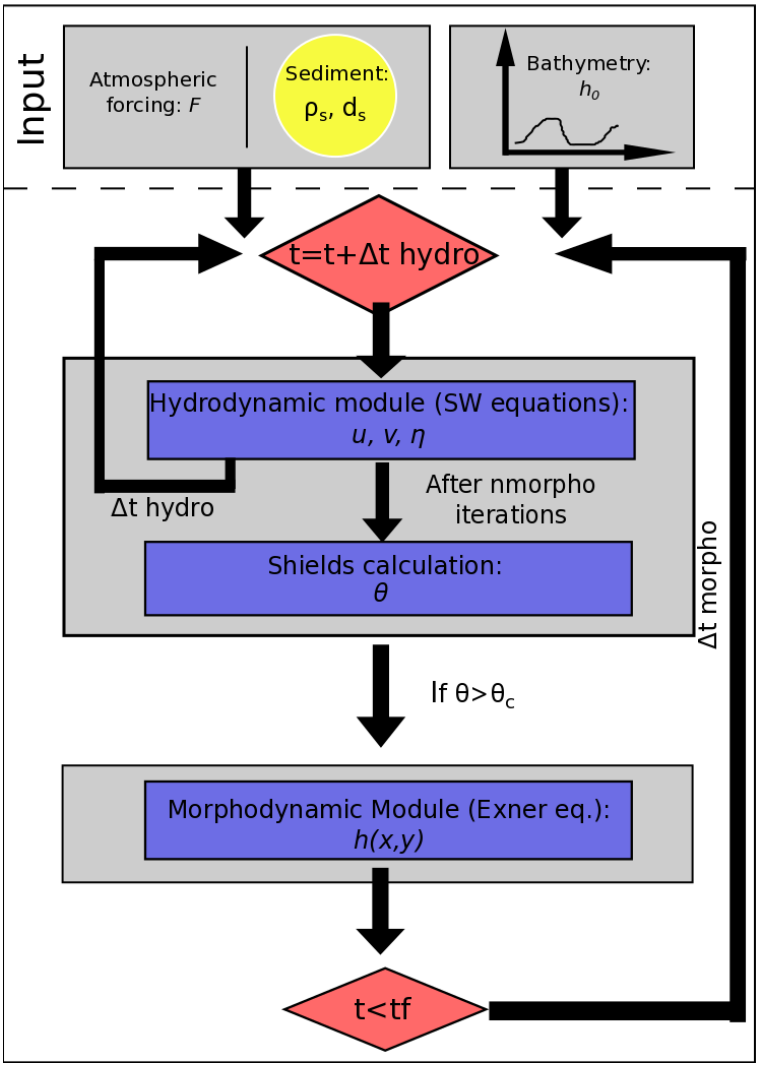

FIGURE 2.2: Flowchart of the solving procedure, $nmorpho = \Delta t_{morpho}/\Delta t$.

2.3.2 Numerical Grid, Boundary Conditions and Stability Criterion

The ocean and the sediment are considered in a rectangle of size $L_x \times L_y$. For eddy resolving simulations (consigned in table 2.2) the numerical grid is regular and contains $n_x \times n_y$ points, with $n_x = 1997$ when $L_x = 2000$m and $n_y = 597$ or 997 when $L_y = 600$m or 1000m, respectively. For these configurations, the spatial resolution is around 1m in both horizontal directions.

For the shallow water and the morphological modules, the variables value calculated at grid point i involves values at points $i-1$ and $i+1$, if we consider one direction only. Thus, at the boundaries, values of each variable have to be given. Here, periodic boundary conditions are used. Every point which is coming out of the domain at a boundary reappears at its opposite side. The same process is applied in the second horizontal direction.

Concerning the stability of the numerical scheme, the Courant-Friedrichs-Lewy criterion (CFL)

has to be satisfied for the ocean and sediment layers. While ocean waves propagation celerity is classically defined as $c_{ocean} = \sqrt{gh}$ (with h being the ocean layer thickness), sand waves propagation celerity (c_{sand}) corresponds to the dunes migration speed. As in the model $h \in [15; 60]$ m, $c_{ocean} \in [12; 24]$ m.s^{-1} and $c_{sand} \approx 10^{-4}$ m.s^{-1}, if the CFL conditions for the ocean is satisfied, it is also the case for the morphodynamic CFL. The ocean thus set the maximum time step at $\Delta t = 0.02$s.

A global overview of the numerical experiments performed is given in table 2.2. In the reference case (H15) the water depth is 15m and the domain width is 600m. The rotor diameter and height, $D = 80$m, $H_r = 70$m, correspond to a Vestas V80−2.0 MW turbine, one of the most widespread offshore wind turbine. The wind speed 10 meters above the sea level (u_{10}) is equal to 20m.s^{-1}, corresponding to the high range of these turbines good working conditions [2]. Simulations have been undertaken for six different water layer thicknesses, 15, 20, 30, 40, 50 and 60m, and three different wind velocities (u_{10} =10, 15 and 20 m.s^{-1}). Run H20CD2P3 has a bottom friction coefficient $C'_D = (2/3)C_D$. Runs H20w, H30w, H40w, H50w and H60w have a domain width of 1000m in order to limit the lateral confinement. Finally, runs H60CD3P4 and H60wCD3P4 have a bottom friction coefficient $C'_D = (3/4)C_D$. For each case, the initial free surface and seabed elevation fields are set to zero.

Most of the results presented in the following section are obtained after 14 days of dynamic, when a statistically steady state has been obtained. As the code is parallelized using MPI it represents, for a 1000m domain width run, around 85 hours of computations on 128 Intel E5-2670 processors (approximatively 11k core hours).

2.4 Results

The first part of this section focuses on the wake impact upon the ocean dynamics, particularly with the generation of instabilities, while the second part is dedicated to the morphodynamics impact. Results of the numerical experiments are consigned in table 2.2.

2.4.1 Ocean dynamics

Figure 2.3 shows the vorticity fields ($\zeta = \partial_x v - \partial_y u$) in the oceanic layer after 14 days of dynamics for 15, 20, 30 and 50m of water layer thickness. The 15m water layer thickness case (H15, figure 2.3.a) has a laminar dynamics and the vorticity is higher (or lower) at the wake boundaries showing that they are high shear-stress zones. Figure 2.3 also shows that increasing the water layer thickness leads to a generation of oceanic instabilities. Indeed, for the 20 and 30m water layer cases (H20 and H30, figure 2.3.b and 2.3.c, respectively), vortices formed at the wake impact location continue to develop along the wake boundaries and form two distinct vortex streets. The eddies diameter (D_e) and spacing (L_e) depend on the water layer thickness too (see table 2.2 or figure 2.4, representing the variations of the eddies diameter for the different numerical simulations undertaken), both increasing with an increasing water layer thickness. When the latter exceeds 40m, the vortex streets interact one with the other leading to a domain-wide turbulence.
For the 50m case (H50, figure 2.3.d) parts of the vortices are leaving the computational domain

2. Vestas V80-2.0 MW product brochure : *http ://www.vestas.com*

Tableau 2.1: Model input parameters.

Parameter	**Value (unit)**
temporal parameters	
Δt : time scale for ocean dynamics	0.02 (s)
n_{morpho} : time scale for morphodynamics ($\Delta t_{\text{morpho}} = n_{\text{morpho}} \times \Delta t$)	1000 (-)
n_{iter} : iteration number for one run	60 000 000 (-)
domain parameters	
L_x : Domain length in the x-direction	2000 (m)
L_y : Domain length in the y-direction	600 or 1000 (m)
H : Initial water depth	from 15 to 60 (m)
ocean parameters	
ρ : sea water density	1025 (kg.m^{-3})
C_{Da} : atmosphere/ocean friction coefficient	2.0×10^{-3} (-)
sediment parameters	
ρ_s : sediment density	2650 (kg.m^{-3})
d_s : sediment grain diameter	200 (μm)
C_D : ocean/sediment friction coefficient	from 3.3×10^{-3} to 5.0×10^{-3} (-)
atmosphere parameters	
ρ_a : atmosphere density	1.2 (kg.m^{-3})
u_{10} : input wind velocity	10, 15 or 20 (m.s^{-1})
wake and turbine parameters	
H_r : wind turbine hub height	70 (m)
D_r : wind turbine rotor diameter	80 (m)
k : slope of the linear Jensen wake model	0.05 (-)
C_w : wind turbine drag coefficient	0.87 (-)

at one side and reenter at the opposite side due to the periodic boundary conditions. In order to ged rid of this confinement phenomenon, additional runs have been carried out with a wider domain of 1000m [H20w, H30w, H40w, H50w, H60w and H60wCD3P4]. From a physical point of view, the 1000m width cases can be seen as a lesser densely packed wind farm. For the H50w case (figure 2.3.e), because the confinement phenomenon is not occurring, the vortices shape is closer to the one observed for H30 than for H50. Finally, for all the water layer thicknesses where vortices are well formed (*i.e* from 30 to 60m), the presence of filaments inside the vortices is noteworthy. These filaments correspond to high shear-stress zones and appear initially at the wake boundaries. They are then advected in the x-direction and rotated around the vortices center. As these filaments intensity decreases with their advection and rotation they are slowly reduced by viscosity.

Tableau 2.2: Numerical experiments and results main parameters, S is the stability wake parameter, ΔU is the velocity difference between outside and inside the wake at the impact location, D_e is the eddies diameter, L_e is the eddies spacing, the maximum deposition and erosion values correspond to maximum seabed elevation (positive or negative, respectively) noticed at the end of each run (14 days).

Run name	**H**	**L_y**	**u_{10}**	**C_D**	**D_r**	**S**	**ΔU**	**D_e**	**L_e**	**Max deposition**	**Max erosion**
Unit	**m**	**m**	**m.s^{-1}**	**(10^{-3})**	**m**	**(10^{-2})**	**m.s^{-1}**	**m**	**m**	**mm**	**mm**
H15	15	600	20	5	80	7.33	8.19	-	-	1.75	-2.12
H20	20	600	20	5	80	5.50	8.19	120	500	1.28	-1.61
H30	30	600	20	5	80	3.67	8.19	250	650	0.89	-1.10
H40	40	600	20	5	80	2.75	8.19	550	1000	0.74	-0.83
H50	50	600	20	5	80	2.20	8.19	550	1000	0.64	-0.66
H60	60	600	20	5	80	1.83	8.19	550	1000	0.56	-0.53
H60CD3P4	60	600	20	3.75	80	1.375	8.19	550	1000	0.54	-0.49
H20CD2P3	20	600	20	3.3	80	3.63	8.19	250	650	0.88	-1.07
H30Dr	30	600	20	5.	40	4.68	8.19	130	500	1.41	-1.52
H20w	20	1000	20	5	80	5.50	8.19	120	500	1.39	-1.50
H30w	30	1000	20	5	80	3.67	8.19	200	650	0.92	-1.02
H40w	40	1000	20	5	80	2.75	8.19	250	650	0.71	-0.77
H50w	50	1000	20	5	80	2.20	8.19	450	1000	0.62	-0.63
H60w	60	1000	20	5	80	1.83	8.19	580	1000	0.52	-0.52
H60wCD3P4	60	1000	20	3.75	80	1.375	8.19	600	1000	0.56	-0.47
H50U15	50	600	15	5	80	2.20	6.14	550	1000	0.17	-0.21
H50U10	50	600	20	5	80	2.20	4.10	550	1000	-	-

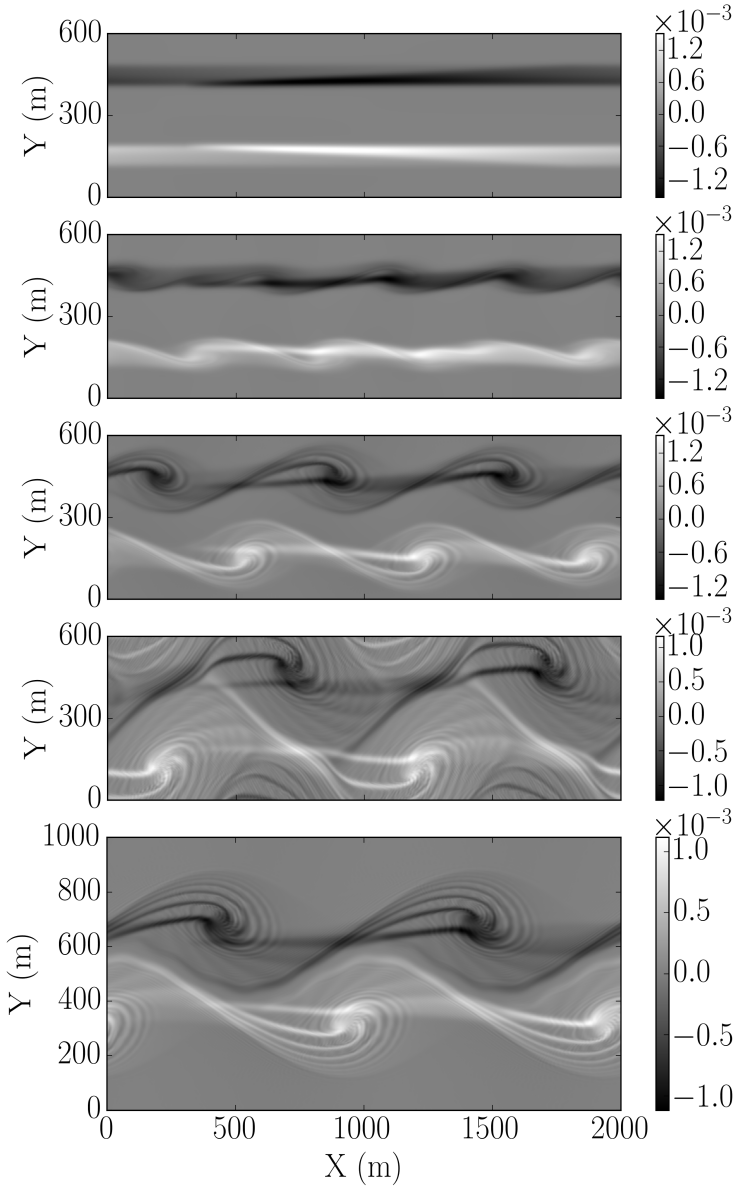

FIGURE 2.3: 2D vorticity fields after 14 days of dynamics for H15, (a) H20 (b), H30 (c), H50 (d) and H50w (e). Increasing the water layer thickness leads to a generation of two types of oceanic instabilities, distincts and interacting ones. This instabilities generation is controled by the wake stability parameter S.

The confinement phenomenon can be highlighted thanks to the eddies diameter. Indeed, figure 2.4 shows that for larger domain width, the vortex size is slightly smaller for all the layer thicknesses from 30 to 50m. The largest difference between the confined and the unconfined situations is found between runs H40 and H40w : if run H40 is similar to run H50 in terms of

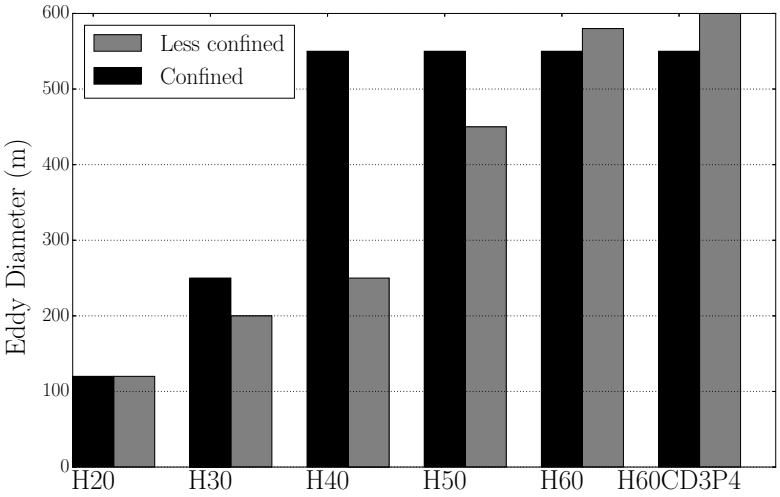

FIGURE 2.4: Comparison between the eddies diameter for the different numerical simulations undertaken.

vortex size, spacing and vorticity intensity, run H40w is closer to runs H30 and H30w. Qualitatively, two distinct vortex streets are formed in the domain for H40w rather than two interacting ones as for run H40. The explanation comes from a combination of confinement and periodic boundary conditions : the confinement leads to a slight increase of the Reynolds shear stress, thus of the turbulence intensity and of the eddies size. For the confined domain, at H=40m, the eddies diameter becomes more important than the half domain width and the periodic boundary conditions allow part of the vortices to leave the domain and reenter on the opposite side. The vortex streets are thus perturbed, deviated by the reentering vortices and both vortex streets start to interact one with the other leading to a domain-wide turbulence.
Figure 2.4 also shows that once the domain-wide turbulent state is reached, the eddies size remains constant when increasing the water layer thickness. Thus, for 60m water layer thickness the unconfined eddies become larger than the confined ones.

The computational variable allowing a quantitative characterization of the domain's turbulence for a given run is the Turbulent Kinetic Energy integral over the domain :

$$\langle TKE \rangle = \frac{1}{2} H \iint_A (u'^2 + v'^2)\, dA \ , \tag{2.18}$$

where A is the domain surface, and u' and v' are the velocity fluctuations, defined according to the Reynolds decomposition.
Figure 2.5 presents the normalized turbulent kinetic energy ($\langle \text{TKE} \rangle^* = \langle \text{TKE} \rangle / {u_{10}}^2$) versus the S parameter (see section 2.2.4) for the runs described in the table 2.2. It clearly appears that, for a given domain witdh, the $\langle \text{TKE} \rangle^*$ collapses as a function of the S parameter. The S dependency of the normalized TKE is shown by runs H20CD2P3 and H30Dr. Indeed, decreasing the bottom friction coefficient by a factor 2/3 in order to conserve S for the two cases with different water depth (H20CD2P3 and H30) gives very similar results on the normalized TKE but also on the oceanic vorticity field (not shown here). Furthermore, changing the S parameter by changing

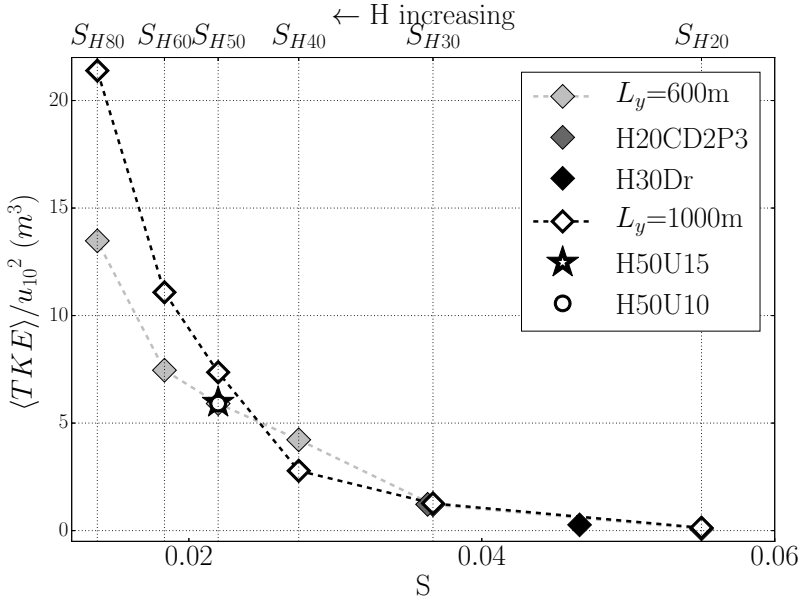

FIGURE 2.5: Plot of the normalized TKE as a function of the S parameter. Full and empty diamonds symbols correspond to confined (H15, H20, H30, H40, H50, H60, H60CD2P3) and less-confined (H20w, H30w, H40w, H50w, H60w, H60wCD2P3) cases, respectively. The wake stability parameter is a control parameter of the oceanic turbulent dynamic, even if a dependency on the domain width remains.

the wake diameter at the impact location (D), which is done in run H30Dr, also keeps the normalized TKE value on the same curve. This shows that the S parameter is a control parameter of the oceanic turbulent dynamics, even if a dependency on the wind turbine spacing remains. Furthermore, as the S parameter appears in the bottom-friction term in the SW equation (see eq. 2.19), when increasing the water layer thickness S is decreasing and the importance of bottom friction decreases, allowing for stronger instabilities to develop. This explains the phenomenon observed in figure 2.3.

$$\mathbf{G} = \frac{1}{h}\,\tau_{\mathbf{b}} = \frac{S}{D}\;\;||\,\mathbf{u}\,||\,\mathbf{u}. \tag{2.19}$$

Concerning the dependency on the domain width, it can be seen that for a S parameter corresponding to 30m water layer thickness (S_{H30}) or less, the normalized TKE has the same values for both domain width. For S higher than S_{H30}, the normalized TKE is affected by the lateral confinement. At 40m water layer thickness (S_{H40}), because of the vortex streets destabilization, turbulence becomes domain-wide) and the normalized TKE is higher for the confined case. At H=50m, the turbulence becomes also domain-wide for the less confined situation, so the normalized TKE becomes higher than for the confined case. Finally, for increasing water depth, the less-confined situation values of the normalized TKE will remain higher and the difference with the more confined case will continue to grow. This result can be correlated with the eddies size variation presented in figure 2.4.

The topology of the oceanic flow is particular due to the forcing by the wind turbine wake. Indeed, vorticity is not created at a fixed point, through the contact with an object and the corresponding formation of a boundary layer, but it is instead continuously injected at the boun-

dary of the atmospheric turbine-wake and advected downstream by the oceanic flow. This is clearly seen when inspecting movies (provided as additional online material) of the vorticity in the ocean, where a continuous formation of a vortex filament and its advection superpose.
For large values of the wake stability parameter (H $\leq$ 15m), two elongated vortex-filaments of opposite vorticity appear and the flow reflects the symmetry of the forcing with respect to the center-line (y=300m). For smaller values of the wake stability parameter (S $<$ 5.50 10^{-2}) the vortex filaments role up through a Kelvin-Helmholtz instability and eddies appear. Initially the symmetry is conserved but after some time the two vortex streets interact leading to the classical alternating von Karmann vortex street, in which the symmetry of the forcing is recovered in the time averaged variables. Further downstream the vortex filaments have a spiral structure.
When the vortex filament reenters the domain, due to periodic boundary conditions, another filament is imprinted on top of the existing one. This mechanism leads to the particular spaghetti-type structure of the vorticity field (figure 2.3). The signature of the vortex filaments are also clearly seen in a cut through the vorticity field of figure 2.3 at x=1340 m shown in figure 2.6. The result is a particular type of turbulence, composed of generated and decaying vortex filaments, where both processes are co-located in space and continuous in time.

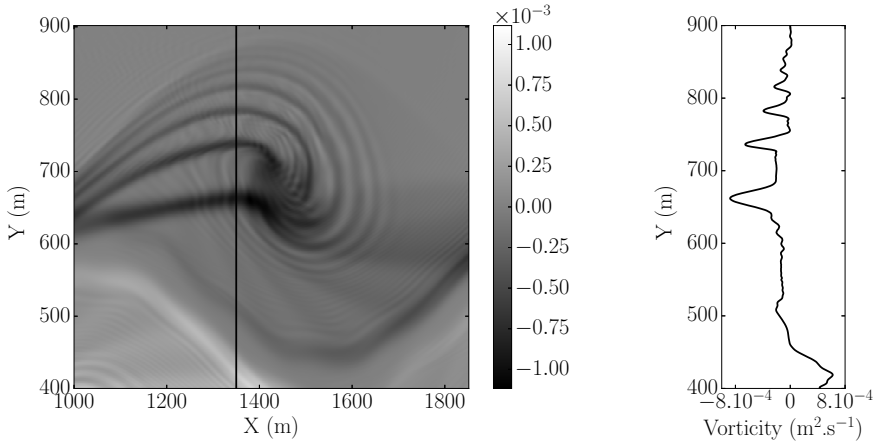

FIGURE 2.6: Zoom (a) and transect along the y-direction (b) of an eddy presented in figure 2.3, for the H50w case. The spaghetti-type structure of the vorticity field induced by atmospheric wake forcing and periodic boundary conditions but also the decaying vorticity intensity of the rotated filaments are clearly identifiable in the transect plot.

2.4.2 Sediment dynamics

Figure 2.7 shows the seabed elevation after 14 days of dynamics. For a given wind velocity (here u_{10}=20 m.s^{-1}), the qualitative spatial impact of the wake upon the seabed is similar for all the water layer thicknesses considered. The impact can be described as follows : first, the oceanic velocity deficit induced by the wake leads to a sediment accumulation, *i.e* a dune (corresponding to the local wake width) is formed close to the impact location, between x = 300m and x = 500m. The same phenomenon occurs at the wake boundaries. Such formations are due to the non uniformity of the oceanic velocity field and thus of the local bottom shear stress. Downstream in the wake, the velocity deficit becomes less important, corresponding to a bottom shear stress that induces bed erosion. Outside the wake, the flow velocity is higher, increasing

the bottom shear stress and the sediment transport, leading to the formation of a hole on each side of the dune. Further downstream, at $x = 1000$m, the velocity and the bottom shear stress decrease, the erosion stops and aggradation occurs.
However, from a quantitative point of view, the local seabed elevation at a given time and for a given wind forcing depends on the water layer thickness. Indeed, in figure 2.7 and in table 2.2 it is shown that the maximum values of seabed erosion and deposition are decreasing when increasing the water layer thickness. The explanation can be found by looking at the bathymetry variation in a short time interval ($\Delta t \approx 1$ h) as shown in figure 2.8. The spatial patterns of the morphodynamical evolution between the turbulent and the laminar cases are completely different. The oceanic vortices strongly affect the seabed morphodynamics. For 20 m water layer thickness with a laminar dynamics (figure 2.8.a), the bathymetry variations are similar to the seabed elevation variation after 14 days of dynamics and thus linear in time. This is not the case for water layer thickness from 30 m to 50 m (figure 2.8.b, and 2.8.c, respectively), the wakes imprint on the seabed is totally annihilated by the signature of the large scale vortices. The differences in vortex scale observed in the ocean is recovered in the seabed, showing that vortex formation in the ocean can have a significant impact on the seabed morphodynamics.
Considering the morphodynamical evolution, three cases are observed, depending on whether the ocean dynamics is laminar, has a localized (H20, H30) or a domain wide (H40, H50) turbulent behavior. In the first case, changes in seabed elevation are around a few millimeters per month. Results are similar for the localized turbulence case. For the domain wide turbulence case, instantaneous seabed changes are of the order of a few millimeters per month, whereas the transport averaged over several days decreases to a few tenths of millimeter per month. This behavior is easily explained by the oscillating local velocity which transports sediments back and forth leading to strong transport when averaged over short-time intervals but small transport when average over long-time intervals. It is important to notice that in this study only bedload is considered, the suspended load is neglected and may lead to underestimation of sediment transport. An increase of sediment transport, especially by suspension is not free of environmental issues as it increases the local turbidity and may reduce the light in the water column, affecting marine life (*Abrahams and Kattenfeld*, 1997).
The above observations also apply to the less confined simulations, in which, for each case maximum of deposition and erosion values are close to the corresponding confined case.

In the present model, the oceanic velocity depends on the wind velocity at 10 meters above the surface. The bottom shear stress depends on the oceanic velocity via the MPM threshold transport formula (eq. (2.12)), when the bottom shear stress is under the critical value, no bedload transport occurs. In the present configuration, such phenomenon appears for u_{10}=10 m.s^{-1}, meaning that in the idealized model presented here, under a given wind velocity, the wake presence has no impact on the seabed. These results are based on the assumption that the seabed is composed of sand, if mud is considered, then the suspended sediment transport would be way more important.

2.5 Discussion

2.5.1 Parametrization

The turbulent ocean dynamics presented in the previous section is obtained thanks to eddy-resolving time dependent simulations. These simulations are performed at fine horizontal reso-

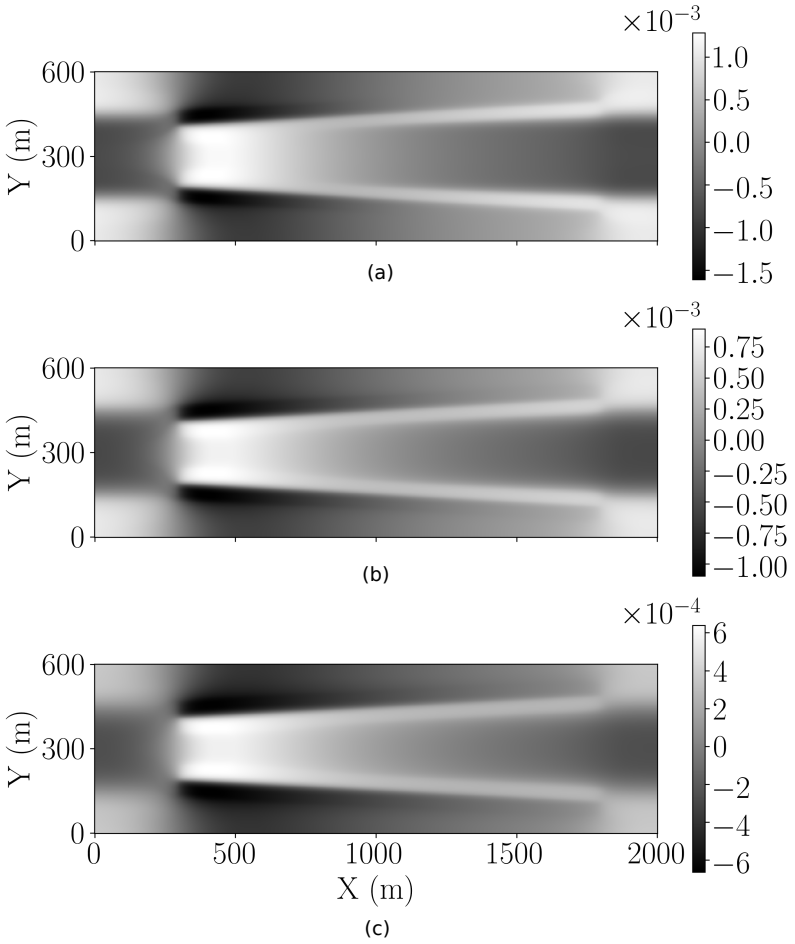

FIGURE 2.7: Seabed elevation after 14 days of dynamics for H20 (a), H30 (b) and H50 (c). The non-uniformity of the oceanic velocity field induced by the wake presence is recovered in the local bottom shear stress responsible for sand erosion and deposition.

lution (1m). Such fine resolution simulations can not be performed at a larger-scale (regional-scale) where it has been shown that offshore wind farms presence influence the ocean dynamics (*Broström*, 2008; *Rivier et al.*, 2016). The aim of this section is to propose an eddy viscosity model to be used in larger-scale RANS models. To this end we propose different parametrizations on a coarser grid where $dx = 26$m and $dy = 16$m.
The simplest parametrization proposed is a local model, in which advection and horizontal friction are neglected and the velocity field is calculated as a local equilibrium between the atmospheric forcing and the bottom friction :

$$u = \sqrt{\frac{C_{Da}\ \rho_a}{C_D\ \rho}}\ u_{10}\ . \tag{2.20}$$

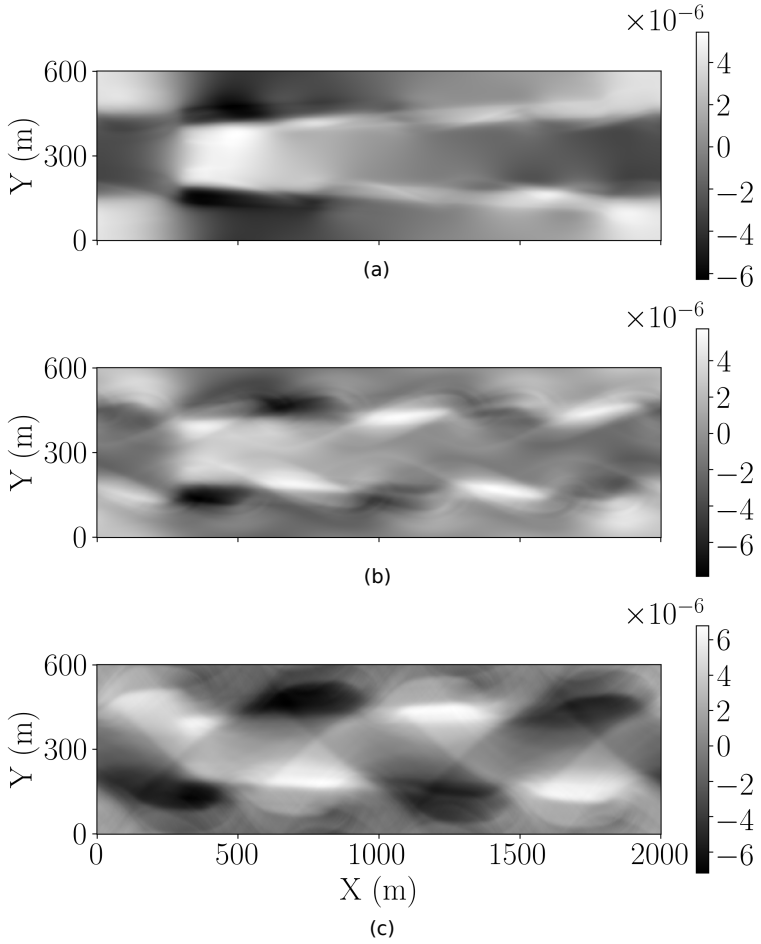

FIGURE 2.8: Short term seabed elevation changes, Δt =4000 s, for H20 (a), H30 (b) and H50 (c). As the vortices strongly affect the seabed morphodynamics, for localized (b) and domain wide turbulence (c), the wakes imprint tends to be reduced by large scale vortices and the oscillating local velocity which transports sediments back and forth.

The parametrization of the turbulent ocean dynamic can also be undertaken using the Reynolds-averaged Navier-Stokes equations, denoted as RANS equations. The RANS simulations solve the time-filtered SW equations. Thanks to Reynolds decomposition, an instantaneous quantity (such as u) is decomposed into its time-averaged ($\overline{u}$) and fluctuating (u') part :

$$u = \overline{u} + u' \tag{2.21}$$

The two types of RANS parametrizations undertaken in the present work are the simplest possible, involving a constant eddy viscosity and a mixing length approach. This is consistant with state of the art coastal morphodynamics models.

From eddy resolving simulations, the eddy viscosity ν_{eddy} can be obtained a posteriori using :

$$\nu_{\text{eddy}} = -\frac{\overline{u'v'}}{\partial_y \overline{u}} \ , \tag{2.22}$$

where $\overline{u'v'}$ is a component of the Reynolds stress tensor and $\partial_y \overline{u}$ is the horizontal transverse gradient of the mean flow velocity (see figure 2.9). Once determined from a fine resolution eddy resolving numerical simulation, the ν_{eddy} constant is simply added in the viscosity term in the equations of a coarse resolution simulation, which then rapidly converges to a stationary state.
For the Mixing Length L_m approach, the eddy viscosity can be written as :

$$L_m = \frac{\sqrt{|\ \overline{u'v'}\ |}}{|\ \partial_y \overline{u}\ |} \text{ and } \ \nu_{\text{eddy}} = |\ \partial_y \overline{u}\ |\ \ {L_m}^2. \tag{2.23}$$

The mixing length approach is more refined compared with a constant eddy viscosity. In this model, the eddy viscosity is space dependent and applied only where $\partial_y \overline{u}$ is important, *i.e* in the high shear stress zones, where the eddies are located.
All the three models presented above are compared with the eddy resolving results in order to determine their accuracy and efficiency. A y−direction transect of the mean velocity field is shown in figure 2.9. It clearly appears that for all the water layer thicknesses considered, the local model is far from the eddy resolving simulations, whereas both RANS models are very close to it, especially for larger water layer thicknesses (i.e for stronger turbulence states). These results may easily be explain by the hypothesis underlying each parametrization : the local model doesn't take into account the momentum transport, which is present in both RANS simulation and appears to be important in the dynamics. Furthermore, by looking at both, the 20m and the 50m water layer thickness cases, it appears that for $\overline{u}$, both RANS approaches give similar results. This is not the case when the shear is considered (left panel on figure 2.9), where the use of a mixing length gives better results than a constant eddy viscosity model, at least for the lowest water layer thickness. For the 20m water layer thickness the eddies are localized whereas they are domain wide in the 50m case, an eddy viscosity resulting from a local varying mixing length approach is thus not surprisingly better for the shallow cases than using a constant eddy viscosity.

Nevertheless, if a RANS parametrization seems to give satisfactory results this is only an a-posteriori parametrization, meaning that for each set of parameters an eddy resolving simulation is required to obtain the corresponding eddy viscosity or mixing length. In figure 2.10, the dimensionless eddy viscosity $\nu^*_{\text{eddy}} = \nu_{\text{eddy}}/D\ u_{10}$ is plotted versus the S parameter. For a given domain width, ν^*_{eddy} collapses on a master curve as a function of the S parameter. As the shear stress is higher in the confined situation it leads to higher values of ν^*_{eddy}. Consistently with the observation made in section 2.4.1, there is no confinement for H=20m. The dimensionless eddy viscosity is the same for both, the wide and the narrow domain.
For each domain width, a phenomenological law can be fitted to the data points. We propose a hyperbolic tangent function for $\nu^*_{\text{eddy}}(S)$:

$$\nu^*_{\text{eddy}}(S) = A\frac{1}{2}\left[1 + tanh\left(\frac{B-S}{C}\right)\right] \tag{2.24}$$

For the two situations considered here, the values of coefficients A, B and C are consigned in table 2.3.

Tableau 2.3: Numerical values of parameters A,B and C involved in eq. (2.24).

Situation	**A**	**B**	**C**
Confined	$1.173\ 10^{-4}$	$3.119\ 10^{-2}$	$7.420\ 10^{-3}$
Less confined	$1.200\ 10^{-4}$	$2.0\ 10^{-2}$	$1.0\ 10^{-2}$

The numerical values of the parameters A, B and C are different for each domain width. In this way, the correspondant eddy-viscosity function of S can only be applicable for a given domain width. Indeed, as show on figure 2.9, running a confined case RANS simulation with parameter value obtained from the less confined case gives satisfactory results on the mean velocity field $\overline{u}$, but not for the shear stress. The latter highligths the predominance of advection terms in the problem.

2.5.2 Atmospheric energy budget

The source of the oceanic mechanical energy is the shear between the atmosphere and the ocean. The atmosphere looses energy due to the friction with the ocean surface. The power lost by the atmosphere (P_{tot}) is the integral over the domain of the product between the wind stress and the wind velocity.

$$P_{\text{tot}} = C_{Da}\rho_a \iint_A || \ \mathbf{u_{10}} \tag{2.25}$$

Several hypothesis lead to a simplification of the energy budget computation and are presented hereafter : first of all, the y components of the velocity vectors can be neglected. Indeed, they are vanishing for the atmosphere and subdominant in the ocean ($v \ll u, u_{10}$), eq. (2.25) can be approximated by :

$$P_{\text{tot}} \approx C_{Da}\rho_a \iint_A \mid u_{10} - u \mid (u_{10} - u)u_{10}\ dA. \tag{2.26}$$

Furthermore, as the velocity in the atmosphere is always larger than in the ocean ($u_{10} > u,\ \forall x,\ \forall y,\ \forall t$) we have :

$$P_{\text{tot}} \approx C_{Da}\rho_a \iint_A (u_{10} - u)^2 u_{10}\ dA. \tag{2.27}$$

The power taken up by the ocean (P_{o}) is the integral over the domain of the product between the wind stress and the ocean velocity. Using the above simplifications, it can be written as :

$$P_{\text{o}} \approx C_{Da}\rho_a \iint_A (u_{10} - u)^2 u\ dA. \tag{2.28}$$

Furthermore, the total power taken out of the atmosphere can be seen as the sum of the one lost into friction and the one taken up by the ocean itself. The latter is also composed of two terms, the power taken by the mean flow (P_{mean}) and the one taken by the turbulent fluctuations (P_{turb}) :

$$P_{\text{tot}} = P_{\text{fric}} + \underbrace{P_{\text{mean}} + P_{\text{turb}}}_{P_{\text{o}}} \tag{2.29}$$

Computations have been undertaken using the different eddy resolving and RANS models described in the previous section to quantify the energy transfer, the results are presented in figure

2.11. First of all, the results show that for all the cases investigated, the power taken by the ocean from the atmosphere is several orders of magnitude lower than the one lost by the atmosphere. The major part of the power lost by the atmosphere is thus dissipated through friction between the atmosphere and the ocean. Furthermore, taking into account the ocean velocity in the wind forcing leads to a decrease by 4% of the power lost by the atmosphere (comparison between cases with u=0 and the other ones in figure 2.11.a). It must be kept in mind that the influence of the ocean dynamics on the energetic budget may be different with an oceanic current that is not only forced by a local wind but due to a large scale or a tidal current.
Figure 2.11 shows that for the power taken out from the atmosphere and the power taken up by the ocean, the values estimated with the local model are close to the ones given by the eddy resolving model. The differences between the two models are of the order of 0.001% for the power lost by the atmosphere and of the order of 0.03% for the power received by the ocean, showing that the oceanic turbulence, which is not present in the local model, has a subdominant role in the air-sea energetic budget balance.

An analytical development can confirm and explain the above observations. The time average equation (2.27) can be written for laminar and turbulent oceanic flows :

$$\overline{P_{\text{tot}}} = C_{Da}\rho_a \iint_A \underbrace{{u_{10}}^3}_{a_1} \underbrace{-2{u_{10}}^2\overline{u} + u_{10}\overline{u^2}}_{a_2} + \underbrace{u_{10}\overline{u'^2}}_{a_3}\ dA, \tag{2.30}$$

where $\overline{u}$ is the mean flow velocity and $\overline{u'^2}$ is the square of the velocity fluctuations, or the streamwise component of the Reynolds stress tensor. If the flow is laminar, $\overline{u'^2} = 0$ and thus $a_3 = 0$.
The same procedure can be applied to the energy taken up by the ocean eq. (2.28) and gives for laminar and turbulent oceanic flows :

$$\overline{{P_{\text{o}}}^t} = C_D\rho_a \iint_A \underbrace{{u_{10}}^2\overline{u}}_{o_1} \underbrace{-2u_{10}\overline{u^2} + \overline{u^3}}_{o_2} + \underbrace{\overline{u'^2}(3\overline{u} - 2u_a)}_{o_3}\ dA\ . \tag{2.31}$$

Equations (2.30) and (2.31) highlight the importance of the different terms in the air-sea energetic balance. The term $o_1 = {u_{10}}^2\overline{u}$ is linked to the power taken by the ocean without taking into account the oceanic velocity in the atmospheric forcing. This term is predominant in laminar and turbulent equations. The terms $a_2 = -2{u_a}^2\overline{u^2} + u_a\overline{u^2}$ and $o_2 = -2u_{10}\overline{u^2} + \overline{u^3}$ correspond to mean flow correction occurring when the oceanic velocity is taking into account in the atmospheric forcing. As the velocity in the atmosphere is always much larger and in the same direction than in the ocean, these correction terms are negative here. Taking into account the oceanic velocity in the atmospheric forcing reduces the shear and thus leads to a reduction of both P_{tot} and P_{o}. The terms $a_3 = u_{10}\overline{u'^2}$ and $o_3 = \overline{u'^2}(3\overline{u} - 2u_{10})$ correspond to the contributions of the turbulent fluctuations in the energetic balance. We have $a_3 > 0$ and $o_3 < 0$, for the idealized situation considered here. When turbulence occurs, it increases the power lost by the atmosphere but decreases the one received by the ocean. This can be explained by the fact that a part of the turbulent fluctuations is not in the same direction as the oceanic motion and the atmospheric forcing and increases the friction between the two layers. Furthermore, these fluctuations certainly reduce the energy transfer efficiency to the mean flow which may explain that they decrease the power received by the ocean.

2.6 Conclusion & Perspectives

An idealized 2D numerical model has been proposed to study the impact of an offshore wind turbine wake on the ocean and sediment dynamics. To the best of our knowledge, no study has ever been done on this subject so far. A simplified physical model has been proposed and a mathematical model has been built and solved numerically.

The results show that the turbine wake has an impact on both the ocean and the sediment bed layers. Turbine wake impact on the ocean surface can generate instabilities and vortex streets. Size and spacing between these vortices are controlled by the wake stability parameter $S = C_D D/H$. When S is decreased, large scale instabilities are more easily generated, leading to a domain wide turbulence state in the ocean. Furthermore, the results have also highlighted the important role of the confinement (the spacing of wind turbines in a farm) in the generation of instabilities.
The oceanic turbulence observed with eddy-resolving time dependent simulations can be parametrized using a simple zero equation RANS model : using a constant Boussinesq eddy viscosity in the shallow water equations, or using a mixing length approach. A phenomenological law for the non−dimensional eddy viscosity as a function of the S parameter has been proposed. This RANS parametrization of the turbulent oceanic dynamics allows for upscaling simulations (in a regional model, for example).
Concerning the seabed, it has been shown that the non-uniformity of the oceanic velocity field induced by the wake presence is observed in the local bottom shear stress responsible for sand erosion and deposition. As the vortices strongly affect the seabed morphodynamics, for localized and domain wide turbulence, the wake imprint on the seabed tends to be reduced by large scale vortices and oscillating local velocity which transports sediment back and forth and may increase the turbidity.
Taking into account the ocean velocity in the wind forcing leads to a decrease of the power lost through friction by the atmosphere, through reducing the relative velocity between the two layers. This result seems to show that the ocean dynamics is important for the energy budget around wind turbines. The results also show that even if the turbulence strongly influences both, ocean and seabed dynamics, its role is negligible in the air-sea energetic balance. Furthermore, as the atmospheric dynamics is not resolved here, the oceanic turbulence has a no retro-action on the atmosphere. Resolving the atmospheric dynamics may further increase the importance of these interactions.

Other processes can be considered with this idealized model by adding tidal currents and time changes in the atmospheric forcing (simulating a storm event) or by including the suspended load sediment transport for example. The parametrization proposed is promising but the determination of the dependence on the confinement deserves further investigation.
To the best of our knowledge, the present work is the first study on the wake interaction with the ocean-sediment dynamics. In contrast, turbine wake models and wind farms interactions with the atmosphere are the subject of a consequent literature. Coupling the present ocean-sediment model with an atmospheric model will increase our understanding of the interaction of a wind turbine with the environment.

The results presented previously clearly show that the turbine wake has an impact on both the ocean and the sediment bed layers but that the impact on the seabed is relatively small,

creating slight bedforms. In the cases where the velocity is oscillating back and forth under turbulent vortices, the turbidity may be increased in the water column and the question of it's contribution to the turbididy sediment wakes recently observed in offshore wind farms by *Vanhellemont and Ruddick* (2014) may be asked. However, if this contribution may exist, it should be minor compared to the scour occurring at the pile foundations. The latter has clearly be identified as the main responsible of these turbid wakes in several studies, either from fields observations as in *Vanhellemont and Ruddick* (2014) and *Baeye and Fettweis* (2015), numerical simulations as in *Yin et al.* (2014) or experiments as in *Rogan et al.* (2016).
The scour phenomenon is well described from an experimental point of view in the literature, but small-scale processes involved are usually not well accounted for in numerical models. The simulation of tridimensional scour around a cylindrical pile in a steady current proposed in the following chapters aim to identify and investigate these small-scale interactions between the fluid flow and the sediment phase using a two-phase flow approach.

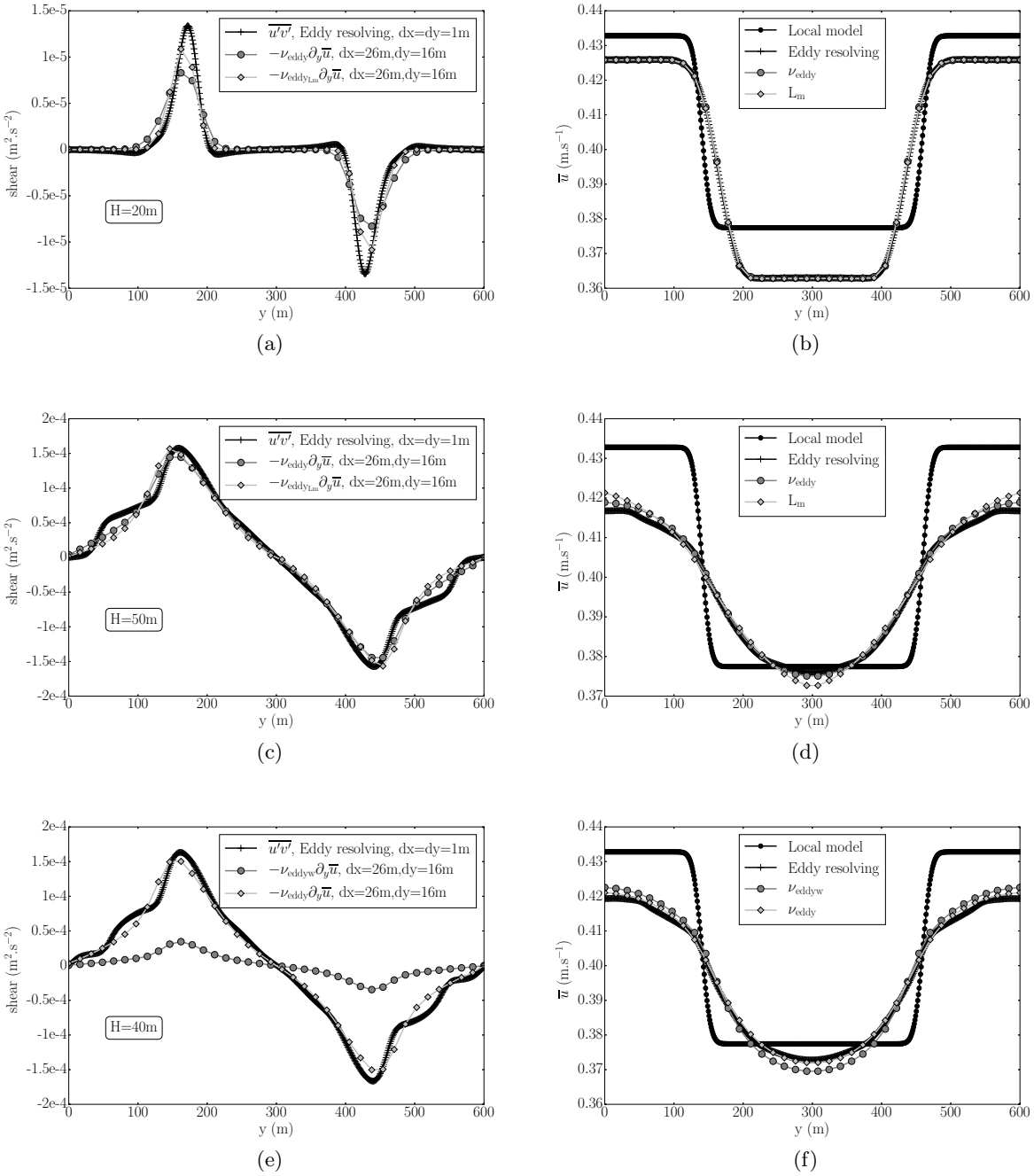

FIGURE 2.9: Confined runs y− direction transect at x=1300m of the shear (a,c,e) and mean velocity field $\overline{u}$ (b,d,f) for different water layer thicknesses. Eddy resolving computations (cross) and the three parametrizations are represented. For the 40m water layer thickness case (e,f), the circles symbols show the results obtained with an eddy viscosity computed from the non-confined configuration, when the diamonds curve is obtained with a eddy viscosity computed from the confined configuration. The results are satisfactory on the mean velocity field $\overline{u}$, but they are incorrects on the shear.

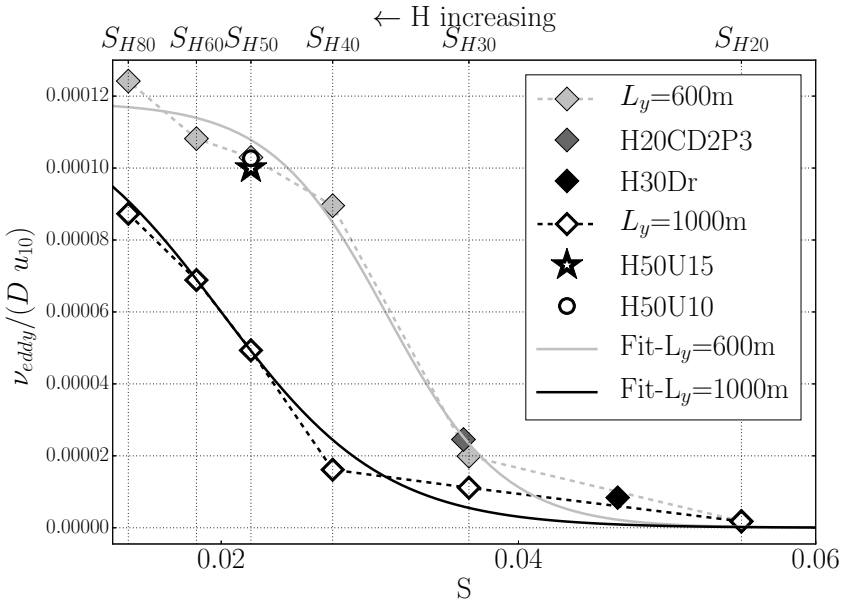

FIGURE 2.10: Plot of the non-dimensionalized ν_{eddy} as a function of the S parameter. For a given domain width, ν^*_{eddy} collapses on a curve as a function of the S parameter and can be fitted by a hyperbolic tangent function of S. Full and empty diamonds symbols correspond to confined (H15, H20, H30, H40, H50, H60, H60CD2P3) and less-confined (H20w, H30w, H40w, H50w, H60w, H60wCD2P3) cases, respectively.

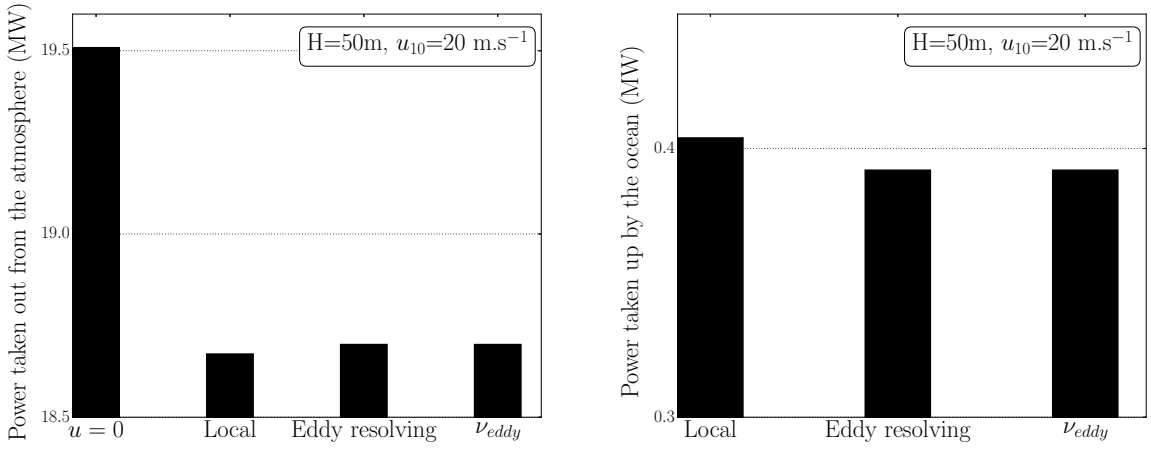

FIGURE 2.11: Comparison of the power taken out from the atmosphere (a) and the one taken up by the ocean (b) for the different models. Case presented here is H50.

Chapitre 3

sedFoam : a 3D two-phase flow numerical model for sediment transport

3.1 Résumé

SedFoam est un code de calcul diphasique Eulérien-Eulérien multidimensionnel pour le transport de sédiment. Il s'agit plus précisément d'un solveur écrit dans la boite à outils numériques OpenFOAM, codé en C++. L'un des avantages majeur d'OpenFOAM est qu'une grande diversité de schémas numériques est disponible pour l'utilisateur. A partir des schémas préexistants, l'utilisateur peut également choisi d'en écrire de nouveaux. SedFoam est développé conjointement entre le LEGI et le Center for Coastal Applied Research de l'Université du Delaware (USA). La version présentée dans ce chapitre et utilisée dans la suite de ce manuscrit est une version augmentée de SedFoam, basée sur twoPhaseEulerFoam (*Cheng and Hsu*, 2014; *Cheng et al.*, 2017) et compatible avec plusieurs versions d'openFOAM (2.4.0, 5.0, v1712plus, 4.0extend).

L'approche diphasique du transport sédimentaire développée ici permet de traiter la phase sédimentaire comme un continuum et de s'affranchir des approximations classiquement utilisées comme la distinction du flux sédimentaire généré par le charriage et la suspension (voir Chapitre 1). Cette approche nécessite néanmoins des modèles de fermeture permettant la determination des termes de contrainte présents dans les équations de quantité de mouvement, et ce pour les deux phases. Dans SedFoam deux modèles peuvent être utilisés pour déterminer les contraintes inter-granulaires, la théorie cinétique des écoulements granulaires ou bien la rhéologie des écoulements granulaires dense, $\mu(I)$. Concernant les contraintes fluides, le code peut modéliser des écoulements laminaires ou turbulents et quatre modèles de turbulence sont disponibles : un modèle de longueur de mélange (pour des configurations 1D uniquement) et plusieurs modèles à deux équations de type URANS et diphasiques qui sont des extensions des modèles classiques comme le $k-\epsilon$, le $k-\omega$ et le $k-\omega 2006$. Les contributions principales de mon travail de thèse au développement de SedFoam sont le modèle de turbulence $k-\omega 2006$ pour le diphasique, les lois de parois rugueuses (voir Chapitre 4) et l'écriture d'un modèle permettant d'utiliser un nombre de Schmidt local. Ces contributions ne sont pas encore incluses dans le version publique de SedFoam mais le seront lors d'une prochaine publication.

Ce chapitre décrit le modèle mathématique et numérique de SedFoam et s'inspire fortement d'une

partie de l'article publié dans la revue Geoscientific Model Development (*Chauchat et al.*, 2017). Conformément à la philosophie d'OpenFOAM, le code est Open-Source et un effort particulier a été dédié à sa diffusion. Les sources sont disponibles librement (*https ://github.com/sedfoam/sedFoam*). A ces sources sont associés une documentation et des tutoriels d'utilisation sur des cas 1D et 2D (*https ://servforge.legi.grenoble-inp.fr/pub/soft-sedfoam/*). Ce travail de thèse a également contribué à l'élaboration d'un package python, fluidfoam (*https ://bitbucket.org/fluiddyn/fluidfoam*) facilitant le post-traitement de données OpenFOAM. Ce package a été utilisé pour la plupart des résultats présentés dans ce manuscrit.

3.2 Mathematical Model

The mathematical formulation of the Eulerian two-phase flow model is obtained by averaging the local and instantaneous mass and momentum conservation equations over fluid and dispersed particles (*Hsu et al.*, 2004). In the literature, two different averaging operators can be found, the ensemble averaging *Drew* (1983) and the spatial averaging developed by *Jackson* (2000), that should lead to the same conservation equations (*Jackson*, 1997; *Zhang and Prosperetti*, 1997). The resulting system of governing equations can be considered as the counterpart of the one for clear fluid (i.e Navier-Stokes equations for single phase flow). When applying these equations to turbulent flow, additional turbulence averaging (*i.e* filtering) has to be used. The filter used in the present work is the RANS (Reynolds-Averaged Navier-Stokes) one, in which the eulerian two-phase flow equations of motion are time averaged. In the present model, the turbulence-averaged Eulerian two-phase flow equations described in *Chauchat et al.* (2017) are used and a new closure is developed.

3.2.1 Two-phase flow model equations for incompressible fluid

The mass conservation equations for the particle phase and fluid phase are written as :

$$\frac{\partial \phi}{\partial t} + \frac{\partial \phi u_i^s}{\partial x_i} = 0, \tag{3.1}$$

$$\frac{\partial (1-\phi)}{\partial t} + \frac{\partial (1-\phi) u_i^f}{\partial x_i} = 0, \tag{3.2}$$

where ϕ, and $1-\phi$ are the particle and fluid volume fractions, u_i^s, u_i^f are the sediment and fluid phase velocities, and $i = 1, 2, 3$ represents streamwise, spanwise and vertical component, respectively. Following *Chauchat et al.* (2017), the momentum equations for fluid and particle phases can be written as :

$$\begin{aligned}\frac{\partial \rho^s \phi u_i^s}{\partial t} + \frac{\partial \rho^s \phi u_i^s u_j^s}{\partial x_j} = &-\phi \frac{\partial p}{\partial x_i} + \phi f_i - \frac{\partial \tilde{p}^s}{\partial x_i} + \frac{\partial \tau_{ij}^s}{\partial x_j} + \phi \rho^s g_i + \phi(1-\phi) K (u_i^f - u_i^s) \\ &- \frac{1}{S_c}(1-\phi) K \nu_t^f \frac{\partial \phi}{\partial x_i},\end{aligned} \tag{3.3}$$

$$\begin{aligned}\frac{\partial \rho^f (1-\phi) u_i^f}{\partial t} + \frac{\partial \rho^f (1-\phi) u_i^f u_j^f}{\partial x_j} = &-(1-\phi)\frac{\partial p}{\partial x_i} + (1-\phi) f_i + \frac{\partial \tau_{ij}^f}{\partial x_j} \\ &+ (1-\phi)\rho^f g_i - \phi(1-\phi) K (u_i^f - u_i^s) \\ &+ \frac{1}{S_c}(1-\phi) K \nu_t^f \frac{\partial \phi}{\partial x_i},\end{aligned} \tag{3.4}$$

where ρ^s, ρ^f are the particle and the fluid density, respectively, g_i is the gravitational acceleration and p is the fluid pressure. f_i is the external force that drives the flow. The fluid stress τ_{ij}^f includes fluid grain-scale (viscous) stress and fluid Reynolds stresses, $\tilde{p}^s, \tau_{ij}^s$ are particle normal stress and shear stress. The last two terms on the right-hand-side (RHS) of equations 3.3 and 3.4 are momentum coupling between the fluid phase and particle phase through drag force, where K is the drag parameter. The second to the last term represents averaged drag force due to mean relative velocity between fluid and particle phases, while the last term represents the fluid turbulent suspension term, also called drift velocity *Deutsch and Simonin* (1991). Finally, ν_t^f is the turbulent viscosity that has to be calculated using a turbulence closure and S_c is the Schmidt number.
The drag parameter K, is modeled following *Schiller and Naumann* (1933) :

$$K = 0.75 C_d \frac{\rho^f}{d_{eff}} \mid\mid \boldsymbol{u^f} - \boldsymbol{u^s} \mid\mid (1-\phi)^{-h_{Exp}} \tag{3.5}$$

where $d_{eff} = \psi d$ is the effective sediment diameter, in which ψ is the shape factor and d is the particle diameter. The hindrance function $(1-\phi)^{-h_{Exp}}$ represents the drag increase when the particle volume fraction increases. h_{Exp}=2.65 is the hindrance exponent that depends on the particulate Reynolds number. Here, following *Chauchat et al.* (2017) its value is constant.
The drag coefficient C_d is calculated as :

$$C_d = \begin{cases} \dfrac{24}{Re_p}(1 + 0.15 Re_p^{0.687}), Re_p \leq 1000 \\ 0.44, Re_p > 1000 \end{cases}, \tag{3.6}$$

in which, the particulate Reynolds number Re_p is defined as : $Re_p = (1-\phi) \mid\mid \boldsymbol{u^f} - \boldsymbol{u^s} \mid\mid d_{eff}/\nu^f$, where ν^f represents the fluid kinematic viscosity.

3.2.2 Fluid phase shear stress

Due to the fact that the present model equations are obtained by averaging over turbulence, the fluid stresses consist in a large-scale component R_{ij}^f (*i.e.*, Reynolds stress) and a grain-scale stress r_{ij}^f, including the viscous stress and an additional effect due to fluid-particle interaction at the grain scale. The total fluid stress is written as :

$$\tau_{ij}^f = R_{ij}^f + r_{ij}^f = \rho^f (1-\phi)\Big[2\nu_{Eff}^f \; S_{ij}^f - \frac{2}{3} k \delta_{ij}\Big], \tag{3.7}$$

where, $\nu_{Eff}^f = \nu_t^f + \nu^{mix}$ is the fluid phase effective viscosity in which ν_t^f is the eddy viscosity, and ν^{mix} is the mixture viscosity and k the turbulent kinetic energy. S_{ij}^f is the deviatoric part of the fluid phase strain rate tensor and is defined as :

$$S_{ij}^f = \frac{1}{2}\left(\frac{\partial u_i^f}{\partial x_j} + \frac{\partial u_j^f}{\partial x_i}\right) - \frac{1}{3}\frac{\partial u_k^f}{\partial x_k}\delta_{ij}, \tag{3.8}$$

in which $\overline{S_{ij}^f} = \dfrac{1}{2}\left(\dfrac{\partial u_i^f}{\partial x_j} + \dfrac{\partial u_j^f}{\partial x_i}\right)$ is the Favre averaged strain-rate tensor.
The Reynolds stress tensor R_{ij}^f and the viscous stress tensor r_{ij}^f are modeled as :

$$R_{ij}^f = \rho^f (1-\phi)\Big[2\nu_t^f \; S_{ij}^f - \frac{2}{3} k \delta_{ij}\Big], \tag{3.9}$$

$$r_{ij}^f = 2\rho^f(1-\phi)\nu^{mix}\ S_{ij}^f, \tag{3.10}$$

In SedFoam, several viscosity or turbulence closures are implemented and can be selected depending on the flow conditions of the study case. The mixture viscosity can be selected in combination of granular rheology model for the granular stresses determination (see section b)). Concerning the turbulent eddy viscosity, different turbulence closures incorporating sediment effects are available and presented in subsection b).

a) Mixture viscosity

The mixture viscosity model used here is the one proposed by *Boyer et al.* (2011), based on detailed rheological experiment :

$$\frac{\nu^{mix}}{\nu^f} = 1 + 2.5\phi\left(1 - \frac{\phi}{\phi_{max}}\right)^{-1}. \tag{3.11}$$

This model is consistent with both, the *Einstein* (1906) model (eq. 3.12) valid for very dilute situations (i.e $\phi < 0.01$) and the phenomenological model from *Krieger and Dougherty* (1959), valid for very dense situations (eq. 3.13). These two models read respectively as :

$$\frac{\nu^{mix}}{\nu^f} = 1 + 2.5\phi. \tag{3.12}$$

$$\frac{\nu^{mix}}{\nu^f} = \left(1 - \frac{\phi}{\phi_{max}}\right)^{-n}, \tag{3.13}$$

where ϕ_{max} is the maximum volume fraction and n is an empirical exponent usually taken as $n = 2.5\phi_{max}$ for consistency with Einstein's model at low volume fraction.
Please note that a special treatment of the terms $1-\phi/\phi_{max}$ is needed to avoid dividing by zero. In other world, a clipping of ϕ/ϕ_{max} is performed.

b) Turbulence modeling

The turbulence averaged formulation requires a closure for the eddy viscosity. In this work, only linear eddy viscosity models are used. All of these models are based on the Boussinesq eddy viscosity assumption, assuming a linear relationship between the Reynolds shear stress and the mean strain rate tensor (see eq. 3.9). The linear eddy viscosity models are usually classified into several categories based on the number of transport equations solved to compute the eddy viscosity : algebraic models, one-equation models and two-equations models. In this work one algebraic and four two-equations turbulence models are detailed. The algebraic model is the mixing length model. This eddy viscosity model is only valid for 1D situations.
The two-equation models include two extra transport equations representing the turbulent properties of the flow. The turbulent kinetic energy k is generally the first additional transported variable. The second transported variable depends on the type of two-equations model. In this work, I will only use the turbulent dissipation, ε and the specific turbulence dissipation rate, ω. The turbulent dissipation ε is used in the two-phase flow version of the $k-\varepsilon$ model that has been written in *Cheng et al.* (2017). The specific turbulence dissipation rate ω is encountered in three turbulence models. The first one is the two-phase flow version of $k-\omega$ turbulence model

introduced in *Chauchat et al.* (2017). The second model using ω is one of the original contribution of my phD work, a two-phase flow version of the $k-\omega$ 2006 turbulence model. The original single phase version of this turbulence model can be found in *Wilcox* (2008). Finally, the specific turbulence dissipation rate ω is also used in the $k-\omega$ SST turbulence model (*Menter*, 1993) implemented in OpenFOAM. Please note that this turbulence model is a the single phase model only, being used for simulation without sediment phase. It's transformation for two-phase flow applications has not been undertaken as it will be detailed in section v).

i) Laminar

For laminar flow applications, the turbulence viscosity vanishes and $\nu_t^f = 0$. However, the mixture viscosity model can describes the sediment effect on the mixture viscosity. Thus the effective fluid viscosity is determined as : $\nu_{Eff}^f = \nu^{mix}$.
This model will not be used in the present manuscript.

ii) Mixing length (1D only)

In the mixing length approach the eddy viscosity is modelled using a simple algebraic equation :

$$\nu_t{}^f = l_m^2 \parallel \nabla \mathbf{u^f} \parallel \tag{3.14}$$

$$l_m = \kappa \int_0^y 1 - \left(\frac{\phi(\xi)}{\phi_{max}}\right)^{1.66} d\xi, \tag{3.15}$$

where κ is the von Karman constant, the exponent 1.66 has been proposed by *Chauchat* (2018) based on experimental data from *Revil-Baudard et al.* (2015). This model is only working in 1D configuration for which the direction of gravity is y. This turbulence model has been implemented in SedFoam mostly for compatibility with earlier works (*Chauchat*, 2018; *Revil-Baudard and Chauchat*, 2013).

iii) $k-\varepsilon$ model

Cheng et al. (2017) have implemented the $k-\varepsilon$ model from *Hsu et al.* (2004) and *Yu et al.* (2010), in which the turbulent eddy viscosity ν_t^f is calculated by :

$$\nu_t^f = C_\mu \frac{k^2}{\varepsilon}, \tag{3.16}$$

where C_μ is an empirical coefficient (see Table 3.1). The Turbulent Kinetic Energy (TKE) k is computed from the solution of equation (3.17), appropriate for sand particles in water (*Hsu et al.*, 2004; *Yu et al.*, 2010) :

$$\begin{aligned}\frac{\partial k}{\partial t} + u_j^f \frac{\partial k}{\partial x_j} =& \frac{R_{ij}^{ft}}{\rho^f}\frac{\partial u_i^f}{\partial x_j} + \frac{\partial}{\partial x_j}\Big[\Big(\nu^f + \frac{\nu_t^f}{\sigma_k}\Big)\frac{\partial k}{\partial x_j}\Big] - \varepsilon \\ &- \frac{2K(1-t_{mf})\phi k}{\rho^f} - \frac{1}{S_c(1-\phi)}\,\nu_t^f \frac{\partial \phi}{\partial x_j}\big(\frac{\rho^s}{\rho^f} - 1\big)g_j,\end{aligned} \tag{3.17}$$

The above k-equation is similar to the clear fluid $k-\varepsilon$ closure, the first three terms on the RHS describe respectively production, diffusion and dissipation of TKE. The last two terms on

the RHS in Eq. (3.17) describe the modification of the classical k-transport equation induced by the presence of particules. The fifth term on RHS accounts for the sediment damping effect on the carrier flow turbulence through density stratification. It can be seen as the buoyancy production/dissipation due to sediment-induced density stratification (*Kranenburg et al.*, 2014). For typical sediment concentration with an upward decaying profile, this term represents the well-known sediment-induced density stratification that provide another source of turbulence dissipation.
The fourth term on RHS is a damping term modeling the drag-effect of sediment particles on the carrier flow turbulence. Indeed, if their inertia is important enough, particles cannot completely follow the turbulent fluid velocity fluctuations. In this drag-induced damping term, the parameter t_{mf} is introduced to characterize the degree of correlation between particles and fluid velocity fluctuations. Following *Kranenburg et al.* (2014), its value can vary between 0 and 1, where $t_{mf} = 1$ denotes completely passive particles, that are not induced any turbulence damping through drag. *Danon et al.* (1977) and *Chen and Wood* (1985) proposed an exponential function for t_{mf}, which is also used in (*Cheng et al.*, 2017) :

$$t_{mf} = e^{-B \cdot St}, \tag{3.18}$$

where B is an empirical coefficient. The degree of correlation between particles and fluid velocity fluctuations can be quantified by the Stokes number St (*Benavides and van Wachem*, 2008) :

$$St = \frac{t_p}{t_l}, \tag{3.19}$$

where $t_p = \rho^s/((1-\phi)\ K)$ is the particle response time, $t_l = k/(6\varepsilon)$ is the characteristic time scale of energetic eddies.

Finally, the balance equation for the rate of turbulent kinetic energy dissipation ε is written as :

$$\begin{aligned} \frac{\partial \varepsilon}{\partial t} + u_j^f \frac{\partial \varepsilon}{\partial x_j} =& C_{1\varepsilon} \frac{\varepsilon}{k} \frac{R_{ij}^{ft}}{\rho^f} \frac{\partial u_i^f}{\partial x_j} + \frac{\partial}{\partial x_j}\Big[\Big(\nu^f + \frac{\nu_t^f}{\sigma_\varepsilon}\Big)\frac{\partial \varepsilon}{\partial x_j}\Big] - C_{2\varepsilon}\frac{\varepsilon^2}{k} \\ &- C_{3\varepsilon}\frac{\varepsilon}{k}\frac{2K(1-t_{mf})\phi k}{\rho^f} - C_{4\varepsilon}\frac{1}{S_c}\frac{\varepsilon}{k(1-\phi)}\ \nu_t^f \frac{\partial \phi}{\partial x_j}\big(\frac{\rho^s}{\rho^f} - 1\big) g_j \end{aligned} \tag{3.20}$$

As in reported *Hsu et al.* (2004), due to lack of comprehensive experimental data, the coefficients $C_{1\varepsilon}$ and $C_{2\varepsilon}$ associated with the present two-equation closure are adopted from their clear fluid counterpart (see table 3.1). The coefficient $C_{3\varepsilon}$ in the ε equation (3.20) is chosen to be 1.2. For the coefficient associated with the buoyancy term, $C_{4\varepsilon} = 0$ is used in stably stratified condition, while it is set to 1 for unstably stratified condition. Table 3.1 summarizes the model coefficients. According to previous studies (*Cheng et al.*, 2017; *Hsu et al.*, 2004; *Yu et al.*, 2010) these coefficients work well for typical medium to coarse sand transport. It was also found that the coefficient B (see Eq. (3.18)) is sensitive to the model result, and becomes therefore a free parameter to be calibrated based on comparison with measured data.

iv) Standard $k-\omega$ model
The two-phase $k-\omega$ turbulence model presented here is the one introduced in *Chauchat et al.*

Tableau 3.1: $k-\varepsilon$ model coefficients.

C_μ	$C_{1\varepsilon}$	$C_{2\varepsilon}$	$C_{3\varepsilon}$	$C_{4\varepsilon}$	σ_k	σ_ε	S_c
0.09	1.44	1.92	1.2	0 or 1	1.0	1.3	1

(2017). It is based on *Cheng et al.* (2017) and *Hsu et al.* (2004) work for the $k-\varepsilon$ model, presented in the previous section. Following the same method of developing the two-phase $k-\varepsilon$ turbulence model for sediment transport, the modification to the equations for the fluid TKE and the fluid specific rate of turbulent energy dissipation ω are made by adding the effect of the particle phase presence to the clear fluid $k-\omega$ model (i.e the particle drag and the buoyancy terms).
The Turbulent Kinetic Energy (TKE) k is therefore computed from the solution of equation (3.21), appropriate for sand particles in water (*Hsu et al.*, 2004; *Yu et al.*, 2010) :

$$\begin{aligned}\frac{\partial k}{\partial t}+u_j^f\frac{\partial k}{\partial x_j} =&P-C_\mu k\omega+\frac{\partial}{\partial x_j}\left[\left(\nu^f+\sigma_k\nu_t^f\right)\frac{\partial k}{\partial x_j}\right]\\ &-S_1\frac{2K(1-tmf)\phi k}{\rho^f}-S_1\frac{1}{S_c(1-\phi)}\nu_t^f\frac{\partial\phi}{\partial x_j}\left(\frac{\rho^s}{\rho^f}-1\right)g_j,\end{aligned} \tag{3.21}$$

where $P=R_{ij}^f\dfrac{\partial u_i^f}{\partial x_j}$ is the TKE production term for the two-phase k-ω and the two-phase k-ω 2006 models. Its definition is slightly different for the SST model (see table 3.2). In order to make the turbulence model consistent with single-phase expression, the terms accounting for the particle presence are activated using the S_1 coefficient, it value being 0 or 1, for single-phase or two-phase flow configurations, respectively.
Please note that for reading simplicity, eq. (3.21) is written one time only for the three versions of the k-ω turbulence model used in the present paper. Therefore, most of the terms are associated to a coefficient depending on the version of the turbulence model. The values of these coefficients are given in table 3.2 and detailed explanations are given for each turbulence model in their description section. The previous statement also apply on the fluid specific rate of turbulent energy dissipation (ω) equation, which reads :

$$\begin{aligned}\frac{\partial\omega}{\partial t}+u_j^f\frac{\partial\omega}{\partial x_j} =&\frac{C_{1\omega}}{\nu_t^f}P-C_{2\omega}\omega^2+\frac{\partial}{\partial x_j}\left[\left(\nu^f+\sigma_\omega\nu_t^f\right)\frac{\partial\omega}{\partial x_j}\right]+\ CD_{k\omega}\\ &-S_1\ C_{3\omega}\frac{2K(1-tmf)\phi\omega}{\rho^f}-S_1\ C_{4\omega}\frac{1}{S_c}\frac{\omega}{k(1-\phi)}\nu_t^f\frac{\partial\phi}{\partial x_j}\left(\frac{\rho^s}{\rho^f}-1\right)g_j.\end{aligned} \tag{3.22}$$

For the standard $k-\omega$ turbulence model, the turbulent eddy viscosity ν_t^f involved in k-equation and ω-equation is calculated by :

$$\nu_t^f=\frac{k}{\omega} \tag{3.23}$$

The different coefficient values can be found in table 3.2. The coefficients associated with the present two-equation closure are adopted from their clear fluid counterpart. The last two terms on the RHS of eq. (3.21) and (3.22) account for the sediment damping effect on the fluid carrier

flow turbulence through drag and density stratification, respectively. According to the numerical experiments described in *Chauchat et al.* (2017), the coefficient $C_{3\omega}$ in eq. (3.22) is chosen to be 0.35. The coefficient associated with the buoyancy term $C_{4\omega} = 0$ is used in stably stratified condition, while it is set to 1 for unstably stratified condition. Like in the k-ε model, B is left as the only free model calibration parameter.
The fourth term on the RHS of eq. (3.22), denoted as $CD_{k\omega}$ is different from zero for the $k-\omega$ 2006 and the $k-\omega$ SST models only (see table 3.2) as it will be detailed further in this section.

v) $k-\omega$ SST model

Amongst the family of RANS turbulence models, the k-ω SST developed by *Menter* (1993) is known to provide the best results in the case of boundary-layer flows with a strong adverse pressure gradient, such as the flow around a vertical cylinder. The superiority of the k-ω SST upon other turbulence models on configurations with a strong adverse pressure gradient stands in two main reasons. The first and minor one is that this model does not have a strong sensitivity to freestream boundary conditions on turbulence properties. To achieve such purpose the idea of *Menter* (1993) is to use the standard k-ω model close to the wall and the standard k-ε in the free shear layers away from walls.
Obtaining these different behavior in the different regions is done through the use of a blending function F_1, which will take the value of one in the near wall region of the boundary layer (activating thus the standard k-ω) and then progressively switch to zero in the free-shear layers. The blending function is encountered first in the additional cross diffusion term (depending upon gradients of k and ω) in the ω equation appearing when rewriting the k-ε turbulence model into a standard k-ω formulation (see (*Menter*, 1993)). The blending function is also involved in several constants definitions that are becoming blends of inner ($_1$) and outer ($_2$) constants :

$$\sigma_k = F_1\sigma_{k1} + (1 - F_1)\sigma_{k2}, \tag{3.24}$$

$$\sigma_\omega = F_1\sigma_{\omega1} + (1 - F_1)\sigma_{\omega2}, \tag{3.25}$$

$$\gamma = F_1\gamma_1 + (1 - F_1)\gamma_2, \tag{3.26}$$

$$\beta = F_1\beta_1 + (1 - F_1)\beta_2. \tag{3.27}$$

where the blending function F_1 is depending of the distance to the wall as :

$$F_1 = \tanh\left\{\left\{\min\left[\max\left(\frac{\sqrt{k}}{C_\mu\omega z}, \frac{500\nu^f}{z^2\omega}\right), \frac{4\sigma_{\omega2}k}{CD_{k\omega}z^2}\right]\right\}^4\right\}, \tag{3.28}$$

This new turbulence model, is denoted as the baseline (BSL) model (*Menter*, 1993).

Tableau 3.2: $k-\omega$ model coefficients.

Model	P	C_μ	$C_{1\omega}$	$C_{2\omega}$	$C_{3\omega}$	$C_{4\omega}$
k-ω	$R_{ij}^f \frac{\partial u_i^f}{\partial x_j}$	0.09	5/9	3/40	0.35	1
k-ω SST	$\min\left(R_{ij}^f \frac{\partial u_i^f}{\partial x_j}, 10C_\mu k\omega\right)$	0.09	γ	3/40	0.35	1
k-ω 2006	$R_{ij}^f \frac{\partial u_i^f}{\partial x_j}$	0.09	5/9	$C_{2\omega 0} f_{C_{2\omega}}$	0.35	1
Model	σ_k	σ_ω	σ_d	$\mathrm{CD}_{k\omega}$	S_c	S_1
k-ω	0.5	0.5	0	0	1.0	1.0
k-ω SST	f(σ_{k1},σ_{k2})	f($\sigma_{\omega 1}$,$\sigma_{\omega 1}$)	$\sigma_{\omega 2}$	2(1-F_1)max$\left(\frac{\sigma_d}{\omega}\frac{\partial k}{\partial x_j}\frac{\partial \omega}{\partial x_j}, 10^{-10}\right)$	1.0	0
k-ω 2006	3/5	0.5	$\mathcal{H}\left(\frac{\partial k}{\partial x_j}\frac{\partial \omega}{\partial x_j}\right)\sigma_{d0}$	$A\frac{\sigma_d}{\omega}\frac{\partial k}{\partial x_j}\frac{\partial \omega}{\partial x_j}$	1.0	1.0

Tableau 3.3: Blending functions coefficients of the k-ω SST turbulence model

Constants for the inner (wall) region :			
β_1	γ_1	σ_{k1}	$\sigma_{\omega 1}$
0.075	5/9	0.85	0.5
Constants for the outer (free-stream) region :			
β_2	γ_2	σ_{k2}	$\sigma_{\omega 2}$
0.0828	0.44	1	0.856

The main improvement in the prediction of adverse pressure gradient flows is due to a modification in the eddy viscosity definition of the BSL model. *Menter* (1992) has shown that the best eddy-viscosity models in adverse pressure gradient are those whom are accounting for the transport of the principal turbulent shear stress as the Johnson-King model *Johnson and King* (1985). The latter includes a transport equation for the turbulent shear stress that is "based on Bradshaw's assumption (*Bradshaw et al.*, 1967) that the shear stress in a boundary layer is proportional to the TKE" (*Menter*, 1993) :

$$R_{ij}^f = \rho^f \ a_1 k, \tag{3.29}$$

where a_1=0.31. However, in two-equation models, the shear stress is usually computed as follows :

$$R_{ij}^f = \rho^f \ {\nu_t}^f \boldsymbol{S^f}, \tag{3.30}$$

with $\boldsymbol{S^f} = \sqrt{2\overline{S_{ij}}^f \ \overline{S_{ij}}^f}$.
According to *Menter* (1992), the equation 3.30 can be rewritten to :

$$R_{ij}^f = \rho^f \sqrt{\frac{Production_k}{Dissipation_k}} \ a_1 k. \tag{3.31}$$

In adverse pression gradient flows, *Driver* (1991) shows that the production of TKE exceeds its dissipation. As a consequence, eq. 3.31 leads to an over estimation of the Reynolds shear stress. In order to satisfy the *Bradshaw et al.* (1967) assumption in the framework of eddy-viscosity model, *Menter* (1993) proposition is to rewrite the eddy viscosity as :

$${\nu_t}^f = \frac{a_1 k}{max(a_1\omega; F_2 \boldsymbol{S^f})}, \tag{3.32}$$

where the function F_2 is a blending function written as follows :

$$F_2 = \tanh\left[\left[\max\left(\frac{2\sqrt{k}}{C_\mu \omega z}, \frac{500\nu^f}{z^2\omega}\right)\right]^2\right], \tag{3.33}$$

with z being the distance to the wall. F_2 is equal to one in the boundary-layer. In adverse pressure gradient boundary-layer, the production of TKE exceeds its dissipation so that $\boldsymbol{S^f} > a_1\omega$ and the Bradshaw's assumption (eq. 3.29) is respected in that region. When moving away from the wall, the blending function F_2 takes gradually values from one to zero so that the standard formulation of the eddy viscosity (${\nu_t}^f = k/\omega$) is used outside of the boundary layer.
Please note that the definition of the eddy viscosity, the blending function F_2, the production limiters and the constants γ_1 and γ_2 (see table 3.3) have been taken according to the last revision of the k-ω SST model that can be found in *Menter et al.* (2003).

If the superiority of the SST model is clearly admitted in the literature (*Roulund et al.*, 2005), its adaptation into a two-phase flow version is however extremely difficult. Indeed, the blending functions as defined in *Menter* (1993) and *Menter et al.* (2003) depend on the distance to the wall. Here, the bed interface is also supposed to act as a wall. The transformation of the pure fluid k-ω SST into a two-phase flow version becomes non trivial and was not successful. Therefore, this model will be used in its single-phase flow formulation and for hydrodynamics validation only.

vi) $k-\omega$ 2006 model

As a consequence of the improvements obtained with the SST model, Wilcox has presented a reformulated version of the standard k-ω (see *Wilcox* (2008)). This "revisited" model formulation incorporates the two key modifications highlighted in *Menter* (1993) with a slightly different approach and will be denoted as k-ω 2006 in the present manuscript.

The first key modification introduced in the k-ω 2006 turbulence model is the addition of a cross diffusion term in the specific dissipation equation (fourth term on the RHS of eq. (3.22)) :

$$CD_{k\omega} = A\frac{\sigma_d}{\omega}\frac{\partial k}{\partial x_j}\frac{\partial \omega}{\partial x_j}, \tag{3.34}$$

where A is a smoothing term and σ_d a coefficient that reads :

$$\sigma_d = \mathcal{H}\left(\frac{\partial k}{\partial x_j}\frac{\partial \omega}{\partial x_j}\right)\sigma_{d0}, \tag{3.35}$$

where $\sigma_{d0} = 1/8$ and $\mathcal{H}(.)$ is the Heaviside step function which has a value of unity if the argument is zero or positive and a value of zero if the argument is negative. The role of this cross-diffusion term is to increase the dissipation of TKE in the free-shear flow by enhancing the production of specific dissipation ω in that region. This will reduce the free-shear flow spreading rates sensitivity to the free-stream boundary conditions (*Wilcox*, 2008). However, similarly to what is done in the SST model, it is important to suppress the cross-diffusion term near a solid boundary (*Wilcox*, 2006). This is done by the Heaviside step function, because k and ω are respectively decreasing and increasing in the viscous sublayer when approaching the wall.
The A coefficient is a smoother imposing a gradual transition between the regions where the cross-diffusion term is activated or not. A is only present in the two-phase flow version of the model and allows to avoid instabilities :

$$A = \frac{1}{2}(1 + tanh(-40(\phi - 0.1))). \tag{3.36}$$

The closure coefficients used are consigned in table 3.2. Amongst them, the coefficient involved in the dissipation of dissipation term (second term on the RHS of eq. (3.22)) follows the generalization of the Pope correction (*Pope*, 1988) given by *Wilcox* (2008) :

$$C_{2\omega} = C_{2\omega 0} f_{C_{2\omega}}, \tag{3.37}$$

where

$$C_{2\omega 0} = 0.0708, \quad f_{C_{2\omega}} = \frac{1 + 85\chi_\omega}{1 + 100\chi_\omega}, \tag{3.38}$$

and

$$\chi_\omega = \left|\frac{\Omega_{ij}\Omega_{jk}\overline{S^f_{ki}}}{(C_\mu \omega)^3}\right|, \quad \Omega_{ij} = \frac{1}{2}\left(\frac{\partial u_i^f}{\partial x_j} - \frac{\partial u_j^f}{\partial x_i}\right). \tag{3.39}$$

The Pope correction has originally been proposed by *Pope* (1988) on the ε equation in order to resolves the round jet/plane jet anomaly. This anomaly, common to many two-equations turbulence models, predict, that round jet spreading rate is higher than plane jet one, whereas measurements predict the inverse phenomenon. The idea behind Pope correction is to introduce the χ_ω parameter as a "non dimensional measure of the vortex stretching", the latter being the

main mechanism for energy transfer from large to small eddies. Accounting for this mechanism increases the rate of energy transfer between the different turbulent scales and thus the dissipation for the smallest eddies. Of course, because vortices cannot be stretched in 1D or 2D, the Pope correction must be turned off for 1D or 2D configurations.

As in the SST model, the turbulent eddy viscosity ν_t^f is calculated incorporating a stress-limiting term :

$$\nu_t^f = \frac{k}{\tilde{\omega}} = \frac{k}{max\left(\omega, C_{lim}\sqrt{\frac{2S_{ij}^f\ S_{ij}^f}{C_\mu}}\right)}, \tag{3.40}$$

where $C_{lim} = 7/8$. In *Wilcox* (2006) definition, the stress limiting term in equation 3.40 uses the zero-trace version of the mean strain-rate tensor $\overline{S_{ij}^f}$. With the stress-limiting term, the eddy viscosity becomes defined as the ratio of the TKE and the specific dissipation multiplied by a factor taking account of the TKE production to dissipation ratio.
In the shear layer, $2S_{ij}^f S_{ij}^f \approx (\partial u_j^f/\partial x_j)^2$ so that the shear stress can be rewritten using eq. (3.40) as :

$${R_{ij}}^{tf} = \rho^f\ {\nu_t}^f \frac{\partial u_j^f}{\partial x_j} = \min\left(\rho^f \frac{k}{\omega}\frac{\partial u_j^f}{\partial x_j}, \rho^f C_{lim}^{-1}\sqrt{C_\mu}k\right) \tag{3.41}$$

Without the stress-limiting term, the ratio of TKE production over dissipation can be written as :

$$\frac{P_{TKE}}{D_{TKE}} = \frac{(k/\omega)(\partial u_j^f/\partial x_j)^2}{C_\mu k\omega}. \tag{3.42}$$

The stress-limited term is activated for $P_{TKE}/D_{TKE} \geq C_{lim}^{-2}$ and the shear stress reads :

$${R_{ij}}^f = \rho^f C_{lim}^{-1}\sqrt{C_\mu}k \tag{3.43}$$

As for the SST model, the stress-limiter acts when the ratio of TKE production to dissipation is above a given limit value in the boundary layer. It forces the shear stress to respect Bradshaw's assumption (*Bradshaw et al.*, 1967) in the shear layer.

3.2.3 Particle phase stress

The particle phase stress tensor can be split into the normal and off-diagonal components corresponding to the particle pressure $\tilde{p}^s$ and the particle shear stress τ_{ij}^s, respectively. As established by *Johnson and Jackson* (1987) the particle normal stresses (or pressure) can be generally classified into two contributions : a shear induced or collisional component (super-script 's') and a permanent contact component (super-script 'ff') :

$$\tilde{p}^s = p^{ff} + p^s, \tag{3.44}$$

where the permanent contact component p^{ff} is calculated as :

$$p^{ff} = \begin{cases} 0, \phi < \phi_{min}^{Fric} \\ Fr\frac{(\phi-\phi_{min}^{Fric})^{\eta_0}}{(\phi_{max}-\phi)^{\eta_1}}, \phi \geq \phi_{min}^{Fric}, \end{cases} \tag{3.45}$$

with $\phi_{min}^{Fric} = 0.57$, $\phi_{max} = 0.635$ for spheres. Fr, η_0 and η_1 are empirical coefficients. Following *Cheng et al.* (2017) the values are set to : $Fr = 0.05, \eta_0 = 3$ and $\eta_1 = 5$. The permanent contact

component is due to enduring contact in highly concentrated region that are often close to quasi-static/immobile bed. This normal pressure increases rapidly when the sediment concentration is close to maximum packing limit, and prevents unphysical sediment concentration in the sediment bed.

The second term in equation 3.44 accounts for the shear-induced/collisional particle normal stress. As mentioned in Chapter 1, there are two main approaches for calculating the collisional or the shear-induced particle stresses (p^s, τ^s_{ij}, respectively) : the kinetic theory of granular flows or the dense granular flow rheology. Both of them are implemented in SedFoam, and are described in subsection a) and b), respectively.

a) Kinetic theory of granular flows

The kinetic theory of granular flows is the first attempt to model the collisional or the shear-induced particle stresses. The dense phase kinetic theory of gases (*Chapman and Cowling*, 1970) was adapted and applied to granular flow by many researchers in the 1980's (*Jenkins and Savage*, 1983; *Lun et al.*, 1984; *Savage*, 1988).
The main ideas are that the intergranular interactions are assumed to be dominated by binary collisions for low to moderate sediment concentration, and that the collisional shear stresses are quantified by particle velocity fluctuations represented by the granular temperature Θ. The model, originally developed for dry granular flow, consists of smooth, slightly inelastic, spherical particles (*Jenkins and Savage*, 1983; *Lun*, 1991; *Lun and Savage*, 1987). The model suggested by *Ding and Gidaspow* (1990), accounting for the fluid phase is used in the present work. The balance equation for granular temperature is written as :

$$\frac{3}{2}\Big[\frac{\partial \phi \rho^s \Theta}{\partial t} + \frac{\partial \phi \rho^s u^s_j \Theta}{\partial x_j}\Big] = \big(- p^s \delta_{ij} + \tilde{\tau}^s_{ij}\big)\frac{\partial u^s_i}{\partial x_j} - \frac{\partial q_j}{\partial x_j} - \gamma + J_{int}, \tag{3.46}$$

where the first term on the RHS is the production of granular temperature, q_j is the flux of granular temperature, γ is the energy dissipation rate due to inelastic collision and J_{int} is the production/dissipation due to the interaction with the carrier fluid phase.

The closure of particle collisional pressure suggested by *Ding and Gidaspow* (1990) is used in SedFoam :

$$p^s = \rho^s \phi [1 + 2(1+e)\phi g_{s0}]\Theta, \tag{3.47}$$

where e is the coefficient of restitution during the collision. As the kinetic theory of granular flow is build on binary collision assumption, the crowdedness of a particle is described by the radial distribution function g_{s0}. Here, the radial distribution function for dense rigid spherical particles gases of *Carnahan and Starling* (1969) is adopted :

$$g_{s0} = \frac{2 - \phi}{2(1-\phi)^3}. \tag{3.48}$$

The particle collisional stress is calculated following *Gidaspow* (1994) proposition :

$$\tilde{\tau}^s_{ij} = \mu^s \ S^s_{ij} + \lambda \frac{\partial u^s_k}{\partial x_k}\delta_{ij}. \tag{3.49}$$

where S^s_{ij} is the deviatoric part of sediment phase strain rate tensor (see eq. (3.50)), μ^s is the particle shear viscosity and λ the bulk viscosity. The last two terms are defined as a function of the granular temperature and the radial distribution function (eq. 3.51 and eq. 3.52, respectively) :

$$S^s_{ij} = \frac{1}{2}\Big(\frac{\partial u^s_i}{\partial x_j} + \frac{\partial u^s_j}{\partial x_i}\Big) - \frac{2}{3}\frac{\partial u^s_k}{\partial x_k}\delta_{ij}, \tag{3.50}$$

$$\mu^s = \rho^s d\sqrt{\Theta}\Big[\frac{4}{5}\frac{\phi^2 g_{s0}(1+e)}{\sqrt{\pi}} + \frac{\sqrt{\pi}g_{s0}(1+e)(3e-1)\phi^2}{15(3-e)} + \frac{\sqrt{\pi}\phi}{6(3-e)}\Big]. \tag{3.51}$$

$$\lambda = \frac{4}{3}\alpha^2\rho^s d g_{s0}(1+e)\sqrt{\frac{\Theta}{\pi}}. \tag{3.52}$$

The closure of granular temperature flux in eq. (3.46) is assumed to be analogous to the Fourier's law of conduction :

$$q_j = -D_\Theta \frac{\partial \Theta}{\partial x_j}, \tag{3.53}$$

where the D_Θ is the conductivity of granular temperature :

$$D_\Theta = \rho^s d\sqrt{\Theta}\Big[\frac{2\phi^2 g_{s0}(1+e)}{\sqrt{\pi}} + \frac{9\sqrt{\pi}g_{s0}(1+e)^2(2e-1)\phi^2}{2(49-33e)} + \frac{5\sqrt{\pi}\phi}{2(49-33e)}\Big]. \tag{3.54}$$

The dissipation rate due to inelastic collision, γ , is calculated following *Ding and Gidaspow* (1990) :

$$\gamma = 3(1-e^2)\phi^2\rho^s g_{s0}\Theta\Big[\frac{4}{d}\Big(\frac{\Theta}{\pi}\Big)^{1/2} - \frac{\partial u^s_j}{\partial x_j}\Big]. \tag{3.55}$$

Finally, because of the presence of a carrier fluid phase, the carrier flow turbulence can also induce particle fluctuations, i.e granular temperature production or dissipation. The last term on the RHS of eq. (3.46) is accounting for the fluid-particle interaction term can be expressed following *Hsu et al.* (2004) :

$$J_{int} = \phi K(2t_{mf}k - 3\Theta). \tag{3.56}$$

The total shear stress τ^s_{ij} can be calculated as a sum of the collisional-kinetic component and a frictional component :

$$\tau^s_{ij} = \tilde{\tau}^s_{ij} + \tau^{ff}_{ij}, \tag{3.57}$$

where the frictional shear stress due to frictional contact is modeled as :

$$\tau^{ff}_{ij} = -2\rho^s \nu^s_{Fr} S^s_{ij}. \tag{3.58}$$

in which ν^s_{Fr} is the frictional viscosity. This shear stress generated by the frictional contact is added here to extend the capability of SedFoam to resolve the quasi-static bed. In this region, the KT is known to reach its limitations, because particles interactions are not only driven by binary collisions but more by shearing which has, therefore to be accounted for.
Following *Srivastava and Sundaresan* (2003) work, in which the combination of the frictional normal stress from *Johnson and Jackson* (1987) model (Eqn. 3.45) and the frictional viscosity from *Schaeffer* (1987) model is provided, the friction viscosity is calculated by :

$$\nu^s_{Fr} = \frac{p^{ff}\sin(\theta_f)}{\rho^s \ \big(\parallel \mathsf{S^s} \parallel^2 + D^2_{small}\big)^{1/2}}, \tag{3.59}$$

where a constant friction angle θ_f is used. $D_{small} = 10^{-10}s^{-1}$ is the regularization parameter to avoid numerical singularity.

b) Dense granular flow rheology

The other approach avalaible in SedFoam for shear-induced particle normal stress and shear stress modelling is the dense granular flow rheology or the so-called $\mu(I)$ rheology (*Forterre and Pouliquen*, 2008; *GDRmidi*, 2004). It has already successfully been used by *Revil-Baudard and Chauchat* (2013) and *Chauchat* (2018) to model turbulent sheet flows for instance. Contrary to the kinetic theory of granular flows, this approach is phenomenological, and based on dimensional analysis. The total particle phase shear stress reads :

$$\tau_{ij}^s = R_{ij}^s + r_{ij}^s, \tag{3.60}$$

in which R_{ij}^s represents a Reynolds stress like contribution for the solid phase and r_{ij}^s is the granular stress contribution coming from particle-particle interactions. The Reynolds stress contribution is modeled according to *Rusche* (2003) using the C_t model. C_t is defined as the ratio of particle rms velocity fluctuations to the fluid rms velocity fluctuations. This leads to the following Reynolds stress contribution for the particle phase :

$$R_{ij}^s = \rho^s \phi \Big[C_t^2 \nu_t^f \ S_{ij}^s - \frac{2}{3} C_t^2 k \delta_{ij} \Big], \tag{3.61}$$

According to *Rusche* (2003) C_t depends on the local value of the particle concentration and varies between 1 and 3. In the present model a value of 1 has been tested and the influence of this contribution is evaluated in chapter 4. This C_t model is also one of the original contribution, provided in this manuscript to the development of SedFoam.
The granular contribution is written as :

$$r_{ij}^s = \nu_{Fr}^s S_{ij}^s, \tag{3.62}$$

where the frictional viscosity ν_{Fr}^s is defined following *Chauchat and Médale* (2014) :

$$\nu_{Fr}^s = \min \left(\frac{\mu(I)\ \tilde{p}^s}{\rho^s \ \left(|| \ \boldsymbol{S^s} \ ||^2 + D_{small}^2 \right)^{1/2}}, \nu_{max} \right), \tag{3.63}$$

in which ν_{max} is the maximum solid phase viscosity, $|| \ \boldsymbol{S^s} \ ||$ is the norm of the shear rate tensor and $D_{small} = 10^{-6} s^{-1}$ is a regularization parameter that is introduced to avoid singularity. In addition to the viscosity regularization, ν_{Fr}^s is also clipped by ν_{max} for numerical stability. The influence of the clipping term value on the sediment flux prediction will be investigated in Chapter 4.

The frictional shear viscosity ν_{Fr}^s allows to relate the total particle phase shear stress to the total particle pressure $\tilde{p}^s$ by a dynamic friction coefficient μ (*Jop et al.*, 2006) depending on the dimensionless number I. In the present study, the regime of the granular flow rheology is in the free fall or grain inertia regime. In this regime, the friction coefficient depends on the inertial number $I = || \ \nabla \boldsymbol{u^s} \ || \ \ d\sqrt{\rho^s / \tilde{p}^s}$ according to :

$$\mu(I) = \mu_s + \frac{\mu_2 - \mu_s}{I_0 / I + 1}, \tag{3.64}$$

with μ_s the static friction coefficient, μ_2 an empirical dynamical coefficient and I_0 an empirical constant of the rheology.

The shear induced contribution to the particle pressure can be obtained from the dilatancy law $\phi(I)$ as proposed by *Boyer et al.* (2011) for the viscous regime of the granular flow rheology. The adaptation to the inertial regime leads to the expression suggested by *Maurin et al.* (2016) :

$$\phi(I) = \frac{\phi_{max}}{1 + B_\phi I}. \tag{3.65}$$

Inverting equation (3.65) and substituting the definition of the inertial number I gives the following expression for the shear induced pressure :

$$p^s = \left(\frac{B_\phi \ \phi}{\phi_{\max} - \phi} \right)^2 \rho^s d \ || \ \boldsymbol{S^s} \ ||^2 \ . \tag{3.66}$$

Finally, the total particle pressure $\tilde{p}^s$ can be calculated by Eqn. (3.44).

3.2.4 Local Schmidt Number model

In the model description of *Chauchat et al.* (2017), the Schmidt number S_c present in the two-phase flow momentum and turbulent quantities equations (Eqs. 3.3, 3.4, 3.21 and 3.22) is a constant. However, *Van Rijn* (1984b) has established that the Schmidt number depends on the ratio of the grains free fall velocity (w_{fall0}) to the friction velocity u_*. In the present work, a local Schmidt number definition for the two-phase flow model inspired from *Jha and Bombardelli* (2009) is proposed :

$$S_c = \min \left[\left(1 + 2 \left(\frac{w_{\text{fall0}}}{u_* + u_{\text{small}}} \right)^2 \right)^{-1} , \frac{1}{3} \right], \tag{3.67}$$

where $u_{\text{small}} = 10^{-10}\text{m.s}^{-1}$ is a regularization parameter that is introduced to avoid singularity. The grains free fall velocity is calculated following an iterative procedure. First the particulate Reynolds number of a isolated gravity falling particle is computed from a input velocity :

$$Re_p^{'} = \frac{w_{fall0}^i d}{\nu^f}. \tag{3.68}$$

Following the value of the particulate Reynolds number, the drag coefficient C_d is computed from equation 3.6. Then, an new estimation of the free fall velocity is given by :

$$w_{fall0}^{i+1} = \sqrt{\frac{4(s-1)gd}{3C_d}}. \tag{3.69}$$

The variation between both iterations is calculated as :

$$\epsilon_w = \frac{w_{fall0}^{i+1} - w_{fall0}^i}{w_{fall0}^{i+1}}. \tag{3.70}$$

The new estimation of the free fall velocity w_{fall}^{i+1} is injected in equation 3.68 and the same operations are repeated until $\epsilon_w < 10^{-6}$.
The friction velocity changes spatially and temporally, it is computed as :

$$u_* = \sqrt{\frac{| \ R_{ij}^f \ |}{\rho^f}}. \tag{3.71}$$

3.3 Numerical model implementation

The numerical implementation SedFoam is based on OpenFOAM, an open-source finite volume CFD library providing the numerical discretization schemes, solvers and the framework of Finite Volume Method (FVM). Here, the two-phase flow governing equations are implemented by modifying the solver twoPhaseEulerFoam (*Peltola et al.*, 2009; *Rusche*, 2003; *Weller*, 2002). FVM is extensively used for the numerical resolution of partial differential equations in CFD. The domain is divided into Control Volumes (CV) in which the integral form of conservation equations are applied. OpenFOAM uses the FVM over a collocated grid arrangement. All dependent variables are stored at the cell center and interpolated to the CV boundaries. Furthermore, the same CV is used for all variables, the computational effort is therefore minimized. The advantage of the FVM is that the system of partial differential equations can be discretized on arbitrary three-dimensional structured or unstructured meshes, so that complex geometries can be easily handled. The Gauss theorem is applied to the convection and diffusion terms leading to conservative schemes.

The numerical implementation presented here is similar to the one described in *Chauchat et al.* (2017). The main difference lies in the pressure solver used. In the present numerical implementation, the pressure solver iterates on the reduce pressure p^* :

$$p^* = p - \rho^f \mathbf{g}.\mathbf{h}, \tag{3.72}$$

where p is the total pressure and $\rho^f \mathbf{g}.\mathbf{h}$ is the hydrostatic pressure. This way of solving the pressure system is similar to what is done in other validated OpenFOAM solvers such as inter-Foam (*Deshpande et al.*, 2012). It has also been found that this solver is more stable compared to the one described in *Chauchat et al.* (2017), allowing to increases the CFL condition and increase the computational time step, as it will be detailed in the following.

The fluid phase momentum equation is taken as an example to illustrate the numerical discretization. Rearranging eq. (3.4) by dividing $(1-\phi)\rho^f$, leads to :

$$\begin{aligned}\frac{\partial \mathbf{u}^f}{\partial t} + \nabla\cdot(\mathbf{u}^f\mathbf{u}^f) - (\nabla\cdot\mathbf{u}^f)\mathbf{u}^f =& -\frac{1}{\rho^f}\nabla p^* - \frac{\phi K}{\rho^f}(\mathbf{u^f}-\mathbf{u}^s) + \frac{K}{\rho^f}\frac{1}{\sigma_c}\,\nu_t^f\nabla\phi \\ &+ \frac{\mathbf{f}}{\rho^f} + \frac{1}{(1-\phi)}\nabla\cdot\boldsymbol{\tau}^f\end{aligned} \tag{3.73}$$

The fluid phase shear stress can be written according to equation (3.7) and reads :

$$\begin{aligned}\frac{1}{(1-\phi)}\nabla\cdot\boldsymbol{\tau}^f =& \nabla\cdot\left(\nu_{Eff}^f\nabla\mathbf{u}^f\right) + \nu_{Eff}^f\frac{\nabla(1-\phi)}{(1-\phi)}\nabla\mathbf{u}^f \\ &+ \frac{1}{(1-\phi)}\nabla\cdot\left\{(1-\phi)\,\nu_{Eff}^f\left[\left(\nabla\mathbf{u}^f + \nabla\mathbf{u}^{fT}\right) - \frac{2}{3}\nabla\cdot\mathbf{u}^f\right]\right\}.\end{aligned} \tag{3.74}$$

In the expanded shear stress equation just above, the first two terms on the RHS are treated implicitly while the last two terms are treated explicitly. Substituting eq. (3.74) in the momentum

equation (3.73) leads to the following expression :

$$\frac{\partial \mathbf{u}^f}{\partial t} + \nabla\cdot(\mathbf{u}^f\mathbf{u}^f) - (\nabla\cdot\mathbf{u}^f)\mathbf{u}^f - \nabla\cdot\left(\nu^f_{Eff}\nabla\mathbf{u}^f\right) - \nu^f_{Eff}\frac{\nabla(1-\phi)}{(1-\phi)}\nabla\mathbf{u}^f + \frac{\alpha K}{\rho^f}\mathbf{u}^f = -\frac{1}{\rho^f}\nabla p^*$$

$$+ \frac{\phi K}{\rho^f}\mathbf{u}^s + \frac{1}{\sigma_c}\,\frac{K\nu^f_t}{\rho^f}\nabla\phi + \frac{1}{(1-\phi)}\nabla\cdot\left\{(1-\phi)\;\nu^f_{Eff}\left[\nabla\mathbf{u}^{fT} - \frac{2}{3}\nabla\cdot\mathbf{u}^f\right]\right\}, \tag{3.75}$$

which is more useful rewritten into a matrix form :

$$\left[\mathsf{A^f}\right]\cdot\mathbf{u}^f = \mathbf{H}^f + \mathbf{R}^f + \frac{\phi K}{\rho^f}\mathbf{u}^s - \frac{1}{\rho^f}\nabla p^*, \tag{3.76}$$

where $\left[\mathsf{A^f}\right]$ is a matrix composed of the diagonal terms of the algebraic system associated with equation (eq. 3.75), $\mathbf{H}^f$ include the off-diagonal terms and the source term $\mathbf{R}^f$ is composed of the turbulent suspension term and the explicit diffusion terms :

$$\mathbf{R}^f = \frac{\mathbf{f}}{\rho^f} + \frac{1}{\sigma_c}\frac{K\;\nu^f_t}{\rho^f}\nabla\phi + \frac{1}{(1-\phi)}\nabla\cdot\left\{(1-\phi)\;\nu^f_{Eff}\left[\nabla\mathbf{u}^{fT} - \frac{2}{3}\nabla\cdot\mathbf{u}^f\right]\right\} \tag{3.77}$$

If the same reasoning is applied for the solid phase momentum equation (eq. 3.3), the latter reads :

$$\frac{\partial \mathbf{u}^s}{\partial t} + \nabla\cdot(\mathbf{u}^s\mathbf{u}^s) - (\nabla\cdot\mathbf{u}^s)\mathbf{u}^s - \frac{1}{\tilde{\phi}}\nabla\cdot(\nu^s_{Fr}\nabla\mathbf{u}^s) - \nabla\cdot\left(\nu^s_{Eff}\nabla\mathbf{u}^s\right) - \nu^s_{Eff}\frac{\nabla\phi}{\tilde{\phi}}\nabla\mathbf{u}^s + \frac{(1-\phi)K}{\rho^s}\mathbf{u}^s$$

$$= -\frac{1}{\tilde{\phi}\rho^s}\nabla p^{ff} - \frac{1}{\rho^s}\nabla p^* + \frac{(1-\phi)K}{\rho^s}\mathbf{u}^f - \frac{1}{\sigma_c}\frac{(1-\phi)K\;\nu^f_t}{\tilde{\phi}\rho^s}\nabla\phi + \frac{\mathbf{f}}{\rho^s} + \mathbf{g}\left(1-\frac{\rho^f}{\rho^s}\right) - \frac{1}{\tilde{\phi}\rho^s}\nabla p^s$$

$$+ \frac{1}{\tilde{\phi}}\left\{\nabla\cdot\left[(\phi\nu^s_{Eff} + \nu^s_{Fr})\nabla\mathbf{u}^{sT}\right] + \nabla\left[\left(\lambda - \frac{2}{3}(\alpha\nu^s_{Eff} + \nu^s_{Fr})\right)\nabla\cdot\mathbf{u}^s\right]\right\}, \tag{3.78}$$

where the sediment volume fraction ϕ at the denominator is substituted by $\tilde{\phi} = \phi + \phi_{Small}$ to avoid dividing by zero when the solid phase volume fraction tends to zero. Equation 3.78 can also be rewritten into a matrix form :

$$\left[\mathsf{A^s}\right]\cdot\mathbf{u}^s = \mathbf{H}^s + \mathbf{R}^s + \frac{(1-\phi)K}{\rho^s}\mathbf{u}^f - \frac{1}{\rho^s}\nabla p^*, \tag{3.79}$$

with $\mathbf{R}^s$ containing the turbulent suspension term, the gravity term, the shear induced pressure term and the explicit diffusion terms :

$$\mathbf{R}^s = -\frac{1}{\sigma_c}\frac{(1-\phi)K\;\nu^f_t}{\tilde{\phi}\rho^s}\nabla\phi + \frac{\mathbf{f}}{\rho^s} + \mathbf{g}\left(1-\frac{\rho^f}{\rho^s}\right) - \frac{1}{\tilde{\phi}\rho^s}\nabla p^s$$

$$+ \frac{1}{\tilde{\phi}}\left\{\nabla\cdot\left[(\phi\nu^s_{Eff} + \nu^s_{Fr})\nabla\mathbf{u}^{sT}\right] + \nabla\left[\left(\lambda - \frac{2}{3}(\alpha\nu^s_{Eff} + \nu^s_{Fr})\right)\nabla\cdot\mathbf{u}^s\right]\right\} \tag{3.80}$$

Following *Rusche* (2003) the terms involving the ratio of particle phase volume gradient to the volume fraction are treated at the cell face level in the predictor-corrector algorithm. An unique exception is made for the particle phase normal stress p^{ff} gradient for which a reconstruction of the surface normal gradient at the cell centre stabilizes the solution.

The advantage of separating the RHS of the momentum equations as the sum of two terms ($\mathbf{R}^k$ and $\mathbf{H}^k$, with k describing one phase) applies when writing the pressure-velocity algorithm. For the gradient terms, the method used here is similar as what can be found in *Rhie and Chow* (1983).

3.3.1 Velocity-pressure algorithm

The PISO (Pressure-Implicit with Splitting of Operators) algorithm is used to solve fluid and particle velocities (*Peltola et al.*, 2009; *Rusche*, 2003; *Weller*, 2002). Rather than solving all the equations in an iterative manner, PISO splits the operators into an implicit predictor and multiple explicit corrector steps. A very few corrector steps are needed to obtain a satisfactory accuracy.

First, in the predictor step, the intermediate velocities ($\tilde{\mathbf{u}}^s$, $\tilde{\mathbf{u}}^f$) are computed at the cells centres using the corresponding momentum equations without the pressure gradient term and the explicit part of the drag term :

$$\begin{aligned} \tilde{\mathbf{u}}^s &= \left[\mathsf{A^s}\right]^{-1}\mathbf{H}^s, \\ \tilde{\mathbf{u}}^f &= \left[\mathsf{A^f}\right]^{-1}\mathbf{H}^f, \end{aligned} \tag{3.81}$$

where $\left[\mathsf{A^s}\right]^{-1}$ and $\left[\mathsf{A^f}\right]^{-1}$ represent the inverse matrices of $\left[\mathsf{A^s}\right]$ and $\left[\mathsf{A^f}\right]$, respectively.
At this stage, these intermediate velocities do not satisfy the mass conservation equations for each phase (eqs. (3.2) and (3.1)).

The second step consist in estimating the velocity fluxes at the cell faces. The right hand side of equations (3.76)-(3.79) are computed at the cell faces :

$$\Phi^f_R = \left[\mathsf{A^f}\right]_f^{-1}\mathbf{R}^f{}_f \quad \text{and} \quad \Phi^s_R = \left[\mathsf{A^s}\right]_f^{-1}\mathbf{R}^s{}_f, \tag{3.82}$$

where the f subscript design the cell face.
The velocity flux associated with the predictor step is interpolated at the cell faces :

$$\Phi^f_U = \left(\left[\mathsf{A^f}\right]^{-1}\mathbf{H}^f\right)_f \quad \text{and} \quad \Phi^s_U = \left(\left[\mathsf{A^s}\right]^{-1}\mathbf{H}^s\right)_f \tag{3.83}$$

Introducing the notation :

$$AK^f = \left(\left[\mathsf{A^f}\right]^{-1}\phi K/\rho^f\right)_f \quad \text{and} \quad AK^s = \left(\left[\mathsf{A^s}\right]^{-1}(1-\phi)K/\rho^s\right)_f \tag{3.84}$$

one can write the volume averaged velocity flux at the cell faces as :

$$\Phi^* = \phi_f\left[\Phi^s_U + \Phi^s_R + AK^s\Phi^f\right] + (1-\phi_f)\left[\Phi^f_U + \Phi^f_R + AK^f\Phi^s\right] \tag{3.85}$$

where $\Phi^f = \mathbf{u}^f|_f.\mathbf{n}|_f S_f$ and $\Phi^s = \mathbf{u}^s|_f.\mathbf{n}|_f S_f$ denote the fluid and particle phases velocity fluxes at the previous iteration or time step and at the cell faces, respectively, and S_f is the cell

face area associated with the face f. At this stage, the drag force is partially treated explicitly for the mixture flux Φ^*.

In the third step, the velocity fluxes at the cell faces have to be corrected by including the pressure term. First of all, the semi-discrete fluxes equations including the pressure gradient term are written :

$$\Phi^{s**} = \Phi^s_U + \Phi^s_R + \left(\frac{(1-\phi)K}{\rho^s \left[\mathsf{A^s}\right]}\right)_f \Phi^{f**} - \frac{\nabla^\perp p^*|_f}{\rho^s \left[\mathsf{A^s}\right]_f} \tag{3.86}$$

$$\Phi^{f**} = \Phi^f_U + \Phi^f_R + \left(\frac{\phi K}{\rho^f \left[\mathsf{A^f}\right]}\right)_f \Phi^{s**} - \frac{\nabla^\perp p^*|_f}{\rho^f \left[\mathsf{A^f}\right]_f} \tag{3.87}$$

Then, by taking the divergence of the volume averaged mixture velocity face flux given by the equations (3.86 and 3.87) and by imposing the incompressibility constraint ($\nabla \cdot \mathbf{U}^{**} = \nabla \cdot (\phi \mathbf{u}^{s**} + (1-\phi)\mathbf{u}^{f**}) = 0$), one can built the pressure equation as a function of the predicted velocity or predicted face fluxes :

$$\int_{Vp} \nabla \cdot \left[\left(\frac{\phi}{\rho^s \left[\mathsf{A^s}\right]} + \frac{(1-\phi)}{\rho^f \left[\mathsf{A^f}\right]}\right) \nabla p^*\right] dV = \int_{Vp} \nabla \cdot \mathbf{U}^* dV \tag{3.88}$$

$$\text{or} \quad \oint_S \left(\frac{\phi_f}{\rho^s \left[\mathsf{A^s}\right]_f} + \frac{(1-\phi)_f}{\rho^f \left[\mathsf{A^f}\right]_f}\right) \nabla^\perp p^*|_f \ \mathbf{n}|_f \ dS = \oint_S \mathbf{U}^*|_f \ \mathbf{n}|_f \ dS. \tag{3.89}$$

$$\int_{Vp} \nabla \cdot \left[\phi \mathbf{u}^{s**} + (1-\phi)\mathbf{u}^{f**}\right] dV = \oint_S \left[\phi_f \mathbf{u}^{s**}|_f + (1-\phi_f)\mathbf{u}^{f**}|_f\right] \cdot \mathbf{n} \ dS = 0 \tag{3.90}$$

The two expressions shown in equation 3.90 are equivalent by using the Gauss theorem. At the discrete level, this equation is written as :

$$\sum_f \left[\phi_f \Phi^{s**} + (1-\phi_f)\Phi^{f**}\right] = 0 \tag{3.91}$$

substituting the velocity fluxes correction equations (3.86) and (3.87) into the previous equation, the Poisson equation for the pressure reads :

$$\sum_f \left(\frac{\phi_f}{\rho^s \left[\mathsf{A^s}\right]_f} + \frac{(1-\phi)_f}{\rho^f \left[\mathsf{A^f}\right]_f}\right) \nabla^\perp p^*|_f \ \mathbf{n}|_f \ S_f = \sum_f \Phi^*. \tag{3.92}$$

This equation leads to a matrix system written at the cell faces. The resulting algebraic system is usually solved using an multigrid solver (GAMG). The resulting pressure field p^* is used for the correction step in which the mixture velocity face flux is corrected using equations (3.86) and (3.87) :

$$\Phi^{**} = \Phi^* - \sum_f \nabla^\perp p^*|_f S_f \tag{3.93}$$

Both, the fluid and the particle phase face fluxes can be corrected :

$$\Phi_s^s = \Phi_U^s + \Phi_R^s - \frac{\nabla^\perp p^*|_f}{\rho^s \left[\mathsf{A^s}\right]_f} \tag{3.94}$$

$$\Phi_s^f = \Phi_U^f + \Phi_R^f - \frac{\nabla^\perp p^*|_f}{\rho^f \left[\mathsf{A^f}\right]_f} \tag{3.95}$$

in which the explicit drag contributions coming from the other phase are still missing. The corrected fluxes for each phase can be rewritten as :

$$\Phi^{s**} = \Phi_s^s + AK^s \Phi^{f**} \tag{3.96}$$

$$\Phi^{f**} = \Phi_s^f + AK^f \Phi^{s**} \tag{3.97}$$

The face flux associated with the relative velocity, Φ^{r**} is :

$$\Phi^{r**} = \Phi^{s**} - \Phi^{f**} = \Phi_s^s + AK^s(\Phi_s^f + AK^f \Phi^{s**}) - \left[\Phi_s^f + AK^f(\Phi_s^s + AK^s \Phi^{f**})\right] \tag{3.98}$$

$$\Phi^{r**} = \Phi_s^f + AK^s \Phi_s^f - \left[\Phi_s^f + AK^f \Phi_s^s\right] + AK^s AK^f \left[\Phi^{s**} - \Phi^{f**}\right] \tag{3.99}$$

$$(1 - AK^s AK^f)\Phi^{r**} = \Phi_s^s + AK^s \Phi_s^f - \left[\Phi_s^f + AK^f \Phi_s^s\right] \tag{3.100}$$

$$\Phi^{r**} = \frac{1}{1 - AK^s AK^f} \left\{ \Phi_s^s + AK^f \Phi_s^f - \left[\Phi_s^f + AK^f \Phi_s^s\right] \right\} \tag{3.101}$$

This last expression for the relative flux allows to treat the drag force almost implicitly. This is supposed to stabilize the coupling between the two momentum equations and allows thus for longer time steps with regard to the particle response time.

The predicted fluxes for each phase are then obtained from the mixture flux plus a correction coming from the relative flux. The mixture velocity and relative velocity expression reads :

$$\Phi^{**} = \phi_f \Phi^{s**} + (1 - \phi_f)\Phi^{f**} \quad \text{and} \quad \Phi^{r**} = \Phi^{s**} - \Phi^{f**} \tag{3.102}$$

leading to the following relationships :

$$\Phi^s = \Phi^{**} + (1 - \phi_f)\Phi^{r**} \quad \text{and} \quad \Phi^f = \Phi^{**} - \phi_f \Phi^{r**} \tag{3.103}$$

The same type of procedure is applied for the reconstruction of the velocities at the cell centres : U, U^s, U^f.

In order to ensure the mass conservation an iterative procedure of N cycles may be required. In the following conducted simulations, three iterations (N=3) is usually enough for convergence. The finite volume discretization of the equations have not been shown here but all the details can be found in *Jasak* (1996) and *Rusche* (2003).

3.3.2 Summary of the solution procedure

The numerical solution procedure for the proposed two-phase flow model is outlined as follow :

1. Solve for sediment concentration ϕ, i.e., Eq. (3.1) ;
2. Update the volume concentration of the fluid : $1-\phi$;
3. Update the drag parameter K in the drag term, e.g., Eqn (3.5) ;
4. Solve for the fluid turbulence closure, update k, ε or ω (depending on the turbulence closure $k-\varepsilon$, $k-\omega$ or $k-\omega 2006$), and then calculate the eddy viscosity and effective fluid total viscosity ;
5. Solve for the particle phase stress (KT model or the dense granular rheology) ;
6. PISO-loop, solving velocity-pressure coupling for N loops :
   (a) Construct the coefficient matrix $\left[\mathsf{A}^{\mathbf{s}}\right]$ and $\left[\mathsf{A}^{\mathbf{f}}\right]$ and explicit array $\mathbf{H^s}$ and $\mathbf{H^f}$ using Eqn (3.79) and (3.76).
   (b) Update the other explicit source terms $\mathbf{R^s}$ and $\mathbf{R^f}$, Eq. (3.80) and (3.77).
   (c) Calculate $\mathbf{u^{s*}}$,$\mathbf{u^{f*}}$ using equations (3.81) without fluid pressure gradient term ;
   (d) Construct and solve the pressure Eq. (3.92) ;
   (e) Correct fluid and particle velocities after solving pressure and update fluxes Eqns (3.102)-(3.103) ;
   (f) Go to a) if the number of loops is smaller than N (no tolerance criteria).
7. Advance to the next time step

In the above solution procedure, the velocity-pressure coupling steps are looped for N times. The advantage of this loop is to avoid velocity-pressure decoupling caused by the direct solving method. In the cases encountered here, the loop number $N = 1$ to 3 is usually enough to shows a good convergence, especially for steady flows.

The time step, Δt, can be set to a constant value or adjusted automatically based on two Courant numbers, one related to the local flow velocity and the local grid size $Co = 1/2 \sum_f \Phi_f^f \Delta t / V_p$ (the same as for single phase problems) and one related to the relative velocity $Co_r = 1/2 \sum_f \left| \Phi_f^s - \Phi_f^f \right| \Delta t / V_p$ which is specific to the coupling of the fluid and sediment phase momentum equations in the two-phase flow model. The most limiting time step is used as the criterion for setting the adjustable time step. My practice is to set these two Courant numbers to 0.8. If numerical instabilities appears for such value, they can be decreased down to 0.1.

Chapitre 4

Model verification and benchmarking

4.1 Résumé

L'objectif de ce chapitre est de valider le code SedFoam présenté au chapitre précédent en le confrontant à des résultats expérimentaux ou numériques issus de la littérature sur plusieurs configurations. Ces comparaisons avec la littérature ont également pour but de montrer les capacités de SedFoam à résoudre des problèmes complexes nécessitant de résoudre le transport sédimentaire et la turbulence dans le fluide. Dans ce chapitre je m'attache à tester toutes les différentes possibilités offertes par SedFoam pour déterminer les contraintes granulaires et les contraintes de Reynolds pour le fluide.
Dans un premier temps, le sédiment n'est pas considéré. Une description des différentes conditions aux parois (lisses et rugueuses) implémentées dans SedFoam ainsi que leur validation sur le cas canonique de couche limite turbulente de *Moser et al.* (1999) sont proposées.
Ensuite, les trois cas considérés portent sur la validation de SedFoam avec présence de sédiment. On présente deux cas 1D et un cas 2D. Les cas 1D sont le cas du sheet-flow turbulent de *Revil-Baudard et al.* (2015) ainsi qu'un cas de transport uniforme par charriage issu des travaux de *Roulund et al.* (2005). La configuration 2D quant à elle, est un cas d'affouillement derrière un tablier dans un écoulement unidirectionnel (*Amoudry and Liu*, 2009; *Breusers*, 1967; *Cheng et al.*, 2017).

Concernant les cas 1D, l'accord obtenu entre les simulations et les données de la littérature pour les profils verticaux de vitesses, de concentration, de flux et d'énergie cinétique turbulente est très satisfaisant aussi bien dans une configuration de type sheet-flow qu'en charriage. On retrouve un bon accord pour l'ensemble des combinaisons utilisées pour déterminer les contraintes granulaires et les contraintes de Reynolds. De plus, les estimations de l'évolution du taux de transport de sédiments ou de l'épaisseur de la couche de transport en fonction du nombre de Shields sont en très bon accord avec les lois de référence pour ce type de quantité : *Meyer-Peter and Müller* (1948) et *Wilson* (1966) pour le taux de transport et *Wilson* (1987) pour l'épaisseur de la couche de transport. Un résultat que l'on retrouve pour une large gamme de nombre de Shields (entre 0.1 et 3) avec différents types de particules : sables moyens, acrylique, PMMA et pour différents diamètres (de 250μm à 3mm).

Pour le cas 2D, les résultats montrent que SedFoam est capable de prédire des résultats en

accord avec la littérature pour une configuration multidimensionnelle. Les lois d'échelles proposées dans la littérature pour décrire l'évolution de la profondeur d'érosion en fonction du temps (*Breusers*, 1967) sont bien retrouvées avec SedFoam même si une sensibilité non négligeable au choix des modèles de fermeture est observée.

4.2 Introduction

The purpose of the present chapter is to test SedFoam on three one-dimensional cases and one 2D case. All of these test cases aim to test the capabilities of the model presented in Chapter 3 to deal with complex turbulent sediment transport problems with different combinations of inter-granular stress and turbulence models.
First of all, a study of the different advection schemes available in OpenFOAM is presented. Then, the different wall boundary conditions implemented in SedFoam are described and detailed. Their validation on the state of the art case from *Moser et al.* (1999) is proposed and discussed further.
When including sediment, two 1D cases, based on literature experimental configurations are studied, the unidirectional turbulent sheet-flow case of *Revil-Baudard et al.* (2015) and the unidirectional bedload configuration that can be found in *Roulund et al.* (2005). First, the sheet flow configuration of *Revil-Baudard et al.* (2015) is chosen because this is one of the most recent and complete experimental work on the subject, providing more variables (velocities, concentration and Reynolds shear stress profiles) as compared with other literature data. Concerning the unidirectional bedload configuration, its purpose is to validate the use of the two-phase approach and more particularly SedFoam for low Shields numbers. Moreover, this configuration will also provide the initial flow and the boundary conditions for the 3D configuration for the scour around a vertical cylinder, studied in Chapter 5.
The multidimensional case that will be detailed here is the two-dimensional scour downstream of an apron that can be found in *Amoudry and Liu* (2009) and *Cheng et al.* (2017). This configuration presents several advantages. First of all, it involves the scour phenomenon discussed in Chapter 5 of this manuscript. The configuration of scour downstream of an apron is two-dimensional, which is very important for the multidimensional validation of SedFoam intended in this chapter, but also quite simple and therefore not too computationally demanding, allowing multiple runs with different turbulence or inter-granular stress models. Finally, this is a configuration that have been studied both experimentally (*Breusers*, 1967; *Breusers and Raudkivi*, 1991) and numerically using a two-phase flow approach (*Amoudry and Liu*, 2009; *Cheng et al.*, 2017). The literature provides two empirical laws to describe the initial development of the scour hole and the evolution of the upstream scour angle and recent two-phase flow results to compare with.

4.3 Numerical schemes in OpenFOAM

One of the main advantages on the OpenFOAM numerical toolbox is that it provides a large choice of available numerical schemes to the user. This section aims to summarize the behavior of the different OpenFoam numerical schemes. First, a technical description of the different OpenFOAM scheme is proposed. Then, a qualitative illustration of the different schemes on a simple 1D scalar advection test case is undertaken. The purpose is to have a clear knowledge of the numerical schemes that should be used in SedFoam for the different configurations studied.

The test case presented here is a simple 1D scalar advection using the *scalarTransportFoam* solver. The latter solves a incompressible advection-diffusion equation :

$$\frac{\partial T}{\partial t} + \nabla \cdot (u^f T) - \nabla^2 (D_T T) = 0, \tag{4.1}$$

where T is the transported scalar, u^f is the constant fluid velocity, and $D_T = 0$ is the diffusion coefficient.
T, has a initial gaussian shape :

$$T(x) = e^{-\gamma(x-x_c)^2} \tag{4.2}$$

where $0 < x < 1.5$m, x_c=0.5m and $\gamma = 150\text{m}^{-2}$.
The same simulation is run with different numerical schemes for the time and the spatial discretization. All the different schemes used are summarized in table 4.1. They are divided into the following categories :

- *ddtSchemes* : first time derivative, $\partial/\partial t$
- *gradSchemes* : gradient, ∇
- *divSchemes* : divergence, $\nabla\cdot$
- *laplacianSchemes* : laplacian, ∇^2

The discretization schemes for each term can be selected from those summarized in table 4.1. The present section is a partial description of the numerical schemes implemented in OpenFOAM, more details can be found in the OpenFOAM user guide (*Greenshields*, 2017) or in the OpenFOAM programmer's guide (*Greenshields*, 2015).

Temporal Schemes :

The first time derivative of T is integrated over a control volume V as follows :

$$\frac{\partial}{\partial t} \int_V T dV \tag{4.3}$$

In OpenFOAM, the term is discretized by simple differencing in time using the following definitions :

- For the new values, $T^n \equiv T(t + \Delta t)$ at the time step that is solving for.
- For the old values, $T^{n-x} \equiv T(t)$ with $x \in [1, .., n-2]$ that is stored from the previous time steps.

The first time derivative terms ($\partial/\partial t$) are specified in the *ddtSchemes* sub-dictionary. Two choices are possible. The first one is *Euler* implicit, that is first order accurate in time :

$$\frac{\partial}{\partial t} \int_V T dV = \frac{(T_P V)^n - (T_P V)^{n-1}}{\Delta t}, \tag{4.4}$$

where T_P is the variable T taken at the centre of the cell of interest P. The second choice is to use a *backward* differencing scheme, that is second order accurate in time :

$$\frac{\partial}{\partial t} \int_V T dV = \frac{3(T_P V)^n - 4(T_P V)^{n-1} + (T_P V)^{n-2}}{2\Delta t} \tag{4.5}$$

Tableau 4.1: OpenFoam numerical schemes description.

Description	OpenFOAM name	Properties
time derivative	*Euler*	transient, first order implicit, bounded (eq. 4.4).
	backward	transient, second order implicit, potentially unbounded (eq. 4.5).
spatial gradient operation	*Gauss linear*	second order linear interpolation (eq. 4.7).
	cellLimited Gauss linear 1	2^{nd} order linear interpolation with gradient limitation.
divergence operators	*Gauss upwind phi*	upwind 1st order (eq. 4.9).
	Gauss linear	second order centered scheme, unbounded (eq. 4.7).
	Gauss linearUpwind grad(T)	upwind 2nd order, unbounded, requires a limited gradient scheme.
	Gauss vanLeer	second order centered scheme including Total Variation Diminishing with van Leer limiter.
	Gauss limitedLinear M	linear scheme stabilized with the introduction of a limiter M (from 0 to 1) (Sweby limiter). With M=1, blend between linear and upwind schemes in the regions of rapidly changing gradient (eq. 4.10).
Laplacian operators	*Gauss linear corrected*	linear interpolation with non-orthogonality correction (eq. 4.12).

Gradient Schemes :

The gradient schemes are specified in the *gradSchemes* sub-dictionary. The gradients are calculated using integral over faces :

$$\int_V \nabla T dV = \oint_{\partial V} T d\boldsymbol{s} = \sum_f \boldsymbol{s}_f T_f, \tag{4.6}$$

where $\boldsymbol{s}_f$ and T_f are the cell surface and the value of T at the face, respectively. According to the OpenFoam documentation the default discretization scheme used for the gradient terms is *Gauss linear*. The *Gauss* entry specifies the standard finite volume discretization of Gaussian integration which requires the interpolation of values from cell centers to face centers due to colocated arrangement of variables. The interpolation scheme is then given by the *linear* entry, meaning either linear interpolation or central differencing :

$$T_f = f_x T_P + (1 - f_x) T_N, \tag{4.7}$$

where $f_x \equiv \overline{fN}/\overline{PN}$ where $\overline{fN}$ is the distance between the face and cell centre of the neighbouring cell N, and $\overline{PN}$ is the distance between cell centers P and N.
In some cases, the discretization of a specific gradient (velocity gradient and/or gradient of turbulent field) terms has to be imposed to improve boundedness and stability. The entry reads : *cellLimited Gauss linear 1*. The use of a *cellLimited* scheme allows to limit the gradient so that when cell values are extrapolated to faces using the calculated gradient, the face values are within the values given by surrounding cells. A limiting coefficient is also required, here the value 1 is used, which guarantees boundedness.

Divergence Schemes :

The divergence schemes are specified in the *divSchemes* sub-dictionary. These assignments have to be set for advection terms, where velocity $\boldsymbol{u}$ provides the advective flux but also for diffusive terms. The non-advective terms are generally treated with a *Gauss linear* interpolation (see eq. 4.7) whereas the advective (also denoted as convective) terms are integrated over a control volume and linearized as follows :

$$\oint_s T(\boldsymbol{n}\cdot\boldsymbol{u})d\boldsymbol{s} = \int_V \nabla\cdot(T\boldsymbol{u}) = \sum_f T_f(\boldsymbol{s}_f\cdot\boldsymbol{u}_f) = \sum_f T_f F, \tag{4.8}$$

where $F = \boldsymbol{s}_f\cdot\boldsymbol{u}_f$ is the face flux, *i.e*, the measure of the flow through the face.
The face field T_f can be determined using a variety of schemes :

- Central differencing (CD) : *Gauss linear*, see eq. 4.7. Second-order accurate, but causes oscillations.
- Upwind differencing (UD) : *Gauss upwind*. Accounts for the transportive property of the term meaning that information comes from upstream. Does not presents oscillations but is generally highly diffusive.

$$T_f = max(F,0)T_P + min(F,0)T_N \tag{4.9}$$

- Blending differencing : *limitedLinear M*, scheme that combine UD and CD to preserve boundedness with reasonable accuracy :

$$T_f = (1-M)(T_f)_{UD} + M(T_f)_{CD}, \tag{4.10}$$

  where M is a blending coefficient, activated in regions of rapidly changing gradient. This scheme is a pure centered second order scheme that transforms to a first order upwind scheme (if M=1) in regions of rapidly changing gradient.
  Other TVD schemes can be chosen, such as Van Leer, SUPERBEE, MINMOD...

Laplacian Schemes :

The laplacian schemes are specified in the *laplacianSchemes* sub-dictionary. The Laplacian term is discretized using the Gauss theorem :

$$\int_V \nabla\cdot(D_T\nabla T)dV = \int_S \boldsymbol{s}\cdot(D_T\nabla T) = \sum_f \nu_f\boldsymbol{s}_f\cdot(D_T\nabla T)_f, \tag{4.11}$$

where D_T is the diffusion coefficient. The Gauss scheme used for Laplacian discretization requires a selection of both an interpolation scheme for the diffusion coefficient and a surface normal gradient scheme (∇T). In the present work, the interpolation scheme for the diffusivity is given by the *linear* entry and the *corrected* entry specified the surface normal gradient schemes. The face gradient discretization is implicit when the length vector $\boldsymbol{d}$ between the centre of the cell of interest P and the centre of a neighbouring cell N is orthogonal to the face plane, i.e. parallel to $\boldsymbol{s}_f$ (first term on the RHS of eq. 4.12) :

$$\boldsymbol{s}_f\cdot(D_T\nabla T)_f = \mid\boldsymbol{s}_f\mid\frac{T_N - T_P}{\mid\boldsymbol{d}\mid} + \boldsymbol{\varpi}_f\cdot(\nabla T)_f. \tag{4.12}$$

The second term on the RHS of equation 4.12 is an explicit correction term, in case of mesh non-orthogonality and it is recommended in the OpenFOAM documentation for unstructured mesh. The correction term is evaluated by interpolating cell centre gradients, themselves calculated by central differencing cell centre values.

Qualitative illustration of the numerical schemes implemented in OpenFOAM :

Different combinations of the numerical schemes described in the previous section are tested on the 1D transport of a passive scalar T. The results can be seen in figure 4.1 which represents the gaussian shape of the scalar T at times 0s (centered in x=0.5m and given by eq. (4.2)) and 0.5s (centered in x=1m). The different numerical schemes combinations leading to the results presented in the figure 4.1 are summarized in table 4.2.
The spacial discretization of the problem has voluntarily been chosen quite coarse (100 elements in the longitudinal direction, Δx=1.5cm) to emphasize the different schemes weaknesses.

Tableau 4.2: Numerical schemes correspondence table.

Name	**ddtSchemes**	**gradSchemes**	**divSchemes**
sch1	Euler	Gauss linear	Gauss upwind phi
sch2	Euler	cellLimited Gauss linear 1	Gauss linearUpwind
sch3	backward	cellLimited Gauss linear 1	Gauss linearUpwind
sch4	backward	Gauss linear	Gauss linearUpwind
sch5	backward	Gauss linear	Gauss linear
sch6	backward	Gauss linear	Gauss van leer
sch7	backward	Gauss linear	Gauss limitedLinear 1
sch8	backward	Gauss linear	Gauss limitedLinear 0

To improve figure readability, the results are presented on two panels in figure 4.1. In the top panel, run *sch*1 is performed with first order time and divergence schemes (Euler and first order upwind, respectively). It presents a very high numerical diffusion. This type of divergence scheme is generally chosen to test the validity of a given mesh but is too diffusive to predict accurate results. A second order upwind scheme is then used in runs *sch*2 to *sch*4, allowing to reduce the numerical diffusion. The influence of the temporal scheme order is also tested. The results show that using first or second order temporal schemes (*sch*2 or *sch*3, respectively) together with second order upwind schemes doesn't affect the results accuracy. Using a linear interpolation without limiting the gradient (*linear* instead of *cellLimited* for run *sch*4) for the spatial gradient term also reduces the numerical diffusion. Finally, refining the mesh is necessary to reduce numerical diffusion (see *sch*4 with 200 elements instead of 100 in the longitudinal direction).
The results of the same case using second order centered divergence schemes are presented in bottom panel of figure 4.1. First, a pure second order centered scheme is chosen for the divergence term (*sch*5). This kind of scheme are not adapted to treat advection terms and instabilities appear. Here, oscillations are visible close to the x=0.75m abscissa. These instabilities can be corrected by using a Total Variation Diminishing (TVD) scheme. Here, for *sch*6 the Van Leer TVD limiter is chosen and the result is correct although more diffusive than second order upwind.
Finally a centered second order scheme with the *limitedLinear* entry (see *sch*7, *sch*8 and eq 4.10) is tested. Using M=1, the results give similar result than using the Van Leer TVD limiter. However, it behaves more like a *linearUpwind* (*sch*3) as the M coefficient tends to 0. With this scheme, the diffusion seems to become anisotropic at the front and at the rear of the scalar field. Again, increasing the resolution (*sch*7 and 200 elements) allows to reduce the numerical diffusion.

Here, the properties of the different schemes have been investigated on the very simple case

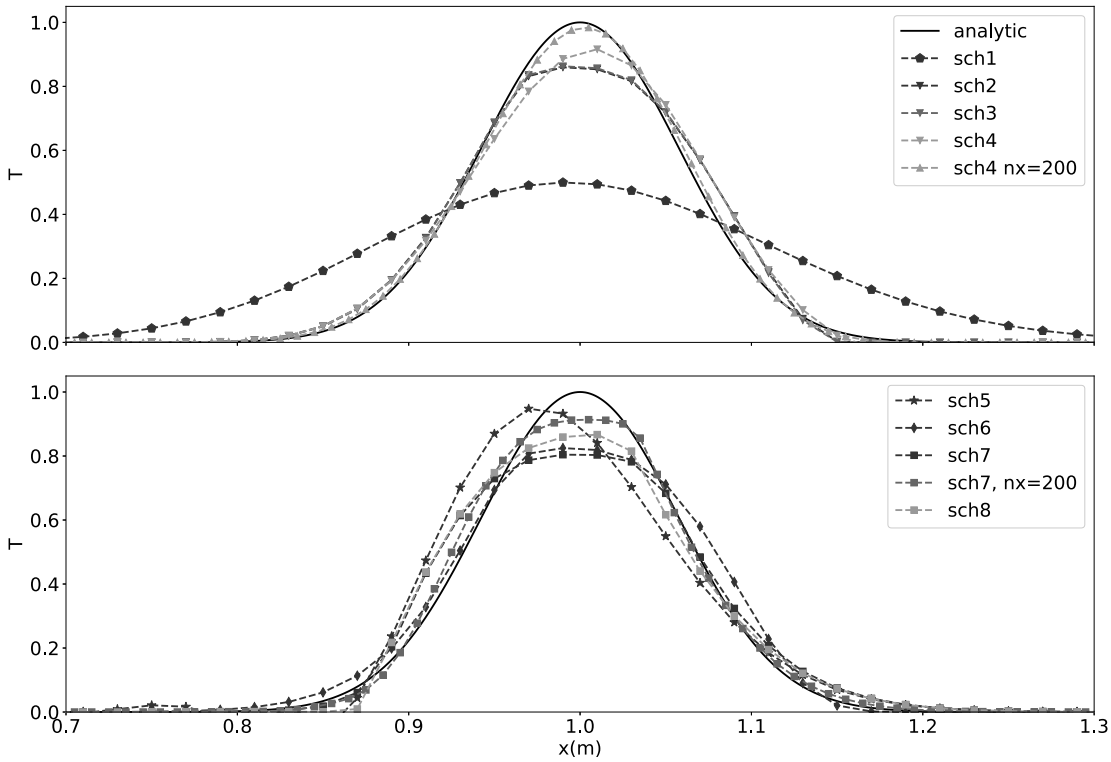

FIGURE 4.1: Advection of scalar T, here shown at t=0.5s using the different numerical schemes available in OpenFOAM.

of pure advection. It shows that some schemes have to be avoided at all time (first order upwind or gauss linear for advection schemes for instance). The other schemes give quite similar similar results between them. However, when dealing with more complex situations (sheet-flow, 3D Scour) a second order centered scheme with the highest Sweby limiter (*limitedLinear* taken to 1) often appears as the more stable than a second order upwind and as the best choice between stability and diffusion for the divergence operators.

4.4 Wall Boundary Conditions

In all of the different configurations investiguated in the present work, the wall boundary condition treatment is extremely important. In the Rigid-Bed (no sediment) and Live-Bed cases of flow around a vertical cylinder presented in Chapter 5, the flow is modified by the presence presence of a wall. In both cases, the smooth vertical cylinder is responsible for the different flow patterns as streamlines contraction, downflow in front of the cylinder, horseshoe vortex and vortex shedding for example (see Chapter 1). In order to accurately predict the different quantities describing the flow around the cylinder (velocities, TKE, TKE dissipation...) it is thus essential to accurately capture the different above-mentioned flow features. Furthermore, the 3D cases considered in Chapter 5 are bounded by the bottom wall in the Rigid-Bed configuration, presenting a given roughness it is also impacting the flow and its dynamics.

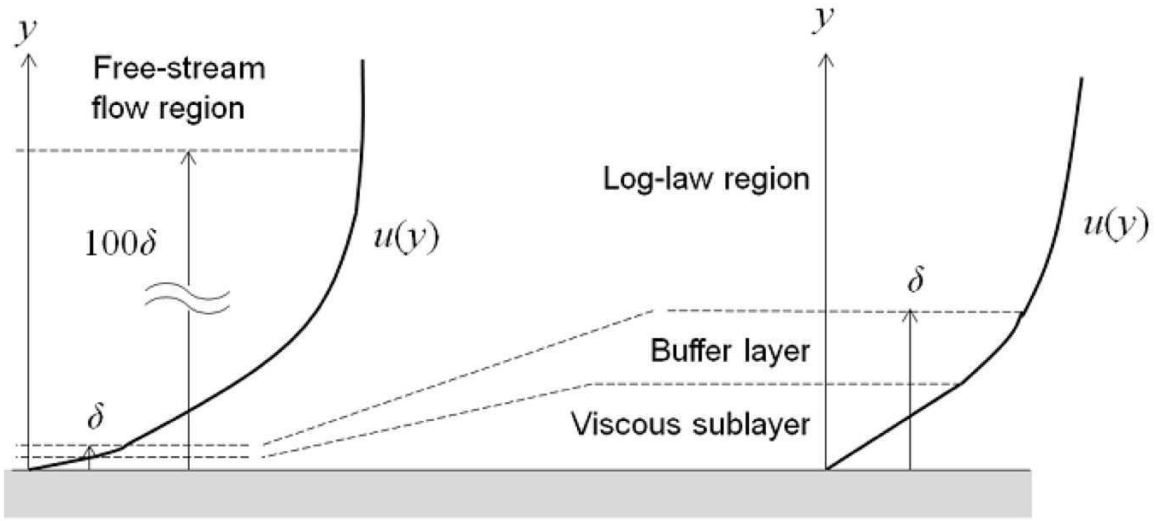

FIGURE 4.2: The four regimes of a turbulent flow near a wall. Source : *www.comsol.com.*

Near a smooth wall, the turbulent flow can be separated into four zones which are represented in figure (4.2). At the wall, the non-Slip boundary condition imposes a velocity equal to zero. Just above, within a thin layer denoted as the viscous sublayer, the flow velocity varies linearly with the distance to the wall. Further away from the wall, in the buffer layer, the flow begins its transition to turbulence. Even further away from the wall, in the log-law region, the flow is fully turbulent and the average flow velocity evolves logarithmically with the distance to the wall. Finally, the furthest region away from the wall is the free-stream region (or outer layer). The viscous and the buffer layers are extremely thin, if the distance from the wall to the top of the buffer layer is equal to δ, then the log-law region will extend to approximatively 100δ from the wall. Computing the flow field in all of the previously described flow regimes is possible by using a RANS model for instance. Two main choices can be made concerning the lower layers : resolve the complete profile of the boundary layer (this choice is expensive in computational resources because of the small size of both, the buffer and the viscous layer) or use wall functions to reduce the number of cells close to the wall. Wall functions ignore the flow field in the buffer region and analytically compute a fluid velocity at the wall that is not zero.

The non-dimensionnal distance to the wall is the key parameter when dealing with wall functions. It is dependent on the friction velocity closest to the wall and of the distance to this wall :

$$z^+ = \frac{z u_*}{\nu^f} \tag{4.13}$$

where ν^f is the kinematic viscosity and $u_* = \sqrt{\tau_0/\rho^f}$ is the friction velocity based on the wall shear stress $\tau_0 = (\mu + \mu_t)(\partial u_i^f/\partial x_j + \partial u_j^f/\partial x_i))$.
When using a wall function it is necessary that the z^+ of the first grid point is not exceeding $\approx$10 in order to ensure that the first node is placed inside the viscous sublayer. If not, the wall function can not correctly calculate the flow properties at this first calculation node which can lead to important errors concerning the velocity results in the outer layer.

Concerning the boundary conditions themselves, at the walls, zero velocity is imposed. Within the OpenFOAM framework, for the TKE, a small fixed value (*fixedValue*, $\mathcal{O}(10^{-10})$) can be used so as the *kqRWallFunction* that acts similarly as a Neumann boundary condition.
As discussed in *Wilcox* (2006), the ω-equation possesses an analytical solution in which, the value of ω may be specified very close to the wall. Here, the ω value can be specified in two different manners :

(i) *Use of a standard wall function* : The OpenFoam software has already several wall functions implemented. To impose ω at the wall, the standard wall function follows the approach of *Menter and Esch* (2001). The solution to ω equations is known for both the viscous and the log layer :

$$\omega_{\text{vis}} = \frac{6\nu^f}{\beta_1 z^2} \tag{4.14}$$

$$\omega_{\log} = \frac{u_*}{C_\mu^{1/4}\kappa z}, \tag{4.15}$$

where z is the cell centroid distance from the wall. Using equations (4.14)-(4.15) in a blending form gives :

$$\omega = \sqrt{\omega_{\text{vis}}^2 + \omega_{\log}^2} \tag{4.16}$$

For low z values the viscous values of ω are recovered and for larger values of z, the logarithmic values are recovered.

(ii) *Use of a tuned wall function* : The standard wall function for ω is written for smooth walls. When dealing with environmental flows the walls are often rough. In these cases, it is necessary to incorporate the effect of surface roughness when specifying ω at the wall. In this tuned wall function we follow Wilcox's recommendations (*Wilcox*, 2006) : a given roughness height is imposed at the wall in order to parametrize the viscous sublayer behavior and appears in the S_r tuning parameter :

$$S_r = \begin{cases} \left(\frac{50}{k_s^+}\right)^2 & k_s^+ < 25 \\ \frac{100}{(k_s^+)} & k_s^+ > 25 \end{cases} \tag{4.17}$$

where $k_s^+ = (k_s u_\tau^f)/\nu^f$ is the dimensionless roughness.
The tuning parameter S_r account for the bed roughness and is needed to compute the mesh independent ω_{wall} value :

$$\omega_{wall} = S_r \frac{{u_*}^2}{\nu^f} \tag{4.18}$$

This tuned wall function is also used by *Roulund et al.* (2005) but with a slightly modified tuning parameter. When working on the *Roulund et al.* (2005) case it is thus recommended to use :

$$S_r = \begin{cases} \left(\frac{40}{k_s^+}\right)^3 & k_s^+ < 20.2 \\ \frac{100}{(k_s^+)^{0.85}} & k_s^+ > 20.2 \end{cases} \tag{4.19}$$

These way of accounting for wall roughness was not originally present in OpenFoam and I have implemented them in SedFoam for the purpose of hydrodynamics validation on *Roulund et al.*

(2005) case. Both wall functions (with S_r written as in eq. 4.17 and eq. 4.19) can be found in SedFoam under the name of *wilcoxOmegaWallFunction* and *roulundOmegaWallFunction*, respectively.

4.5 One-dimensional cases

4.5.1 Unidirectional turbulent boundary layer

The SedFoam boundary layer and turbulence model validation is performed on a classical turbulent boundary layer case which can be found in *Moser et al.* (1999). A sketch of the 1D vertical computational domain is presented in figure 4.3 : under a x-axis oriented pressure gradient, a water column is moving over a flat plate. The fluid height is h^f=0.1m. The latter is water with density $\rho^f = 1000$ kg.m^{-3} and kinematic viscosity $\nu^f = 10^{-6}$ m^2.s^{-1}.

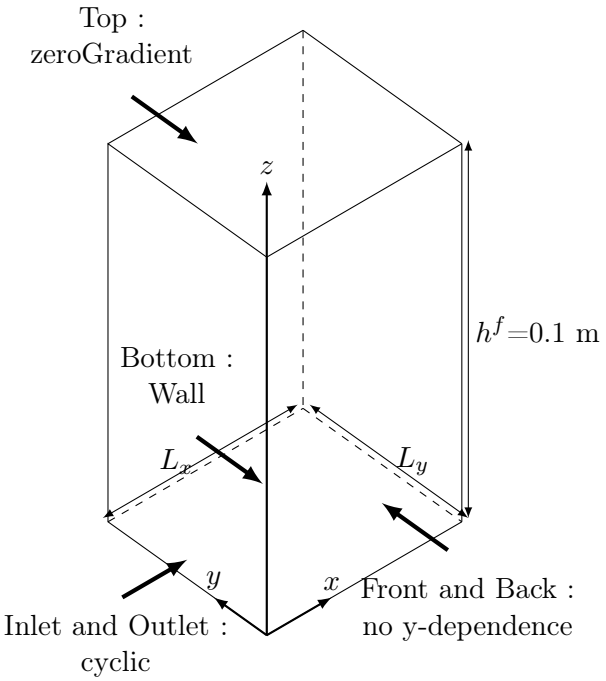

FIGURE 4.3: Sketch of the geometry and of the boundary conditions implemented in the numerical model.

The domain is divided in 64 elements, with a cell expansion ratio of 1.026 along the vertical direction. For such mesh the normalized distance to the wall from the first cell is $z^+ \approx 1$. The numerical schemes for temporal and spatial derivatives are listed in table 4.3, it has been checked that using a second order upwind divergence scheme (*linearUpwind*) or a *limitedLinear* does not change the results. The lateral boundaries (inlet and outlet) are set to *cyclic* while the front and back boundaries are set to empty. The latter boundary condition means that the y-components are not considered by the solver. At the top boundary, the pressure and the sediment concentration ϕ (for stability reason) are fixed to a zero value and a zero gradient (*i.e.* Neumann boundary conditions) is imposed on all the other quantities. At the wall, the velocity is set to zero, a

zeroGradient condition is imposed for the pressure and wall functions are imposed for TKE and TKE dissipation.

The boundary Reynolds number and the mean velocity value in *Moser et al.* (1999) are, $Re_\tau = 180$ and $\overline{U}$=0.0687 m.s^{-1}, respectively. Contrary to classical OpenFOAM solvers, in SedFoam the flow is generated by a pressure gradient acting as an external force in the momentum equations for both phases in equations 3.3 and 3.4. Here, to obtain the pressure gradient corresponding to the mean velocity $\overline{U}$ a first computation has been undertaken with the *boundaryFoam* solver for each case. It gives f_{px}=0.15 kg.m^{-2}.s^{-2}.

Tableau 4.3: Numerical schemes for *Moser et al.* (1999) boundary layer test case[a]

Description	keywords	keywordValue	Formulation
time derivative	*ddtSchemes*	*Euler*	$\partial\varphi/\partial t$
spatial gradient operation	*gradSchemes*	*Gauss linear*	$\nabla\varphi$
divergence operators	*divSchemes*	*Gauss linearUpwind*	$\nabla\cdot\varphi$
Laplacian operators	*laplacianSchemes*	*Gauss linear corrected*	$\nabla\cdot(\nabla\varphi)$

[a] φ denotes a dummy variable for the illustration purpose.

Figure 4.4 shows the comparison between SedFoam and state of the art results for dimensionless velocity (u/u_{max}), dimensionless turbulent kinetic energy (k/u_*^2) and specific dissipation (ω) using the k-ω (standard and low-Reynolds version) and the k-ω2006 combined with wall functions provided in SedFoam. In figure 4.4, $z^+ \approx 1$. Literature results are only available for u/u_{max} and k/u_*^2. Two different manners of imposing the turbulent quantities at the wall are tested : use the standard wall function implemented in OpenFOAM (*omstd*) and use the tuned wall-function following *Wilcox* (2006) recommendations (*omw*).
The results are compared to those obtained by *Wilcox* (1998) with a standard k-ω turbulence model, *Wilcox* (2006) with a low-Reynolds version of the k-ω turbulence model and *Moser et al.* (1999) with Direct Numerical Simulations (DNS). The characteristic signature of a low-Reynolds boundary layer profil is the peak of turbulent kinetic energy close to the wall. In the literature results presented here, only the low-Reynolds version of k-ω is able to recover this peak of TKE. This low-Reynolds k-ω turbulence model integrates *Wilcox* (2006) turbulence damping functions for the k and ω diffusion to reproduce the peak in the turbulence kinetic energy observed close to the wall with DNS simulations. This low-Reynolds version is used for a validation purpose only and is therefore not detailed in the present manuscript.

Without the presence of sediment the two-phase flow version of RANS turbulence models behaves as their single phase version. The results presented in figure 4.4 show that the velocity profile is recovered by all the turbulence models. The two-phase version of the standard k-ω and k-ω2006 turbulence models implemented into SedFoam are not low-Reynolds versions and do not recover the peak of turbulent kinetic energy close to the wall. This can be achieved by using a low-Reynolds k-ω turbulence model.
A point of major importance is that the present results are not influenced by the choice of the wall-function when $z^+ \approx 1$.

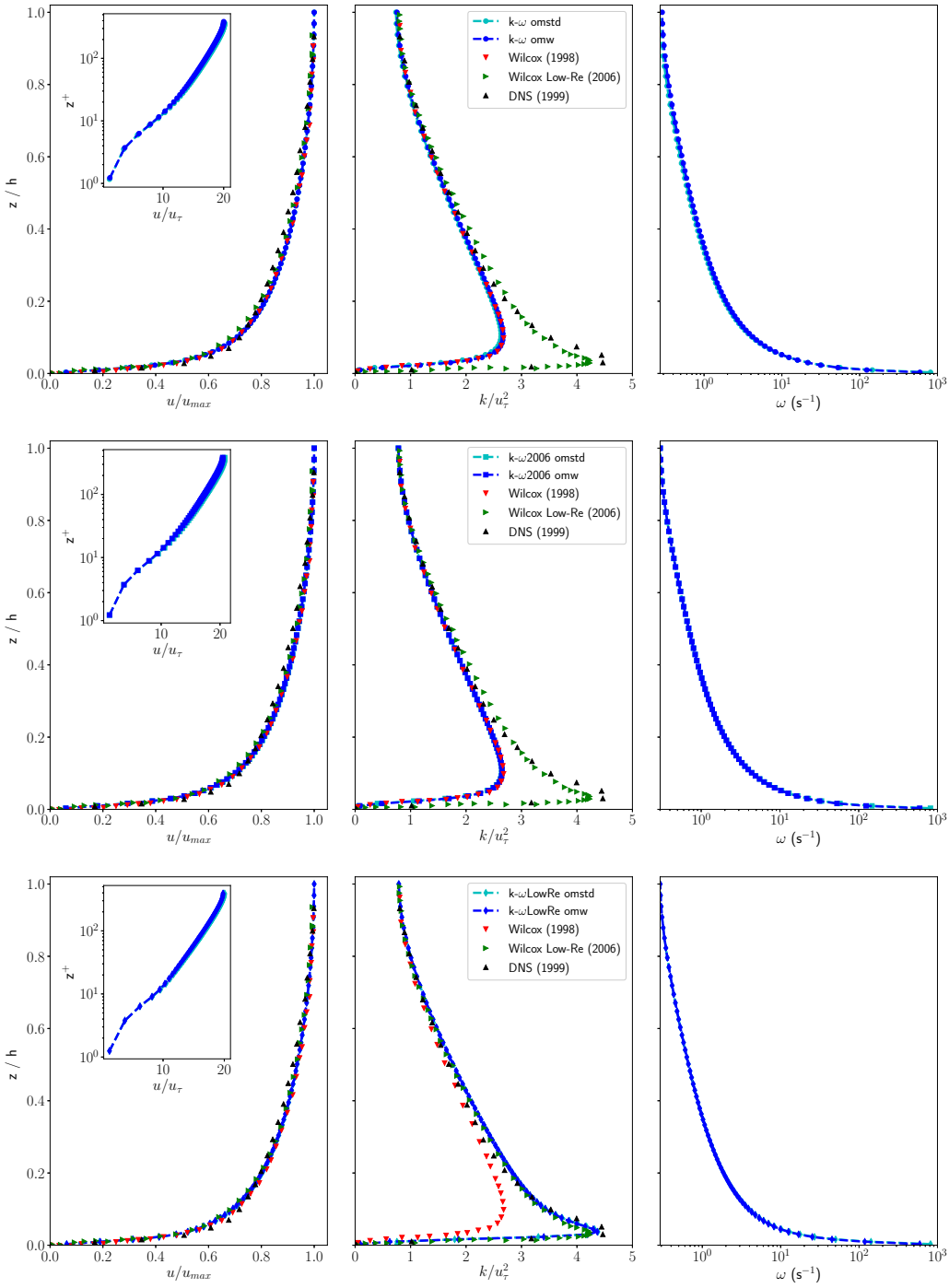

FIGURE 4.4: Comparison between SedFoam and *Moser et al.* (1999); *Wilcox* (1998, 2008) for velocity, TKE and specific dissipation rate profiles using the k-ω (top panel), k-ω2006 (middle panel), and k-ω low-Reynolds (bottom panel) turbulence models and different wall functions. Here, $z^+ \approx 1$.

Figure 4.5 shows the comparison between SedFoam and state of the art results for the same quantities as in figure 4.4 using the k-ω2006 combined with the two wall functions provided in SedFoam for several z^+. Only the k-ω2006 turbulence model is used because this is the best RANS approach available for two-phase flow simulations with a strong adverse pressure gradient (see Chapter 3 discussion on the SST and k-ω2006 models). The standard ω-wall function provides results in very good agreement with the literature for $z^+ \in [0.1 - 10]$ for all quantities (see top panel of figure 4.5). For the tuned ω-wall function when $z^+ \geq 2$, the agreement is acceptable up to $z^+ \approx 10$ (see bottom panel of figure 4.5).

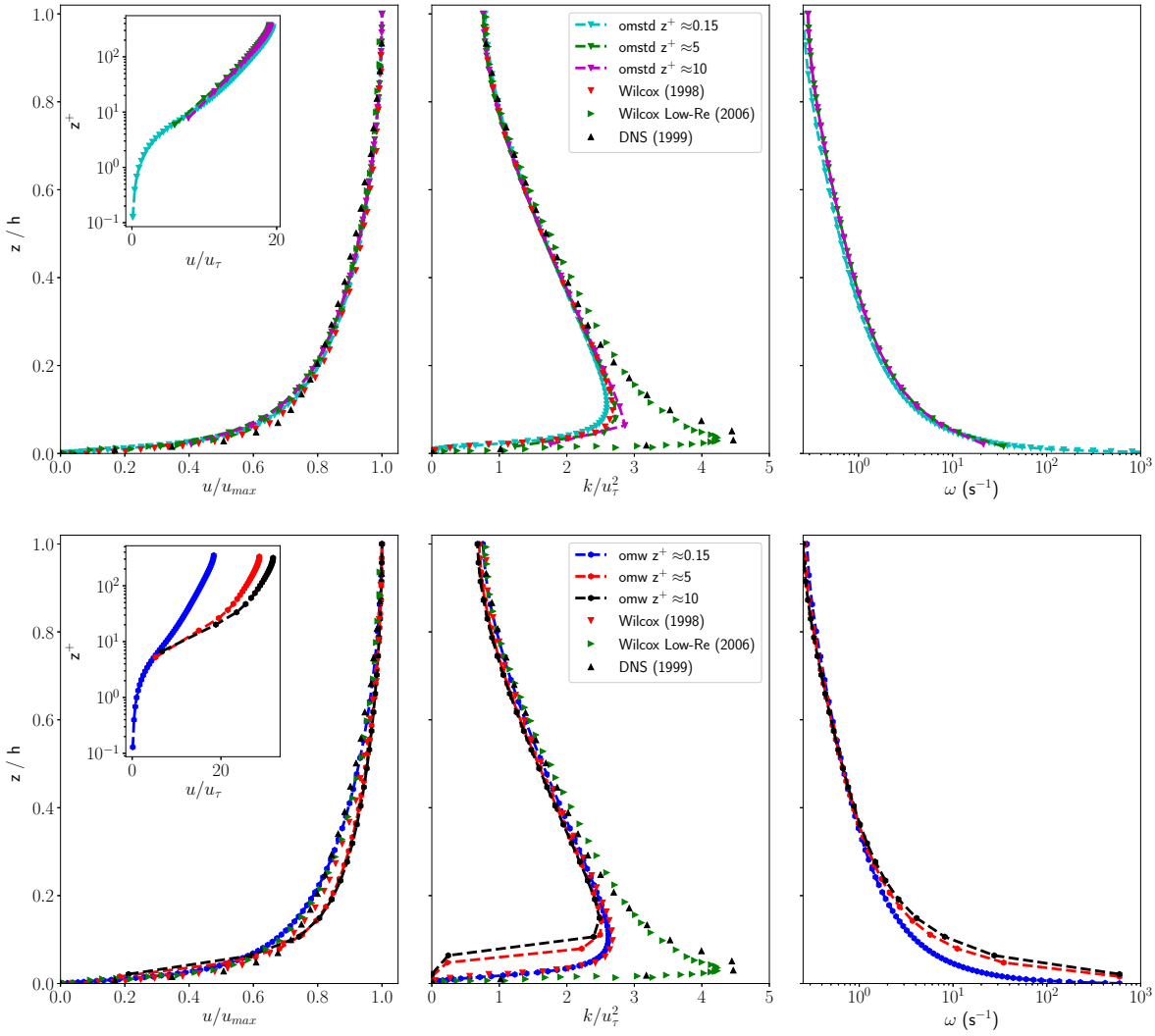

FIGURE 4.5: Comparison between SedFoam and *Moser et al.* (1999); *Wilcox* (1998, 2008) for velocity, TKE and specific dissipation rate profiles using the k-ω2006 turbulence model, different wall functions and different z^+.

The two-phase version of the turbulence models and the different wall functions have been successfully tested on a canonical turbulent boundary layer case. The next step consist in performing similar validation on cases involving sediments.

4.5.2 Unidirectional turbulent Sheet-Flow

The first test case involving sediments corresponds to the unidirectional turbulent sheet flow case from *Revil-Baudard et al.* (2015). A sketch of the 1D vertical computational domain is presented in figure 4.6. Under a pressure gradient, a water column is moving over a sediment layer (grey area). The initial water and sediment heights are h^f=0.149m and h_0^s=0.021m, respectively.

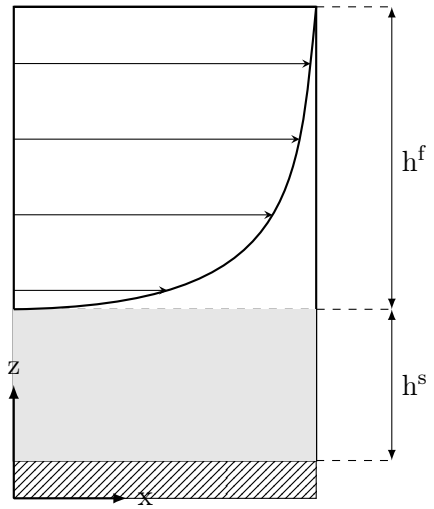

FIGURE 4.6: Sketch of the unidirectional sediment transport configurations.

The sediment is made of non-spherical lightweight PMMA particles with density $\rho^s = 1190$ kg.m^{-3} and mean grain size diameter $d = 3 \pm 0.5$ mm. The fluid is water with density $\rho^f = 1000$ kg.m^{-3} and kinematic viscosity $\nu^f = 10^{-6}$ m^2.s^{-1}. The energy slope is $S_f = 0.19$ % and the mean velocity is $\bar{U} = 0.52$ m.s^{-1}. To obtain this mean velocity, the flow is driven by a pressure gradient f_{px}=18.639 kg.m^{-2}.s^{-2}.
The mesh is composed of 400 cells in the vertical direction with a uniform distribution and the time step is given by the CFL condition that has to be lower than 0.8 for stability reasons. The numerical schemes for temporal and spatial derivatives are listed in table 4.4. Here, to be consistent with *Chauchat et al.* (2017) and *Cheng et al.* (2017) a second order centered scheme with a Sweby limiter (*limitedLinear 1*) is chosen for the divergence operators in the advection terms. However, because the advection is very weak and only present for the vertical components in this case this numerical scheme change has no influence.

Tableau 4.4: Numerical schemes in unidirectional sheet flow test case[a]

Description	keywords	keywordValue	Formulation
time derivative	*ddtSchemes*	*Euler*	$\partial\varphi/\partial t$
spatial gradient operation	*gradSchemes*	*Gauss linear*	$\nabla\varphi$
divergence operators	*divSchemes*	*Gauss limitedLinear 1*	$\nabla \cdot \varphi$
Laplacian operators	*laplacianSchemes*	*Gauss linear corrected*	$\nabla \cdot (\nabla\varphi)$

[a] φ denotes a dummy variable for the illustration purpose.

The lateral boundaries are set to *cyclic* while the front and back boundaries are set to *empty*. At the top boundary, the pressure and the sediment concentration ϕ are fixed with a zero value

Tableau 4.5: Rheological parameters for the numerical simulations of *Revil-Baudard et al.* (2015) unidirectionnal sheet flow experiments.

S_f	h^f	h_0^s	θ	w_{fall0}/u_*	S_c	μ_s	μ_2	I_0	B_ϕ	ϕ_{max}	B
(-)	(m)	(m)	(-)	(-)	(-)	(-)	(-)	(-)	(-)	(-)	(-)
0.0019	0.1489	0.0211	0.44	1.0	0.44	0.52	0.96	0.6	0.66	0.55	0.25-1.25

and a zero gradient (*i.e.* Neumann boundary conditions) is imposed on all the other quantities. At the bottom, the velocity of both phases are set to zero, and Neumann boundary conditions are used for the pressure, the TKE and the TKE dissipation (ε or ω, depending of the turbulence model used). For this test case, the Schmidt number is imposed as a constant with S_c=0.44, as measured in the experiments. All the rheological parameters of the $\mu(I)$ rheology are identical to the ones proposed by *Chauchat* (2018) and are given in table 4.5.

The results are presented in Fig. 4.7 from left to right in terms of averaged mixture velocity profile ($U = u^s \times \phi + u^f \times (1-\phi)$), volume fraction profile (ϕ), sediment flux density profile ($\pi = \phi u^s$), Reynolds shear stress profile (R^f_{xz}, blue lines) and granular stress profile (τ^s_{xz}, red lines). The numerical results are compared with the measurements reported in *Revil-Baudard et al.* (2015) (black dots). Different combinations of granular stress model and turbulence model are presented : in subfigure 4.7.(a) the $\mu(I)$ rheology is used in combination with the Mixing Length (ML), $k-\varepsilon$, $k-\omega$ and $k-\omega$2006 turbulence models while in subfigure 4.7.(b) the Kinetic Theory (KT) model is used with the $k-\varepsilon$, $k-\omega$ and $k-\omega$2006 turbulence models. The ML has not been used with the kinetic theory because equation (3.56) requires an estimation of the TKE that is not straightforward to estimate when using a ML model. Amongst the different configurations, the $\mu(I)$ rheology coupled with the ML model (subfigure 4.7.(a)) corresponds to the model proposed by *Revil-Baudard and Chauchat* (2013) and *Chauchat* (2018), the kinetic theory coupled with the $k-\epsilon$ turbulence model (4.7.(b)) corresponds to the model proposed by *Hsu et al.* (2004) and *Cheng et al.* (2017).

The different parametrization used for the Kinetic Theory closure are summarized in table 4.6. Only these models are used for the KT in all the present work.

Tableau 4.6: Kinetic theory closure models

keywords	keywordValue	Formulation
granularPressureModel	*Lun*	Eqn. (3.47)
radialModel	*CarnahanStarling*	Eqn. (3.48)
viscosityModel	*Syamlal*	Eqn. (3.51)
conductivityModel	*Syamlal*	Eqn. (3.54)
frictionalStressModel	*SrivastavaSundaresan*	Eqn. (3.59)

In sediment transport, the presence of particles can lead to an important turbulence damping in the bed. The turbulence being fully damped in a static bed at maximum particle volume fraction. To reproduce that turbulence damping with the ML model, the von Karman constant has been reduced to $\kappa = 0.225$, according to *Revil-Baudard et al.* (2015). It is well admitted in

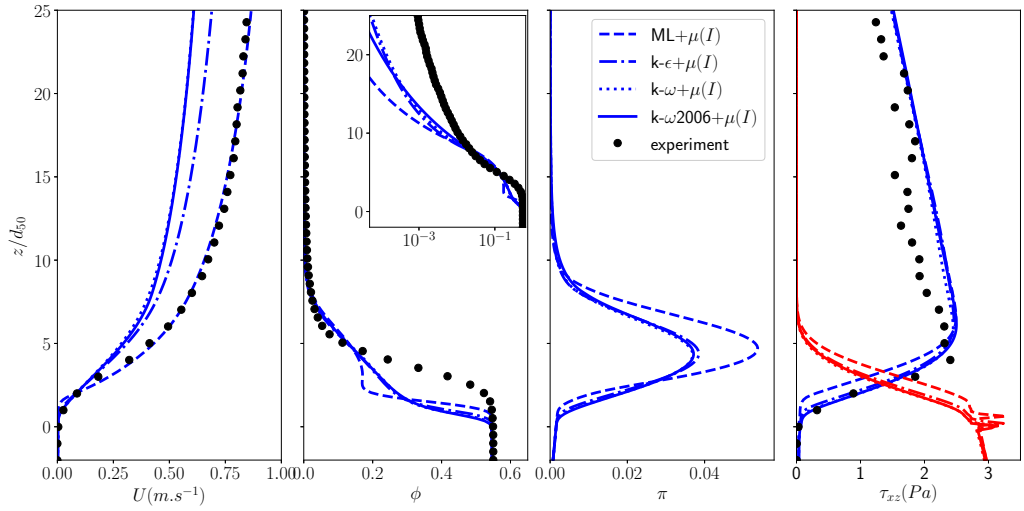

(a)

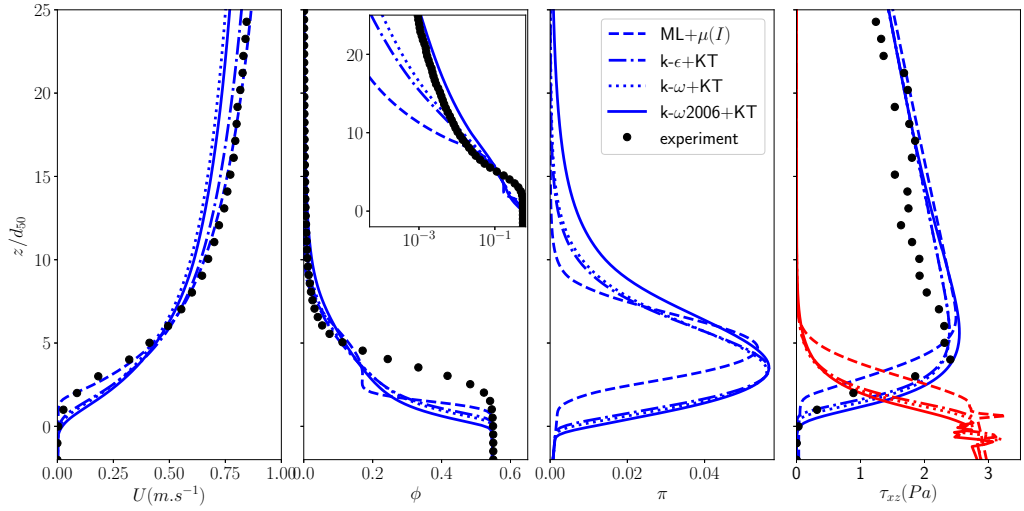

(b)

FIGURE 4.7: Comparison of two-phase numerical results with experiments of *Revil-Baudard et al.* (2015) in terms of velocity profiles, volume fraction, sediment transport flux , Reynolds shear stress (blue lines) and granular stress (red lines) using the dense granular flow rheology ($\mu(I)$) with the four turbulence models (Mixing Length, $k-\varepsilon$, $k-\omega$ and $k-\omega 2006$) in (a) and the Kinetic Theory of granular flows (KT) with the three turbulence models ($k-\varepsilon$, $k-\omega$ and $k-\omega 2006$) in (b).

the literature that the presence of sediment may lead to reduction of the von Karman constant (*Amoudry et al.*, 2008; *Revil-Baudard and Chauchat*, 2013; *Vanoni*, 2006).
In two-equations RANS approaches, the turbulence damping induced by the particles is introduced in the k, ε and ω equations via the drag term (fourth term on RHS of eq. 3.21). As explained in Chapter 3 the turbulent drag damping is related to particle inertia through the term $tmf = e^{-B\ St}$, representing the correlation between particles and fluid fluctuating motions.

The inertia is expressed through the Stokes number. For $tmf = 1$, *i.e* at low Stokes numbers, the particles are completely following the turbulent fluctuations instantaneously. The turbulence damping of the carrier flow fluid is zero. For $tmf = 0$, *i.e* at high Stokes numbers the particles inertia is much higher than the fluid one and generate an important damping of turbulence through drag.
Based on *Cheng et al.* (2018a) LES two-phase flow simulations the parameter B should be taken as 0.25 when using the Kinetic Theory. The same value has been obtained by calibrating this coefficient on *Revil-Baudard et al.* (2015) data using the KT and the k-ε turbulence model (see subfigure 4.7.(b)). For the $k-\omega$ or the $k-\omega 2006$ models, the additional damping terms are similar and the B value has been kept the same as for the $k-\varepsilon$. However, the $C_{3\omega}$ value has been tuned to recover almost the same velocity profile in the dense sheet flow layer as with the k-ε model. The value of $C_{3\omega} = 0.35$, is very close to the value of $C_{3\omega} = 0.4$ reported by *Amoudry* (2014).

As shown in figure 4.7, provided that the turbulence model used is well calibrated, the velocity profiles obtained with both, the $\mu(I)$ rheology and the Kinetic Theory are able to reproduce with a good agreement the experimental data of *Revil-Baudard et al.* (2015). Nevertheless, with the $k-\omega$, the $k-\omega 2006$ or the $k-\varepsilon$ model and the $\mu(I)$ rheology, the velocity profiles are underestimated showing a too strong dissipation in the sheet flow layer where the velocity gradients are too small. As shown in figure 4.8.(a), by calibrating the B coefficient (B=1.25), the velocity profile obtained with the $\mu(I)$ rheology is in much better agreement with the data of *Revil-Baudard et al.* (2015). However this is not the main purpose of the present work and it can be conclude that when looking at the velocity profiles, the numerical solution is not too much depending on the choice of the turbulence model if a $k-\varepsilon$, a $k-\omega$ or a k-ω2006 models are used. This assessment is particularly true for the two versions of the k-ω closure. Looking at the volume fraction profile, it appears that both the Kinetic Theory and the $\mu(I)$ rheology fail to recover accurately the measurements in the denser part of the sheet flow layer. In the water column, the concentration profiles obtained with the KT are in very good agreement with the experimental data of *Revil-Baudard et al.* (2015). This agreement is lower with the $\mu(I)$ rheology as it underpredicts the sediment concentration for $\phi < 0.1$. However, the results do not seem very sensitive to the different turbulence models used.
Because the velocity and the concentration profiles are quite sensitive to the granular stress model chosen, the sediment flux density π predicted using the KT or the $\mu(I)$ rheology are different. Indeed, the transport layer is thicker and deeper when using the KT. However, when using a given granular stress model all the profiles are very close to each other.

It clearly appears that more sediment is transported by suspension into the water column with the KT than with the $\mu(I)$ rheology. This could be explained by the fact that, contrary to the KT, the grains turbulent agitation (responsible for grains momentum mixing) is not originally present in the granular rheology. Figure 4.8.(b) shows the results of the same computation undertaken with $C_t = 1$ in the C_t model. This value of the C_t corresponds to add a Reynolds Stress like contribution to the particle phase momentum balance (see eq. 3.61). This is consistent with the kinetic contribution in the kinetic theory of granular flows (*Gidaspow*, 1994). Including this extra contribution slightly modifies the numerical solution, *i.e* the velocity and the fluid stress profiles are almost not affected whereas the suspended sediment concentration profile, the sediment transport flux and the solid shear stress are slightly increased and are closer to the KT predictions. This contribution seems thus to be needed to better predict the suspended load.
Finally, focusing on the shear stress profiles, it is observed that using the $\mu(I)$ rheology all the

profiles are very close. With the KT, the Reynolds shear stress penetrate deeper into the sheet layer. This is probably due to the presence of the fluid-particle interaction term in the granular temperature equation (eq 3.56).

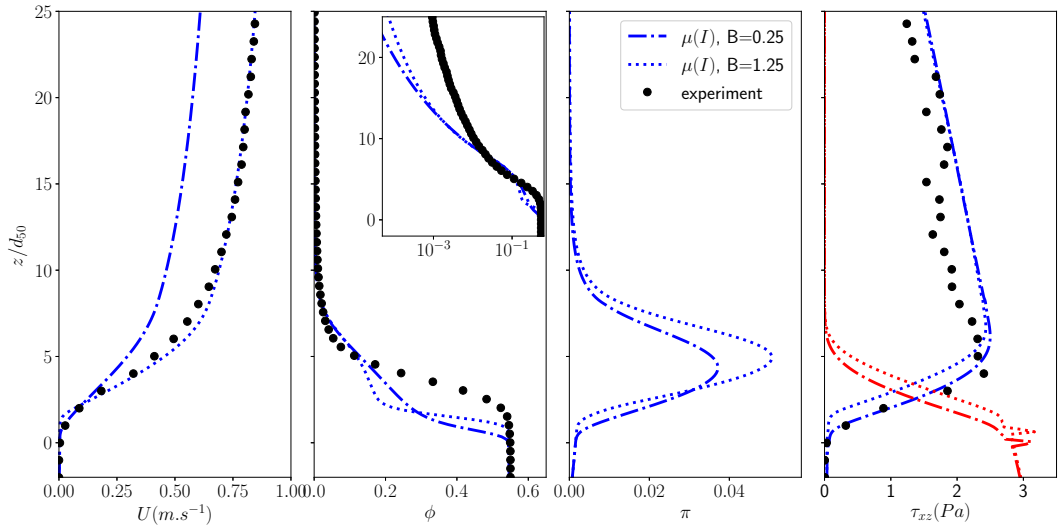

(a)

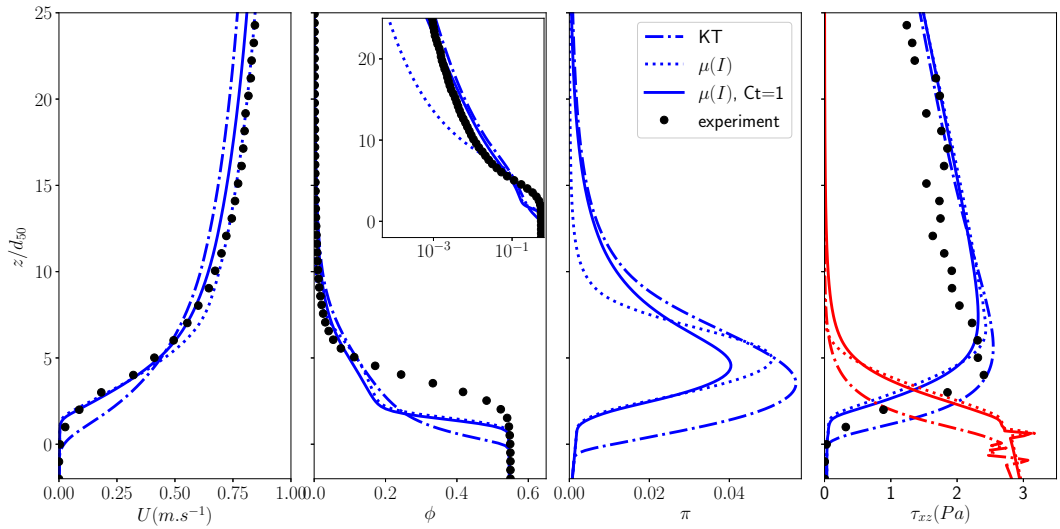

(b)

FIGURE 4.8: Comparison of two-phase numerical results with experiments of *Revil-Baudard et al.* (2015) in terms of velocity profiles, volume fraction, sediment transport flux, Reynolds shear stress (blue lines) and granular stress (red lines) using different B coefficients in (a) and the C_t model in (b). Here, only the k-ω2006 turbulence model is used.

Several of the discrepancies observed on the present case can be explained following different hypotheses. First of all, according to *Maurin et al.* (2016), if the $\mu(I)$ rheology is able to describe accurately the dense granular flow regime in turbulent sheet flows it fails to predict the granular shear stress in the more dilute suspended layer at intermediate concentrations ($\phi \leq 0.3$). As

already explained, the turbulence model is tuned in a way that the turbulent stress is overestimated leading to an underestimation of the streamwise velocity. As shown in figure 4.8.(a), using B=1.25 gives results in better agreement with the data of *Revil-Baudard et al.* (2015). Concerning the KT, it is well known that it only applies for binary particle collisions (*Jenkins*, 2006), that is to say when the concentration is not too high ($\phi \leq 0.3$). For higher concentration, the particle-particle collisions involve more than two particles and the particle-particle contacts become predominent. To this end, *Jenkins* (2006) proposed an extended Kinetic Theory. It has been successfully applied to study turbulent sheet flows by *Berzi* (2011); *Berzi and Fraccarollo* (2013). In the present model, the frictional stress model used with the KT, a Coulomb-type frictional model, is probably too simple and can not reproduce the granular behavior in the denser part of the sheet layer whereas the $\mu(I)$ rheology is better suited.

A first point of conclusion is that the present test case demonstrates the capabilities included in SedFoam to deal with unidirectional sheet flows. In particular, it shows that one of the original contribution of this thesis, the k-ω2006 turbulence model, behaves very similarly to the standard two-phase k-ω model for unidirectional sheet flows.

4.5.3 Unidirectional bedload

The second test case corresponds to a unidirectional bedload sediment transport case. The height of both layers is taken following the Live-Bed (LB) configuration of *Roulund et al.* (2005), where the water column height is h_f=0.2m and the sediment layer height is h_s=0.1m. The profiles obtained here for the different quantities such as velocities, TKE, concentration, will be used as initial and inlet boundary conditions for the 3D Scour around a vertical cylinder presented in Chapter 5.
The sediment is made of medium sand with density $\rho^s = 2650$ kg.m^{-3} and mean grain size diameter d =0.26 mm. The corresponding fall velocity of an individual grain in quiescent water is $w_{fall0} = 3.4$ cm/s. The fluid is water with density $\rho^f = 1000$ kg.m^{-3} and kinematic viscosity $\nu^f = 10^{-6}$ m^2.s^{-1}. The mean fluid flow velocity is $\bar{U} = 0.46$ m.s^{-1}. The initial concentration profile is imposed using a hyperbolic tangent profile. The flow is driven by a pressure gradient computed from the bed friction velocity of $u_* = 2.8$ cm/s estimated from the experiments by (*Roulund et al.*, 2005) :

$$f_{px} = \frac{\rho^f u_*^2}{h^f} \tag{4.20}$$

The Shields parameter at the inlet is the same as is in *Roulund et al.* (2005), θ=0.19. The water column is discretized using 64 vertical levels with a geometric common ratio r$_f$=1.075 (from the interface to the top). In the sediment bed 50 vertical levels with r$_s$ = 1.086 (from the interface to the bottom) are used. Sensitivity tests have shown that further refining the mesh in the sediment layer does not change the results.
The numerical time step is given by the CFL condition. The latter can go up to 0.8. The numerical schemes for temporal and spatial derivatives are the same as the one for the unidirectional sheet flow case and are listed in table 4.4. The boundary conditions are identical as in the sheet-flow case (see section 4.5.2).

Except stated otherwise, the $\mu(I)$ rheology and an effective fluid viscosity model from *Boyer et al.* (2011) are used. The granular rheology parameters are set up as follows, the static friction coefficient is imposed at μ_s=0.63 corresponding to the tangent of the angle of repose for sand in water,

the dynamical friction coefficient is fixed to μ_2 =1.13 and I_0 =0.6. Usually, μ_2 should not exceed the value of 1. It has been checked here that taking μ_2 =1.13 has no significant influence on the results. It allows to preserve the same difference between μ_2 and μ_s as in *Chauchat* (2018). For the shear induced particle pressure, the parameter B_ϕ is equal to 0.66. These parameter values are consistent with the one proposed in *Chauchat et al.* (2017) except for the value of μ_s that was lower.

a) Vertical profiles and sensitivity analysis

Figure 4.9 shows the vertical profiles of volume averaged mixture velocity ($U = u^s\phi + u^f(1-\phi)$), sediment concentration ϕ, sediment flux π and TKE using the k-ε, the k-ω and k-ω 2006 turbulence models. The results are similar for all the turbulence models, especially both version of the k-ω turbulence model. The velocity and the TKE predictions difference between the ε and ω based models are slightly increasing when moving to the outer layer. This is consistent with the free-stream boundary conditions sensitivity of the k-ω model. The differences observed between *Roulund et al.* (2005) experimental velocity profile (dark dots) and the present numerical simulations can be explained by the presence of ripples at the bed interface that are not represented in my unidirectional simulations. Nevertheless, the numerical predictions and the experimental results are in fair good agreement. For all the turbulence models presented here, the depth averaged mixture velocity is similar. No adjustable parameter has been used to fit the different profiles. The empirical coefficient B, usually left as a free parameter to calibrate the velocity profiles is equal to the default value of 0.25 for all the runs. The concentration profile exhibits a very sharp interface that requires a fine resolution to capture the vertical gradients (here $\min(\Delta_z)$=1.5 $\times$ 10^{-4} m).

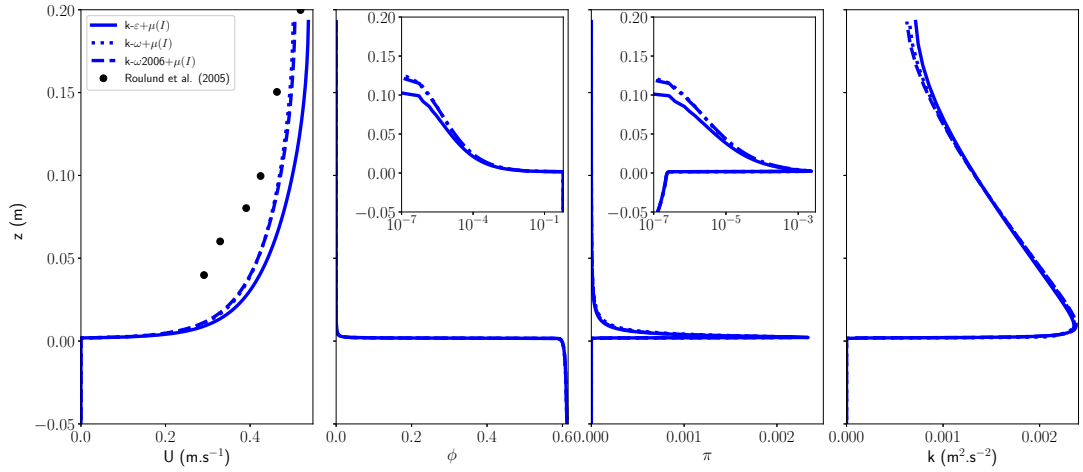

FIGURE 4.9: Velocity, sediment concentration ϕ, sediment flux and TKE profiles using the k-ε, the k-ω and the k-ω 2006 turbulence model for a two-phase flow simulation including sediment. Here, θ=0.19. Experiment (black dots) correspond to the velocity profile measured by *Roulund et al.* (2005).

Figure 4.10 shows the same quantities as figure 4.9 using the k-ω 2006 turbulence model and different models for the Schmidt number and the C_t model. For the parameters considered here, the suspension number value is $w_{fall0}/u_* = 1.33$ and according to *Van Rijn* (1984b) the Schmidt

number value should be around 0.33. In figure 4.10 we compare the results obtained using different Schmidt number definitions (either a constant or a local value as in eq. 3.67). The model results in terms of velocity, concentration and sediment flux density profiles are sensitive to the Schmidt number value, a result in agreement with the work of *Jha and Bombardelli* (2009). For a Schmidt number equal to 1 (dash-dotted line), the velocity is underestimated and there is almost no suspension while the TKE profile is marginally modified. The results obtained from the simulations using a constant Schmidt number of 0.33 (dotted line) and a local Schmidt number are very similar for all the quantities. Under uniform flow conditions, no significant difference is expected using the appropriate constant value or a local definition for the Schmidt number. This result validate the local Schmidt number model implementation.
Using a local definition for the Schmidt number becomes necessary when dealing with complex non-uniform and unsteady flow conditions. Typically, in the scour problem, the local value of the bed friction velocity is changing in space and time with huge consequences on the concentration profile and the sediment transport flux as observed in figure 4.10.

As for the sheet flow case, activating the C_t model (taking C_t=1) does not affect the velocity and the TKE profiles whereas it slightly increases the suspended sediment concentration profile and the sediment transport flux. In *Roulund et al.* (2005) no concentration measurements are provided but, based on comparison with the sheet flow case, the Reynolds Stress like contribution to the particle phase momentum balance contribution seems to be needed to better predict the suspended load.

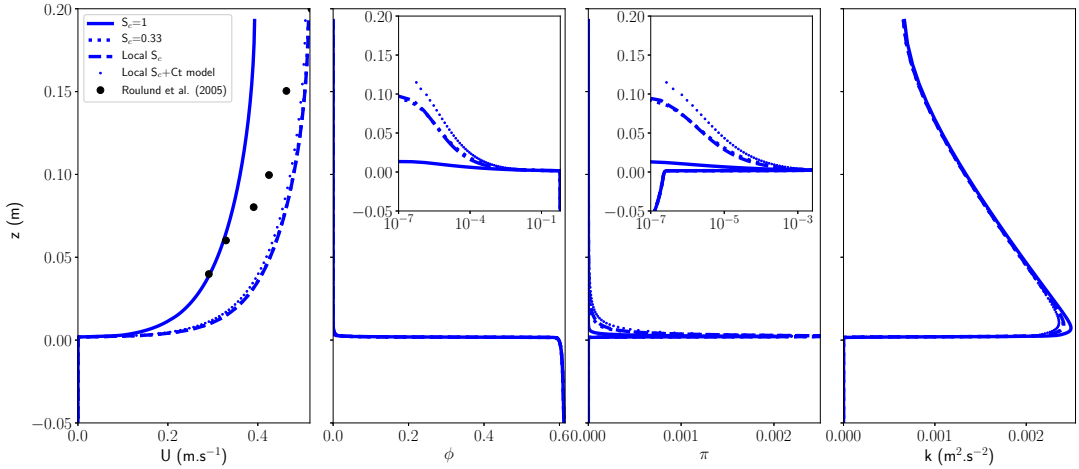

FIGURE 4.10: Velocity, sediment concentration ϕ, sediment flux and TKE profiles using the k-ω 2006 turbulence model for a two-phase flow simulation including sediment. Here, θ=0.19. Experiment (black dots) correspond to the velocity profile measured by *Roulund et al.* (2005).

b) Sediment flux and bedload layer thickness

In order to further validate the model, the dimensionless depth integrated sediment flux is further investigated. It is calculated as the total sediment transport rate including the contribution of

the suspended load :

$$q^* = \frac{\int_{h_b}^{h_t} \pi \, \mathrm{d}z}{\sqrt{(s-1)gd^3}}. \tag{4.21}$$

In particular, the dependency of the sediment flux with respect to the Shields parameter θ is presented in figure 4.11 (left panel) for a Shields parameter ranging from 0.1 to 0.9 and the sensitivity of the predicted sediment flux to the maximum viscosity ν_{Max} of the granular rheology in eq. (3.63) is presented in figure 4.11 (right panel).

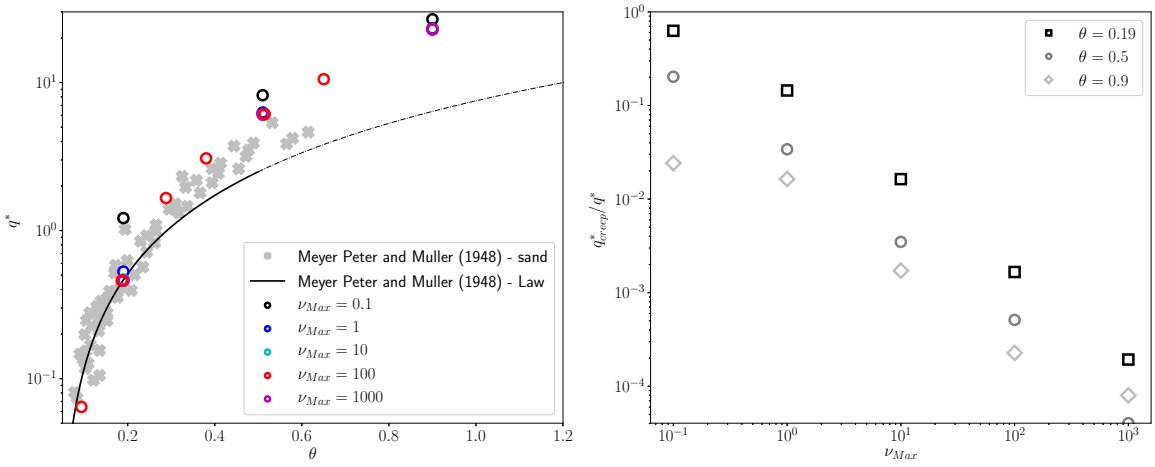

FIGURE 4.11: Left panel : Dimensionless total load plotted as a function of Shields number. Right panel : ratio of the creep flow computed and the total load plotted as a function of the ν_{max} value.

In the left panel, the predicted dimensionless sediment flux is in good agreement with the experimental data of *Meyer-Peter and Müller* (1948) for Shields parameters lower than 0.4. At higher Shields values the sediment flux is slightly overestimated. A sensitivity analysis to the solid phase maximum viscosity (ν_{Max}) has been performed for three Shields numbers $\theta = \{0.19; 0.5; 0.9\}$. Five values of ν_{Max} have been tested : $\{0.1; 1; 10; 100; 1000\}$ $\mathrm{m^2 s^{-1}}$. The model shows a strong sensitivity at low values of ν_{Max} but seems to converge to a constant value when ν_{Max} increases. The error associated with ν_{Max} is called the "creeping flow", if the maximum viscosity is too low a non negligible velocity gradient will be predicted in the static sediment bed that can give rise to a non-negligible sediment transport flux. The visualization of this creeping flow is shown in figure 4.12 where profiles of sediment velocity, sediment concentration and sediment flux are plotted for different values of ν_{Max}. Because part of the shear stress terms are treated explicitly ν_{Max} is used to impose a stability criterion on the diffusion terms. A compromise has to be found between accuracy and numerical stability. In figure 4.11 (right panel), the relative importance of this creeping flux with respect to the total sediment flux is shown as a function of ν_{Max} for the three Shields parameter values mentioned above ($\theta = \{0.19; 0.5; 0.9\}$). The plot is in log-log scale and the creeping flux is arbitrary computed as the integral from the bottom of the computational domain up to the elevation at which the fluid velocity exceeds 1 mm/s. This criteria has been checked to be representative of the creeping flow in the investigated configurations. The relative creeping flux decays exponentially as ν_{Max} increases. It can be observed that for ν_{Max} higher or equal to ten the relative sediment flux error

lower than 1%. In the following a value of $\nu_{Max} = 100$ m^2/s will be used to guarantee a negligible creeping flow.

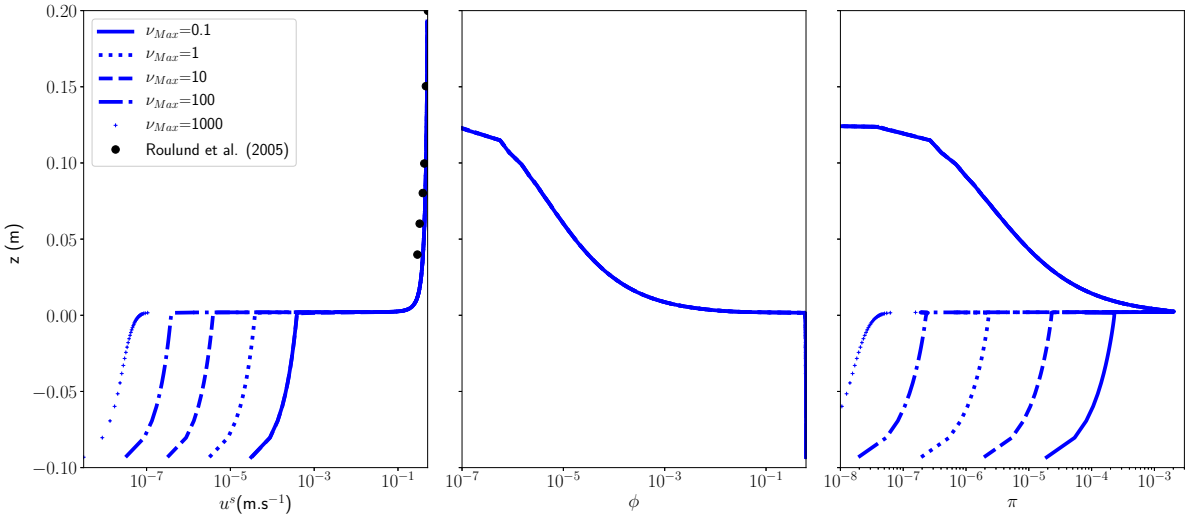

FIGURE 4.12: Velocity, sediment concentration ϕ and sediment flux profiles using the k-ω 2006 turbulence model for a two-phase flow simulation including sediment. Here, θ=0.19 and ν_{Max} is changed from 0.1 to 1000. Experiment (black dots) correspond to the velocity profile measured by *Roulund et al.* (2005).

The previous observations are completed over a larger range of Shields number ($0.1 < \theta < 2.5$) in figure 4.13. In addition to *Roulund et al.* (2005) unidirectional bedload case, the dimensionless sediment transport rate q^* and the dimensionless sheet layer thickness $\delta^* = \delta/d$ are computed based on *Revil-Baudard et al.* (2015) and *Sumer et al.* (1996) unidirectional sheet flow configuration. The bedload transport layer thickness is defined as the vertical distance between the iso-surfaces of sediment concentration $\phi = 0.57$ (the immobile bed) and $\phi = 0.08$ (distinction between bedload and suspended load) according to *Bagnold* (1954); *Dohmen-Janssen et al.* (2001). The results are plotted as a function of the Shields number in figure 4.13 for q^* (left panel) and δ^* (right panel).

The three configurations chosen provide a large range of particle density and diameter. As previously detailed, the particles in *Revil-Baudard et al.* (2015) are made of PMMA, with a mean diameter of 3mm and a density ratio s=1.19. In the case of *Roulund et al.* (2005), particparticleules are made of medium sand of 0.26mm mean diameter and s=2.65. Finally, in the case of *Sumer et al.* (1996) (described in *Chauchat et al.* (2017)), the particles are made of acrylic, with d=2.6mm and s=1.14.

The present model predictions for both quantities are compared with experimental data from the literature (*Meyer-Peter and Müller* (1948), *Wilson* (1966) for q^* and *Sumer et al.* (1996) for δ^*) and other model prediction (*Wilson* (1987) for both quantities). Concerning the dimensionless sediment transport rate (left panel of figure 4.13), all the three configurations presented are in the scatter of the literature experimental data, namely *Meyer-Peter and Müller* (1948) for $\theta \leq 0.5$ and *Wilson* (1966) for $\theta \geq 0.5$.

The definition of the bed shear stress involved in the Shields number calculation has also been investigated. In figure 4.13, the Shields number for the sand particles is obtained from

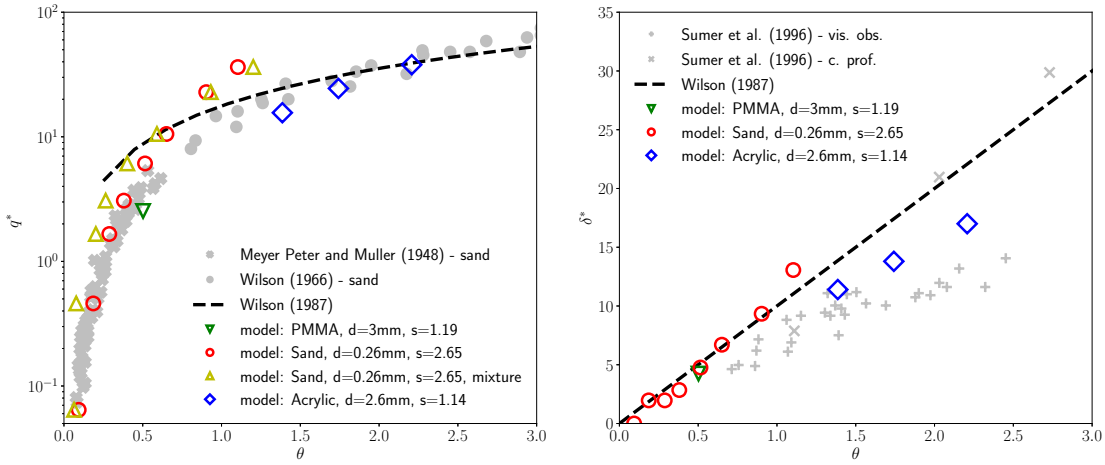

FIGURE 4.13: Dimensionless sediment transport rate q^* (left) and dimensionless sheet layer thickness $\delta^* = \delta/d$ (right) versus the Shields number predicted by SedFoam : red and yellow circles correspond to *Roulund et al.* (2005) unidirectional bedload configuration, green triangle and blue diamonds correspond to *Sumer et al.* (1996) and *Revil-Baudard et al.* (2015) unidirectional sheet flow configuration, respectively.

two different shear stress definitions. The first definition used here follows the proposition of *Chauchat* (2018), where the bed shear stress is calculated as the maximum of the Reynolds shear stress :

$$\tau = max(R^f_{xz}) \tag{4.22}$$

This definition corresponds to the red empty circles plotted in left panel of figure 4.13, using the local Schmidt number, $C_t = 1$ and $\nu_{max} = 100$ m^2.s^{-1}. In a unidirectional case, computing the bed shear stress as the maximum of the fluid shear stress results in very good agreement with the literature data (see *Chauchat* (2018), figure A4 or the present results). However, when dealing with complex 3D flow configurations this definition may lead to an error as the fluid shear stress profile does not present a constant slope anymore. An alternative is to compute the bed shear stress as the mixture shear stress at a given concentration level ϕ :

$$\tau = \tau^f_{xz}(\phi) + \tau^s_{xz}(\phi) \tag{4.23}$$

Several concentration values have been tested for the unidirectional configuration. For clarity, only the results obtained using $\phi = 0.45$ are plotted with the green empty circles in left panel of figure 4.13. This second method for computing the shear stress results in a slightly different relationship between q^* and θ (see figure 4.13).

The relationship between the dimensionless sediment transport rate q^* and the Shields parameter over a range from 0.1 to 1.5, in the case of sand particles can be fitted using a power law of the excess Shields number :

$$q^* = a(\theta - \theta_c)^b, \tag{4.24}$$

where θ_c=0.047 is the critical Shields number. The a and b coefficients obtained from a best fit of the results presented in the left panel of figure 4.13 are summarized in table 4.7. First of all, the values obtained are coherent between the different estimations of the bed shear stress

presented here, a is varying approximatively between 25 and 32 whereas b is varying approximatively between 1.5 and 2.2. It is hard to affirm which estimation has the best agreement with *Meyer-Peter and Müller* (1948) or *Wong and Parker* (2006) empirical formulae, since the value are quite different for the prefactor a. Nevertheless, the model is able to recover a power law, with an accurate estimation of the b exponent. The exponent 2 was already observed in former studies using two-phase flow models applied to sheet-flows (*Chauchat*, 2018; *Hsu et al.*, 2004; *Revil-Baudard and Chauchat*, 2013). It is very interesting to observe that estimating the bed shear stress with the mixture approach at higher sediment concentration reduces the b exponent to the value of 1.5 given by *Meyer-Peter and Müller* (1948) or *Wong and Parker* (2006).

Tableau 4.7: Estimated value of the power law coefficients of the excess Shields parameter.

Way of computing the bed shear stress	Concentration (ϕ)	a	b
Meyer-Peter and Müller (1948)	-	8.0	1.50
Wong and Parker (2006)	-	3.97	1.50
eq. 4.22	-	32.13	2.18
eq. 4.23	0.45	31.06	1.57
eq. 4.23	0.3	28.56	1.59
eq. 4.23	0.08	26.14	2.09

The right panel of figure 4.13 shows the dependency of the dimensionless sediment transport layer thickness upon the Shields number. For *Revil-Baudard et al.* (2015) and *Roulund et al.* (2005) configurations the results exactly follow *Wilson* (1987) prediction ($\delta^* = 10\theta$). The dimensionless sediment transport layer thickness for *Sumer et al.* (1996) does not exactly follow that law but the tendency is similar and results are in the scatter of *Sumer et al.* (1996) results.

One point of particular importance is that the present results are in very good agreement with state of the art laws for sand particles at low Shields numbers ($\theta \leq 0.3$). Indeed, in the literature, the majority of the two-phase flow configurations for unidirectional flows are restricted to sheet-flow (*Chauchat*, 2018; *Hsu et al.*, 2004; *Lee et al.*, 2016; *Revil-Baudard and Chauchat*, 2013) involving plastic or acrylic particles. The good agreement between the two-phase flow model prediction and the literature data even at low Shields configurations (θ down to 0.1), shows the robustness of the two-phase flow approach. Following *Wilson* (1987) formula, when decreasing the Shields number the thickness of the transport layer is also decreasing. At $\theta = 0.1$, $\delta^* \approx 1$ the thickness of the transport layer is approximatively corresponding to one particle diameter. For such case, the continuous hypothesis used to define the two-phase flow equations (eps 3.3 and 3.4) reaches its limit. The present results are particularly interesting, they show that the sediment flux is still in good agreement with the literature results even when approaching the limit of validity of the continuous approach. A result that has already been found for laminar flows configurations by *Aussillous et al.* (2013).

These results further demonstrate the capabilities of SedFoam and here particularly of the k-ω2006 turbulence model and the $\mu(I)$ rheology to deal with unidirectional flows from bedload to sheet flow over a wide range of Shields number and particle type and diameter. Furthermore, in addition to accurate vertical profiles of different quantities, state of the art laws describing two fundamental parameters of the sediment transports (the dimensionless sediment transport rate

q^* and the dimensionless sheet layer thickness δ^*) are accurately recovered.

4.6 Two-dimensional case : Scour downstream of an apron

SedFoam has been validated on several one-dimensional cases in the previous section. In order to demonstrate the multi-dimensional capability of the code, another test case corresponding to the development of the scour downstream an apron is presented, following the numerical study of *Amoudry and Liu* (2009) and *Cheng et al.* (2017). A sketch of the configuration is shown in figure 4.14.

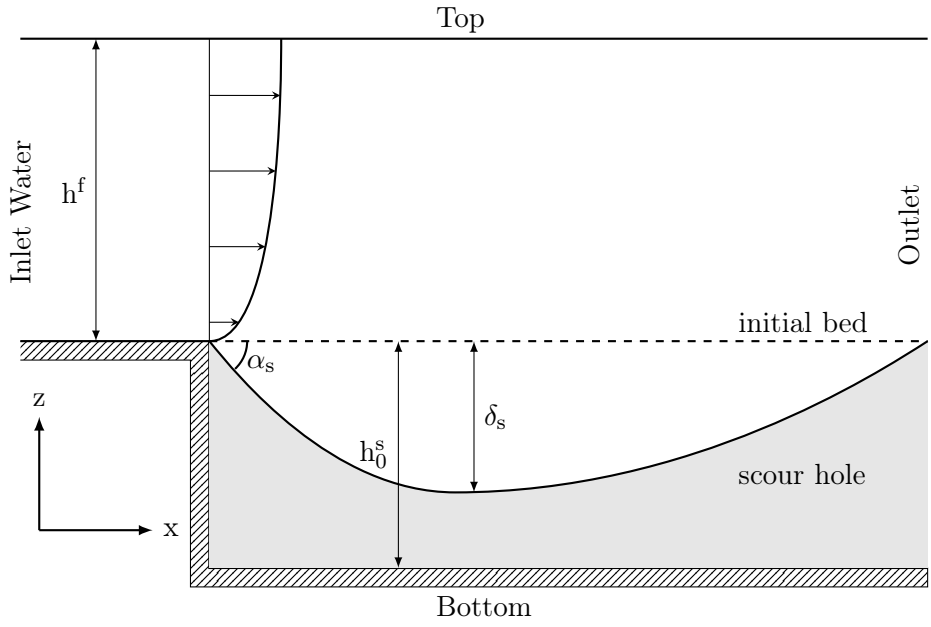

FIGURE 4.14: Sketch of the scour downstream an apron (adapted from *Cheng et al.* (2017).)

The sediment particles are made of medium sand, density $\rho^s = 2650$ kg.m^{-3} and diameter d= 0.25 10^{-3}m. The fluid is water with density ρ^b= 1000 kg.m^{-3} and kinematic viscosity $\nu^b = 10^{-6}$ m^2.s^{-1}. The flow depth is fixed to $h^f = 0.15$m, and the initial bed thickness is $h^s = 0.05$m. The length of the domain downstream the apron is $L_x = 1$m.
A uniform grid is used in the streamwise direction ($\Delta x = 10^{-3}$ m) while the mesh is refined vertically at the bed interface : $\Delta z \in [1.15 \times 10^{-4}\ m\ -1.15 \times 10^{-2}\ m]$ in the water column and $\Delta z \in [1.15 \times 10^{-4}\ m\ -4.66 \times 10^{-4}\ m]$ in the sediment bed.

Front and back boundaries are set to *empty* (no y-dependence). The bottom boundary, the lower part of the inlet (forming the step) are set as wall boundaries. The upper part of the inlet is an inlet boundary where the velocity profile is imposed according to the rough wall log law (eq. 4.25) and turbulent quantities are imposed following recommendation from the ESI group [1]. At the outlet, Neumann boundary conditions are specified for all quantities, except for the pressure for which a homogeneous Dirichlet boundary condition is imposed for the reduced pressure p^*.

1. https ://myesi.esi-group.com/tipstricks/guidelines-specification-turbulence-inflow-boundaries, requires a login.

For the velocities, a homogeneous Neumann boundary condition is used when the velocity vector points outside of the domain at the outlet, and a homogeneous Dirichlet boundary condition is used otherwise (*inletOutlet* condition). The top boundary is a plane of symmetry (*symmetryPlane*) for all quantities. Such boundary acts as a Neumann boundary for scalar. For a vector, all components parallel to the boundary are mirrored whereas the normal components are set to zero. The numerical schemes are the ones described in table 4.4. As initial condition, the velocity of both phases, the sediment concentration, the TKE and the TKE dissipation are set based on one-dimensional simulation results using the *funkySetFields* tool and routines from the $fluidfoam$ python package. The details of the boundary conditions are summarized in table 4.8. The rough wall log-law is written as follows :

$$\frac{u^f}{u_*} = \frac{1}{\kappa} ln\left(\frac{30z}{k_s}\right), \tag{4.25}$$

where $u_* = 3.69$ cm.s^{-1} is the bed friction velocity, κ=0.41 is the von Karman constant, and k_s=2.5d is the Nikuradse roughness length.

Tableau 4.8: Summary of the boundary conditions implemented in the 2D scour downstream of an apron configuration : sP = *symmetryPlane*, zG = *zeroGradient*, iO = *inletOutlet*, fV = *fixedValue*, i0 = *inletOutlet*, fFP = *fixedFluxPressure*, *1Dp*= 1D profile and *hp*=hydrostatic pressure.

Boundary	type	ϕ	k	ε or ω	u^s	u^f	p	Θ (for KT)
top	sP	sP	sP	sP	sP	sP	sP	sP
bottom	wall	zG	zG	zG	fV, u^s=0	fV, u^f=0	fFP	zG
inlet (flow)	patch	1Dp	fV, $k = 1.10^{-4}$	zG	1Dp	1Dp	zG	fV, $k = 1.10^{-6}$
inlet (sed)	wall	zG	fV, $k = 1.10^{-12}$	zG	fV, u^s=0	fV, u^f=0	zG	zG
outlet	patch	zG	zG	zG	iO	iO	hp	zG

Six combinations of fluid turbulence models (namely k-ε, k-ω and k-ω2006) and granular stress models (KT and $\mu(I)$) have been tested for this configuration. A summary is proposed in table 4.9.
The figure 4.15 shows three snapshots of sediment concentration contour at different times during the scour process (10s, 30s and 60s), using $k-\varepsilon$ and kinetic theory (left pannels) and $k-\omega$2006 and $\mu(I)$ granular rheology (right pannels). At t = 10 s, the development of a scour hole near the inlet can be identified (see Fig. 4.15, top panels). With time, the maximum scour depth is increasing and the scour perturbation is propagating downstream. In the case of the $k-\varepsilon$ coupled with the Kinetic Theory, ripples generated downstream of the apron are propagating. This is particularly clear at t=30s where a bed shape similar to a dune or a ripple can be observed between 0.3m and 0.4m. At the same time, the bed remains almost flat between 0.3m and 0.4m using $k-\omega$2006 and $\mu(I)$ (figure 4.15, right pannel). However, the snapshots presented in Fig. 4.15 show that in terms of scour erosion just downstream the apron (between 0m and 0.3m) the results are very similar using the different closures.

According to the experimental studies from *Breusers* (1967) or *Breusers and Raudkivi* (1991), the development of the scour hole is rapid at the initial stage, and may reach an equilibrium state. *Breusers* (1967) has suggested an empirical law to describe the rapid initial development

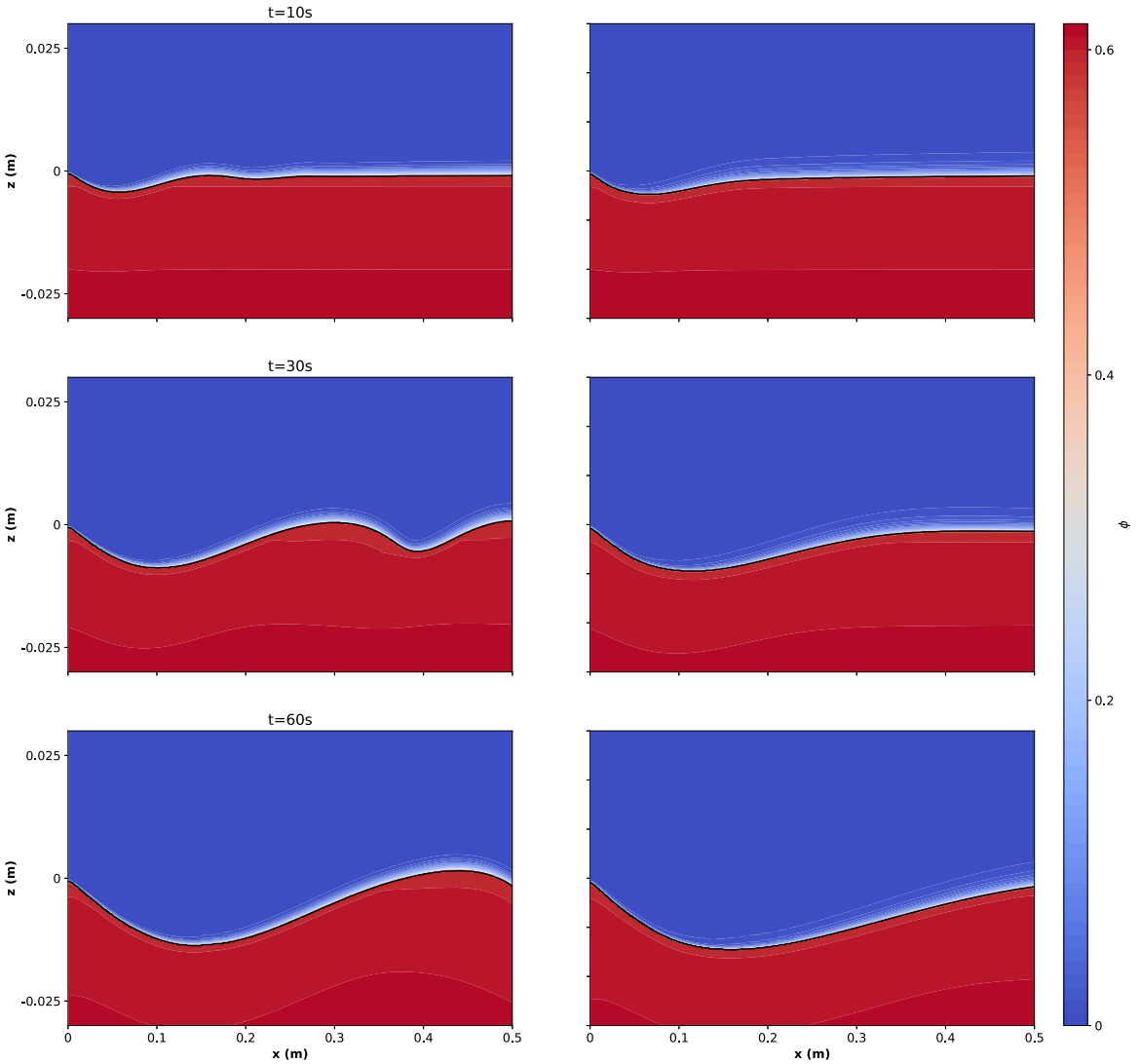

FIGURE 4.15: Sediment concentration contour at different time during the scour process using k-ε and kinetic theory (left pannels) and k-ω2006 and $\mu(I)$ granular rheology.

of the scour hole :

$$\frac{\delta_s}{{h_0}^s} = \left(\frac{t}{T_s}\right)^{n_s} \tag{4.26}$$

where T_s is a characteristic timescale, and the exponent n_s characterizes the speed of the scour development. T_s has no real physical meaning and n_s is the main parameter to recover. Equation (4.26) can only describes the initial development of the scour depth, and the equilibrium scour depth can not be determined from this empirical formula. As the scour depth increases, the flow velocity decreases near the sediment bed, when the flow becomes too weak to transport sediment, *i.e* below the critical Shields number, and an equilibrium scour depth can be obtained.

The equilibrium scour shape is generally independent of the flow velocity and grain size if the Shields parameter is sufficiently large compared with the critical Shields parameter (*Chane et al.*, 1984; *Laursen*, 1952). The development of the upstream bed angle α_s can reach an equilibrium more rapidly. *Breusers* (1967) proposed the following empirical formula :

$$\frac{\alpha_s}{\alpha_s^\infty} = \left(1 - e^{-t/T_{\alpha_s}}\right), \tag{4.27}$$

where T_{α_s} is the equilibrium timescale for upstream bed angle and α_s^∞ is the upstream bed angle at equilibrium.

Tableau 4.9: Summary of the numerical results obtained for the scour at an apron using the different combinations of turbulence and granular stress models and comparison with existing two-phase numerical results on this configuration.

Case	δ_s^{max}/h_0^s	n_s	T_s (s)	α_s^∞ (degrees)	T_{α_s} (s)
Amoudry and Liu (2009)	0.2	0.56	600	-11.4	4
Cheng et al. (2017)	0.16	0.54	1100	-14.55	15.2
k-ϵ + KT	0.092	0.64	2491	-9.85	3.07
k-ϵ + $\mu(I)$	0.076	0.69	2377	-3.98	0.97
k-ω + KT	0.096	0.53	4918	-9.06	1.50
k-ω + $\mu(I)$	0.103	0.55	3677	-8.59	3.33
k-ω2006 + KT	0.101	0.61	2612	-9.41	2.21
k-ω2006 + $\mu(I)$	0.098	0.62	2585	-8.72	4.71

In figure 4.16, the numerical results for the six simulations presented above are shown in terms of these two quantities together with a best fit of the two empirical formula Eqs (4.26) and (4.27). A summary of the fitted parameters is given in table 4.9. First of all, the model is able to reproduce the power law for the initial development of the scour depth with values of n_s in the range reported by other studies. T_s values are higher with the present simulations but this parameter has no physical meaning and only the n_s exponent matters to accurately recover the power law. The fitted values for the upstream bed angle are slightly different from previous studies. One simulation can be distinguished from the other : the combination of $k-\varepsilon$ and $\mu(I)$ where the upstream bed angle is highly underestimated. This can be due to the generation of the bedforms which may affects the scour dynamics.
Finally all the combinations of models predicts a final erosion in the scour hole that is twice lower than what is reported in *Amoudry and Liu* (2009). As described in *Lee et al.* (2016), the results are more sensitive to the turbulence model than to the granular stress parameters. Improving the present results in term of erosion depth may be possible by changing the calibration of some turbulence parameters but this is not the objective here, especially as their is no experimental data to compare with.

The eventual presence of particular bedforms for given combination of closure models is done by looking at the bed interface at t=60s. In a two-phase flow model the position of the bed is not defined like in classical sediment transport models. The vertical elevation of the isosurface of sediment concentration $\phi = 0.57$ is used as a proxy for the static bed elevation. In a 2D configuration, the maximum sediment concentration is $\phi_{\max}$=0.625. The results for all combinations are shown in figure 4.17. It clearly appears that for some combinations of turbulence and granular stress models ($k-\varepsilon$+KT, $k-\varepsilon$+$\mu(I)$, $k-\omega$+KT) bedforms are predicted and

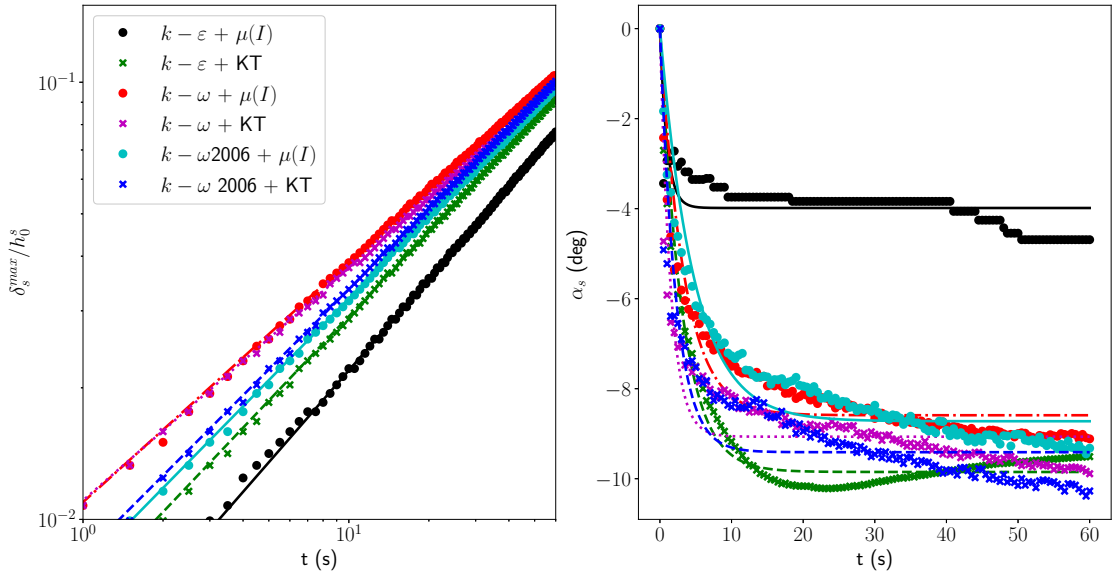

FIGURE 4.16: Numerical results for time evolution of the normalized maximum scour depth and upstream bed angle. Best fit using Eqs (4.26) and (4.27) are shown and the fit parameters are given in table 4.9.

propagate downstream of the scour hole. For the other combinations the interface downstream of the scour hole remains approximatively flat as reported in *Amoudry and Liu* (2009).
For the $k-\varepsilon$+KT and $k-\omega$+KT combinations, the bedforms height decreases too rapidly to correctly estimate their height (Δ) and wavelength (λ) . This is not the case for the $k-\varepsilon+\mu(I)$ results, where the average wavelength and height of the bedforms are about λ =0.1m and Δ=0.005m, respectively. According to *Garcia* (2008), most studies indicates that the ripples dimensions are controlled by the sediment size and are independent of the flow depth. The range of values found for ripple wavelength and steepness (Δ/λ) with SedFoam for the $k-\varepsilon+\mu(I)$ and the $k-\varepsilon$+KT combinations are in good agreement with the empirical formula proposed by *Raudkivi* (1997) (eqs. 4.28 and 4.29, respectively) :

$$\lambda = 245 d^{0.35} \tag{4.28}$$

$$\Delta/\lambda = 0.074 d^{-0.253}, \tag{4.29}$$

where d is given in mm.

This result suggests that the two-phase flow model is able to predict the formation of ripples. This subject is still a matter of debate in the scientific community and two-phase flow simulations could be an ideal framework to study the formation of bedforms and their equilibrium characteristics.

4.7 Conclusions

In this chapter the capability of the eulerian-eulerian two-phase flow model SedFoam have been tested on several one and two-dimensional test cases. First, the model has been applied to a

Tableau 4.10: Dimensions of the bedform observed in the scour downstream of an apron test case. The grain size diameter is given in millimeter.

Dimensions	Ripple wavelength (mm)	Ripple steepness
Raudkivi (1997) formula	150	0.10
$k-\varepsilon+\mu(I)$	[90-170]	[0.03-0.04]
$k-\varepsilon+KT$	[160-200]	[0.02-0.04]

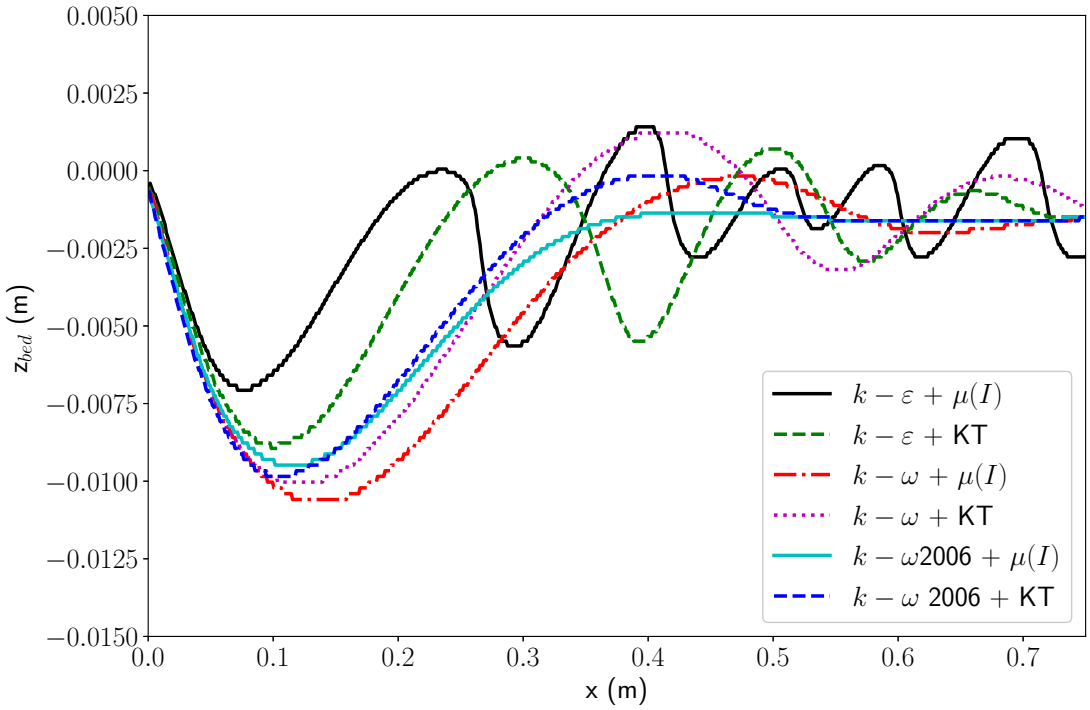

FIGURE 4.17: Bed interface at t=60s using the different combinations of turbulence and granular stress closure summarized in table 4.9.

turbulent boundary layer without sediment. This configuration allows to validate the turbulent model and the wall-functions implemented in SedFoam. Then computations on a sheet-flow case are presented to discuss the sensitivity of the model results to different combinations of inter-granular stress and turbulence models. The set of tuning coefficients validated on this first case are then used on a bedload case. This test further demonstrates the capabilities of SedFoam and here particularly of the k-ω2006 turbulence model and the $\mu(I)$ rheology to deal with unidirectional flows. In the 1D test cases, for sheet-flow and bedload, the vertical profiles of velocity, concentration, fluid and solid shear stress or TKE are in good agreement compared with the literature results. More importantly, state of the art laws describing the dimensionless transport rate and the dimensionless bedload layer thickness as a function of the Shields number are also

accurately recovered with SedFoam. A careful attention has been on low Shields number configurations, showing that the transport rate is still in good agreement with the literature results even when approaching the limit of validity of the continuous approach.
The last application on scour downstream of an apron illustrates the multi-dimensional capabilities of the solver. The scaling laws proposed by earlier works are recovered by the model even if the results are sensitive to the choice of the inter-granular and turbulence models. Further work is needed to improve the model validation on this test case as well as the model sensitivity to flow turbulence and rheological parameters but this requires more detailed experimental data.

Chapitre 5

Two-phase flow simulations of scour around a vertical cylinder

5.1 Résumé

Ce chapitre présente les résultats obtenus pour la modélisation du phénomène d'affouillement 3D autour d'une pile verticale dans un écoulement constant. Les configurations étudiées sont issues des travaux expérimentaux et numériques de *Roulund et al.* (2005), références pour ce problème.
Je me suis intéressé à deux configurations, la première considère un fond rigide, sans sédiments et permet de vérifier que SedFoam est à même de prédire correctement les principales caractéristiques hydrodynamiques de l'écoulement autour du cylindre. Je m'intéresse tout particulièrement aux champs de vitesses, aux structures turbulentes comme le tourbillon en fer à cheval (HSV) et le lâché tourbillonnaire en aval du cylindre. Un intérêt particulier est également porté aux contraintes sur le fond, cruciales pour le mise en mouvement des sédiments. L'ensemble des résultats obtenus pour ces quantités est en très bon accord avec ce qui a été obtenu par *Roulund et al.* (2005) ou dans des travaux plus récents comme ceux de *Baykal et al.* (2015).

Une fois la validation hydrodynamique effectuée, je me suis intéressé à la configuration d'affouillement de type lit-mobile ou Live-Bed en anglais, présentée dans *Roulund et al.* (2005). Les premières comparaisons montrent que l'approche diphasique permet de capturer de façon correcte l'érosion liée au HSV. En raison des temps de calcul très coûteux, les simulations ont porté sur les dix premières minutes du phénomène d'affouillement (soit 60% de la profondeur d'affouillement observée à l'équilibre) et ces résultats apportent la preuve de concept que l'approche diphasique est à même de traiter des configurations où les interactions entre les deux phases et la structures sont tridimensionnelles et complexes.

5.2 Chapter Introduction

In this chapter, three-dimensional two-phase flow simulations of scour around a vertical cylindrical pile are presented. The results are analyzed and compared with the experimental and numerical work (using a classical approach) of *Roulund et al.* (2005).
The configuration of *Roulund et al.* (2005) has been chosen for three main reasons. The first one

is that this work has become widely used as a reference in recent studies (*Baykal et al.*, 2015; *Stahlmann et al.*, 2013). Secondly, the work of *Roulund et al.* (2005) not only provides scour results but also results without sediments, very useful for hydrodynamics validation purpose. Finally, the scour case presented in *Roulund et al.* (2005) is in the live-bed regime, where the equilibrium is reached more rapidly compared with clear-water cases. As the two-phase flow simulations are time consuming, working on a live-bed case was necessary.

The chapter is organized as follows, first the hydrodynamic validation of the flow around a vertical cylindrical pile mounted on a flat bed is presented (section 5.3.1). In a second part, the description of the Live-Bed (LB) configuration for scour and the associated results (section 5.4) are presented. Finally, a discussion on the new insight provided by the two-phase flow approach for scour process understanding is presented.

5.3 Hydrodynamic of rigid bed flow

5.3.1 Hydrodynamic setup, computational mesh, boundary conditions

The numerical domain is a three-dimensional box with a stream-wise length Lx=12D, a span-wise length Ly=8D and a height H=D where D=53.6cm is the pile diameter (see fig. 5.1). This is the exact configuration of the Rigid-Bed (RB) case presented in *Roulund et al.* (2005) work. As no sediments are involved, the sediments concentration is set to zero. The Reynolds number based on the pile diameter is $Re_D = \overline{U}D/\nu^f$=1.7 $\times$ 10^5 where the mean flow velocity is $\overline{U}$=0.326 m.s^{-1}.

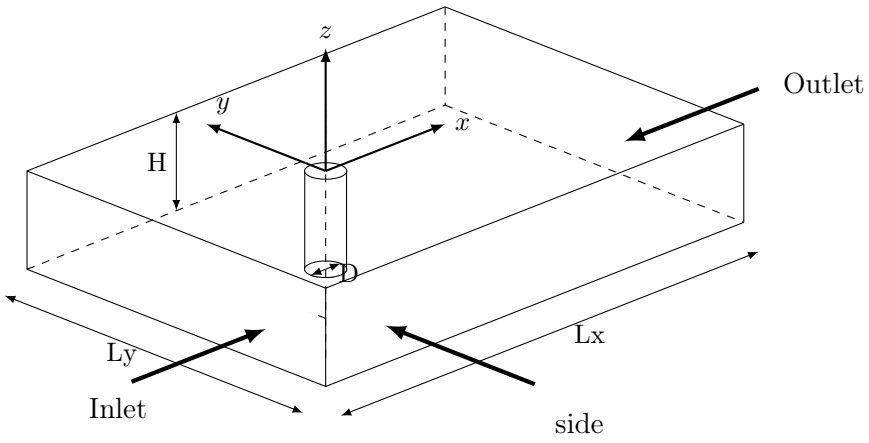

FIGURE 5.1: Sketch of the geometry used for the computational domain in the Rigid-Bed case.

a) Computational mesh

The computational domain is discretized using a unstructured mesh. Two different grids are used and their characteristics are summarized in table 5.1. Both meshes are refined around the cylinder and at the bottom boundary in order to obtain a boundary layer mesh type. The mesh refinement area around the cylinder is axisymmetric. The two meshes differ by their horizontal resolution around the cylinder, MeshII has a double horizontal resolution (four times more points)

Tableau 5.1: Summary of the two meshes used for the Rigid-Bed configuration

Characteristics	MeshI	MeshII
Turbulence model	k-ω SST, k-ω2006	k-ω2006
Total number of cells	1 761 280	2 451 264
Number of cells around the cylinder perimeter	256	512
Horizontal resolution around the cylinder perimeter (m)	6.5×10^{-3}	3.25×10^{-3}
Number of cells across the water depth	64	32
Vertical cell aspect ratio	1.076	1.196
Bottom cell height (m)	4.15×10^{-4}	4.15×10^{-4}

as compared with MeshI. The vertical grid refinement is different in both meshes but the first grid cell is at the same z^+ value. Following *Baykal et al.* (2015), having 32 cells in the vertical direction and a fine resolution close to the bottom is enough to accurately capture the hydrodynamics. A snapshot of the mesh is proposed in the figure 5.2.

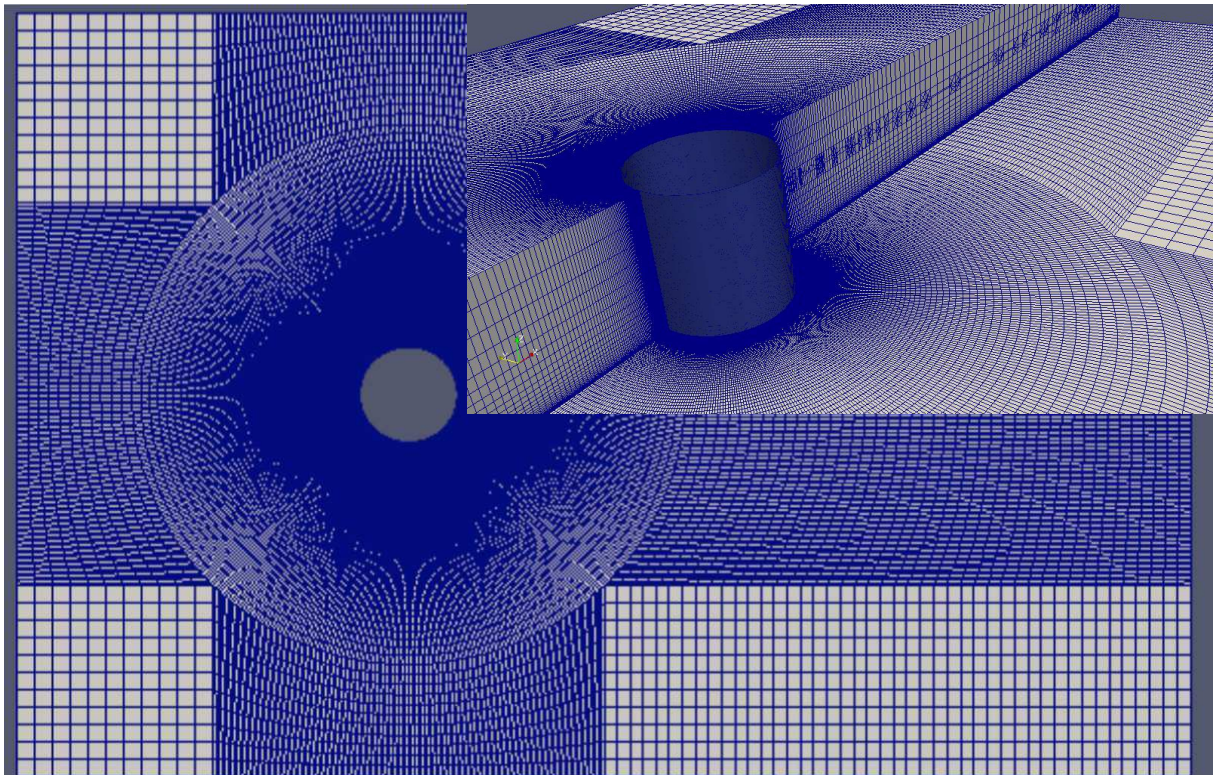

FIGURE 5.2: Bird and lateral views of MeshII.

b) Boundary conditions

The boundary conditions are identical to the ones used by *Roulund et al.* (2005) :
(i) At the inlet, profiles obtained from a 1D vertical simulation driven by a pressure gradient are

imposed for u^k, w^k, k and ω, whereas zero transverse velocities are prescribed. The k exponent stands for one of the two phases.
(ii) At the outlet, zero-gradient conditions (Neumann conditions, $\partial/\partial_n = 0$), are specified for all quantities, except for the reduce pressure p^* for which a uniform Dirichlet condition is imposed.
(iii) At the top surface of the computational domain, Neumann conditions are applied for k and ω and for the three components of the velocity (u^k, v^k and w^k). As in *Roulund et al.* (2005) work, the model does not have free a surface. Consequently, it cannot handle situations where the free surface is deformed near the structure, i.e when the Froude number is higher than about 0.2.
(iv) At the side, cyclic conditions are used.
(v) At the walls (bottom and cylinder), a zero value is imposed for the velocity and a very small turbulent kinetic energy is specified for k ($O(10^{-6}$ $m^2.s^{-2})$). The conditions for ω are specified using a wall function. For the bottom wall, in order to account for the bed roughness, a roughness height of $k_s = 2.68\times10^{-3}$m is imposed through the tuned ω-wall function described in *Roulund et al.* (2005). For the cylinder, the classical smooth wall function from openFOAM is used (*omegawallfunction*). The description and the advantages/drawbacks of the different wall functions used in the rigid-bed case can be found in Chapter 4.

For the initial condition, the 1D vertical solution used for the inlet is imposed over the entire numerical domain.

5.3.2 Results

a) General hydrodynamics features

Figure 5.3 shows a comparison of the RB hydrodynamic simulation with *Roulund et al.* (2005) experimental and numerical results for longitudinal profiles of stream-wise (fig. 5.3, left panel) and wall-normal (fig. 5.3, right panel) velocities in the plane of symmetry at different elevations from the bed 0.5cm, 1cm, 5 cm and 20cm). The results have been averaged over 10 vortex shedding periods corresponding to approximatively 60 seconds of dynamics. For the results obtained with MeshI, the flow upstream the pile is in good agreement with *Roulund et al.* (2005) experimental data. The horseshoe vortex (HSV), defined as the the area in front of the cylinder where the longitudinal velocities are negative, is very well captured by the k-ω 2006 and the SST model (see fig. 5.3, left panel, at 0.5 and 1cm height). Downstream the pile, the change of sign in the velocities shows that there is a counterclockwise recirculation cell. All the turbulence models are able to capture the counterclockwise circulation observed in the experiments of *Roulund et al.* (2005). This was not reproduced by *Roulund et al.* (2005) steady numerical simulations (see fig 5.3, right panel) which confirms the importance of unsteady flow simulations for this flow configuration (*Stahlmann et al.* (2013) ; *Baykal et al.* (2015)). The present numerical simulation results show that the SST and k-ω 2006 model tend to underestimate by approximatively a factor 2 the size of the recirculation cell at the downstream side of the pile. This is probably due to the horizontal mesh resolution used here (see MeshII discussion below).
The major observation is that the k-ω 2006 and the SST model give very similar results. According to the literature, the SST turbulence model is the best turbulence model in the presence of an adverse pressure gradient. As detailed in Chapter 3 the k-ω 2006 turbulence model has similar properties but has no dependency of the model coefficients to the distance to the wall, which makes it more suitable for two-phase flow simulations.

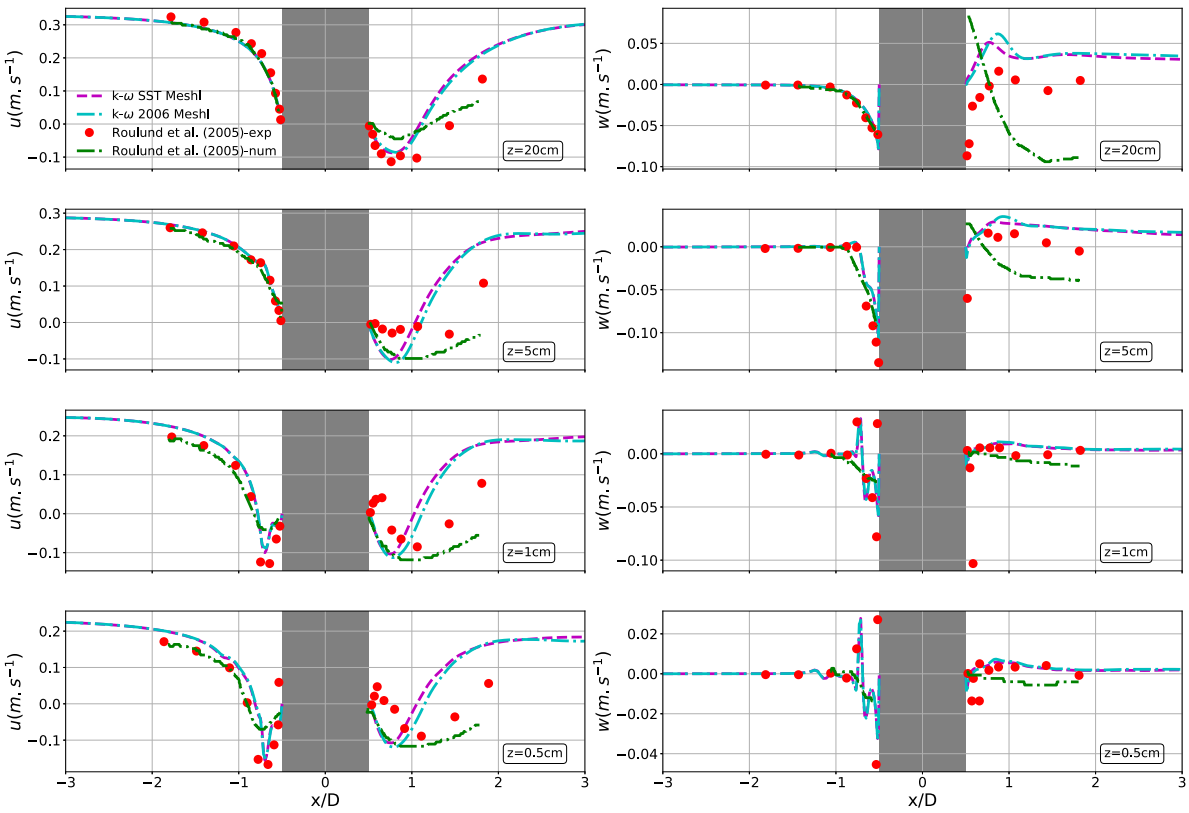

FIGURE 5.3: Horizontal and vertical velocities, u (left panel) and w (right panel), in the plane of symmetry at different distances from the bed for the two turbulence models k-ω2006 and SST using MeshI.

Figure 5.4 shows the same plot as figure 5.3 for the k-ω 2006 model only with MeshI and MeshII. Refining the mesh in the horizontal directions (Mesh II see full blue lines in figure 5.3) allows to improve the hydrodynamic predictions. The HSV is still accurately predicted whereas the counterclockwise recirculation cell downstream of the pile has now the correct size compared with experimental data. Only this refined configuration will be investigated further in this section.
It must be pointed-out that for the k-ω 2006 and the SST models, a shift is observed for the wall-normal velocities downstream of the pile at 20 cm in the water layer, compared with *Roulund et al.* (2005) results. This is probably due to rigid-lid effects and accounting for the free surface could resolve these discrepancies as shown in *Zhou* (2017).

b) Horseshoe vortex

One of the main hydrodynamic feature in the case of solid wall junction flow is the horseshoe vortex in front of the structure. Its presence is encountered experimentally in numerous configurations such as wing body junction (*Devenport and Simpson*, 1990) or low-aspect-ratio pin-fin array (*Anderson and Lynch*, 2016). The HSV formation in front of a bluff body is the

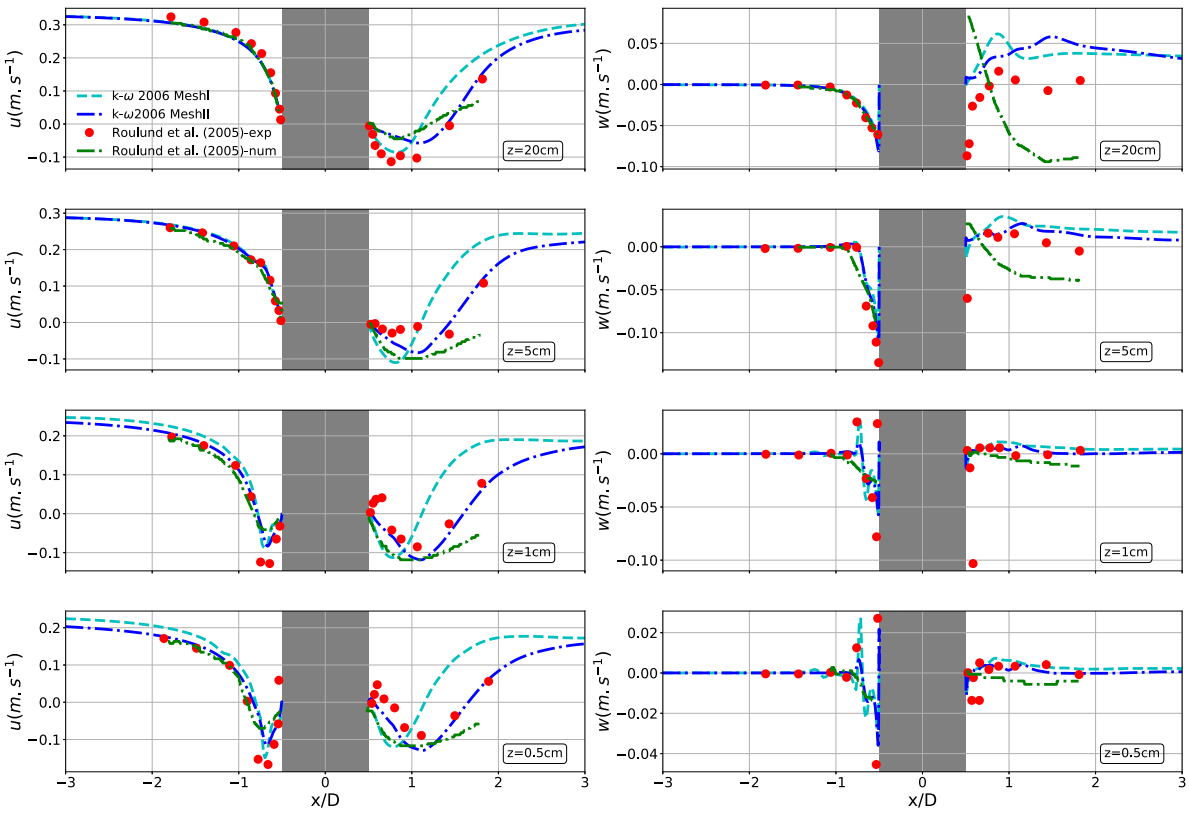

FIGURE 5.4: Horizontal and vertical velocities, u (left panel) and w (right panel), in the plane of symmetry at different distances from the bed for the k-ω 2006 turbulence model with MeshI and MeshII.

result of the adverse pressure gradient at the bed upstream of the object. The adverse pressure gradient increases the 3D boundary layer separation in front of the body and creates the HSV which extends in front and around the solid structure.

A 3D view of the HSV system is shown in figure 5.5, where the isovalue (Q=1.5s^{-2}) of the Q criterion is plotted. The Q criterion is often used to describe coherent structures and is calculated as the second invariant of the velocity gradient tensor :

$$Q = \frac{1}{2}\left[\left(\mathrm{tr}\left(\nabla \boldsymbol{u^f}\right)\right)^2 - \mathrm{tr}\left(\nabla \boldsymbol{u^f} \cdot \nabla \boldsymbol{u^f}\right)\right] \tag{5.1}$$

This result indicates that the HSV is present in the model, upstream the pile but also up to an angle $\pm\Gamma$=90° along the cylinder perimeter, where Γ is the angle measured with respect to the upstream x-axis.
It has been found here that the HSV position is time independent, meaning that the bimodal oscillation of the HSV observed in various configurations (*Anderson and Lynch*, 2016; *Devenport and Simpson*, 1990; *Simpson*, 2001) is not recovered here. This is probably due to the URANS (Unsteady

Reynolds Averaged Navier-Stokes) approach for turbulence modeling used in the present work. Indeed, successful turbulence modeling approaches able to capture this bimodal oscillation are LES or DES (*Kirkil et al.*, 2008).

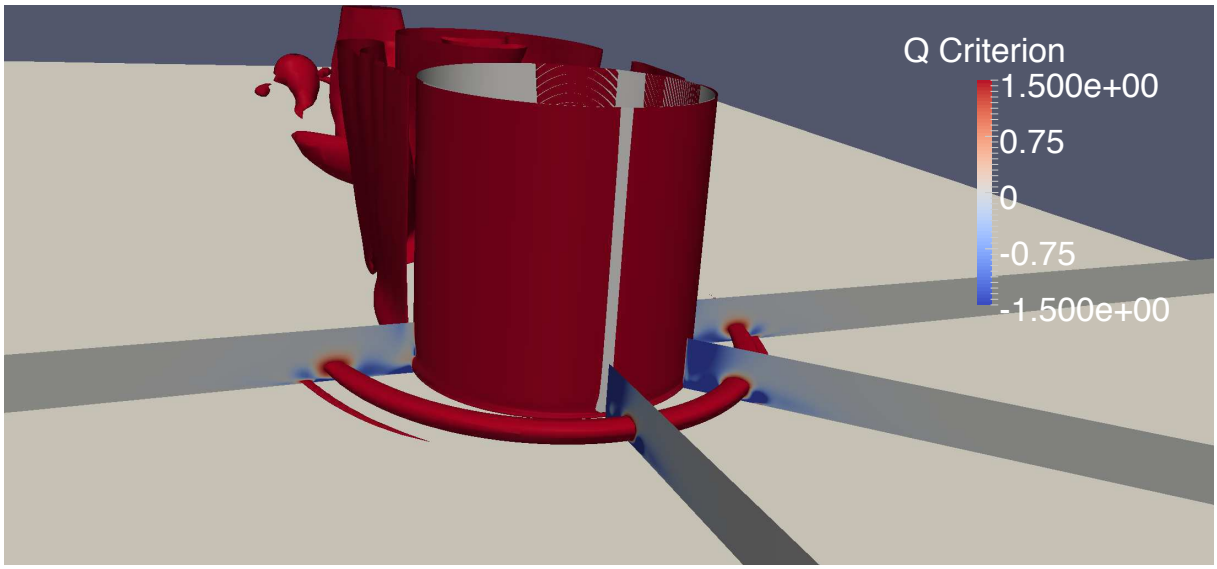

FIGURE 5.5: Instantaneous Q criterion around the cylinder. The isovalue Q=1.5s^{-2} shows the coherent structures. In the plan Q is plotted in the range Q$\in [-1.5 - 1.5]$.

Figure 5.6 shows a comparison between the bed shear stress amplification τ_b/τ_0 along the longitudinal axis in the plane of symmetry predicted by the model (blue dots) and *Roulund et al.* (2005) experimental and numerical results. Only the results obtained with MeshII are presented. The bed shear stress amplification is computed as the ratio between the local bed shear stress and its value at the inlet, where the flow is undisturbed by the cylinder presence. The local bed shear stress τ_b is computed as :

$$\tau_b = \sqrt{{\tau_{xz}^f}^2 + {\tau_{yz}^f}^2} \times \ sign(\tau_{xz}^f), \tag{5.2}$$

where τ_{xz}^f and τ_{yz}^f are the components of the fluid shear stress tensor τ^f at the bed vertical position. In figure 5.6 the zero-crossing of the bed shear stress amplification in front of the pile, between x/D=-1 and x/D=-0.5, shows the location of the HSV. The two-phase flow model results are in very good agreement with *Roulund et al.* (2005) results outside of the HSV region (x/D<-1). However, inside the HSV region the negative bed shear stress amplification is underestimated by SedFoam. The difference with amplification found in *Roulund et al.* (2005) experimental work is about 25%. The latter is slightly improved compared with the findings of *Roulund et al.* (2005) and *Baykal et al.* (2015) numerical work, but no clear explanation can be provided for these discrepancies between experimental observations and numerical predictions.

c) Lee-wake vortices

The regime of the lee-wake vortices generated downstream of a vertical cylinder in a steady flow is depending on the Reynolds number of the flow. A summary of the different regimes can be found in *Sumer et al.* (2006). Here, Re_D=1.7 $\times$ 10^5, the flow is in the so-called subcritical

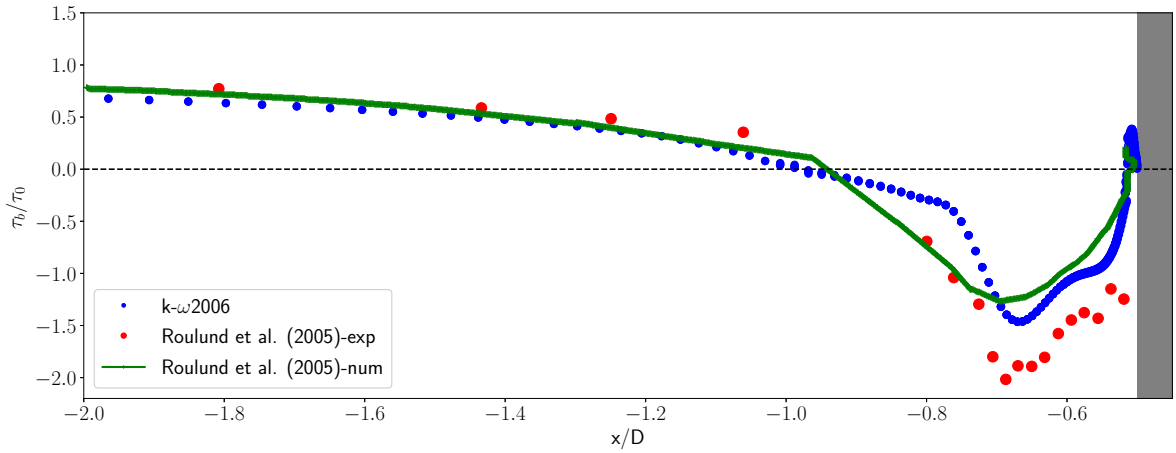

FIGURE 5.6: Comparison between the bed shear stress amplification τ_b/τ_0 along the longitudinal axis predicted by the SedFoam (blue dots) and *Roulund et al.* (2005) experimental and numerical results. Only the result with MeshII is presented.

regime. For such Reynolds number, the wake flow is completely turbulent and vortices are shed alternatively at each side of the pile. Along the pile surface, a boundary layer is forming and at one point this boundary layer will separate under the action of the adverse pressure gradient generated by the divergent geometry of the flow at the downstream side of the pile (*Sumer et al.*, 2006). The boundary layer is containing a given amount of vorticity which is fed into the shear layer formed downstream of the separation point. This will cause the shear layer to roll-up and generate vortices (*Sumer et al.*, 2006). In the case of a cylinder mounted over a flat bed, the incoming velocity profile is non-uniform over the depth of the domain. The separation point position at the cylinder side will change with the height and the boundary layer separation close to the bottom starts earlier than in the upper part of the fluid layer (*Baykal et al.*, 2015).
Because of the bed presence, the velocities close to the bottom are smaller in magnitude. This results in a smaller vorticity production at the cylinder close to the bottom. The vortex-shedding mechanism slows down and a delay can be observed between vortices shed near the bottom and in the rest of the water column. This phenomenon is shown in figure 5.7, where the instantaneous vertical vorticity snapshot highlights that vortices shed downstream of the cylinder are divided in two distinct cells along the vertical direction. This result is in agreement with the observations of (*Baykal et al.*, 2015). Downstream of the pile, each vortex generates a local excess-stress on the bottom and the overall vortex-shedding phenomenon is responsible for the scour downstream of the pile when the bed is composed of cohesion-less sediments (*Dargahi*, 1990).

Figure 5.8 shows the bed shear stress vectors and the contour lines of the magnitude of bed shear stress amplification over one period of vortex shedding at the bottom of the RB case. Only the magnitude of the bed shear stress is considered :

$$\tau_b = \sqrt{{\tau_{xz}^f}^2 + {\tau_{yz}^f}^2} \tag{5.3}$$

First, the position of the maximum bed shear stress in the cylinder vicinity can be found at an angle Γ=65°. This maximum intensity may slightly vary in time but the location remains approximatively around that angle value.
No comparison with *Roulund et al.* (2005) experimental work can be provided here. In *Roulund et al.*

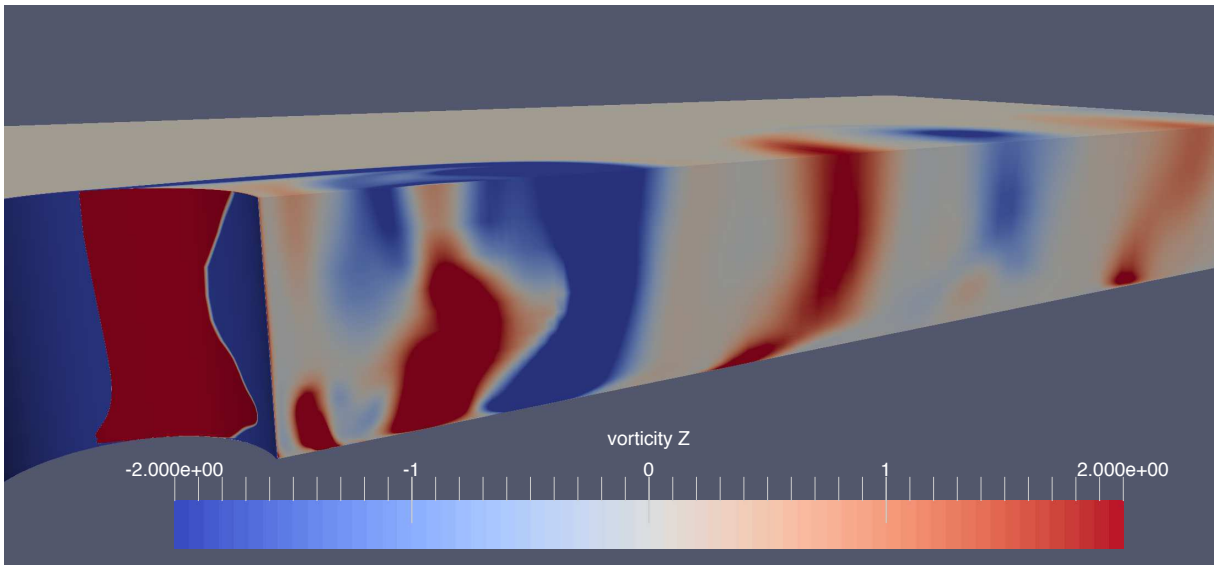

FIGURE 5.7: Instantaneous vertical vorticity (in s^{-1}) around and downstream of the cylinder.

(2005) and *Baykal et al.* (2015) numerical works, the magnitude of the bed shear stress amplification is compared with the experiments of *Hjorth* (1975) where the pile Reynolds number is $Re_D = 1.5 \times 10^4$. However, it is shown in *Roulund et al.* (2005) (see figure 17.) and *Baykal et al.* (2015) (figure 3.) that their numerical simulations predict the maximum bed shear stress around Γ=65°, whereas it is located around Γ=45° in *Hjorth* (1975). So the present results are consistent with former numerical simulations from the literature. The discrepancies between numerical prediction and experimental observation of the Γ position remains unexplained.
Again, no comparison can be provided in term of bed shear stress magnitude intensity but the order of magnitude found with SedFoam is similar to what is reported in *Hjorth* (1975) configuration ($max(\tau_b/\tau_0) \approx 9$).

The orientation of the bed shear stress vectors in negative x-direction highlights the presence of a recirculation zone induced by the HSV in front of the pile. The bed shear stress vectors are maximum where the streamlines are the most contracted. In the recirculation cell, the bed shear stress vectors are close to zero, an expected result.
Figure 5.8 also shows the unsteady behavior of the flow downstream of the cylinder. In the four panels, snapshots during a vortex-shedding period (T) are shown. The generation of two vortices at the opposite sides of the pile, one at $t = 0$ $[T]$ (figure 5.8 top left panel) and the other at t=T+T/2 is clearly visible. Here, the vortex-shedding period is ≈6s. Although higher than the theoretical Strouhal value (S_{tr}=0.2) the present Strouhal number (S_{tr}=0.27) is in good agreement with the one reported in (*Baykal et al.*, 2015). The vortices are also clearly identifiable via their modification of the bed shear stress. Furthermore, the bed shear stress amplification contours shape and intensity reported in 5.8 are in qualitative agreement with the works of *Baykal et al.* (2015) (see figure 8) even if the configurations are different.

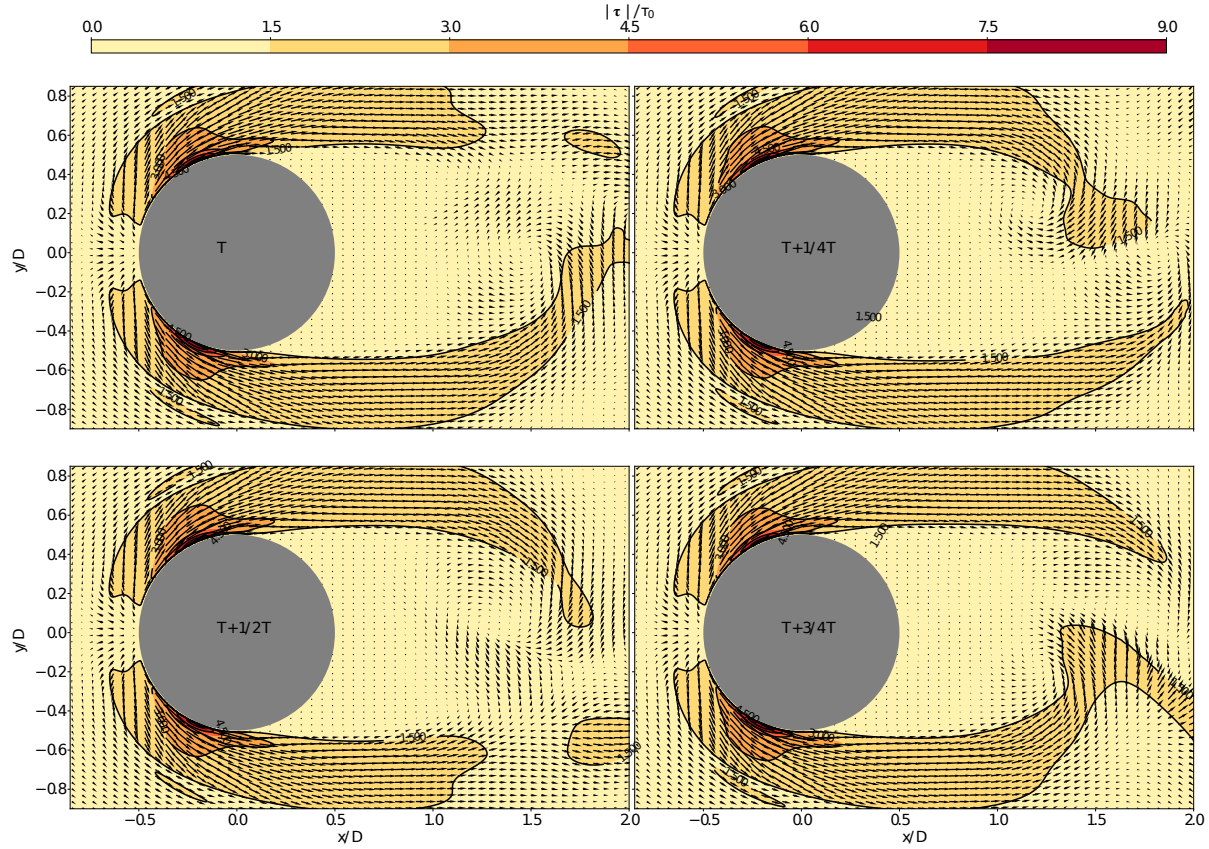

FIGURE 5.8: Bed shear stress vectors and contour lines of the magnitude of bed shear stress amplification over one period of vortex shedding at the bottom. T≈6s is the vortex-shedding period.

d) Hydrodynamics of the "Live-Bed" configuration without sediments

In *Roulund et al.* (2005), the experimental configurations are different for the RB or in the LB cases. The incoming depth-averaged flow velocity, the pile dimensions and the Reynolds numbers are different in the two cases. The hydrodynamics for the RB case has been validated in the previous sections and the case of the scour in the LB configuration will be presented and discussed in section 5.4. The purpose of the present section is to provide a reference for the hydrodynamic features and the bed shear stress in a case presenting the exact same configuration as the LB case (namely flow velocity, pile dimension and Reynolds number) without including sediments. To this end, the same 3D computational domain box than the one presented in figure 5.1 is used but the dimensions are now Lx=13D, Ly=8D, H=2D with D=0.1m, the pile diameter. The Reynolds number is $Re_D = \overline{U}D/\nu^f$=4.6 $\times$ 10^4 and the depth-averaged flow velocity is $\overline{U}$=0.46 m.s^{-1}. The same type of mesh than the one presented for the RB case is used. Here, a sensitivity of the hydrodynamic features to the mesh resolution will be performed. The two mesh resolutions used are presented in table 5.2, the only difference stands in the number of cells around the cylinder perimeter, being twice higher in MeshB (512) than in MeshA (256).
The boundary conditions are the same as the ones detailed for the RB case, except for the value

Tableau 5.2: Summary of the two meshes used for the Live-Bed without sediments configuration

Characteristics	MeshA	MeshB
Turbulence model	k-ω2006	k-ω2006
Total number of cells	750 976	2 504 064
Number of cells across the cylinder perimeter	256	512
Horizontal resolution around the cylinder perimeter (m)	1.2×10^{-3}	0.6×10^{-4}
Number of cells across the water depth	32	32
Vertical cell aspect ratio	1.196	1.196
Bottom cell height (m)	1.5×10^{-4}	1.5×10^{-4}

of the bottom roughness height which is set to $k_s = 6.5 \times 10^{-3}$m. This value corresponds to the roughness of immobile sand grains at the bottom.

Figure 5.9 shows the bed shear stress amplification magnitude obtained with MeshA (figure 5.9.a) and MeshB (5.9.b) at t=60s. For the refined mesh, the vortices in the wake of the cylinder are more accurately resolved. The bed shear stress amplification associated with the eddies is also higher in the case of the refined mesh which may mobilized the sediments more easily and therefore lead to higher erosion downstream of the pile.
It is not shown here but the HSV in front and around the pile is well recovered with both meshes.

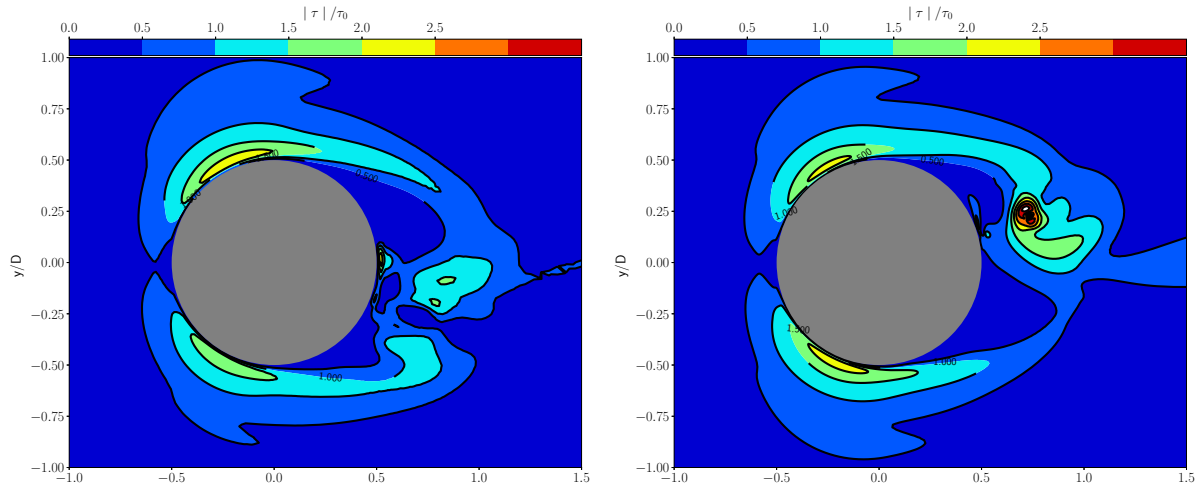

(a) (b)

FIGURE 5.9: t=60s. Bed Shear Stress amplification magnitude in the Rigid-Bed case with MeshA (a), and MeshB (b).

The detailed study of the hydrodynamics features such as the HSV and the lee-wake vortices discussed in sections a), b), c) and d) highlights the good behavior of the proposed model to reproduce the hydrodynamics of the flow around a vertical cylinder in a steady current without sediments. This successful hydrodynamic validation is a necessary step that allows to use

SedFoam to simulate the 3D scour erosion in the Live-Bed case.

5.4 Live-bed configuration

5.4.1 Computational mesh and set-up

In the Live-bed case the water depth is H=2D with D=0.1m being the pile diameter (see figure 5.10). The initial water domain is the same as the one described in section d). Instead of a solid bottom boundary, a thin sediments layer covers (0.25D) the entire domain except in a region around the pile, where a circular scour pit of height H_s=D and radius r_{pit}=2D has been setup. The sediments are made of medium sand with median diameter d =0.26 mm and density ρ^s=2650kg.m^{-3}, the corresponding fall velocity of an individual grain in quiescent water is $w_{fall0} = 3.4$ cm/s. The Shields parameter at the inlet and the Reynolds number are the same as is in *Roulund et al.* (2005), θ=0.19 and Re_D=4.6×10^4, respectively.

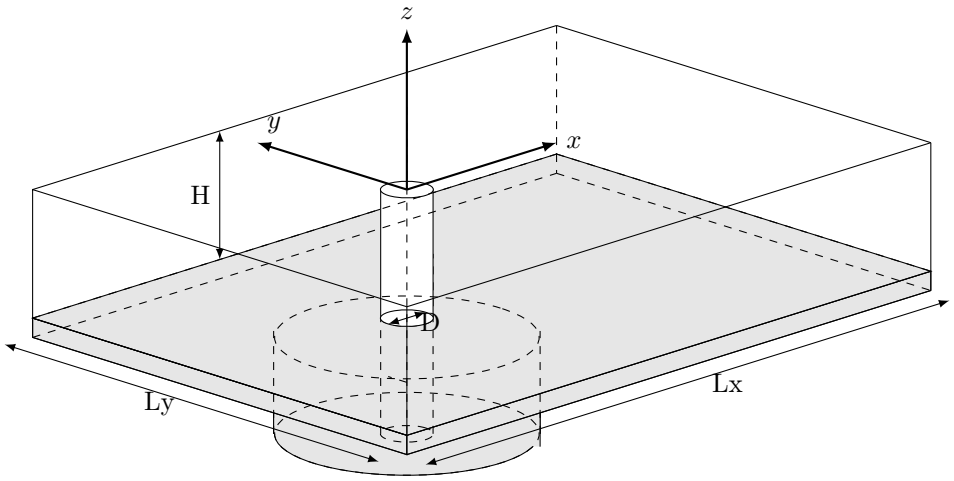

FIGURE 5.10: Sketch of the geometry used for the computational domain in the Live-Bed case (illustration is adapted from *Roulund et al.* (2005)).

The mesh used for the initial water volume (transparent box in figure 5.10) corresponds the one denoted as MeshA in section d).
For the sand layer, outside the scour pit, the mesh is composed of 100 vertical levels having a geometric distribution with a common ratio r_s=1.025. In the scour pit, an additional 100 grid points are used with a geometric common ratio r_{pit}=1.010. The mesh describing both the water and the sediments is denoted as MeshLBA and its characteristics are summarized in table 5.3.

The boundary conditions have to be adapted from the RB case :
(i) At the inlet, vertical profiles obtained from a 1D vertical simulation are imposed for u^s, u^f, k , ω, ϕ. Zero transverse velocity is prescribed.
(ii) At the outlet, Neumann boundary conditions are specified for all quantities, except for the pressure for which a homogeneous Dirichlet boundary condition is imposed for the reduced pressure. For the velocities, a homogeneous Neumann boundary condition is used when the velocity vector points outside of the domain at the outlet, and a homogeneous Dirichlet boundary condition is used otherwise.

Tableau 5.3: Summary of the geometry and mesh characteristics used in the LB configuration

Characteristics	MeshLBA
Lx	13D
Ly	8D
Total number of cells	5 308 368
Number of cells around the cylinder perimeter	256
Number of cells across the water depth	64
Number of cells across the sediments	200
Number of cells across the scour Pit	100
Initial interface cell height (m)	1.5×10^{-4}

(iii) At the top and side boundaries, the same boundary conditions as in the Rigid-Bed case are used.
(iv) At the walls (including the cylinder), zero velocity (no-slip) is imposed for the three components and a small value is imposed for the turbulent kinetic energy (TKE) k. The boundary condition for ω is specified using the classical wall function from openFOAM at the cylinder and using a constant value is imposed at the bottom.

The granular rheology parameters are set up as follows, the static friction coefficient is imposed at μ_s=0.63 corresponding to the tangent of the angle of repose for sand in water, the dynamical friction coefficient is fixed to μ_2 =1.13 and I_0 =0.6. For the shear induced particle pressure, we set the parameter $B_\phi = 0.66$. These parameter values are consistent with those proposed in *Chauchat et al.* (2017) except for the value of μ_s that was lowered.

5.4.2 Methodology

This section aims to present the specific post-processing methodology associated with the two-phase flow approach. The way in which the bed interface, the bed slope angle, the bed shear stress are determined is summarized hereafter. For more details and justifications about the methodology, particularly for the bed shear stress definition, the interested reader is refered to Appendix B.

a) Bed interface determination

The bed interface is defined as the surface of iso-concentration $\phi = 0.57$. In case of spherical particles, the maximum bed fraction is $\phi_{\max}$=0.635. In the two-phase flow literature, other definitions of the interface position can be found. In particular, it can be described as the vertical position at which the sediments velocity u^s is below a given threshold value. Indeed, by definition, the immobile bed is where sediment particles are not moving. Figure 5.11 show the bed interface position at t=600s along the x-axis using different definitions : the interface defined as the vertical elevation of the isosurface of sediments concentration $\phi = 0.57$ (in blue), the vertical elevation of the isosurface of sediments concentration $\phi = 0.6$ (in cyan), and the vertical elevation of the isosurface at which the sediments streamwise velocity magnitude is lower than 10^{-5}m.s^{-1} (magenta). It clearly appears that all definitions provide the same estimation of the bed interface

vertical position except in the recirculation zone where small velocities can be encountered in the water column leading to some discrepancies using the velocity criterion. Therefore, the sediments concentration ϕ=0.57 will be used in the following.

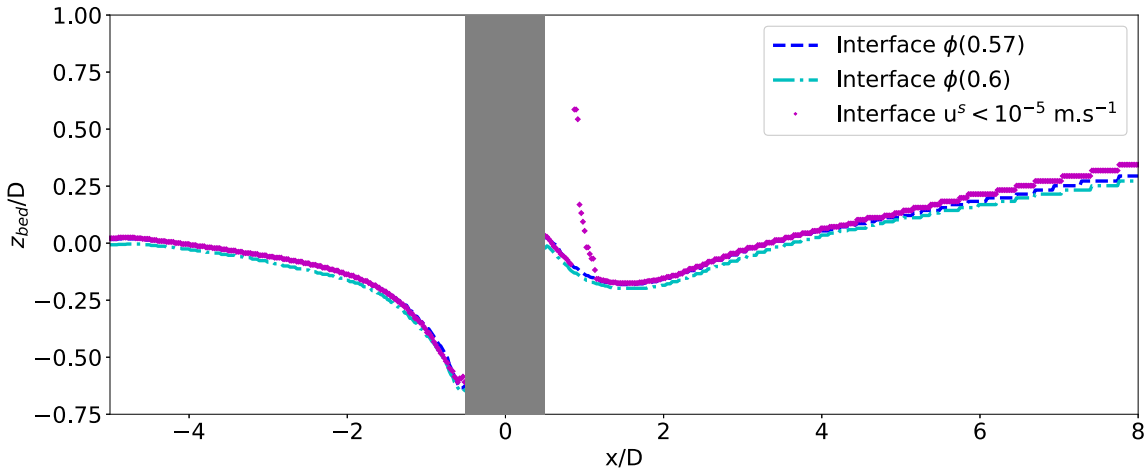

FIGURE 5.11: Bed elevation along the x-axis after t=600s of dynamics using different interface determination criterion : blue (ϕ=0.57), cyan (ϕ=0.6), magenta ($\sqrt{u^{s2}}$ <10^{-5}).

b) Bed shear stress definition in a two-phase flow configuration with sediments

In the present work, the bed shear stress has been determined using the shear stress of the mixture (eq. B.12) at the concentration $\phi = 0.08$. This iso-concentration level corresponds to the vertical position of the top of the bedload transport layer (*Bagnold*, 1954; *Dohmen-Janssen et al.*, 2001).

$$\mid \tau_b \mid = \sqrt{\tau^f_{xz}(\phi)^2 + \tau^f_{yz}(\phi)^2 + \tau^s_{xz}(\phi)^2 + \tau^s_{yz}(\phi)^2}. \tag{5.4}$$

Because the scour is deforming the initial flat sediments bed, the resulting interface slopes variation have to be accounted for in the bed shear stress calculation. To this end, the bed interface is first interpolated from the original unstructured grid to a cartesian one, using the standard *interpolate.griddata* function of python and the *cubic* method for the interpolation [1]. On each cells of this new cartesian grid, the normal ($\overrightarrow{n}$) and the tangential ($\overrightarrow{t_x}$ and $\overrightarrow{t_y}$) vectors are calculated using the bed interface elevation horizontal gradient (see Appendix B for details). The projection of the mixture bed shear stress magnitude on the plane tangential to the local bed surface reads :

$$\mid \tau_b \mid = \sqrt{(\overrightarrow{T^f} \cdot \overrightarrow{t_x})^2 + (\overrightarrow{T^f} \cdot \overrightarrow{t_y})^2 + (\overrightarrow{T^s} \cdot \overrightarrow{t_x})^2 + (\overrightarrow{T^s} \cdot \overrightarrow{t_y})^2}, \tag{5.5}$$

where T^k is the stress vector applied on the sediments bed surface of the phase k. It is obtained from the product between the phase shear stress tensor τ^k and the normal vector $\overrightarrow{n}$:

$$\overrightarrow{T^k} = \tau^k \cdot \overrightarrow{n} \tag{5.6}$$

1. https ://docs.scipy.org/doc/scipy/reference/generated/scipy.interpolate.griddata.html#scipy.interpolate.griddata

Figure 5.12.a shows the bed interface elevation at t=10s, the erosion pattern generated by the HSV is clearly visible. The flow is coming from the left as for all the other bird view figures presented in this work. Figure 5.12.c shows the angle of steepest descent or local maximum slope of the bed β. It is determined from the magnitude of the horizontal gradient of the bed elevation :

$$\beta = \arctan(\nabla_h z_{bed}), \tag{5.7}$$

where $\nabla_h z_{bed} = \sqrt{\left(\frac{\partial z_{bed}}{\partial x}\right)^2 + \left(\frac{\partial z_{bed}}{\partial y}\right)^2}$.
The bed interface variations are important in the HSV area, with a slope angle up to 50°. Figure 5.12.b shows the projected mixture bed shear stress amplification. The bed shear stress amplification is slightly increasing with the slope of the scour hole. It is maximum at the sides of the cylinder, for $\Gamma \in [\pm 65° - \pm 120°]$.
Finally, figure 5.12.d shows the ratio between the bed shear stress obtained with and without the projection on the plan tangential to the local slope. Away from the cylinder, this ratio is between 0.9 and 1.1. The ratio deviates far from unity only where bed slope is significant, that is in the upstream part of the scour hole and around the cylinder. This result allows to validate the projection method for the mixture bed shear stress described above.

5.4.3 Results and discussions

In this section the results on the three-dimensional two-phase flow simulation of scour around a cylindrical pile are presented and discussed. All the simulations have been performed using a maximum viscosity ν_{max} =100 m^2/s and $C_t = 1$ (see eq. 3.61). The different simulations undertaken and their main characteristics are summarized in table 5.4. Three simulations (LB1, LB2 and LB3) are performed using MeshLBA and different combination of turbulence and Schmidt number models. The reference simulation is LB1, undertaken with a k-ω2006 turbulence model and a local Schmidt number. Due to the very high computational cost, only LB1 has been run for 600 s of real time simulation, this computation took 480 hours (20 days) on 224 processors Intel® Xeon® E5-2690 v4. The computational time of the LB1 case is approximatively of 108000 hours, or $\approx$ 12 years.

Tableau 5.4: Summary of the different simulations undertaken for the Live-Bed configuration

Characteristics	LB1	LB2	LB3
Turbulence model	k-ω 2006	k-ω 2006	k-ω
Final time (s)	600	100	60
Schmidt number	Local	0.33	0.33
Vortex shedding	Yes	Yes	No

a) General erosion patterns and maximum erosion depth prediction

In order to illustrate the capacity of the two-phase flow model to predict scour around a structure, snapshots of bed elevation at different times (t=10s, 60s, 300s and 600s) are shown in figures 5.13. The present results can be qualitatively compared with figure 33 in *Roulund et al.* (2005). The two-phase flow model is able to reproduce the following bathymetric bed features

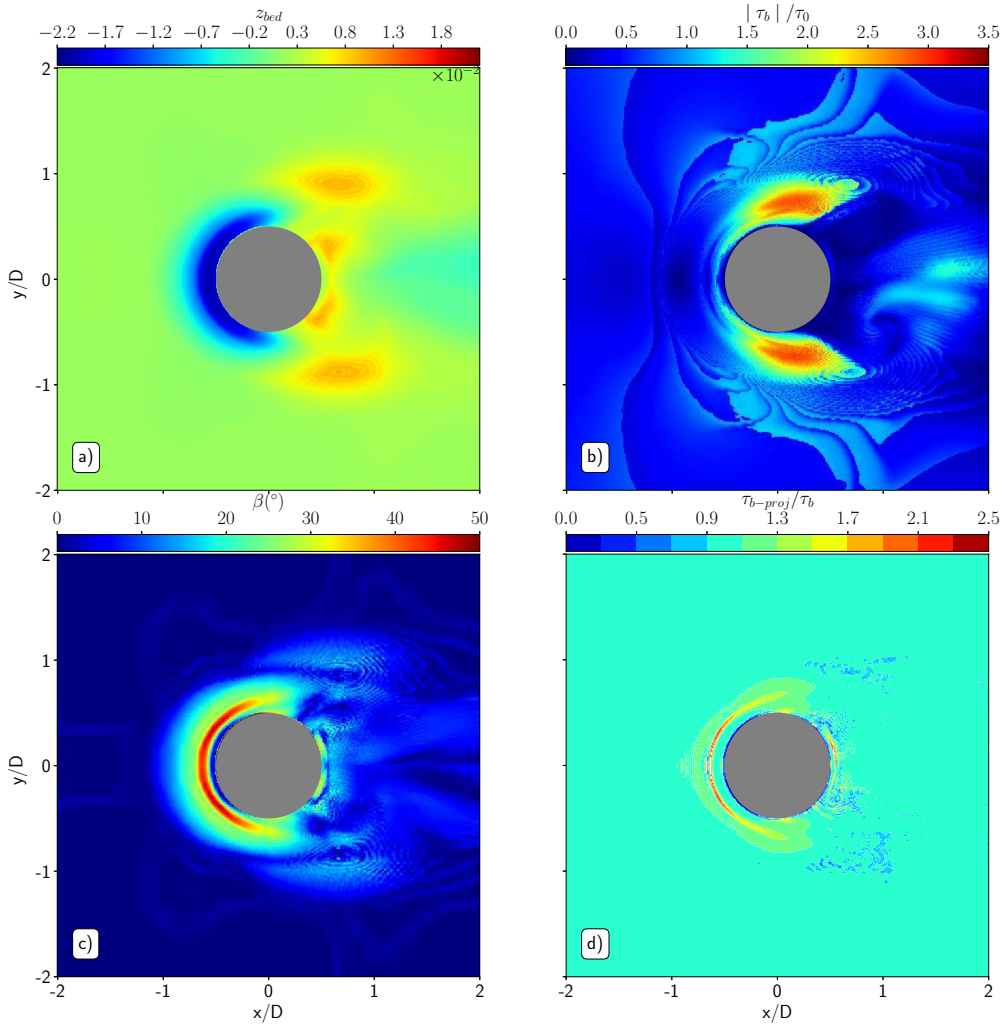

FIGURE 5.12: Bed interface elevation (a), projected mixture bed shear stress amplification estimated with eq. B.12 (b), angle of maximum bed slope (c) and ratio between the bed shear stress obtained with and without the projection on the plane tangential to the local bed surface (d) for t=10s.

(i) a semi-circular shaped scour mark is predicted at the upstream side of the pile (ii) sediments eroded from the scour mark first accumulate downstream the pile (iii) at later stages a scour mark is predicted at the downstream side. However, the downstream bed morphology differs from the one reported in *Roulund et al.* (2005), particularly with the presence of sediments accumulation bars extending in an oblique way downstream of the cylinder, that are not found in *Roulund et al.* (2005).

The bed elevation around the cylinder is shown in figure 5.14, for t=10s (panel a), t=60s (panel b), t=150s (panel c) and t=300s (panel d). The erosion pattern generated by the HSV, in front and around the cylinder is noticeable at t=10s, being more than 5cm wide and up to 2.2cm

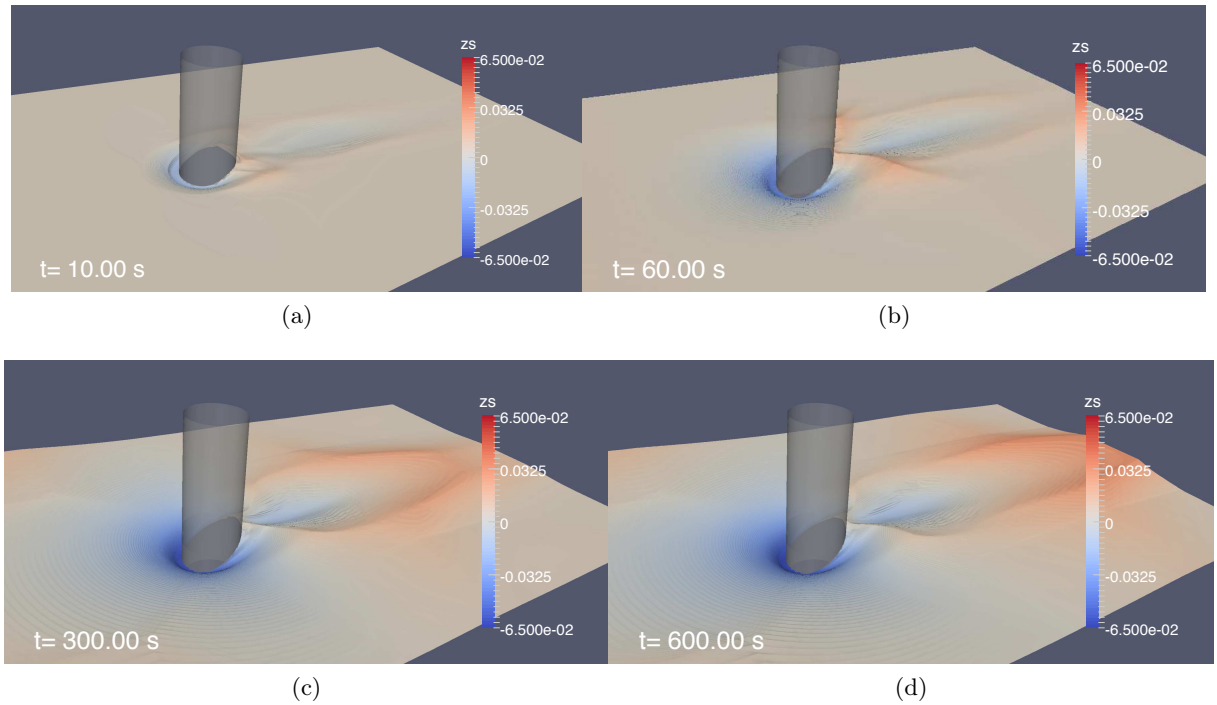

FIGURE 5.13: Bed elevation after 10s (a), 60s (b), 300s (c) and 600s of dynamics for simulation LB1.

deep. The legs of the HSV erosion mark extends further around the cylinder, up to $\Gamma = \pm 90°$. Accumulation of up to 1cm of sediments is found just downstream of the cylinder. With time, the scour hole extends further upstream and becomes deeper (up to 4.8cm at t=60s and 5.4cm at t=150s). The legs of the HSV erosion mark extends further around the cylinder, up to $\Gamma = \pm 145°$ at t=150s.

An accumulation of up to 1.75cm is found just downstream of the cylinder and the sediments bars extend in an oblique way downstream of the cylinder for t=60s. The accumulation is less than 1cm at t=150s. This shows that an erosion process is at work between t=60s and t=150s. The erosion seems to saturate in time. Indeed, the maximum erosion difference between t=150s and t=300s is very low, around 2.5mm. Furthermore, the erosion extension around the cylinder only slightly increases between t=150s and t=300s.

Figure 5.15 shows the time evolution of the maximum dimensionless scour depth $\delta_s^{max*} = \delta_s^{max}/D$ at the upstream side (top panel) and at the downstream side (bottom panel) of the pile in simulation LB1. The two-phase flow numerical results are compared with experimental data (red dots) and numerical results (green curve) from *Roulund et al.* (2005). The good agreement between the two-phase flow model reference simulation LB1 and the experiments at the upstream side shows that the two-phase flow model is able to reproduce quantitatively the upstream scour depth evolution for all the model configurations tested up to 300s. From 300 to 600s the maximum dimensionless scour depth almost saturates to a value of $\delta_s^{max}/D = 0.63$, whereas the experimental data shows a continuous increase with a scour depth of $\delta_s^{max}/D = 0.8$ at $t = 600$s. The two-phase flow approach is thus underestimating the erosion in the upstream scour mark for t>300s.

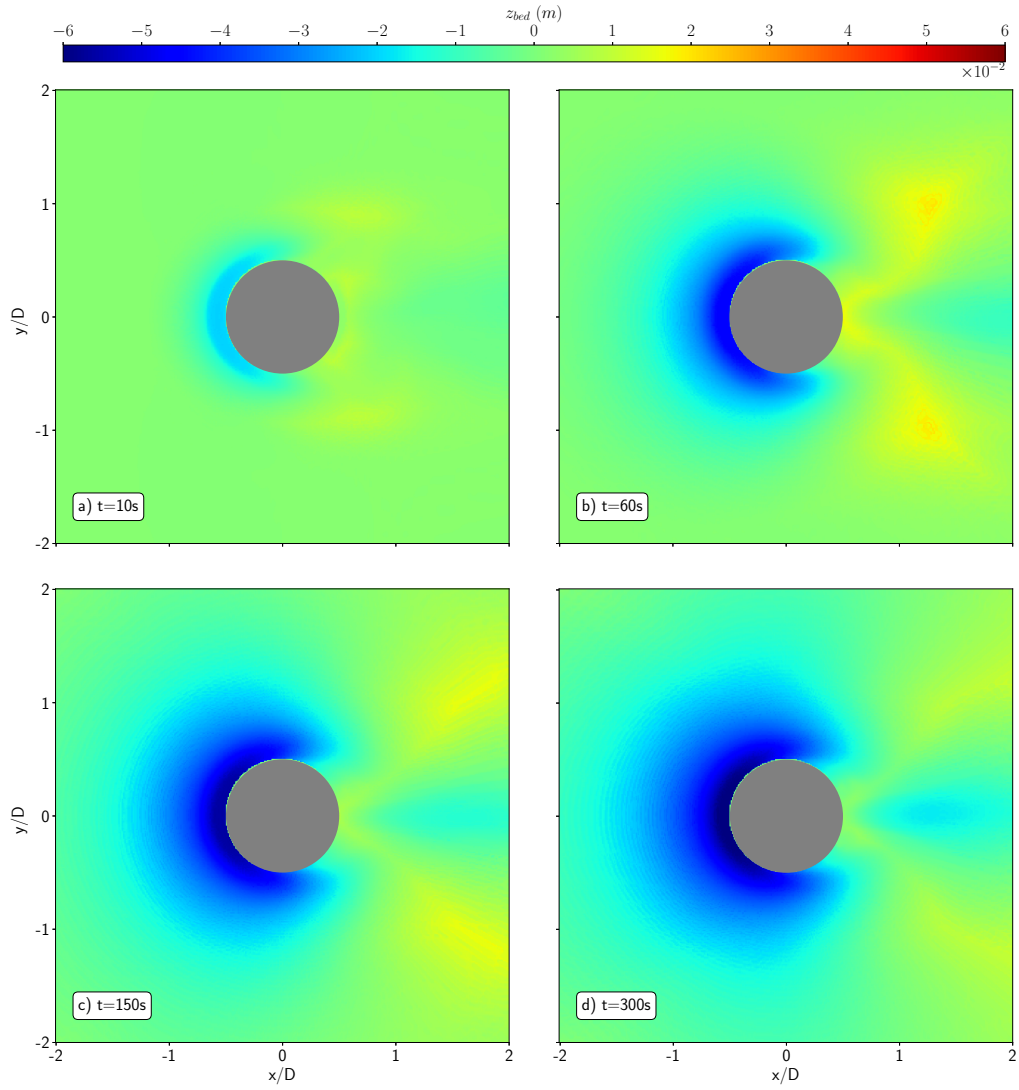

FIGURE 5.14: Vertical elevation of the bed interface elevation defined by the iso-surface of concentration $\phi = 0.57$ at t=10s (a), t=60s (b), t=150s (c),and t=300s (d).

At the downstream side (bottom panel of figure 5.15) the simulation results using the k-ω 2006 shows a temporal fluctuating behavior of the scour depth. The position of the maximum scour depth downstream of the cylinder is not located in the pile vicinity as for the upstream edge, but rather 1 to 2 diameter downstream of the structure (see figure 5.14.d). The high frequency fluctuations of the downstream maximum scour depth are due to the eddies shed downstream of the pile. This result indicates that the downstream scour is influenced by the vortex-shedding, a result that has already been pointed out in former studies using classical sediments transport models (e.g. *Baykal et al.*, 2015; *Stahlmann et al.*, 2013; *Zhao et al.*, 2010). The maximum erosion depth numerically predicted is in good agreement with the experimental results from *Roulund et al.* (2005) up to 300s. For t>300s, the erosion rate decreases compared with the ex-

perimental results from *Roulund et al.* (2005), leading to an underestimation of the erosion depth downstream of the pile.

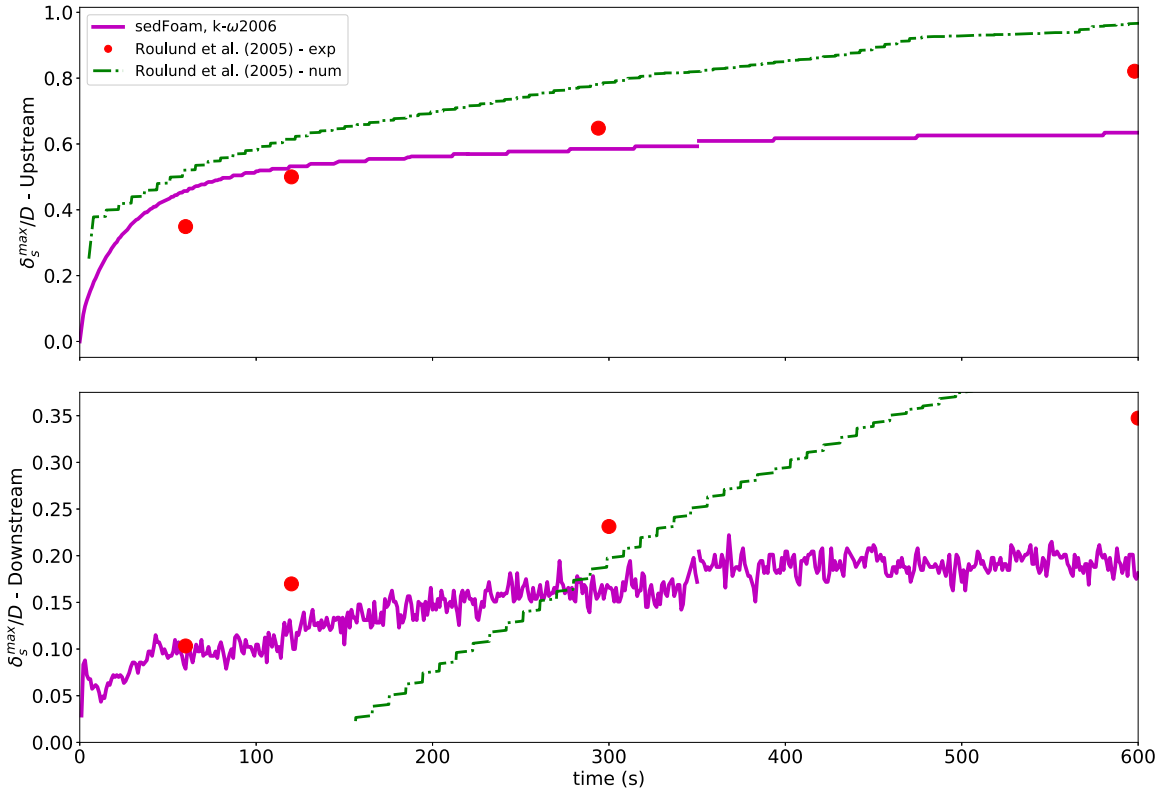

FIGURE 5.15: Time evolution of the dimensionless scour depth at the upstream (top panel) and at the downstream (bottom panel) edge of pile in simulation LB1 (see table 5.4).

Figure 5.16 shows a zoom of figure 5.15 between t=0s and t=100s. In addition to simulation LB1 with the k-ω 2006 turbulence model and the local Schmidt model, simulation LB2 (k-ω 2006, constant Schmidt number) and LB3 (k-ω, constant Schmidt number) are also shown. At the upstream side (top panel), no noticeable differences can be found between LB1, LB2 and LB3 predictions for δ_s^{max*} evolution in time. For the upstream scour mark, the model results are not sensitive to the choice of the turbulence model k-ω or k-ω 2006 or to the choice of the Schmidt number model.

Concerning the downstream edge of the pile, simulation LB3 using the standard k-ω model does not predict erosion. The standard k-ω model can not reproduce correctly the vortex shedding in this configuration and therefore the predicted erosion downstream is very limited.
Using the local Schmidt number model (simulation LB1) seems to improve upon the constant Schmidt number model ($S_c = 0.33$, simulation LB2) for times between 60s and 100s. An explanation could be the important role of the suspended load at the downstream side of the pile. According to (*Baykal et al.*, 2015), the suspension process is important since the early stages and should be accounted for starting at t=0s. Without consideration of the suspended load, the

overall transport is decreasing and sediments accumulation is first observed at the downstream side of the pile (*Baykal et al.*, 2015). This is typically what can be observed in figure 5.15 with *Roulund et al.* (2005) downstream erosion numerical estimation up to approximatively 150s.

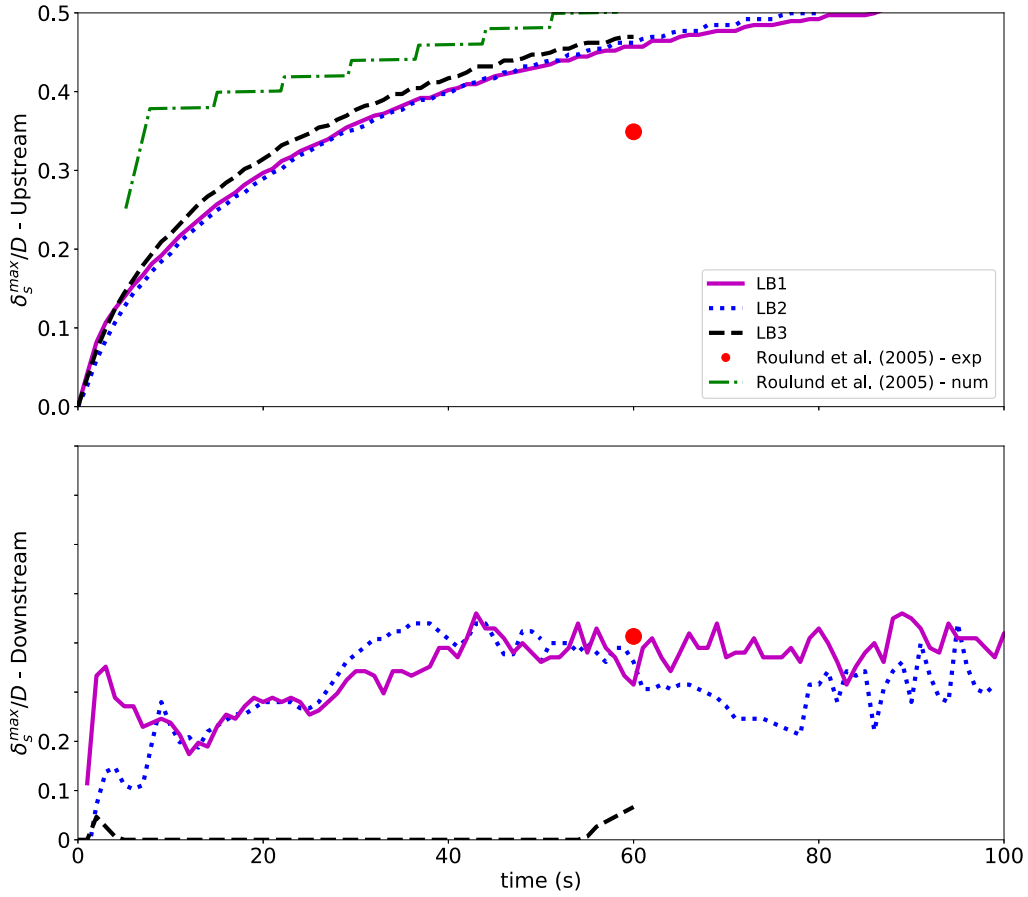

FIGURE 5.16: Time evolution of the dimensionless scour depth at the upstream (top panel) and at the downstream (bottom panel) edge of pile. Zoom between t=0s and t=100s.

The global erosion rate can be investigated by calculating the depth integrated dimensionless sediments flux difference across two consecutive transverse sections, ΔQ^*.
The dimensionless sediments flux across a given transverse section, Q^* is defined as :

$$Q^* = \int_{Ly} q^*. \tag{5.8}$$

where q^* is the instantaneous dimensionless depth integrated sediments flux. It is obtained from the two-dimensional extension of equation 4.21 :

$$q^* = \frac{\int_{h_b}^{h_t} u_p^s dz}{\sqrt{(s-1)gd^3}}, \tag{5.9}$$

in which u_p^s is the sediments velocity projected on the plan tangential to the local slope :

$$u_p^s = \sqrt{(\boldsymbol{u^s} \cdot \overrightarrow{t_x})^2 + (\boldsymbol{u^s} \cdot \overrightarrow{t_y})^2}. \tag{5.10}$$

Figure 5.17 shows the time evolution of the dimensionless sediments flux difference between the transverse section x/D=-2 and the cylinder center section (x/D=0) (in blue) and between cylinder center cross-section (x/D=0) and the transverse section x/D=2 (in red).
A bird view of the computational domain and the cross-sections chosen to compute the dimensionless sediments flux is also shown in figure 5.17. The horizontal dashed line corresponds to the change of sign of ΔQ^*.

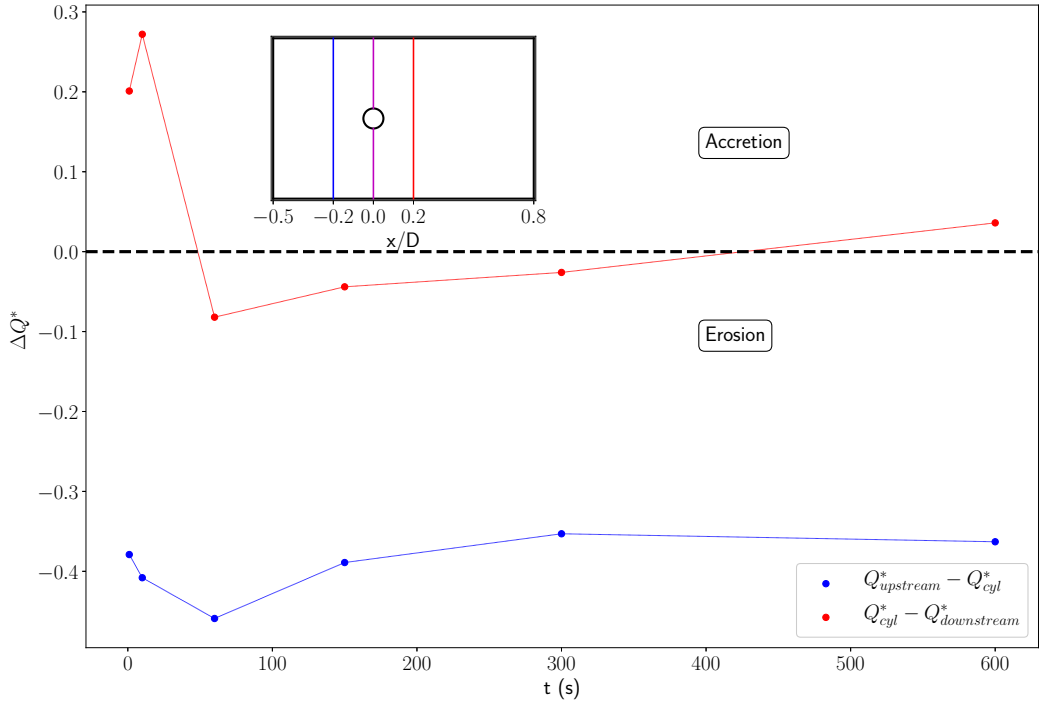

FIGURE 5.17: In blue : dimensionless sediments flux difference between the transverse section at x/D=-2 and the cylinder position (x/D=0). In red : dimensionless sediments flux difference between transverse section at the cylinder position (x/D=0) and at x/D=2.

The difference between the dimensionless sediments flux at the transverse section x/D=-2 and at the cylinder position (x/D=0) (blue points) is negative for the all the times considered. In this region, an erosion process is at work at all the times of the simulation. The erosion rate is more important at the beginning of the simulation, up to t=60s. It is slowly reducing between t=60s and t=300s. Between t=300s and 600s, the upstream erosion rate has a constant non-zero value, meaning that sediments are still excavated from the scour hole and that the equilibrium is not reached despite the erosion rate saturation observed in figure 5.15.
Downstream of the pile, the sign of the dimensionless sediments flux difference between x/D=0 and x/D=2 changes in time. At the beginning up to t≈30s, less sediments are going through the cross-section x/D=2 than x/D=0, indicating that accretion (*i.e* sediments accumulation) is

occurring downstream of the cylinder. This is consistent with the observations obtained from the figure 5.13, showing an increase of the sediments bed elevation just downstream of the pile for early dynamical times. After that transient state, erosion is occurring at the downstream side of the pile. As for the upstream side of the pile, the maximum erosion rate is observed at t=≈60s. For longer times (300s>t>600s), the erosion rate seems to stabilize around zero. However the difference between the two curves is always negative, indicating that, overall, between x/D=-2 than x/D=2, erosion is at work for all the times considered.

The results presented above provide the proof of concept for the applicability of two-phase flow model to complex 3D phenomenon such as the scour evolution around a cylindrical structure.

b) Bed shear stress and sediments transport around the pile

In the case of a flow around a structure, the assumption of uniform flow conditions on which the empirical sediments transport formula (e.g. *Meyer-Peter and Müller*, 1948) is based is not valid. It has been shown in Chapter 4 that the two-phase flow model predicts a power law for the relationship between the sediments transport flux and the Shields parameter under uniform and steady flow conditions. In section 5.4.3 it has been further demonstrated that the two-phase flow model is able to predict reasonably well the bed morphological evolution at the early stages of the scour process. In this section, the numerical results are further analyzed to investigate how the sediments transport flux is locally modified with respect to the one obtained under uniform and steady flow conditions.

Focusing first on early times, the subfigure 5.18.a shows the local slope angle, β at t=10s, allowing to describe the following bed variations :

- Far from the obstacle the bed is flat or almost flat (far upstream, $\beta \approx 0$).
- Closer to the cylinder, there is a semi-circular area where the slope is gently increasing while the distance to the cylinder is decreasing.
- At $R_u/D \approx 0.7$ an important variation of the bed slope angle is visible at the upstream side of the cylinder. R_u/D is the upstream distance to the center of the cylinder made dimensionless by the cylinder diameter, it is equal to x/D on the x-axis. Over a very short distance, β goes from ≈30° to ≈45°. These important variations indicate the presence of a slope break at the upstream side of the cylinder for $R_u/D \approx 0.7$.
- Downstream of the slope break, the slope angle exceeds the angle of repose ($\beta = 32°$) up to R_u/D ≈0.6. The sediments bed is unstable and avalanches may occur in this region. Closer to the cylinder (0.6> R_u/D >0.5), the slope angle is decreasing and the sediments bed is again nearly flat, $\beta \approx 0$.
- Just downstream of the cylinder, up to $x/D = 1$, the bed interface slope angle is noisy and it is hard to distinguish any slope tendency. Further downstream, for $x/D > 1$ the bed variations are very small and β remains below 10°.

Figure 5.18.b shows the instantaneous dimensionless depth integrated sediments flux at t=10s determined with equation 5.9. The sediments flux starts to increase with the increasing bed slope angle. At the slope break, around $R_u/D \approx 0.7$, the sediments flux is strongly increasing. Closer to the cylinder, where the scour hole is the deepest and the bed is almost flat, the sediment flux is decreasing. The maximum of the sediments flux is located in the two legs around the cylinder corresponding to the HSV legs. This result indicates that there is an important transverse flux

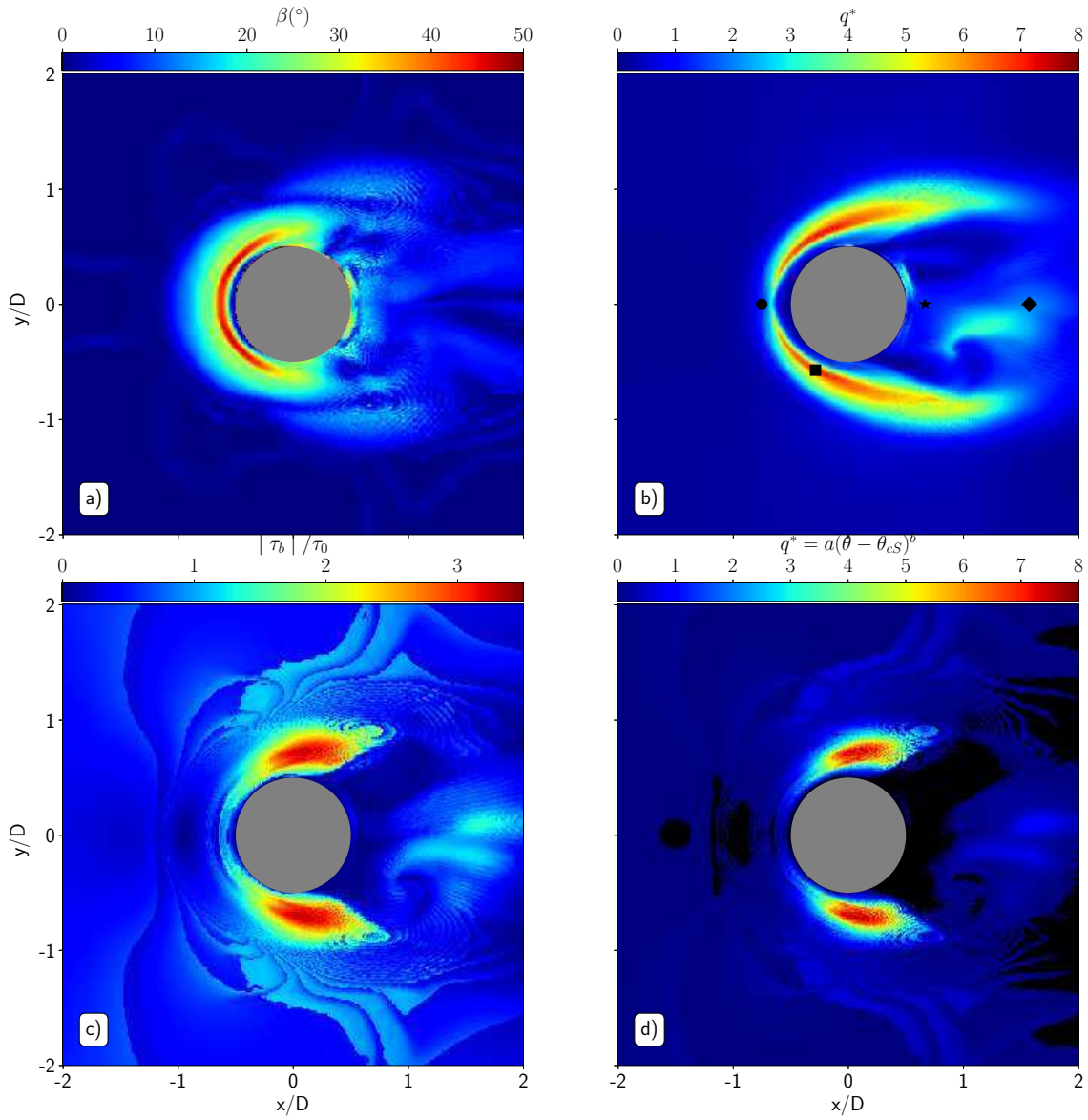

FIGURE 5.18: Sediments bed slope angle (a), dimensionless depth integrated sediments flux (b), bed shear stress amplification (c) and dimensionless sediments flux estimated from "classical" power law with slope correction (d) at t=10s.

driven by the HSV legs around the cylinder and is in agreement with the description of *Link et al.* (2012). The maximum dimensionless sediments flux value within these two legs is $q^*_{max} = 7.9$. The sediments flux is weak downstream of the cylinder at t=10s. This is probably do to the fact that the vortex-shedding is not fully developed at that moment. The sediments transport seems to be more important in a very small area that might be related to the shedding of a vortex from

the pile. Two areas of almost zero sediment flux can also be identified downstream of the pile. There localizations are coherent with the presence of sediment accumulation bars extending in a oblique way downstream of the cylinder that have been observed in figure 5.13.a.

Figure 5.18.c shows the bed shear stress amplification. The bed shear stress amplification is slightly increasing with the slope of the scour hole. It is maximum at the sides of the cylinder, for $\Gamma \in [\pm 65° - \pm 120°]$. Downstream of the pile, an excess-stress area is located around $x/D = 1$ and $y/D = -0.25$ exactly where an increase of sediments transport is observed in figure 5.18.b. Here, the local bed shear stress amplification has a swirl structure confirming that it is generated by a vortex shed from the cylinder.

Figure 5.18.d shows the dimensionless sediments flux estimated from the power law deduced from 1D vertical simulations in Chapter 4 :

$$q^* = a(\theta - \theta_{cS})^b, \tag{5.11}$$

with a=26.14 and b=2.09 as established in Chapter 4 for $\phi = 0.08$. The critical Shields number θ_{cS} is here defined as a function of the bed slope and orientation. The formulation used in the present work has been proposed by *Roulund et al.* (2005) and is a simplification of *Dey* (2003) formulation. The flow velocity at the particle position and the steepest slope are used to adjust the critical Shields number :

$$\theta_{cS} = \theta_c \left(\cos\beta \sqrt{1 - \frac{\sin^2\alpha \, \tan^2(\min(\beta, 32°))}{\mu_s^2}} - \frac{\cos\alpha \, \sin(\min(\beta, 32°))}{\mu_s} \right), \tag{5.12}$$

where $\theta_c = 0.047$ is the critical Shields number used over a flat sediments bed and α is the angle between the near-wall velocity at the bed surface and the direction of maximum slope :

$$\alpha = \arccos\left(\frac{\nabla_h z_{bed} \cdot \boldsymbol{u^f(\phi)}}{|| \nabla_h z_{bed} || \, \boldsymbol{u^f(\phi)} |} \right), \tag{5.13}$$

in which $\boldsymbol{u^f(\phi)}$ is the flow velocity at the iso-concentration $\phi = 0.57$.
Equation 5.12 has been slightly modified from *Roulund et al.* (2005) definition. The original definition provides non physical values for slope angles above the avalanching angle because $\tan(32°) = \mu_s$. In classical sediments transport models, an avalanche module is often used to force the slope angle below the avalanching value. In the two-phase flow model, the bed slope is free to exceed that critical value above which an avalanche is taking place. A limiting term is therefore used in eq 5.12 to avoid non physical values for the critical Shields number.
Equation 5.12 states that when the bed shear stress is acting in the down slope direction, the critical Shields number decreases, resulting in a higher sediments flux (see eq. 5.11), and vice versa.

The dimensionless flux obtained using equation 5.11 is locally correlated to the bed shear stress through the Shields number. Therefore, the dimensionless sediments flux shown in figure 5.18.d and the bed shear stress amplification shown in figure 5.18.c present the same spatial patterns : they increase in the upstream part of the scour hole, are maximum for $\Gamma \in [\pm 65° - \pm 120°]$, but are low for $\Gamma \in [0° - \pm 45°]$ and close to the cylinder. The asymmetric patterns of the sediments flux at each side of the cylinder are due to the fact that instantaneous quantities are shown in

figure 5.18.

The spatial correlation between depth integrated sediments flux predicted directly from the product of the sediment particles velocity and concentration (subfigure 5.18.b) and from the mixture shear stress (subfigure 5.18.d) is rather poor. Indeed, for $\Gamma \in [0° - \pm 65°]$, and more particularly around the slope break position, the important sediments flux observed in subfigure 5.18.b is not found in subfigure 5.18.d. This result suggests that around the slope break position, the sediments transport is driven by another mechanism than the bed shear stress.

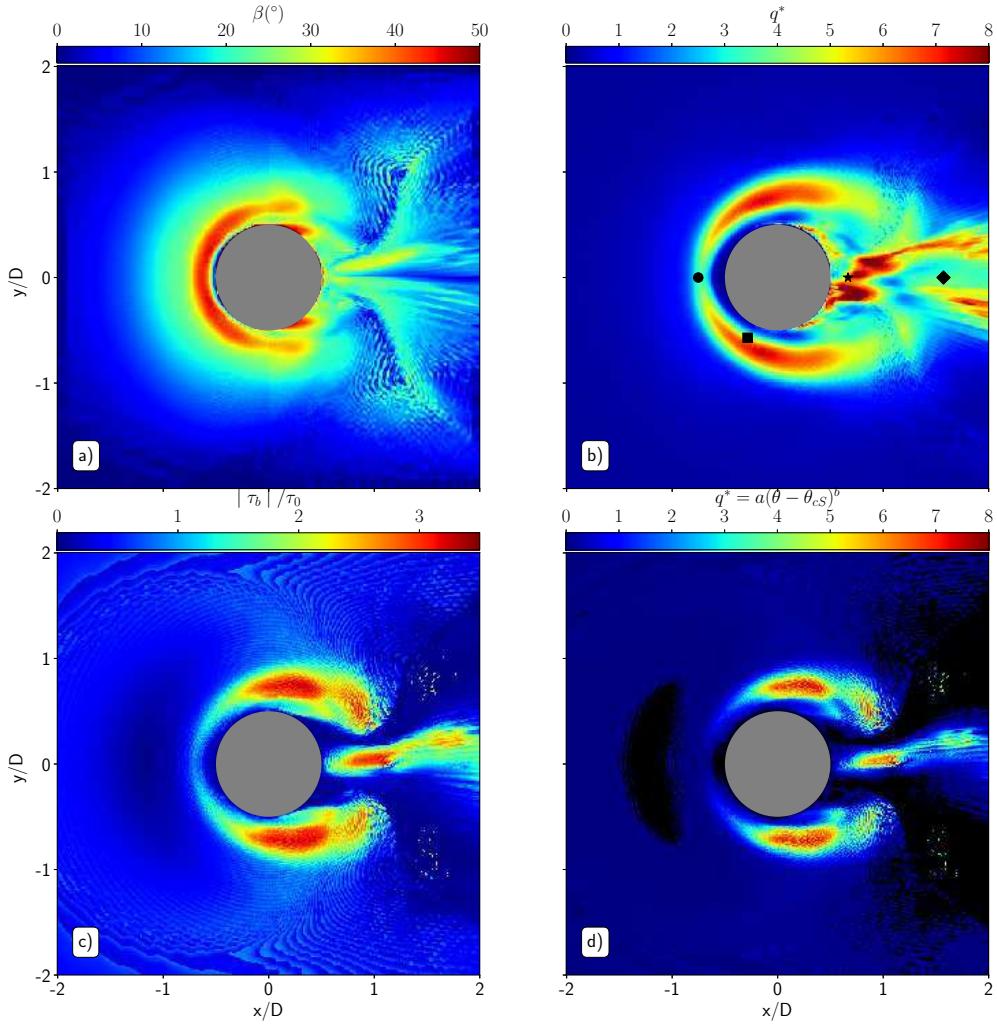

FIGURE 5.19: Sediments bed slope angle (a), dimensionless depth integrated sediments flux (b), bed shear stress amplification (c) and dimensionless sediments flux estimated from "classical" power law with slope correction (d) at t=60s.

The figures 5.19 and 5.20 show the same quantities than figure 5.18 for t=60s and t=150s, respectively. The sediments slope variations are very similar between t=60 and t=150s. In figures

5.19.a and 5.20.a, the slope angle increases gently up to ≈30° at $R_u/D \approx 0.7$. After that location, the slope is strongly increasing, being higher than the angle of repose over a distance of $0.1D$, approximatively. Over that distance, the bed is potentially unstable and avalanches may occur. Closer to the cylinder, the slope decrease rapidly and is almost zero at the immediate vicinity of the cylinder. The main difference between t=60s and t=150s is that the slope starts to be important further upstream at t=150s. This is in good agreement with the upstream extension of the scour hole as time increases, observed also in figure 5.14.

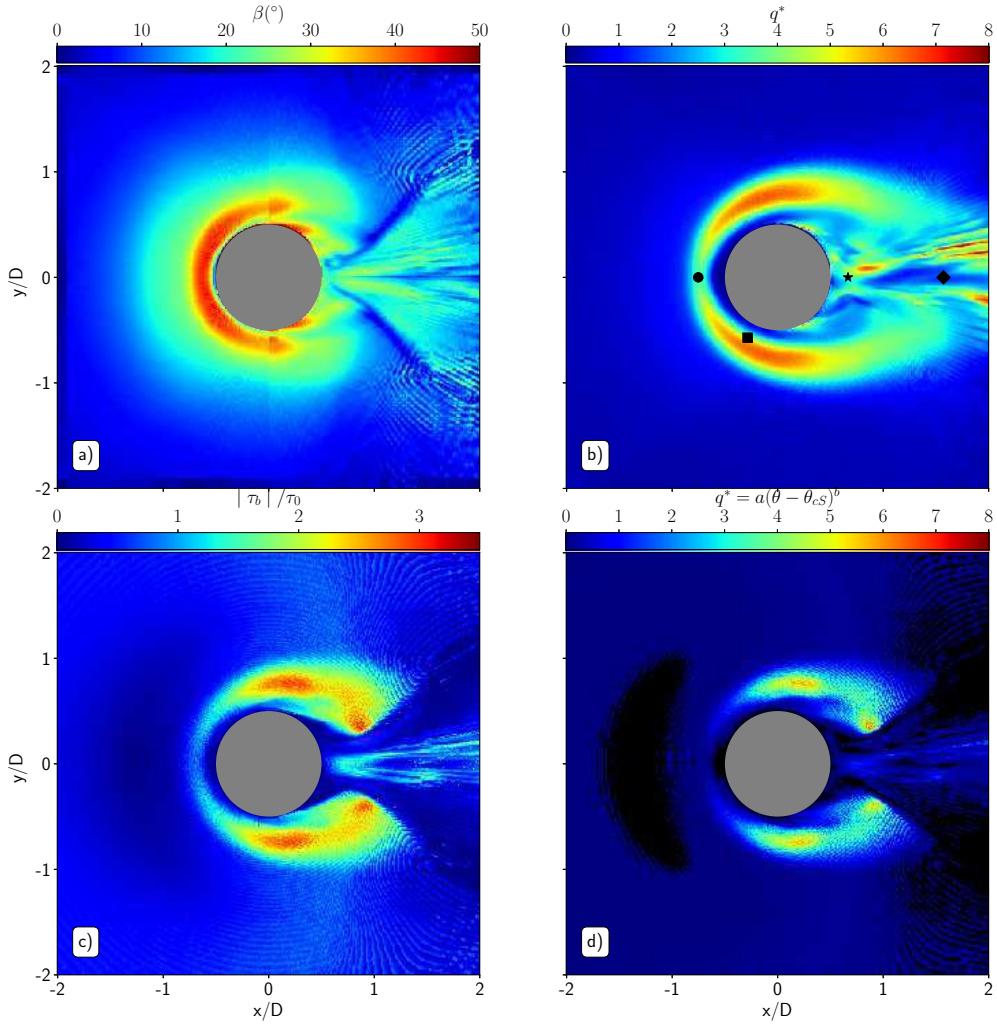

FIGURE 5.20: Sediments bed slope angle (a), dimensionless depth integrated sediments flux (b), bed shear stress amplification (c) and dimensionless sediments flux estimated from "classical" power law with slope correction (d) at t=150s.

The bed shear stress amplification (subfigures 5.19.c and 5.20.c) is increasing with the slope from upstream of the scour hole to $R_u/D \approx 0.7$. For $\Gamma \in [0° - \pm 45°]$. Between $R_u/D \approx 0.7$ and the pile, the bed shear stress amplification is below unity. In that region, the cylinder presence

is blocking the flow, generating a downflow that is reducing the bed shear stress in front of the cylinder. The maximum of bed shear stress amplification is located downstream of the cylinder and at the cylinder sides for $\Gamma \in [\pm 65° - \pm 145°]$. The maximum of the bed shear stress amplification is decreasing in time, from 3.15 at t=60s to 2.78 at t=150s. Downstream of the pile, the bed shear stress amplification is very important in a narrow channel approximatively aligned with the x-axis. This is due to the vortex-shedding.

At t=60s and t=150s, the depth integrated dimensionless sediments flux obtained directly from the velocity and concentration fields (see subfigures 5.19.b and 5.20.b) are similar to the one at t=10s. Far upstream of the cylinder, it increases slightly with the increasing bed slope angle. Around the main slope variation ($R_u/D \approx 0.7$), the flux drastically increases and remains at a high level ($q^* \approx 4.5$) where the bed angle exceeds the angle of repose. Excluding the area just downstream of the cylinder, the maximum of the sediments flux is located in the two legs around the cylinder. Compared with t=10s, the HSV legs are wider and the maximum sediments flux is slightly decreasing in time : $q^*_{max} = 7.1$ at t=60s and $q^*_{max} = 6.6$ at t=150s. The transverse flux driven by the HSV legs around the cylinder seems to decrease in time. This result is coherent with the global erosion rate presented in figure 5.17, meaning that the erosion rate is higher at the beginning of the scour process.
As for t=10s, the important differences between the two-phase flow and the "classical" (assuming a local equilibrium between the excess Shields number and the sediments flux, see eq. 5.11) approach to determine the sediments flux (subfigures 5.19.d and 5.20.d) are mostly located where the slope plays a role on the sediments transport, particularly upstream of the pile for $\Gamma \in [0° - \pm 45°]$, in the scour hole.
Contrary to what is observed at t=10s, the sediments flux from the velocity and concentration fields is extremely important downstream of the cylinder at t=60s and t=150s, being partially above $q^* = 8$ for t=60s. This important flux is localized in an area having the width of the cylinder and extending up to 1.5 diameter downstream. The differences between the flux estimated from the excess Shields number can be explained by the sediments advection from upstream of the pile. This indicates that the traditional assumption of local equilibrium between the excess Shields number and the sediments flux is not appropriate downstream of the pile.

A better understanding of the sediments transport in the cylinder vicinity can be obtained by investigating the flow along the vertical direction. To this end, for t=10s (in blue), t=60s (in magenta) and t=150s (in red), the vertical profiles of the mixture velocity (U), the sediments concentration (ϕ) and the dimensionless sediments flux ($\pi = \phi\sqrt{u^{s2} + v^{s2} + w^{s2}}$) at different locations around the cylinder are shown in figure 5.21. The location of each profile is given in subfigure 5.20.b : at the upstream slope of the scour hole (dark dot), in the HSV legs (squared symbol), 0.25D and 1D downstream of the pile (star and diamond symbols, respectively). The horizontal dotted line in the dimensionless sediments flux panels represent the vertical elevation of the sediments concentration ϕ=0.08, allowing to distinguish between bedload and suspended load.

- The vertical profile upstream of the pile is located where the bed slope angle is approximatively of 25° at t=10s and above the critical angle ($\beta > 32°$) for t=60s and t=150s. The profiles have a similar but vertically shifted z-dependence for the three times considered. Along the vertical direction the velocity is positive (*i.e* downstream oriented) just above the bed. This results in a strong bedload sediments flux oriented toward the cylinder ($\phi \in [0.57 - 0.08]$). Above that dense transport layer, the mixture velocity becomes negative

over more than 5mm height for t=10s and 1cm for t=60,150s. The concentration in that region is lower than 0.08 and a slight suspension sediments transport is observed going up-slope. The distinction between the two direction-opposed sediments fluxes is very clear and corresponds to the traditional distinction between bedload and suspended load. The particles in suspension follow the flow and are moving away from the cylinder whereas, close to the bed interface, the sediments are driven by the gravity and moves toward the cylinder.
Further away from the bed, the mixture velocity is positive again but the sediments concentration is so low that the associated sediments transport is negligible.

- In the HSV legs, the mixture velocity is positive everywhere along the vertical and the concentration profile is smoother at the interface. As a result, there is a positive sediments flux at that location, mostly composed of bedload because the peak of transport is located under the vertical position of concentration ϕ=0.08. Nonetheless, an important positive suspended load is also occurring for all the times considered.
- Just downstream of the pile, the first profile (x/D≈0.75, star symbol) is located in the recirculation cell. The mixture velocity takes negative values of up to U ≈-0.35m.s^{-1} all along the vertical and the concentration is non-negligible ($\phi > 1.10^{-3}$) in the water column. As a consequence, there is a negative (oriented toward the cylinder) suspended sediments flux for all the times considered. Very slight for t=10s this backward suspended load is more important for t=60s and t=150s.
- Further downstream (x/D≈1.75, diamond symbol) the observations are different for the different times considered. For t=10s, the velocity are negative but more important than at x/D≈0.75. It generates a more important suspended sediments load toward the cylinder. For t=60 and 150s, the velocity are positive again and the sediments are advected downstream by the flow and the vortices using bedload and suspended load.

All the profiles for the different times considered are vertically shifted with respect to eachother. Upstream of the pile (dark dot) and in the HSV legs (squared symbol) the profiles are vertically shifted downward for 2cm between t=10s and t=60s and for 0.5cm between t=60s and t=150s. This highlights that an erosion process occurs upstream and at the cylinder sides, for all the times considered.
Focusing on the area just downstream of the cylinder, the bed interface level is at the elevation z/D≈0.04, z/D≈0.1 and z/D≈0.01 for t=10s, t=60s and t=150s, respectively. At early times, the vortex-shedding is not well developed whereas the HSV already erodes large amounts of sediments upstream of the pile. The sediments are transported downstream via the two HSV legs. Part of the sediments transported are deposed just downstream of the pile in the recirculation area, resulting in the accretion observed up to t=60s. Once the vortex-shedding is established, the erosion process becomes important just downstream of the pile. The sediments extracted upstream are still transported and partially deposited but a larger amount is evacuated by the vortices. Therefore the bed interface level is decreasing with time just downstream of the cylinder for t>60s.
Further downstream (x/D≈1.75, diamond symbol), erosion is at work for all the times considered as the bed interface is slightly below z/D=0 for t=10s. However the erosion rate is much smaller than upstream or around the pile, a result in agreement with the erosion rate shown in figure 5.15.

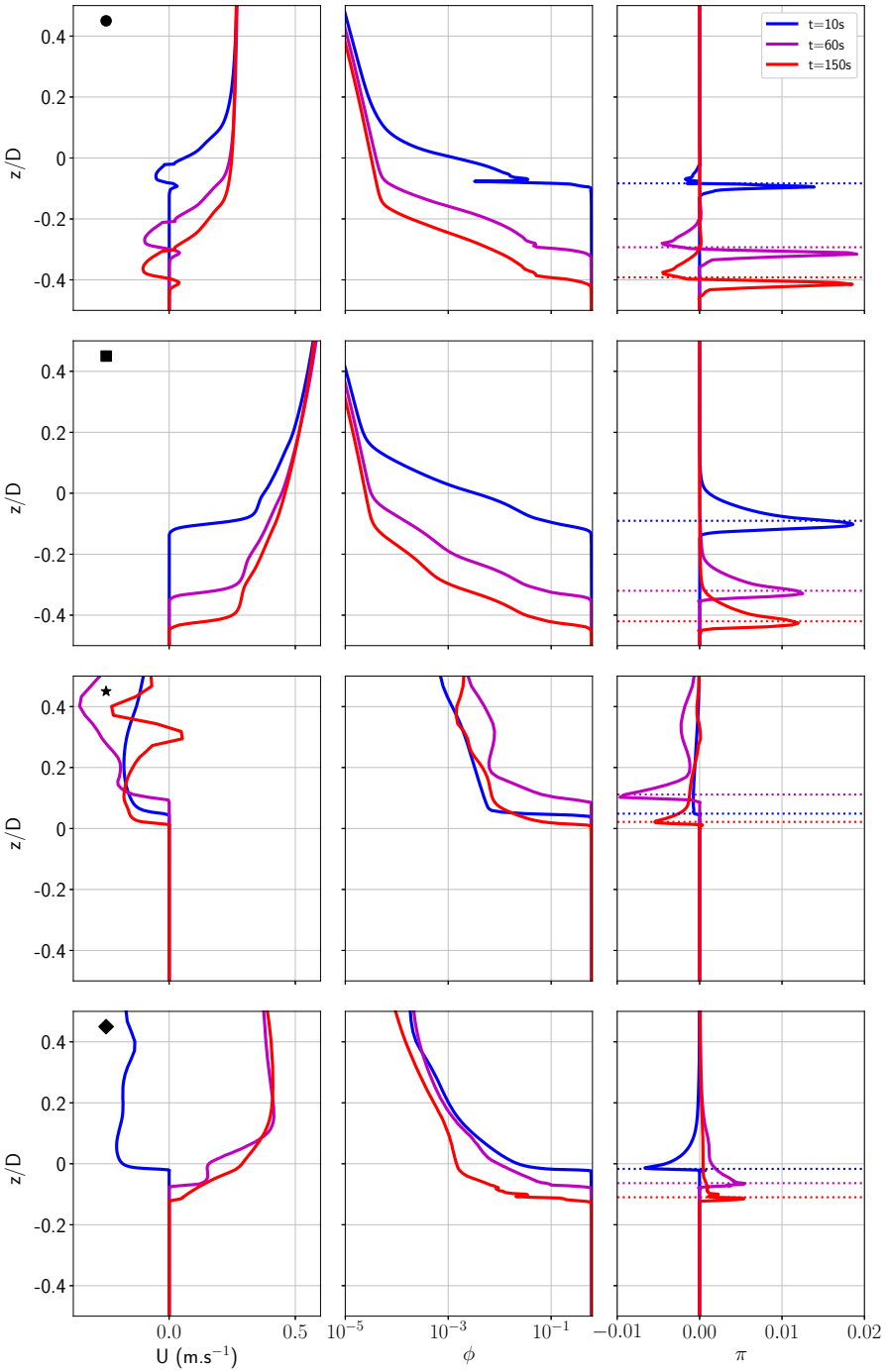

FIGURE 5.21: Vertical profiles of mixture velocity (U), sediments concentration (ϕ) and dimensionless sediments flux (π) at different locations around the cylinder and at t=10s (blue), t=60s (magenta) and t=150s (red). The location of each profile is shown in subfigure 5.20. The horizontal dotted line in the dimensionless sediments flux panels represent the vertical elevation of the sediments concentration ϕ=0.08.

The sediments transport presents important differences for the four profiles investigated. Specific transport regimes can be identified from the two-phase flow results. Along the scour hole slope, the fluid flow is mostly going up the slope because of the recirculation generated by the HSV. However, the sediments transport is for the most part due to bedload and is oriented toward the cylinder, suggesting that it is not driven by the fluid flow through the bed shear stress but rather by gravity. This explains the difference in term of sediments transport predictions obtained from the product of the particles velocity and concentration and from the mixture shear stress estimations upstream the pile for $\Gamma \in [0° - \pm 45°]$. Furthermore, the bedload and the suspended load are oriented in opposite directions. This complex sediments transport can not be reproduced with the traditional models, even when accounting for the suspended load. Thus, the two-phase flow approach allows to overcome the restrictions encountered using the "classical" approach and to reproduce these specific sediments transport processes consistently.
The present results also show the importance of accounting for the suspension to accurately predict the sediments flux around and downstream of the pile and confirm the findings of *Baykal et al.* (2015). Downstream of the pile where the sediments flux results from a combined action of the upstream extracted suspended load advection by the flow and of the local erosion by the vortex shedding. Accounting for the particles in suspension is not only important downstream of the pile but in the all the cylinder vicinity, as a non-negligible part of the sediments excavated upstream by the HSV is advected downstream by suspension in the HSV legs. The sediments in suspension are not depending on the local bed shear stress. Therefore, estimating the sediments flux as a function of the local bed shear stress only, as in eq. 5.11, underestimates the rate of sediments transport.

In order to extend the observations obtained from the vertical profiles, figure 5.22 shows a vertical plan view in the plane of symmetry upstream of the pile. The velocity vectors and the dimensionless sediments flux $\pi^*$are presented at different times (10s, 60s, 150s and 300s). The sediments iso-concentration contours $\phi = 0.57$ and $\phi = 0.08$ are also plotted on all subfigures to materialize the bed-load layer. In all subfigures, the avalanche angle for sand (32 °) is plotted as the red dashed line.

The velocity vector plot allows to identify the position of the HSV. As for the RB case, a single HSV is observed and its position does not evolve in time. By looking at the bed interface evolution and the velocity field it is observed that the downward flow in front the pile acts as a vertical jet impinging the sediments bed leading to sediments erosion and the formation of a HSV. As the scour hole deepens in time the bed slope upstream the pile increases and reaches values higher than the avalanche angle (32°). The observations extracted from the vertical profiles are found again. A competition between the local bed shear stress (resulting of the fluid flow over the sediments bed) and the gravity is taking place in the scour hole. At the upstream part of the scour hole, the slope is mild and the velocity vector are aligned with the sediments flux (figure 5.22 up to $x/D = -1$). Closer to the cylinder part of the mobilized sediments are transported backward by the HSV while the increasing slope in the downstream direction seems to significantly increase the sediments transport flux in the downstream direction. Very close to the pile ($x/D \approx -0.7$), sediments are avalanching in the scour pit. *Link et al.* (2008, 2012) observed several slope breaks in their experiments that are probably related to the existence of multiple HSV. In the present case, only one HSV is predicted. The HSV position corresponds to the point at which the slope becomes steeper than the angle of repose. In the region between the HSV and the pile, the slope is steeper than the angle of repose meanwhile the velocity vectors

and thus the fluid bed shear stress are negative. The gravity and the bed shear stress are counter acting each other, but gravity dominates as the sediments flux in the near bed region remains mostly positive. A small negative flux is observed above the interface $\phi = 0.08$ meaning that the HSV transports sediments backward as suspension. Overall, the sediments flux in this region is dominated by gravity even at early times ($t \approx 10s$).

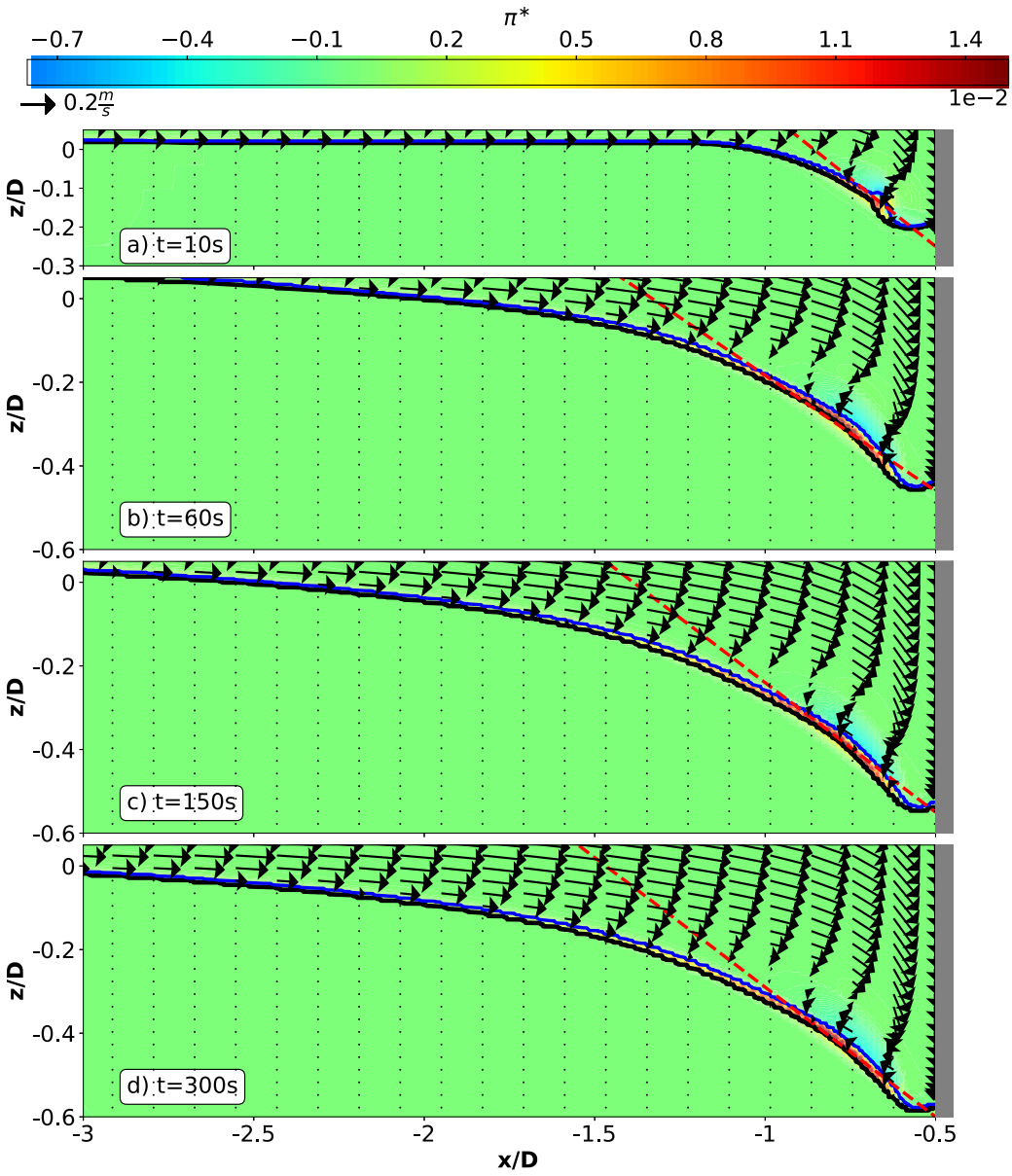

FIGURE 5.22: Flow velocity vectors and sediments flux in the plane of symmetry (y=0) at t=10s (a), t=60s (b), t=150s (c) and t=300s (d). The red dashed line represents the avalanche angle of 32 °. The black and blue lines represent the sediments iso-concentration ϕ=0.57 and ϕ=0.08.

The observations presented in the plane of symmetry upstream of the pile are in good agreement with the two-dimensional depth-integrated ones made previously around the cylinder. The importance of the slope on the sediments transport and the avalanche phenomenon is found again. In the plane of symmetry the sediments flux is mainly oriented toward the cylinder. However, in order to be carried out of the scour hole, sediments are transported in the HSV legs around the cylinder as shown in figures 5.18, 5.19 and 5.20.

The bimodal oscillation of the HSV observed numerically in a scour hole around a circular cylinder (*Kirkil et al.*, 2008; *Link et al.*, 2012) is not observed here. Again is probably due to the URANS approach for turbulence modeling used in the present work (see discussion in section 5.3.2, subsection b)). As the turbulence averaged two-phase flow model is able to reproduce fairly well the upstream scour erosion at short time-scales ($t < 300s$) the bimodal oscillation does not seem important for the scour process at the earliest stages. However, it is possible that at latter stages ($t > 300s$) the discrepancies observed in the development of the upstream scour mark are due to the bimodal oscillation of the HSV.

c) Mesh refinement effects on the scour predictions

In section 5.3.1 it has been shown that the horizontal mesh resolution has an impact on the lee wake vortices in the Rigid-Bed case (see figure 5.9). It has also an impact on the bed shear stress amplification associated with these eddies. The mesh refinement effects on the scour predictions is investigated in the present section. To this end, two different horizontal domain dimensions with different meshes are used leading to the two new Live-Bed configurations summarized in table 5.5, MeshLBB and MeshLBC. For reading convenience, the MeshLBA definition is reminded in table 5.5. MeshLBB has a finer horizontal resolution compared with MeshLBA and 512 cells are used around the cylinder perimeter. The water layer horizontal resolution close to the cylinder is exactly the one detailed in MeshB (see table 5.2). However, in order to avoid a too important computational cost, the horizontal domain dimensions have been reduced from Lx=13D and Ly=8D to Lx=8D and Ly=6D for this geometry. MeshLBC has the horizontal dimensions of MeshLBB and the resolution of MeshLBA. It is used here, to ensure that the horizontal domain change between MeshILB and MeshIILB has no impact on the erosion results. The vertical number of cells in the water layer is lower in MeshLBB , however, the original interface resolution is kept the same for all geometries. Again, geometry MeshLBC is here to ensure that these changes have no effects on the scour erosion predictions.

The computations launched with the new configurations are named LB4 (on MeshLBB) and LB5 (on MeshLBC) and are summarized in table 5.6. In order to determine the influence of the horizontal mesh resolution on the results, a comparison between simulations LB1, LB4 and LB5 is proposed in the following.

Figure 5.23 shows the comparison in terms of erosion between LB1 and LB4 for t=10s and t=60s. The major bathymetric bed features mentioned for LB1 are also recovered with LB4 : (i) a semi-circular shaped scour mark is predicted at the upstream side of the pile (ii) sediments eroded from the scour mark first accumulate downstream the pile (iii) at later stages a scour mark is predicted at the downstream side. However, several differences are found depending on the horizontal resolution of the mesh. First, in LB4, the maximum erosion depth as well as the erosion extension linked to the HSV upstream and around the cylinder are more important. Furthermore, the sediments accumulation bars extending in a oblique way downstream of the

Tableau 5.5: Geometry and meshes used to study the mesh refinement effects.

Characteristics	MeshLBA	MeshLBB	MeshLBC
Lx	13D	8D	8D
Ly	8D	6D	6D
Total number of cells	5 308 368	15 872 008	3 1731 28
Number of cells around the cylinder perimeter	256	512	256
Number of cells across the water depth	64	32	32
Number of cells across the sediments	200	200	200
Number of cells across the scour Pit	100	100	100
Initial interface cell height (m)	1.5×10^{-4}	1.5×10^{-4}	1.5×10^{-4}

Tableau 5.6: Summary of the different simulations undertaken for the Live-Bed configuration

Characteristics	LB1	LB4	LB5
Geometry	MeshLBA	MeshLBB	MeshLBC
Turbulence model	k-ω 2006	k-ω2006	k-ω2006
Final time (s)	600	60	60
Schmidt number	Local	Local	Local
Vortex shedding	Yes	Yes	Yes

cylinder are not found with LB4 at t=60s. For the same dynamical time, the erosion seems also more intense but less extended downstream with LB4. In the end, a better visual agreement with the bed morphology reported in figure 33 of *Roulund et al.* (2005) is obtained with LB4.

As shown in figure 5.23, the main differences in term of bed erosion obtained between simulations LB1 and LB4 are located downstream of the pile. This seems to be a direct consequence of the vortex-shedding resolution. In LB4, the eddies are more accurately resolved, more energetic, generating a higher bed shear stress and thus a deeper erosion downstream of the pile. The erosion in the HSV, upstream and around the pile is also more important in the LB4 simulation.

In order to reduce computational time, LB4 has been launched on a reduced domain compared to LB1 (see table 5.6). The confinement effect can be estimated through the results of simulation LB5. The latter has been launched on a reduced domain identical to LB4 but with an horizontal resolution identical to LB1. Figure 5.24 shows the time evolution of the dimensionless scour depth at the upstream (top panel) and at the downstream (bottom panel) edge of pile, up to 100s. The two-phase flow numerical results are compared with experimental data (red dots) and numerical results (green curve) from *Roulund et al.* (2005).

Concerning the upstream edge of the pile (top panel of figure 5.24), the results clearly show that the dimensionless scour depth is more important with LB4 than with LB1. At t=60s, $\delta_s^{max}/D = 0.58$ with LB4, whereas simulation LB1 predicts a result of $\delta_s^{max}/D = 0.4$. The upstream erosion dynamics is slightly overestimated with the LB4 but the results remain in good agreement with the experiments of *Roulund et al.* (2005). This intense early dynamics might be

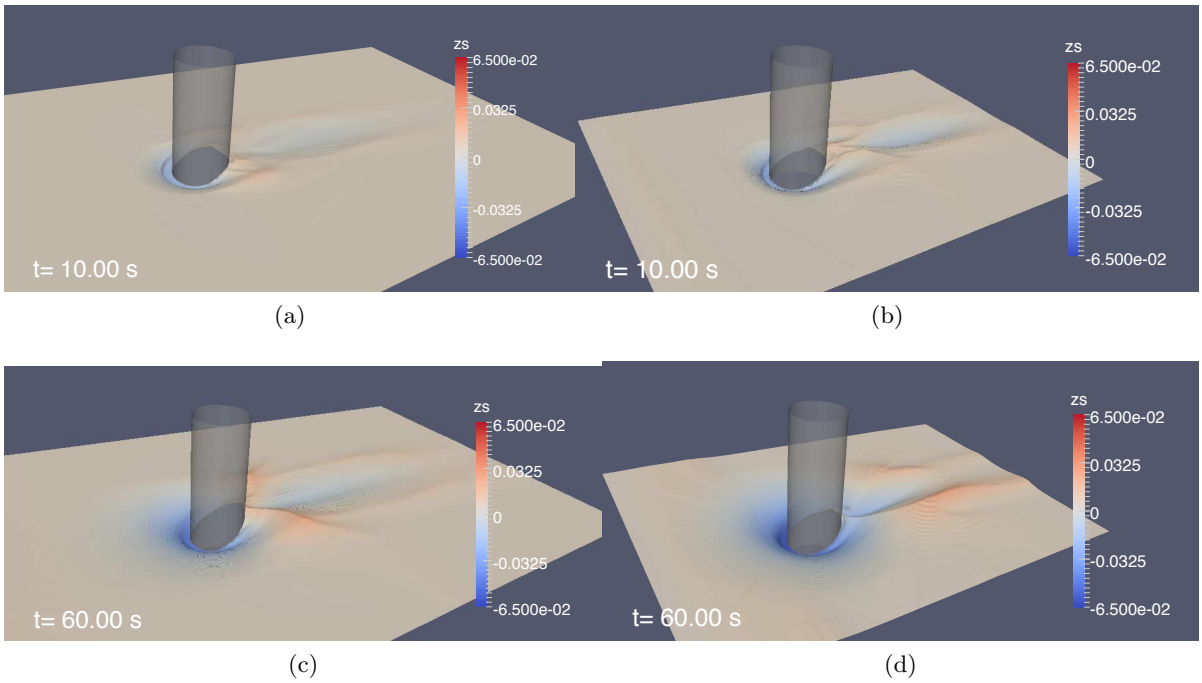

FIGURE 5.23: Bed elevation after 10s and 60s of dynamics for simulations LB1 (a), (c) and LB4 (b) and (d).

due to the initial shock. Indeed, at t=0s, the 1D uniform vertical profiles are imposed all over the domain.
The overall erosion dynamic tendency is similar between LB4 and LB1. Simulation LB4 erosion rates will also probably saturate more rapidly than what is predicted in (*Roulund et al.*, 2005). This underestimation of the erosion for the long times can be due to the turbulence model. Indeed, other work undertaken with sedFoam seems to show that the present two-phase version of the k-ω2006 is qualitatively able to reproduce the scour phenomenon but underestimates it's intensity when applied on a pipeline two-dimensional configuration (*Mathieu et al.*, In prep.). Similar phenomenon has also been observed in a recent study of *Quezada et al.* (2018), where, for the scour around a cylindrical pile, the erosion obtained with a k-ω SST is less than with a k-ε turbulence model using the "classical" computational fluid dynamics tool REEF3D (*Bihs*, 2011). For the upstream scour mark, the model results are almost not sensitive to the confinement as simulation LB5 predicts an dimensionless erosion very similar to the one obtained with LB1.

At the downstream side (bottom panel of figure 5.24) all the simulations show a temporal fluctuating behavior of the scour depth. Again, the erosion predicted with LB4 is more important than with LB1. The confinement seems to play a role between t=0s and t=20s only, where the sediments erosion rate is different for LB4 and LB5. After t=20s, the erosion results obtained with LB1 and LB5 are similar and are not affected by the domain size.

Horizontally refining the mesh seems to predict a scour hole shape in better agreement with the literature results. However, precautions have to be taken with the quantivative difference

obtained in figure 5.24. Indeed, the mesh used in simulation LB4 is so refined that the question of the URANS turbulence approach validity can be asked and turbulence-resolving two-phase flow simulations (*Cheng et al.*, 2018b) should be performed on this configuration.

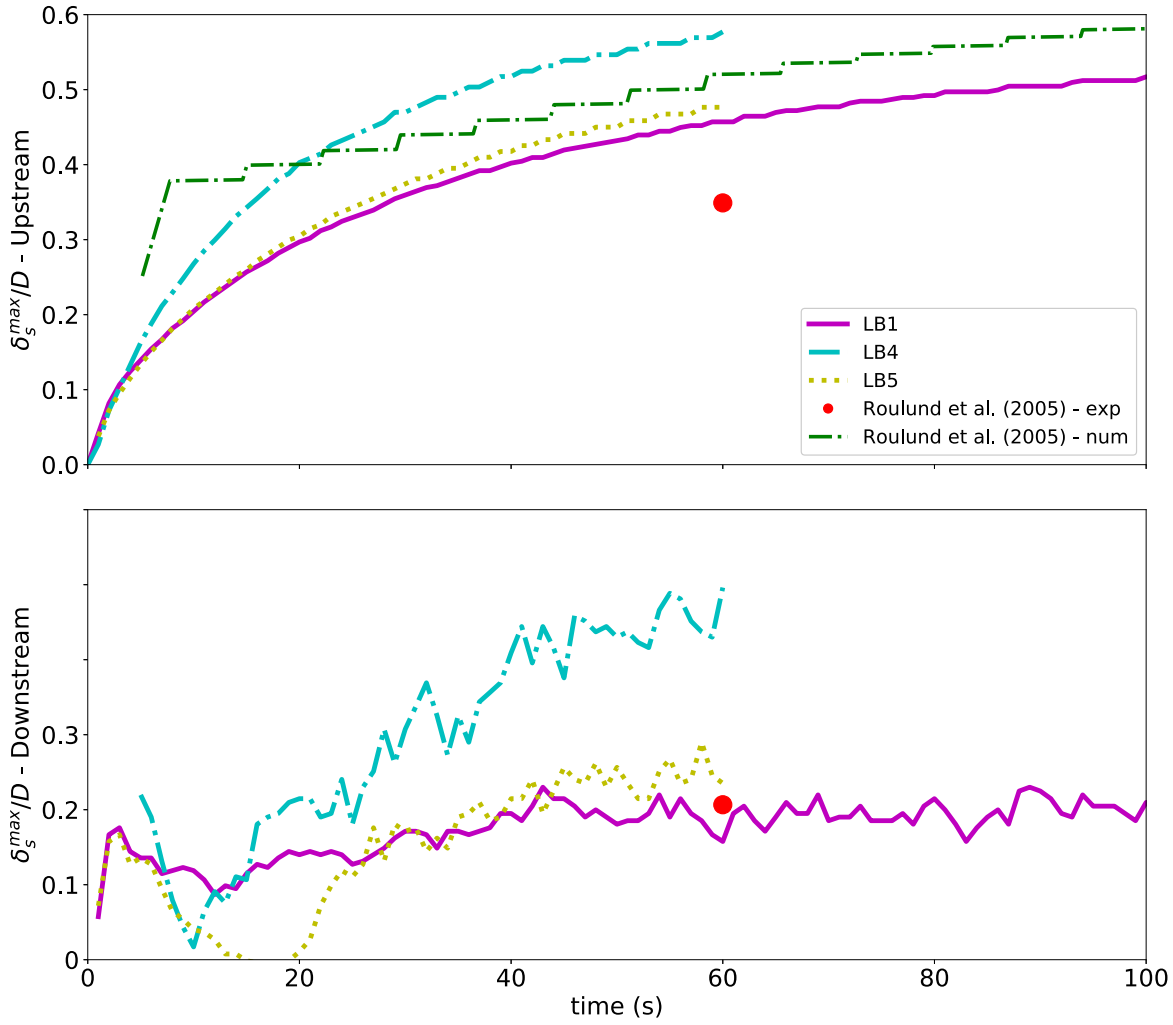

FIGURE 5.24: Time evolution of the dimensionless scour depth at the upstream (top panel) and at the downstream (bottom panel) edge of pile. Zoom between t=0s and t=100s.

5.5 Conclusion

In the present chapter three-dimensional two-phase flow simulations of the flow around a vertical cylinder mounted on a seabed have been presented, discussed and analyzed. The results obtained over a rough rigid-bed without sediments show that the swirl structures responsible for scour, the HSV and the vortex-shedding in the lee of the cylinder are correctly reproduced with the k-ω2006 turbulence model. Moreover, the bed shear stress amplification, the size of the recirculation zone downstream of the pile, the Strouhal number, the delay that can be observed between vortices shed near the bottom and in the rest of the water column are in good agreement with the former studies of *Roulund et al.* (2005) and *Baykal et al.* (2015).

In a second part, two-phase flow simulations of the scour around a cylindrical pile have been carried out in the live-bed configuration of *Roulund et al.* (2005). The longest simulation has been conducted over 10 minutes of physical time, corresponding to 60% of the equilibrium scour depth for the studied configuration. The two-phase flow model is able to reproduce most of the bed features shown in *Roulund et al.* (2005). The time variation of the erosion depths are in good agreement with *Roulund et al.* (2005) experimental data up to 300s of dynamics. At longer times ($300s < t < 600s$), the erosion rate is strongly decreasing and the two-phase flow model is underestimating the maximum scour depth upstream and downstream of the pile compared with *Roulund et al.* (2005) experimental results. Nevertheless, the results provide the proof of concept that the two-phase flow approach can be used to study complex 3D flow configurations.

Important efforts have been devoted to establish the methodology to analyze the results, in particular the determination methods of the bed shear stress in non uniform two-phase flow computation have carefully been investigated. The results show that using the mixture shear stress at the top of the bedload transport layer ($\phi = 0.08$) present the best compromise between a good agreement with the Rigid-Bed case and the noise reduction in the bed shear stress results.
The analysis of the numerical results allows to get more insight into the fine scale sediments transport mechanisms involved in the scour process. In particular, the relationship between the local bed shear stress, the sediments flux and the local bed slope has been further investigated. Under uniform flow conditions the sediments transport is driven by the local bed shear stress. Around the pile, due to the flow non-uniformity, the driving mechanism of sediments transport are far more complex. The sediments excavated upstream of the pile by the HSV is transported by bedload and suspension downstream via the HSV legs around the cylinder. Just downstream of the pile, in the recirculation area, the sediments transport results from a combined action of the suspended load advection of the sediments excavated upstream of the pile and of the local erosion by the vortex shedding. These results highlight that the sediments transport around the pile is not just the result of the local bed shear stress and confirm the importance of accounting for suspended load as shown by *Baykal et al.* (2015).
Furthermore in the upstream scour hole, the slope and the HSV modifies the sediments transport. In the scour hole the sediments flux results from a competition between the bed shear stress and the gravity. Avalanches are continuously occurring and affect the sediments transport.
Around the pile, the flux is deviating from the uniform flow conditions upstream, around and downstream of the pile. In this region the sediments flux estimated from "classical" formula, based on a local relation between the bed shear stress and the sediments flux, is underestimating the sediments transport.

Finally, the numerical results show a grid sensitivity of the morphological predictions, in both, the upstream scour hole and the lee of the cylinder, that could be related to small-scale resolved vortical structures. This highlights the need for two-phase flow Large Eddy Simulations on this configuration in the future.

Chapitre 6

Conclusions et perspectives

In the present thesis, two numerical models have been developed and used to investigate the multi-scale interactions between an offshore wind turbine and the local ocean and sediment dynamics. First, the interactions between an offshore wind turbine wake and the local oceanic and sedimentary dynamics have been investigated using the classical paradigm of sediment transport modeling. Then, an Eulerian-Eulerian two-phase flow model for sediment transport, sedFoam is used to study the scour around a vertical cylinder in a steady flow. The main results are summarized here after and the perspectives of this work are drawn.

6.1 Conclusion

In the first part my Thesis, I have developed an idealized two-dimensional numerical model to study the impact of an offshore wind turbine wake on the ocean and sediment dynamics. The main conclusions of this work can be summarized as follow :

- The turbine wake has an impact on the ocean dynamics as it impacts the ocean surface and can generate instabilities and vortex streets. The size and the spacing between these vortices are controlled by the wake stability parameter $S = C_D D/H$. When S is decreased, large scale instabilities are more easily generated, leading to a domain wide turbulence state in the ocean. Furthermore, the results have also highlighted the important role of the confinement (the spacing of wind turbines in a farm) in the generation of instabilities.
- The oceanic turbulence observed with eddy-resolving time dependent simulations can be parametrized using a simple zero equation RANS model : using a constant Boussinesq eddy viscosity in the shallow water equations, or using a mixing length approach. A phenomenological law for the non−dimensional eddy viscosity as a function of the S parameter has been proposed. This RANS parametrization of the turbulent oceanic dynamics allows for upscaling simulations (in a regional model, for example).
- The turbine wake has also an impact on the seabed dynamics : it has been shown that the non-uniformity of the oceanic velocity field induced by the wake presence is observed in the local bottom shear stress responsible for sand erosion and deposition. As the vortices strongly affect the seabed morphodynamics, for localized and domain wide turbulence, the wake imprint on the seabed tends to be reduced by large scale vortices and oscillating local velocity which transports sediment back and forth and may increase the turbidity.

- Taking into account the ocean velocity in the wind forcing leads to a decrease of the power lost through friction by the atmosphere, through reducing the relative velocity between the two layers. This result seems to show that the ocean dynamics is important for the energy budget around wind turbines. The results also show that even if the turbulence strongly influences both, ocean and seabed dynamics, its role is negligible in the air-sea energetic balance.

The results summarized above show that the atmospheric turbine wake has a limited impact on the seabed. The scour is most probably the main mechanism responsible of the turbid sediment wakes observed in several offshore wind farms (*Baeye and Fettweis*, 2015; *Vanhellemont and Ruddick*, 2014).

The second part of my PhD Thesis has been focused on the two-phase flow simulation of tri-dimensional scour around a cylindrical pile in a steady current. The main conclusions of this second part can be summarized as follow :

- Several contributions are made to the Eulerian-Eulerian two-phase flow model for sediment transport, sedFoam. In particular, the two-phase flow version of the k-ω2006 turbulence model, the ω rough wall functions from *Wilcox* (2006) and *Roulund et al.* (2005), the local Schmidt number model and the C_t model adding a Reynolds shear stress like contribution for the granular stress are original contributions to the model originally presented in *Chauchat et al.* (2017).
- sedFoam has been tested on several one and two-dimensional test cases. The application of this model to turbulent boundary layer flows without sediments allows to validate the turbulent model and the rough wall-functions recently implemented. The computations on a sheet-flow case show a good agreement for velocity, concentration and shear stress profiles when compared with *Revil-Baudard et al.* (2015) experimental data. The results also show that the model does not seems to be very sensitive to the different turbulence closures. However, more sediment is transported by suspension in the water column when using the Kinetic Theory (KT) than when using the $\mu(I)$ rheology. This could be explained by the fact that, contrary to the KT, the grains turbulent agitation (responsible for grains momentum mixing) is not originally present in the granular rheology. Activating the C_t model increases the sediment suspension predicted with the $\mu(I)$ rheology and enhances the agreement between the KT and the $\mu(I)$ rheology for the suspended sediments concentration. From this sheet-flow test case a set of rheological and turbulent tuning coefficients is validated. This set is then used on other flow configurations, such as the bedload case of *Roulund et al.* (2005).
- State of the art formula for the dimensionless sediments transport rate and the dimensionless transport layer thickness as a function of the Shields number are accurately predicted using the two-phase flow approach over a wide range of Shields numbers, particles types and diameters. A careful attention has been payed to low Shields numbers, where the continuous approach should reach its limit. Interestingly, the results presented here are in very good agreement with the literature for a Shields number down to 0.1. These results further demonstrate the capabilities of the two-phase flow model sedFoam to deal with unidirectional flows from bedload to sheet flow.
- The application on scour downstream of an apron illustrates the multi-dimensional capabilities of the solver. The scaling laws proposed in the earlier work of *Breusers* (1967) are recovered by the model even if the results have been found to be sensitive to the modeling choices on the granular interactions and turbulence models.

- The three-dimensional simulations around a vertical cylinder have been first undertaken over a rough Rigid-Bed. The results obtained on this configuration without sediments show that the swirl structures responsible for scouring, namely the Horse Shoe Vortex (HSV) and the vortex-shedding in the lee of the cylinder are correctly reproduced with the k-ω2006 turbulence averaged model. Moreover, the bed shear stress amplification location and intensity, the size of recirculation area downstream of the pile, the Strouhal number, the delay that can be observed between vortices shed near the bottom and in the rest of the water column are in good agreement with the results shown in the former studies of *Roulund et al.* (2005) and *Baykal et al.* (2015).
- Two-phase flow simulations of the scour around a cylindrical pile have been carried out in the live-bed configuration of *Roulund et al.* (2005). The longest simulation has been conducted over 10 minutes of physical dynamics, corresponding to 60% of the equilibrium scour depth for the studied configuration. The two-phase flow model is able to reproduce most of the bathymetric bed features shown in *Roulund et al.* (2005). The temporal evolution of the erosion depth is in good agreement with *Roulund et al.* (2005) experimental data up to 300s of dynamics. After this time ($300s < t < 600s$), the erosion rate drastically slowsdown and the two-phase flow model underestimates the scour depth compared with *Roulund et al.* (2005). This assessment can be made for the erosion at both sides of the pile, upstream and downstream. This is probably linked to the URANS turbulence model developed in the present work. The latter is able to reproduce qualitatively the scour phenomenon but seems to under-predicts the erosion for the long times.
  Nevertheless, the results provide the first proof of concept that the two-phase flow approach can be used to study complex flow configurations.
- The methodology to determine the bed shear stress in non uniform flow configuration have been carefully investigated. The results show that using the mixture shear stress at the top of the bedload transport layer ($\phi = 0.08$) represent the best compromise between a good agreement with the Rigid-Bed case and the noise reduction in the bed shear stress results.
- Under uniform flow conditions the sediment transport is driven by the local bed shear stress. Around the pile, due to the flow non-uniformity, the driving mechanism of sediment transport are far more complex than a simple relation to the bed shear stress. In several locations, the sediment transport is not or at least not only driven by the local bed shear stress, resulting in sediment flux underestimation by classical empirical formula. These locations have been clearly identified : along the scour hole slope, in the HSV legs and downstream in the wake of the pile.
  - ⋆ The upstream part of the scour hole presents three distinct slopes. This is in agreement with several literature observations (*Dargahi*, 1990; *Link et al.*, 2012). In this region, the sediment flux result from a competition between the bed shear stress and the gravity. The first slope increases smoothly from the beginning of the scour hole to the core of the HSV position. When $\beta > 20°$, the flow conditions are similar to debris-flows, the shear stress and the gravity are acting in the same direction, enhancing the sediment transport toward the cylinder. The first slope variation is located under the HSV core and its position ($R_u/D \approx 0.7$) remains constant in time as no HSV bimodal oscillation can be captured with the URANS turbulence model. Below the core of the HSV, the slope becomes steeper than the angle of repose meanwhile the velocity vectors and thus the fluid bed shear stress are negative. The gravity and the bed shear stress are counter acting each other but gravity dominates as the sediment flux in the

near bed region remains positive. The avalanche generates an important bedload flux close to the bed interface. This flux is oriented toward the cylinder whereas, just above, a slight suspended load goes up the slope driven by the HSV. This particular sediment transport type can not be found with the classical models as suspended load and bedload are oriented in opposit directions. The second slope variation is located close to the cylinder, around $R_u/D \approx 0.55$, the slope is decreasing and the sediment bed becomes almost flat in front of the cylinder.

  - ⋆ The maximum of the sediment flux is located in the two branches around the cylinder, indicating that there is an important transverse flux driven by the HSV legs around the cylinder. Within these branches, the sediment excavated upstream of the pile by the HSV is transported downstream by both bedload and suspended load.
  - ⋆ Just downstream of the pile, in the recirculation area, the sediment transport results from a combined action of the upstream suspended load advected by the flow and of the local erosion by the vortex shedding.

- These results highlights that the sediment transport around the pile is not just the result of the local bed shear stress and confirm the importance of accounting for suspended load as shown by *Baykal et al.* (2015) but also of the avalanching process.
- The numerical results show a grid sensitivity of the morphological predictions. However, using a too refined grid rises the question of the URANS turbulence approach validity for such fine meshes. Therefore, turbulence resolving two-phase flow simulations (*Cheng et al.*, 2018b) should be performed on this configuration.

6.2 Perspectives

Concerning the interactions between an offshore wind turbine wake and the local ocean and sediment dynamics, the results summarized in section 6.1 can be extend and improved in several ways :

- The proposed model is extremely idealized, more physical processes could be considered such as tidal currents and time changes in the atmospheric forcing to simulate a storm event for instance. Adding a large scale current could also allow to investigate situations where the winds and the oceanic currents are not spatially aligned.
- The present ocean-sediment model could also be coupled with an atmospheric model. As the atmospheric dynamics is not resolved here, the oceanic turbulence has a no retro-action on the atmosphere. Resolving the atmospheric dynamics may allow to characterize a potential retro-action of the oceanic perturbations on the atmospheric flow. It could also enhance the understanding of the interactions of a wind turbine with the environment.
- For the morphodynamic module, only bedload is considered. The module can be enhanced by including the suspended load sediment transport. This would probably allow to estimate the amount of sediment entrained in suspension in the water layer and to determinate if the increase of turbidity is important enough to affect marine life.
- The parametrization proposed is promising and could be implemented in larger-scale models even if the determination of the dependence on the confinement deserves further investigations.

Concerning the two-phase flow simulation of scour, the main perspectives are :

- To improve the model validation on the scour downstream of an apron case as well as the model sensitivity to flow turbulence and rheological parameters. This requires more detailed experimental data. A set of data has recently been recorded at the LEGI laboratory and is currently being post-processed.
- The two-phase version of the k-ω 2006 needs improvement in order to quantitatively predict the scour phenomenon, especially for the long time. The model needs to be tested on scour configuration where detailed bed interface data are available. The two-dimensional configuration of scour under a pipeline with a steady current of *Mao* (1986) has been investigated during A. Mathieu MsC Thesis (*Mathieu*, 2017). Two-phase numerical simulation have already been performed with a k-ε turbulence model on this configuration by *Lee et al.* (2016). The first results of our work shows that with the k-ε model, the erosion under the cylinder is in good agreement with *Lee et al.* (2016) numerical results and *Mao* (1986) experimental results. However, the vortex-shedding in not predicted, resulting in sediment accumulation downstream of the pipeline that is not observed in *Mao* (1986) experiments. Using the k-ω 2006 model, the vortex-shedding is well captured and washout the sediment accumulation downstream of the cylinder (see figure 6.1), but the erosion under the pipeline is underestimated. The k-ω 2006 is currently rewritten to overcome these discrepancies.

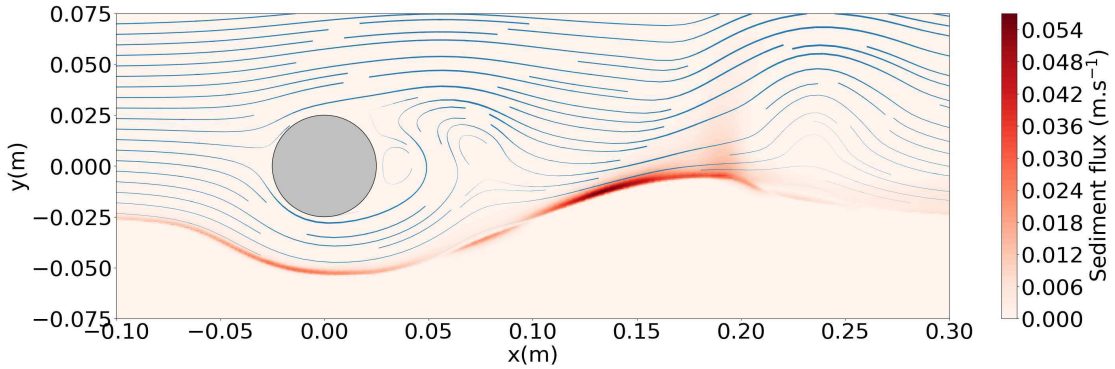

FIGURE 6.1: Fluid flow streamlines and sediment transport rate for the scour under a pipeline. The turbulence used here is the k-ω2006 presented in this manuscript.

- In the vertical pile configuration, the deviation of the sediment flux predictions around the cylinder from "classical" estimations has only be undertaken in a qualitative way. A more quantitative estimation of this deviation is necessary to eventually improve the classical models by including the parametrization of the small-scale phenomenon. The possible ways to quantify this deviation are currently investigated.
- The two-phase flow sediments flux predictions could be compared to other "classical" sediments transport models, in particular by accounting the suspended load.
- The scour downstream of the pile requires further investigation, in particular, the bed morphology should be compared with experiments to better test the models capabilities to reproduce the interaction between lee-wake vortices and sediment transport. It is likely that these interactions are not very well reproduced by the turbulence averaged two-phase flow

model. In future research, turbulence resolving two-phase flow simulations (*Cheng et al.*, 2018b) should be performed on this configuration to better understand and parameterize these processes. This task is currently undertaken, the first simulations on a Rigid-Bed case show that the bi-modal oscillation of the HSV seems recovered. Computations with sediments are running but stability issues have been experienced and have to be overcome.

- Using the LES approach for two-phase flow simulations may also allow to reproduce the ripples presence upstream of the pile that have been observed in *Roulund et al.* (2005) and *Baykal et al.* (2015) but not found with the current URANS two-phase flow model.
- The effect of pressure gradient around the cylinder have to be investigated. In order to characterize the effect of the horizontal pressure gradient, the Sleath number (*Sleath*, 1999) $-\partial_x p^f/(\Delta\rho g)$ has been investigated at the interface around the cylinder location. The Sleath number is higher at the beginning (30s) when the sediment erosion dynamics is more intense. The values of Sleath number encountered in front of the cylinder indicate that horizontal pressure gradient may play a role in the sediment transport dynamics. A qualitative analysis, based on *Maurin et al.* (2017) work for uniform flow is currently undertaken in order to see the importance of this pressure gradient with respect to the fluid bed shear stress and the bed slope in sediment transport.
- Once the discrepancies in term of scour erosion corrected tridimensional scour simulations should be undertaken up to the equilibrium. As the computational time for two-phase flow simulations of scour is important, this could not be achieved on *Roulund et al.* (2005) configuration. In order to reach the equilibrium more rapidly, one of the perspective could be to model scour with lightweight Polystyrene sediments. Scour experiments with such sediments have been realized by *Ettmer et al.* (2015), showing that in the Live-Bed configuration, the scour rapidly reaches equilibrium in the bed of polystyrene pellets.
- The results presented in Chapter 4 suggest that the two-phase flow model approach is able to predict the formation of ripples. This subject is still a matter of debate in the scientific community and two-phase flow simulations could be an ideal framework to study the formation of bedforms and their equilibrium characteristics.

As a general conclusion to the perspectives, my PhD work provides the first proof of concept that a two-phase flow model can be used to simulate complex three-dimensional flow configurations. The main perspectives are linked to the three-dimensional scour configuration that is mentioned above. More generally, the two-phase flow approach is suitable to address numerous physical problems for which the classical sediment transport approach is not working very well. The development of the numerical model as an open-source software will hopefully facilitate the growth of the scientific community working on this topic and contribute to address some of the perspectives mentioned above.

Bibliographie

Abrahams, M. V., and M. G. Kattenfeld, The role of turbidity as a constraint on predator-prey interactions in aquatic environments, *Behavioral Ecology and Sociobiology*, *40*(3), 169–174, 1997.

Amoudry, L., and P.-F. Liu, Two-dimensional, two-phase granular sediment transport model with applications to scouring downstream of an apron, *Coastal Engineering*, *56*(7), 693–702, 2009.

Amoudry, L., T.-J. Hsu, and P.-F. Liu, Two-phase model for sand transport in sheet flow regime, *Journal of Geophysical Research : Oceans*, *113*(C3), 2008.

Amoudry, L. O., Extension of k-ω turbulence closure to two-phase sediment transport modelling : Application to oscillatory sheet flows, *Advances in Water Resources*, *72*, 110–121, 2014.

Amoudry, L. O., and A. J. Souza, Deterministic coastal morphological and sediment transport modeling : A review and discussion, *Reviews of Geophysics*, *49*(2), 2011.

Anderson, C. D., and S. P. Lynch, Time-resolved stereo piv measurements of the horseshoe vortex system at multiple locations in a low-aspect-ratio pin–fin array, *Experiments in Fluids*, *57*(1), 5, 2016.

Archer, C. L., et al., Meteorology for coastal/offshore wind energy in the united states : recommendations and research needs for the next 10 years, *Bulletin of the American Meteorological Society*, *95*(4), 515–519, 2014.

Aussillous, P., J. Chauchat, M. Pailha, M. Médale, and E. Guazzelli, Investigation of the mobile granular layer in bedload transport by laminar shearing flows, *Journal of Fluid Mechanics*, *736*, 594–615, 2013.

Baeye, M., and M. Fettweis, In situ observations of suspended particulate matter plumes at an offshore wind farm, southern north sea, *Geo-Marine Letters*, *35*(4), 247–255, 2015.

Bagnold, R. A., Experiments on a gravity-free dispersion of large solid spheres in a newtonian fluid under shear, *Phil. Trans. R. Soc. Lond.*, *225*, 49–63, 1954.

Bakhtyar, R., A. Yeganeh-Bakhtiary, D. A. Barry, and A. Ghaheri, Two-phase hydrodynamic and sediment transport modeling of wave-generated sheet flow, *Advances in Water Resources*, *32*(8), 1267–1283, 2009.

Baykal, C., B. M. Sumer, D. R. Fuhrman, N. G. Jacobsen, and J. Fredsøe, Numerical investigation of flow and scour around a vertical circular cylinder, *Philosophical Transactions of the Royal Society of London A : Mathematical, Physical and Engineering Sciences*, *373*(2033), 20140,104, 2015.

Benavides, A., and B. van Wachem, Numerical simulation and validation of dilute turbulent gas–particle flow with inelastic collisions and turbulence modulation, *Powder Technology*, *182*(2), 294–306, 2008.

Berzi, D., Analytical solution of collisional sheet flows, *Journal of Hydraulic Engineering*, *137*(10), 1200–1207, 2011.

Berzi, D., and L. Fraccarollo, Inclined, collisional sediment transport, *Physics of Fluids*, *25*(10), 106,601, 2013.

Berzi, D., and L. Fraccarollo, Turbulence locality and granularlike fluid shear viscosity in collisional suspensions, *Physical review letters*, *115*(19), 194,501, 2015.

Berzi, D., and L. Fraccarollo, Intense sediment transport : Collisional to turbulent suspension, *Physics of Fluids*, *28*(2), 023,302, 2016.

Bihs, H., Three-dimensional numerical modeling of local scouring in open channel flow, 2011.

Boyer, F. m. c., E. Guazzelli, and O. Pouliquen, Unifying suspension and granular rheology, *Phys. Rev. Lett.*, *107*, 188,301, doi :10.1103/PhysRevLett.107.188301, 2011.

Bradshaw, P., D. Ferriss, and N. Atwell, Calculation of boundary-layer development using the turbulent energy equation, *Journal of Fluid Mechanics*, *28*(3), 593–616, 1967.

Breusers, H., Time scale of two-dimensional local scour, p. 275âĂŞ282, 1967.

Breusers, H., and A. Raudkivi, *Scouring*, Balkema Rotterdam, 1991.

Breusers, H., G. Nicollet, and H. Shen, Local scour around cylindrical piers, *Journal of Hydraulic Research*, *15*(3), 211–252, 1977.

Briaud, J.-L., F. C. Ting, H. Chen, R. Gudavalli, S. Perugu, and G. Wei, Sricos : Prediction of scour rate in cohesive soils at bridge piers, *Journal of Geotechnical and Geoenvironmental Engineering*, *125*(4), 237–246, 1999.

Broström, G., On the influence of large wind farms on the upper ocean circulation, *Journal of Marine Systems*, *74*(1), 585âĂŞ591, 2008.

Capecelatro, J., and O. Desjardins, An euler–lagrange strategy for simulating particle-laden flows, *Journal of Computational Physics*, *238*, 1–31, 2013.

Carnahan, N. F., and K. E. Starling, Equation of state for nonattracting rigid spheres, *The Journal of Chemical Physics*, *51*(2), 635–636, 1969.

Chabert, J., and P. Engeldinger, Etude des affouillements autour des piles des ponts, *Laboratoire National dâĂŹHydraulique, Chatou, France (in French)*, *118*, 1956.

Chane, B., et al., Two dimensional local scour in erodible bed downstream of solid aprons, in *Two dimensional local scour in erodible bed downstream of solid aprons*, Tampere University of Technology, 1984.

Chapman, S., and T. G. Cowling, *The mathematical theory of non-uniform gases*, Cambridge, 1970.

Chauchat, J., Contribution à la modélisation diphasique du transport sédimentaire en milieux côtiers et estuariens, Ph.D. thesis, Université de Caen, 2007.

Chauchat, J., A comprehensive two-phase flow model for unidirectional sheet-flows, *Journal of Hydraulic Research*, pp. 1–14, 2018.

Chauchat, J., and S. Guillou, On turbulence closures for two-phase sediment-laden flow models, *Journal of Geophysical Research : Oceans*, *113*(C11), 2008.

Chauchat, J., and M. Médale, A three-dimensional numerical model for dense granular flows based on the rheology, *Journal of Computational Physics*, *256*(0), 696 – 712, doi :http://dx.doi.org/10.1016/j.jcp.2013.09.004, 2014.

Chauchat, J., Z. Cheng, T. Nagel, C. Bonamy, and T.-J. Hsu, Sedfoam-2.0 : a 3-d two-phase flow numerical model for sediment transport, *Geoscientific Model Development*, *10*(12), 4367, 2017.

Chen, C., and P. Wood, A turbulence closure model for dilute gas-particle flows, *The canadian journal of chemical engineering*, *63*(3), 349–360, 1985.

Chen, D., and G. H. Jirka, Experimental study of plane turbulent wakes in a shallow water layer, *Fluid dynamics research*, *16*(1), 11, 1995.

Chen, D., and G. H. Jirka, Absolute and convective instabilities of plane turbulent wakes in a shallow water layer, *Journal of Fluid Mechanics*, *338*, 157–172, 1997.

Cheng, Z., and T.-J. Hsu, A multi-dimensional two-phase eulerian model for sediment transport-twophaseeulersedfoam (version 1.0), *Tech. rep.*, Technical Report No. CACR-14-08, University of Delaware, 2014.

Cheng, Z., T.-J. Hsu, and J. Calantoni, Sedfoam : A multi-dimensional eulerian two-phase model for sediment transport and its application to momentary bed failure, *Coastal Engineering*, *119*, 32–50, 2017.

Cheng, Z., J. Chauchat, T.-J. Hsu, and J. Calantoni, Eddy interaction model for turbulent suspension in reynolds-averaged euler–lagrange simulations of steady sheet flow, *Advances in Water Resources*, *111*, 435–451, 2018a.

Cheng, Z., T.-J. Hsu, and J. Chauchat, An eulerian two-phase model for steady sheet flow using large-eddy simulation methodology, *Advances in Water Resources*, *111*, 205–223, 2018b.

Coleman, N. L., Flume studies of the sediment transfer coefficient, *Water Resources Research*, *6*(3), 801–809, 1970.

Dai, K., A. Bergot, C. Liang, W.-N. Xiang, and Z. Huang, Environmental issues associated with wind energy–a review, *Renewable Energy*, *75*, 911–921, 2015.

Danon, H., M. Wolfshtein, and G. Hetsroni, Numerical calculations of two-phase turbulent round jet, *International Journal of Multiphase Flow*, *3*(3), 223–234, 1977.

Dargahi, B., Local scouring around bridge piersâĂŤa review of practice and theory, *Bull*, *114*, 1982.

Dargahi, B., Controlling mechanism of local scouring, *Journal of Hydraulic Engineering*, *116*(10), 1197–1214, 1990.

de Saint-Venant, A. B., Théorie du mouvement non permanent des eaux, avec application aux crues des rivieres et a l'introduction des marées dans leurs lits, *Comptes Rendus des séances de l'Académie des Sciences*, *73*, 237–240, 1871.

De Vos, L., J. De Rouck, P. Troch, and P. Frigaard, Empirical design of scour protections around monopile foundations : Part 1 : Static approach, *Coastal Engineering*, *58*(6), 540–553, 2011.

De Vos, L., J. De Rouck, P. Troch, and P. Frigaard, Empirical design of scour protections around monopile foundations. part 2 : Dynamic approach, *Coastal Engineering*, *60*, 286–298, 2012.

Deshpande, S. S., L. Anumolu, and M. F. Trujillo, Evaluating the performance of the two-phase flow solver interfoam, *Computational science & discovery*, *5*(1), 014,016, 2012.

Deutsch, E., and O. Simonin, Large eddy simulation applied to the motion of particles in stationary homogeneous fluid turbulence, *Turbulence Modification in Multiphase Flows ASME-FED*, *110*, 35 – 42, 1991.

Devenport, W. J., and R. L. Simpson, Time-dependent and time-averaged turbulence structure near the nose of a wing-body junction, *Journal of Fluid Mechanics*, *210*, 23–55, 1990.

Dey, S., Threshold of sediment motion on combined transverse and longitudinal sloping beds, *Journal of Hydraulic Research*, *41*(4), 405–415, 2003.

Diab, R., O. Link, and U. Zanke, Geometry of developing and equilibrium scour holes at bridge piers in gravel, *Canadian Journal of Civil Engineering*, *37*(4), 544–552, 2010.

Ding, J., and D. Gidaspow, A bubbling fluidization model using kinetic theory of granular flow, *AIChE journal*, *36*(4), 523–538, 1990.

Dohmen-Janssen, C. M., W. N. Hassan, and J. S. Ribberink, Mobile-bed effects in oscillatory sheet flow, *Journal of Geophysical Research : Oceans*, *106*(C11), 27,103–27,115, 2001.

Dong, P., and K. Zhang, Two-phase flow modelling of sediment motions in oscillatory sheet flow, *Coastal Engineering*, *36*(2), 87–109, 1999.

Drew, D. A., Mathematical modelling of two-phase flow, *J. Appl. Mech.*, *15*, 261–291, 1983.

Driver, D., Reynolds shear stress measurements in a separated boundary layer flow, in *22nd Fluid Dynamics, Plasma Dynamics and Lasers Conference*, p. 1787, 1991.

Einstein, A., Eine neue bestimmung der molekuldimensionen, *An. Phys.*, *19*, 289 – 306, 1906.

Engelund, F., and J. Fredsøe, A sediment transport model for straight alluvial channels, *Hydrology Research*, *7*(5), 293–306, 1976.

Escauriaza, C., and F. Sotiropoulos, Lagrangian model of bed-load transport in turbulent junction flows, *Journal of Fluid Mechanics*, *666*, 36–76, 2011.

Ettmer, B., F. Orth, and O. Link, Live-bed scour at bridge piers in a lightweight polystyrene bed, *Journal of Hydraulic Engineering*, *141*(9), 04015,017, 2015.

EWEA, *Deep water, the next step for offshore wind energy*, 2013.

Exner, F. M., *Zur physik der dünen*, Hölder, 1920.

Exner, F. M., Uber die wechselwirkung zwischen wasser und geschiebe in flüssen, *Akad. Wiss. Wien Math. Naturwiss. Klasse*, *134*(2a), 165–204, 1925.

Forterre, Y., and O. Pouliquen, Flows of dense granular media, *Annual Review of Fluid Mechanics*, *40*, 1–24, doi :10.1146/annurev.fluid.40.111406.102142, 2008.

Foster, D., A. Bowen, R. A. Holman, and P. Natoo, Field evidence of pressure gradient induced incipient motion, *Journal of Geophysical Research : Oceans*, *111*(C5), 2006.

Fredsøe, J., and R. Deigaard, *Mechanics of coastal sediment transport*, vol. 3, World Scientific Publishing Co Inc, 1992.

Garcia, M. H., Sediment transport and morphodynamics, in *Sedimentation engineering : Processes, measurements, modeling, and practice*, pp. 21–163, 2008.

GDRmidi, On dense granular flows, *The European Physical Journal E*, *14*, 341–365, 2004.

Gidaspow, D., *Multiphase Flow and Fluidization*, Academic Press, San Diego, 1994.

Gove, B., R. Langston, A. McCluskie, J. Pullan, and I. Scrase, Wind farms and birds : an updated analysis of the effects of wind farms on birds, and best practice guidance on integrated planning and impact assessment, *RSPB/BirdLife in the UK. Technical document T-PVS/Inf*, *15*, 2013.

Graf, W. H., *Hydraulics of sediment transport*, Water Resources Publication, 1984.

Greenshields, C. J., Openfoam programmer's guide, *OpenFOAM Foundation Ltd, version 3.0.1*, 2015.

Greenshields, C. J., Openfoam user guide, *OpenFOAM Foundation Ltd, version 5.0*, 2017.

Hanes, D. M., and A. J. Bowen, A granular-fluid model for steady intense bed-load transport, *J. Geophys. Res.*, *Vol. 90*, 1985.

Harris, J., R. Whitehouse, and S. Moxon, *Scour and Erosion : Proceedings of the 8th International Conference on Scour and Erosion (Oxford, UK, 12-15 September 2016)*, CRC Press, 2016.

Hjorth, P., *Studies on the nature of local scour*, Inst. för Teknisk Vattenresurslära, Lunds Tekniska Högskola, Lunds Univ., 1975.

Hsu, T.-J., and D. M. Hanes, Effects of wave shape on sheet flow sediment transport, *Journal of Geophysical Research : Oceans*, *109*(C5), 2004.

Hsu, T.-J., J. T. Jenkins, and P. L.-F. Liu, On two-phase sediment transport : sheet flow of massive particles, in *Proceedings of the Royal Society of London A : Mathematical, Physical and Engineering Sciences*, vol. 460, pp. 2223–2250, The Royal Society, 2004.

Ingram, R. G., and V. H. Chu, Flow around islands in rupert bay : An investigation of the bottom friction effect, *Journal of Geophysical Research : Oceans*, *92*(C13), 14,521–14,533, 1987.

Jackson, R., Locally averaged equations of motion for a mixture of identical spherical particles and a newtonian fluid, *Chemical Engineering Science*, *52*, 2457–2469, 1997.

Jackson, R., *The dynamics of fluidized particles*, Cambridge University Press, Cambridge, 2000.

Jacobson, M. Z., C. L. Archer, and W. Kempton, Taming hurricanes with arrays of offshore wind turbines, *Nature Climate Change*, *4*(3), 195–200, 2014.

Jasak, H., Error analysis and estimation for finite volume method with applications to fluid flow, 1996.

Jenkins, J. T., Dense shearing flows of inelastic disks, *Physics of Fluids*, *18*(10), 103,307, 2006.

Jenkins, J. T., and D. M. Hanes, Collisional sheet flows of sediment driven by a turbulent fluid, *Journal of Fluid Mechanics*, *370*, 29–52, 1998.

Jenkins, J. T., and S. B. Savage, A theory for the rapid flow of identical, smooth, nearly elastic, spherical particles, *Journal of Fluid Mechanics*, *130*, 187–202, 1983.

Jensen, N., *A note on wind generator interaction*, 1983.

Jha, S. K., and F. A. Bombardelli, Two-phase modeling of turbulence in dilute sediment-laden, open-channel flows, *Environmental fluid mechanics*, *9*(2), 237, 2009.

Jiang, G.-S., and E. Tadmor, Nonoscillatory central schemes for multidimensional hyperbolic conservation laws, *SIAM Journal on Scientific Computing*, *19*(6), 1892–1917, 1998.

Jiang, G.-S., D. Levy, C.-T. Lin, S. Osher, and E. Tadmor, High-resolution nonoscillatory central schemes with nonstaggered grids for hyperbolic conservation laws, *SIAM Journal on Numerical Analysis*, *35*(6), 2147–2168, 1998.

Jiménez, J. A., and O. S. Madsen, A simple formula to estimate settling velocity of natural sediments, *Journal of waterway, port, coastal, and ocean engineering*, *129*(2), 70–78, 2003.

Johnson, D. A., and L. King, A mathematically simple turbulence closure model for attached and separated turbulent boundary layers, *AIAA journal*, *23*(11), 1684–1692, 1985.

Johnson, P. A., Comparison of pier-scour equations using field data, *Journal of Hydraulic Engineering*, *121*(8), 626–629, 1995.

Johnson, P. C., and R. Jackson, Frictional-collisional constitutive relations for granular materials, with application to plane shearing, *Journal of Fluid Mechanics*, *176*, 67–93, doi :10.1017/S0022112087000570, 1987.

Jop, P., Y. Forterre, and O. Pouliquen, A constitutive law for dense granular flows, *Nature*, *441*, 727– 730, doi :10.1038/nature04801, 2006.

Kim, Y., Z. Cheng, T.-J. Hsu, R. S. Mieras, and J. A. Puleo, A numerical investigation of sheet-flow under non-breaking and breaking waves, in *Proc. of the 8th International Conference on Coastal Dynamics, June*, pp. 12–16, 2017.

Kirkil, G., S. Constantinescu, and R. Ettema, Coherent structures in the flow field around a circular cylinder with scour hole, *Journal of Hydraulic Engineering*, *134*(5), 572–587, 2008.

Kranenburg, W. M., T.-J. Hsu, and J. S. Ribberink, Two-phase modeling of sheet-flow beneath waves and its dependence on grain size and streaming, *Advances in water resources*, *72*, 57–70, 2014.

Krieger, I. M., and T. J. Dougherty, A mechanism for non-newtonian flow in suspensions of rigid spheres, *Transactions of the Society of Rheology*, *3*(1), 137–152, 1959.

Lachaussée, F., Y. Bertho, C. Morize, A. Sauret, and P. Gondret, Competitive dynamics of two erosion patterns around a cylinder, *Physical Review Fluids*, *3*(1), 012,302, 2018.

Lagasse, P., J. Schall, F. Johnson, E. Richardson, and F. Chang, Stream stability at highway structures (2d ed.) : Federal highway administration, hydraulic engineering circular no. 20, *Tech. rep.*, Publication FHWA-IP-90-014, 1995.

Laursen, E. M., Observations on the nature of scour. proceedings of 5th hydrauric conference., state university of iowa, *Bulletin*, *34*, 179–197, 1952.

Lee, C.-H., Y. M. Low, and Y.-M. Chiew, Multi-dimensional rheology-based two-phase model for sediment transport and applications to sheet flow and pipeline scour, *Physics of Fluids*, *28*(5), 053,305, 2016.

LeVeque, R. J., *Finite volume methods for hyperbolic problems*, vol. 31, Cambridge university press, 2002.

Lillycrop, W. J., and S. A. Hughes, Scour hole problems experienced by the corps of engineers ; data presentation and summary, *Tech. rep.*, COASTAL ENGINEERING RESEARCH CENTER VICKSBURG MS, 1993.

Link, O., F. Pfleger, and U. Zanke, Characteristics of developing scour-holes at a sand-embedded cylinder, *International Journal of Sediment Research*, *23*(3), 258–266, 2008.

Link, O., C. González, M. Maldonado, and C. Escauriaza, Coherent structure dynamics and sediment particle motion around a cylindrical pier in developing scour holes, *Acta Geophysica*, *60*(6), 1689–1719, 2012.

Longo, S., Two-phase flow modeling of sediment motion in sheet-flows above plane beds, *Journal of Hydraulic Engineering*, *131*(5), 366–379, 2005.

Lun, C., Kinetic theory for granular flow of dense, slightly inelastic, slightly rough spheres, *Journal of Fluid Mechanics*, *233*, 539–559, 1991.

Lun, C., and S. Savage, A simple kinetic theory for granular flow of rough, inelastic, spherical particles, *J. Appl. Mech*, *54*(1), 47–53, 1987.

Lun, C., S. B. Savage, D. Jeffrey, and N. Chepurniy, Kinetic theories for granular flow : inelastic particles in couette flow and slightly inelastic particles in a general flowfield, *Journal of fluid mechanics*, *140*, 223–256, 1984.

Mao, Y., The interaction between a pipeline and an erodible bed, Ph.D. thesis, Institute of Hydrodynamics and Hydraulic Engineering, Technical University of Denmark, 1986.

Marieu, V., Modélisation de la dynamique des rides sédimentaires générées par les vagues, Ph.D. thesis, Bordeaux 1, 2007.

Mathieu, A., Two-phase flow simulation of scour below submarine pipelines., Master's thesis, Universityé Grenoble Alpes, 2017.

Mathieu, A., J. Chauchat, C. Bonamy, and T. Nagel, Two-phase flow simulation of tunnel and lee-wake erosion stages of scour below a submarine pipeline in a steady current, In prep.

Matutano, C., V. Negro, J.-S. López-Gutiérrez, and M. D. Esteban, Scour prediction and scour protections in offshore wind farms, *Renewable energy*, *57*, 358–365, 2013.

Maurin, R., J. Chauchat, and P. Frey, Dense granular flow rheology in turbulent bedload transport, *Journal of Fluid Mechanics*, *804*, 490–512, 2016.

Maurin, R., J. Chauchat, and P. Frey, Revisiting slope influence in turbulent bedload transport : consequences for vertical flow structure and transport rate scaling, *arXiv preprint arXiv :1701.02665*, 2017.

Mellor, G., and P. Durbin, The structure and dynamics of the ocean surface mixed layer, *Journal of Physical Oceanography*, *5*(4), 718–728, 1975.

Melville, B., and A. Sutherland, Design method for local scour at bridge piers, *Journal of Hydraulic Engineering*, *114*(10), 1210–1226, 1988.

Melville, B. W., Live-bed scour at bridge piers, *Journal of Hydraulic Engineering*, *110*(9), 1234–1247, 1984.

Melville, B. W., and Y.-M. Chiew, Time scale for local scour at bridge piers, *Journal of Hydraulic Engineering*, *125*(1), 59–65, 1999.

Melville, B. W., and S. E. Coleman, *Bridge scour*, Water Resources Publication, 2000.

Melville, B. W., et al., Local scour at bridge sites, Ph.D. thesis, ResearchSpace@ Auckland, 1975.

Menter, F., and T. Esch, Elements of industrial heat transfer predictions, in *16th Brazilian Congress of Mechanical Engineering (COBEM)*, pp. 26–30, 2001.

Menter, F., M. Kuntz, and R. Langtry, Ten years of industrial experience with the sst turbulence model, *Turbulence, heat and mass transfer*, *4*(1), 625–632, 2003.

Menter, F. R., Performance of popular turbulence model for attached and separated adverse pressure gradient flows, *AIAA journal*, *30*(8), 2066–2072, 1992.

Menter, F. R., Zonal two equation k- omega turbulence models for aerodynamic flows, *AIAA paper*, *2906*, 1993, 1993.

Meyer-Peter, E., and R. Müller, Formulas for bed-load transport, IAHR, 1948.

Moser, R. D., J. Kim, and N. N. Mansour, Direct numerical simulation of turbulent channel flow up to re= 590, *Phys. Fluids*, *11*(4), 943–945, 1999.

Moulin, A., Air-sea interaction at the synoptic-and the meso-scale, Ph.D. thesis, Grenoble Alpes University, 2015.

Moulin, A., and A. Wirth, A drag-induced barotropic instability in air–sea interaction, *Journal of Physical Oceanography*, *44*(2), 733–741, 2014.

Nagel, T., J. Chauchat, A. Wirth, and C. Bonamy, On the multi-scale interactions between an offshore-wind-turbine wake and the ocean-sediment dynamics in an idealized framework–a numerical investigation, *Renewable Energy*, *115*, 783–796, 2018.

Nessyahu, H., and E. Tadmor, Non-oscillatory central differencing for hyperbolic conservation laws, *Journal of computational physics*, *87*(2), 408–463, 1990.

Nielsen, A. W., X. Liu, B. M. Sumer, and J. Fredsøe, Flow and bed shear stresses in scour protections around a pile in a current, *Coastal Engineering*, *72*, 20–38, 2013.

Olsen, N. R., and H. M. Kjellesvig, Three-dimensional numerical flow modeling for estimation of maximum local scour depth, *Journal of Hydraulic Research*, *36*(4), 579–590, 1998.

Olsen, N. R., and M. C. Melaaen, Three-dimensional calculation of scour around cylinders, *Journal of Hydraulic Engineering*, *119*(9), 1048–1054, 1993.

Ouriemi, M., P. Aussillous, and E. Guazzelli, Sediment dynamics. Part I : Bed-load transport by shearing flows, *Journal of Fluid Mechanics*, *636*, 295–319, 2009.

Paik, J., L. Ge, and F. Sotiropoulos, Toward the simulation of complex 3d shear flows using unsteady statistical turbulence models, *International journal of heat and fluid flow*, *25*(3), 513–527, 2004.

Paik, J., C. Escauriaza, and F. Sotiropoulos, On the bimodal dynamics of the turbulent horseshoe vortex system in a wing-body junction, *Physics of Fluids*, *19*(4), 045,107, 2007.

Peltola, J., et al., Dynamics in a circulating fluidized bed : Experimental and numerical study, 2009.

Petersen, T. U., Scour around offshore wind turbine foundations, Ph.D. thesis, Technical University of Denmark. Department of Mechanical Engineering, 2014.

Petersen, T. U., B. M. Sumer, J. Fredsøe, T. C. Raaijmakers, and J.-J. Schouten, Edge scour at scour protections around piles in the marine environmentâĂŤlaboratory and field investigation, *Coastal Engineering*, *106*, 42–72, 2015.

Pope, S., An explanation of the turbulent round jet/plane jet anomaly, *AIAA Journal*, *16*(3), 279âĂŞ281, 1988.

Quezada, M., A. Tamburrino, and Y. Niño, Numerical simulation of scour around circular piles due to unsteady currents and oscillatory flows, *Engineering Applications of Computational Fluid Mechanics*, *12*(1), 354–374, 2018.

Raudkivi, A. J., Ripples on stream bed, *Journal of Hydraulic Engineering*, *123*(1), 58–64, 1997.

Revil-Baudard, T., and J. Chauchat, A two-phase model for sheet flow regime based on dense granular flow rheology, *Journal of Geophysical Research : Oceans*, *118*(2), 619–634, doi :10.1029/2012JC008306, 2013.

Revil-Baudard, T., J. Chauchat, D. Hurther, and P.-A. Barraud, Investigation of sheet-flow processes based on novel acoustic high-resolution velocity and concentration measurements, *Journal of Fluid Mechanics*, *767*, 1–30, doi :10.1017/jfm.2015.23, 2015.

Rhie, C., and W. Chow, Numerical study of the turbulent flow past an airfoil with trailing edge separation, *AIAA Journal(ISSN 0001-1452)*, *21*, 1525–1532, 1983.

Rivier, A., A.-C. Bennis, G. Pinon, V. Magar, and M. Gross, Parameterization of wind turbine impacts on hydrodynamics and sediment transport, *Ocean Dynamics*, *66*(10), 1285–1299, 2016.

Rogan, C., J. Miles, D. Simmonds, and G. Iglesias, The turbulent wake of a monopile foundation, *Renewable Energy*, *93*, 180–187, 2016.

Roulund, A., B. Sumer, J. Fredsøe, and J. Michelsen, Numerical and experimental investigation of flow and scour around a circular pile, *Journal of Fluid Mechanics*, *534*, 351–401, 2005.

Rouse, H., Experiments on the mechanics of sediment suspension, 1939.

Rusche, H., Computational fluid dynamics of dispersed two-phase flows at high phase fractions, Ph.D. thesis, Imperial College London (University of London), 2003.

Savage, S. B., Streaming motions in a bed of vibrationally fluidized dry granular material, *Journal of Fluid Mechanics*, *194*, 457–478, 1988.

Schaeffer, D., Instability in the evolution equations describing incompressible granular flow, *Journal of Diferential equations*, *66*, 19–50, 1987.

Schiller, L., and A. Naumann, Uber die Grundlegenden Berechungen bei der Schwerkraftaufbereitung, *Ver. Deut. Ing.*, *77*, 1933.

Schlichting, H., and K. Gersten, *Boundary-layer theory*, Springer, 2016.

Shields, A., Anwendung der aehnlichkeitsmechanik und der turbulenzforschung auf die geschiebebewegung, *Tech. rep.*, Preussischen Versuchsanstalt für Wasserbau, 1936.

Simpson, R. L., Junction flows, *Annual Review of Fluid Mechanics*, *33*(1), 415–443, 2001.

Sleath, J., Conditions for plug formation in oscillatory flow, *Continental Shelf Research*, *19*(13), 1643–1664, 1999.

Smith, S., Coefficients for sea surface wind stress, heat flux, and wind profiles as a function of wind speed and temperature, *Journal of Geophysical Research : Oceans (1978–2012)*, *93*(C12), 15,467–15,472, 1988.

Srivastava, A., and S. Sundaresan, Analysis of a frictional-kinetic model for gas-particle flow, *Powder Technology*, *129*, 72–85, 2003.

Stahlmann, A., et al., Numerical and experimental modeling of scour at foundation structures for offshore wind turbines, in *The Twenty-third International Offshore and Polar Engineering Conference*, International Society of Offshore and Polar Engineers, 2013.

Sumer, B. M., Flow–structure–seabed interactions in coastal and marine environments, *Journal of Hydraulic Research*, *52*(1), 1–13, 2014.

Sumer, B. M., A. Kozakiewicz, J. Fredsøe, and R. Deigaard, Velocity and concentration profiles in sheet-flow layer of movable bed, *Journal of Hydraulic Engineering*, *122*(10), 549–558, 1996.

Sumer, B. M., J. Fredsøe, K. Bundgaard, et al., Global and local scour at pile groups, in *The Fifteenth International Offshore and Polar Engineering Conference*, International Society of Offshore and Polar Engineers, 2005.

Sumer, B. M., et al., *The mechanics of scour in the marine environment*, vol. 17, World Scientific Publishing Company, 2002.

Sumer, B. M., et al., *Hydrodynamics around cylindrical strucures*, vol. 26, World scientific, 2006.

Vallis, G. K., *Atmospheric and oceanic fluid dynamics : fundamentals and large-scale circulation*, Cambridge University Press, 2006.

Van der Veen, H. H., S. Hulscher, and B. Perez Lapena, Seabed morphodynamics due to offshore wind farms, in *River, Coastal and Estuarine Morphodynamics : RCEM*, 2007.

Van Rijn, L., Sediment transport, part i : Bed load transport, *J. Hydraul. Eng.*, 1984a.

Van Rijn, L., Sediment transport, part ii : Suspended load transport, *J. Hydraul. Eng.*, *110*, 1613âĂŞ1641, 1984b.

Van Rijn, L. C., Sediment pick-up functions, *Journal of Hydraulic engineering*, *110*(10), 1494–1502, 1984c.

Vanhellemont, Q., and K. Ruddick, Turbid wakes associated with offshore wind turbines observed with landsat 8, *Remote Sensing of Environment*, *145*, 105–115, 2014.

Vanoni, V. A., *Sedimentation engineering*, 2006.

Vautard, R., F. Thais, I. Tobin, F.-M. Bréon, J.-G. Devezeaux de Lavergne, A. Colette, P. Yiou, and P. M. Ruti, Regional climate model simulations indicate limited climatic impacts by operational and planned european wind farms, *Nature communications*, *5*, 2014.

Weller, H., Derivation, modelling and solution of the conditionally averaged two-phase flow equations, *Nabla Ltd, No Technical Report TR/HGW*, *2*, 2002.

Whitehouse, R., *Scour at marine structures : A manual for practical applications*, Thomas Telford, 1998.

Whitehouse, R. J., J. M. Harris, J. Sutherland, and J. Rees, The nature of scour development and scour protection at offshore windfarm foundations, *Marine Pollution Bulletin*, *62*(1), 73–88, 2011.

Wilcox, D. C., *Turbulence modeling for CFD, 2nd edition*, DCW industries La Canada, CA, 1998.

Wilcox, D. C., *Turbulence modeling for CFD, 3rd edition*, DCW industries La Canada, CA, 2006.

Wilcox, D. C., Formulation of the k-omega turbulence model revisited, *AIAA J*, *46*(11), 2823–2838, 2008.

Wilson, K. C., Bed-load transport at high shear stress, *Journal of the hydraulics division*, *92*(6), 49–59, 1966.

Wilson, K. C., Analysis of bed-load motion at high shear stress, *Journal of Hydraulic Engineering*, *113*(1), 97–103, 1987.

Wong, M., and G. Parker, Reanalysis and correction of bed-load relation of meyer-peter and müller using their own database, *Journal of Hydraulic Engineering*, *132*(11), 1159–1168, 2006.

Wu, J., Wind-stress coefficients over sea surface from breeze to hurricane, *Journal of Geophysical Research : Oceans (1978–2012)*, *87*(C12), 9704–9706, 1982.

Yin, Y., E. Christie, M. Li, C. Moulinec, and D. Emerson, 3d morphological impact modelling of offshore wind farms using les and hpc, *Coastal Engineering Proceedings*, *1*(34), 48, 2014.

Yu, X., T.-J. Hsu, and D. M. Hanes, Sediment transport under wave groups : Relative importance between nonlinear waveshape and nonlinear boundary layer streaming, *Journal of Geophysical Research : Oceans*, *115*(C2), 2010.

Zanke, U., Berechung der sinkgeschwindigkeiten von sedimenten., *Tech. rep.*, Mitt. des Franzius-Instituts fur Wasserbau, 46(243), Technical University, Hannover, Germany., 1977.

Zhang, D. Z., and A. Prosperetti, Momentum and energy equations for disperse two-phase flows and their closure for dilute suspensions, *Int. J. Multiphase Flow*, *23*, 425 – 453, 1997.

Zhao, M., L. Cheng, and Z. Zang, Experimental and numerical investigation of local scour around a submerged vertical circular cylinder in steady currents, *Coastal Engineering*, *57*(8), 709–721, 2010.

Zhou, L., Numerical modelling of scour in steady flows, Ph.D. thesis, Université de Lyon, 2017.

Zhou, L., Y. Tian, S. B. Roy, C. Thorncroft, L. F. Bosart, and Y. Hu, Impacts of wind farms on land surface temperature, *Nature Climate Change*, *2*(7), 539–543, 2012.

Annexe A

Morphodynamic Model

This section describes the morphodynamic module implemented into the code to solve Exner equation (2.10). Following *Marieu* (2007) work, a conservative shock-capturing schemes has been implemented is the code. But, instead of using, a NOCS (Non-Oscillatory Central Scheme) collocated with the mesh (*Nessyahu and Tadmor*, 1990) as in *Marieu* (2007) work, a NOCS staggered with the mesh has been chosen because it 2D extension was already done by *Jiang et al.* (1998). This type of scheme is able to solve the conservative forms of equations and have a strong stability on shock areas (*LeVeque*, 2002).
With the smooth slope shapes finally obtained in 2D simulations it has been decided that local avalanches can not occurs in the present study and therefore no avalanche management module has been added to the morphodynamic model.
For notation simplification reason, the seabed elevation denoted previously as h_s is written without it's subscript 's' for the present section.

A.1 One Dimensional NOCS Staggered Scheme

The NOCS scheme solves the Exner equation in two steps : a predictor-step, that gives a temporary bedform from which fluxes are recalculated and the corrector-step in which the definitive bedform is obtained.
The predictor step gives the bed elevation at grid point i after one half time-step calculation (n+1/2) :

$$h_i{}^{n+\frac{1}{2}} = h_i{}^{n} - \frac{1}{2}\frac{\delta t}{\delta x}\, q_i{}' \,, \tag{A.1}$$

where $q_i{}'$ is the sediment flux derivative approximation at grid point i. The temporary flux depends only on the bed elevation $h_i{}^{n+\frac{1}{2}}$:

$$q_i{}^{n+\frac{1}{2}} = q\left(h_i{}^{n+\frac{1}{2}}\right) \,, \tag{A.2}$$

The calculation of $q_i{}'$ and $h_i{}'$ involves a slope limiter, in order to ensure TVD (Total Variation Diminishing) properties of the solution. In the present work, $\beta-$limiter has been used. In order to compute the derivative approximation of a function ϕ, the $\beta-$limiters are define as follow :

$$\phi_i{}' = \text{MinMod}\left[\beta(\phi_\text{i} - \phi_\text{i-1}),\ \frac{1}{2}(\phi_\text{i+1} - \phi_\text{i-1}),\ \beta(\phi_\text{i+1} - \phi_\text{i})\right] \,, \tag{A.3}$$

where β is the limiter parameter and $MinMod$ the function such as :

$$\text{MinMod}\{\text{x}_1, \text{x}_2, \text{x}_3\} = \begin{cases} min\{x_1, x_2, x_3\} & if\ x_k > 0;\ \forall k = 1, 2, 3, \\ max\{x_1, x_2, x_3\} & if\ x_k < 0;\ \forall k = 1, 2, 3, \\ 0 & \text{else} \end{cases} \tag{A.4}$$

when $\beta = 1$, the limiter is the so-called $MinMod$ and when $\beta = 2$ it is the *Superbee* limiter, the latter is less diffusive.

The corrector is on a staggered grid and it is based on the reconstruction of a piecewise-linear interpolant from the known staggered cell-averages at time t^n :

$$\bar{h}(x, t^n) = \sum_i \left[{h_i}^n - {h_i}' \left(\frac{x - x_i}{\Delta x} \right) \right] \chi_i(x), \tag{A.5}$$

where ${h_i}'$ is the discrete slope involving the slope limiter described in equations A.3 and A.4, and where $\chi_i(x)$ is the characteristic function of the cell $I_i := \mid x - x_i \mid \leq \Delta x/2$.
This interpolant is then projected on the staggered cell-averages on the next time step, t^{n+1} :

$${h_{i+\frac{1}{2}}}^{n+1} = \frac{1}{2} \left({h_i}^n + {h_{i+1}}^n \right) + \frac{1}{8} \left({h_i}' - {h_{i+1}}' \right) - \frac{\delta t}{\delta x} \left({q_{i+1}}^{n+\frac{1}{2}} - {q_i}^{n+\frac{1}{2}} \right), \tag{A.6}$$

The staggered corrector has to be reprojected on the non-staggered grid by using a piecewise-linear interpolant through the calculated staggered cell-averages at time t^{n+1} :

$$\bar{h}_{i+\frac{1}{2}}{}^{n+1} = {h_{i+\frac{1}{2}}}^{n+1} - {h_{i+\frac{1}{2}}}' \left(\frac{x - x_{i+\frac{1}{2}}}{\Delta x} \right), \tag{A.7}$$

where ${h_{i+\frac{1}{2}}}'$ is the staggered discrete derivative of the staggered corrector term.
Finally, the cell-averages at time t^{n+1} are obtained by averaging this interpolant,resulting in the non-staggered corrector scheme :

$$\begin{aligned} {h_i}^{n+1} = & \frac{1}{\Delta x} \left[\int_{x_{i-\frac{1}{2}}}^{x_i} \bar{h}_{i-\frac{1}{2}}{}^{n+1} + \int_{x_i}^{x_{i+\frac{1}{2}}} \bar{h}_{i+\frac{1}{2}}{}^{n+1} \right] \\ {h_i}^{n+1} = & \frac{1}{4} \left({h_{i-1}}^n - 2{h_i}^n + {h_{i+1}}^n \right) - \frac{1}{16} \left({h_{i+1}}' - {h_{i-1}}' \right) - \frac{1}{8} \left({h_{i+\frac{1}{2}}}' - {h_{i-\frac{1}{2}}}' \right) \\ & - \frac{\delta t}{2\delta x} \left({q_{i+1}}^{n+\frac{1}{2}} - {q_i}^{n+\frac{1}{2}} \right) \end{aligned} \tag{A.8}$$

Figure 3.1 from *Jiang et al.* (1998) shows the second order construction process leading to the non-staggered corrector scheme and may be useful to the reader.
For staggered variables, boundary conditions slightly differ from the ones described in section 2.3.2. Indeed, as the grid is staggered extreme points are out of the domain. In 1D, the non staggered grid has the size n, while the staggered one has the size $n + 1$, starting from 0 to n. For a given f function, periodic boundary conditions are given by :

$$\begin{gathered} f(0) = f(n-2) \\ f(n) = f(2) \\ f(n-1) = f(1) \end{gathered}$$

A.2 Two Dimensional Extension

The arguments applied in the one-dimensional case can be easily extended to higher dimensions. This extension is straightforward and is based on exactly the same procedure described in the previous section. A non-staggered scheme is created from a staggered scheme by averaging the interpolants constructed from the given staggered values. In two dimensions, predictor and staggered corrector become respectively :

$$h_{i,j}{}^{n+\frac{1}{2}} = h_{i,j}{}^{n} - \frac{1}{2}\frac{\delta t}{\delta x}\ qx_{i,j}{}' - \frac{1}{2}\frac{\delta t}{\delta y}\ qy_{i,j}{}' \ , \tag{A.9}$$

where $qx_{i,j}{}'$ and $qy_{i,j}{}'$ are the flux derivative approximation in the x and y directions respectively.

$$\begin{aligned} h_{i+\frac{1}{2},j+\frac{1}{2}}{}^{n+1} = \ & \frac{1}{4}\left(h_{i,j}{}^{n} + h_{i+1,j}{}^{n} + h_{i,j+1}{}^{n} + h_{i+1,j+1}{}^{n}\right) \\ & + \frac{1}{16}\left(h'_{i,j} + h'_{i+1,j} + h'_{i,j+1} + h'_{i+1,j+1}\right) \\ & + \frac{1}{16}\left(h\text{`}_{i,j} + h\text{`}_{i+1,j} + h\text{`}_{i,j+1} + h\text{`}_{i+1,j+1}\right) \\ & - \frac{\delta t}{2\delta x}\ \left(qx_{i+1,j}{}^{n+\frac{1}{2}} - qx_{i,j}{}^{n+\frac{1}{2}} + qx_{i+1,j+1}{}^{n+\frac{1}{2}} - qx_{i,j+1}{}^{n+\frac{1}{2}}\right) \\ & - \frac{\delta t}{2\delta y}\ \left(qy_{i,j+1}{}^{n+\frac{1}{2}} - qy_{i,j}{}^{n+\frac{1}{2}} + qy_{i+1,j+1}{}^{n+\frac{1}{2}} - qy_{i+1,j}{}^{n+\frac{1}{2}}\right) \end{aligned} \tag{A.10}$$

The prime and back-prime notation denote the discrete derivatives in the x and y directions, respectively. The piecewise-linear interpolant reconstruction is then averaged, resulting in the non-staggered corrector at time step t^{n+1} and in cell $I_{i,j}$:

$$\begin{aligned} h_{i,j}{}^{n+1} = \ & \frac{1}{4\Delta x\Delta y}\left[\int\int_{I_{i+\frac{1}{2},j+\frac{1}{2}}} \bar{h}_{i+\frac{1}{2},j+\frac{1}{2}}{}^{n+1} + \int\int_{I_{i-\frac{1}{2},j+\frac{1}{2}}} \bar{h}_{i-\frac{1}{2},j+\frac{1}{2}}{}^{n+1}\right] + \\ & \frac{1}{4\Delta x\Delta y}\left[\int\int_{I_{i-\frac{1}{2},j-\frac{1}{2}}} \bar{h}_{i-\frac{1}{2},j-\frac{1}{2}}{}^{n+1} + \int\int_{I_{i+\frac{1}{2},j-\frac{1}{2}}} \bar{h}_{i+\frac{1}{2},j-\frac{1}{2}}{}^{n+1}\right] \\ h_{i,j}{}^{n+1} = \ & \frac{1}{4}\left(h_{i+\frac{1}{2},j+\frac{1}{2}}{}^{n+1} + h_{i-\frac{1}{2},j+\frac{1}{2}}{}^{n+1} + h_{i-\frac{1}{2},j-\frac{1}{2}}{}^{n+1} + h_{i+\frac{1}{2},j-\frac{1}{2}}{}^{n+1}\right) \\ & + \frac{1}{16}\left[\left(h'_{i-\frac{1}{2},j-\frac{1}{2}} - h'_{i+\frac{1}{2},j-\frac{1}{2}}\right) + \left(h'_{i-\frac{1}{2},j+\frac{1}{2}} - h'_{i+\frac{1}{2},j+\frac{1}{2}}\right)\right] \\ & + \frac{1}{16}\left[\left(h\text{`}_{i-\frac{1}{2},j-\frac{1}{2}} - h\text{`}_{i-\frac{1}{2},j+\frac{1}{2}}\right) + \left(h\text{`}_{i+\frac{1}{2},j-\frac{1}{2}} - h\text{`}_{i+\frac{1}{2},j+\frac{1}{2}}\right)\right] \end{aligned} \tag{A.11}$$

The two-dimensional staggered (red) and non staggerred (black) grids are sketched on figure A.1, adapted from *Jiang et al.* (1998).

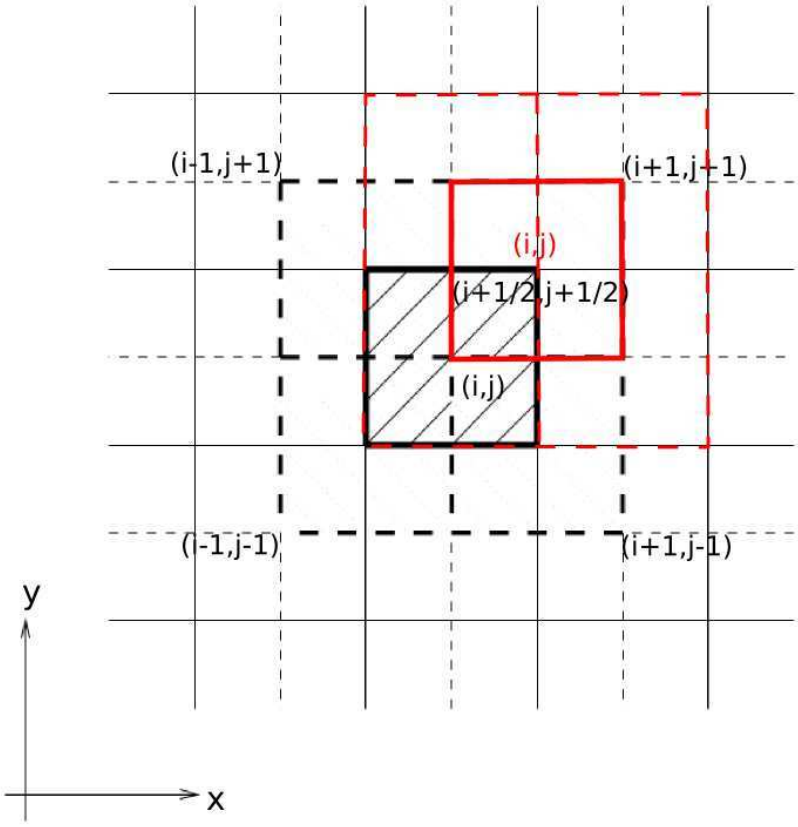

FIGURE A.1: Two-dimensional staggered (red) and non staggerred (black) grids. Adapted from *Jiang et al.* (1998).

Annexe B

Two-phase flow bed shear stress determination methodology

This Appendix aims to present the specific post-processing methodology associated to the two-phase flow approach. Here the focus is done on the way the bed shear stress is determined in a two-phase flow case with sediment.

B.1 Bed surface normal and tangent vectors calculation

The scour is deforming the initial flat sediment bed. The resulting interface slopes variation have to be accounted for in the bed shear stress calculation. To this end, the bed interface is first interpolated from the original unstructured grid to a cartesian one, using the standard *interpolate.griddata* function of python with the *cubic* method of interpolation [1].
The new cartesian grid is defined by the orthogonal vectors $\overrightarrow{e_x}$, $\overrightarrow{e_y}$ and $\overrightarrow{e_z}$. The bed interface becomes a surface defined in the space as a function of x and y coordinates :

$$z_{bed} = f(x, y) \tag{B.1}$$

In order to account for the slope effect, the shear stress has to be projected on the plane tangent to the slope and defined by the vectors $\overrightarrow{t_x}$ and $\overrightarrow{t_y}$, as illustrated in figure B.1. The determination of these tangent vectors and of the bed interface normal ($\overrightarrow{n}$) at each cell of the interpolated cartesian gris is detailed in the present section. In each point of the (x,y) cartesian grid the normal vector reads :

$$\overrightarrow{n} = \frac{\nabla z_{bed}}{|| \nabla z_{bed} ||} \tag{B.2}$$

Equation B.2 can be rewritten :

$$\overrightarrow{n} = \frac{1}{\sqrt{1 + \left(\frac{\partial z_{bed}}{\partial x}\right)^2 + \left(\frac{\partial z_{bed}}{\partial y}\right)^2}} \left(\frac{\partial z_{bed}}{\partial x}\overrightarrow{e_x} + \frac{\partial z_{bed}}{\partial y}\overrightarrow{e_y} + 1\overrightarrow{e_z} \right) \tag{B.3}$$

The normal vector $\overrightarrow{n}$, is obtained from the gradient of the bed interface is both horizontal direction. The knowledge of $\overrightarrow{n}$ is necessary to calculate $\overrightarrow{t_x}$ and $\overrightarrow{t_y}$ that are the vectors defining

1. https ://docs.scipy.org/doc/scipy/reference/generated/scipy.interpolate.griddata.html#scipy.interpolate.griddata

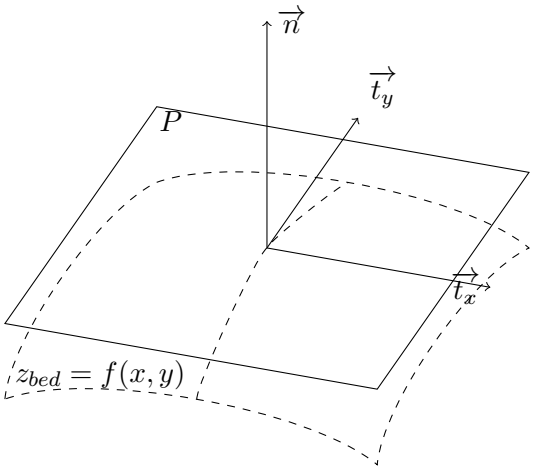

FIGURE B.1: Sketch of the interface surface.

the plan tangent (P) to the bed interface at each point of the (x,y) cartesian grid.

On a cartesian grid, the definition of $\overrightarrow{t_x}$ is straightforward :

$$\overrightarrow{t_x} = t_x \overrightarrow{e_x} + t_z \overrightarrow{e_z} \tag{B.4}$$

$\overrightarrow{n}$ and $\overrightarrow{t_x}$ are orthogonal, therefore, $\overrightarrow{t_x}$ has to verify :

$$\overrightarrow{t_x} \cdot \overrightarrow{n} = 0 \quad \Leftrightarrow \quad t_x n_x = -t_z n_z \tag{B.5}$$

Furthermore, $\overrightarrow{t_x}$, $\overrightarrow{t_y}$ and $\overrightarrow{n}$ are unit vectors in the $(\overrightarrow{e_x}, \overrightarrow{e_y}, \overrightarrow{e_z})$ vector space. Thus :

$$|| \overrightarrow{t_x} || = 1 \quad \Leftrightarrow \quad t_x^2 + t_y^2 = 1 \tag{B.6}$$

$$\begin{cases} t_x = \beta n_z = \beta \dfrac{1}{\sqrt{1+\left(\frac{\partial z_{bed}}{\partial x}\right)^2+\left(\frac{\partial z_{bed}}{\partial y}\right)^2}} \\ t_z = -\beta n_x = -\beta \dfrac{1}{\sqrt{1+\left(\frac{\partial z_{bed}}{\partial x}\right)^2+\left(\frac{\partial z_{bed}}{\partial y}\right)^2}} \dfrac{\partial z_{bed}}{\partial x} \end{cases} \tag{B.7}$$

Injecting eq. B.7 in eq. B.6 gives :

$$\beta^2 = \frac{1 + \left(\frac{\partial z_{bed}}{\partial x}\right)^2 + \left(\frac{\partial z_{bed}}{\partial y}\right)^2}{1 + \left(\frac{\partial z_{bed}}{\partial x}\right)^2} \tag{B.8}$$

$\overrightarrow{t_x}$ reads thus :

$$\overrightarrow{t_x} = \frac{1}{\sqrt{1 + \left(\frac{\partial z_{bed}}{\partial x}\right)^2}} \left(\overrightarrow{e_x} - \frac{\partial z_{bed}}{\partial x} \overrightarrow{e_z} \right) \tag{B.9}$$

Finally, $\overrightarrow{t_y}$ can be calculated from the cross product between $\overrightarrow{n}$ and $\overrightarrow{t_x}$:

$$\overrightarrow{t_y} = \overrightarrow{n} \wedge \overrightarrow{t_x} = \frac{1}{\sqrt{1 + \left(\frac{\partial z_{bed}}{\partial x}\right)^2} \sqrt{1 + \left(\frac{\partial z_{bed}}{\partial x}\right)^2 + \left(\frac{\partial z_{bed}}{\partial y}\right)^2}} \left[\frac{\partial z_{bed}}{\partial x} \frac{\partial z_{bed}}{\partial y} \overrightarrow{e_x} + \left(1 + \left(\frac{\partial z_{bed}}{\partial x}\right)^2\right) \overrightarrow{e_y} - \frac{\partial z_{bed}}{\partial y} \overrightarrow{e_z} \right] \tag{B.10}$$

B.2 Bed shear stress determination in a two-phase flow configuration with sediment

In the case of a multi-dimensional single phase computation, the determination of the bed shear stress amplification is done as :

$$\frac{\mid \tau_b \mid}{\tau_0} = \frac{\sqrt{{\tau_{xz}^f}^2 + {\tau_{yz}^f}^2}}{\tau_0}, \tag{B.11}$$

where τ_{xz}^f and τ_{yz}^f are components of the fluid shear stress tensor at the wall and τ_0 is the undisturbed bed shear stress.
When dealing with two-phase flow configurations, the bed shear stress can be computed by considering either the shear stress of the mixture (eq. B.12), the maximum of the fluid shear stress (eq. B.13) or the fluid shear stress at a given concentration (eq. B.14) :

$$\mid \tau_b \mid = \sqrt{\tau_{xz}^f(\phi)^2 + \tau_{yz}^f(\phi)^2 + \tau_{xz}^s(\phi)^2 + \tau_{yz}^s(\phi)^2}, \tag{B.12}$$

$$\mid \tau_b \mid = max(\sqrt{{\tau_{xz}^f}^2 + {\tau_{yz}^f}^2}). \tag{B.13}$$

$$\mid \tau_b \mid = \sqrt{\tau_{xz}^f(\phi)^2 + \tau_{yz}^f(\phi)^2}. \tag{B.14}$$

Because of the erosion process, the bed shear stress has to be projected on the plane tangent to the slope. The product between the phase shear stress tensor τ^k and the normal vector $\overrightarrow{n}$ gives shear stress vector at each cell :

$$\overrightarrow{T^k} = \tau^k \cdot \overrightarrow{n} \tag{B.15}$$

The projection of the mixture bed shear stress magnitude on the plan tangential to the local slope reads :

$$\mid \tau_b \mid = \sqrt{(\overrightarrow{T^f} \cdot \overrightarrow{t_x})^2 + (\overrightarrow{T^f} \cdot \overrightarrow{t_y})^2 + (\overrightarrow{T^s} \cdot \overrightarrow{t_x})^2 + (\overrightarrow{T^s} \cdot \overrightarrow{t_y})^2} \tag{B.16}$$

It has been verified that the bed shear stress amplification obtained from equations B.12 and B.16 over a flat bed are identical. The iso-surface of concentration taken to compute the normal and tangential vectors has been carefully investigated. Strictly speaking, the iso-surface of concentration $\phi = 0.57$ should obviously be chosen. However, it has been observed that this interface is noisy and that it impacts the quality of the resulting normal vector. This can be seen in figure B.2. Although no overall bed elevation difference is visible between the iso-surfaces of concentration $\phi = 0.45$ (subfigure B.2.a) and $\phi = 0.57$ (subfigure B.2.b), the bed elevation is more noisy with $\phi = 0.57$. This appears more clearly with the vertical component of the bed interface normal plotted in subfigures B.2.c ($\phi = 0.45$) and B.2.d ($\phi = 0.57$).

Figure B.2 shows that higher in the transport layer, the iso-surface of concentration are smoother. Furthermore, the ratio between the vertical component of the bed interface normal estimated at $\phi = 0.57$ and $\phi = 0.45$ is shown in figure B.3. On the major part of the domain, the ratio is between 0.9 and 1.1. Out of this agreement range, the discrepancies may be explained by the noise found at $\phi = 0.57$.

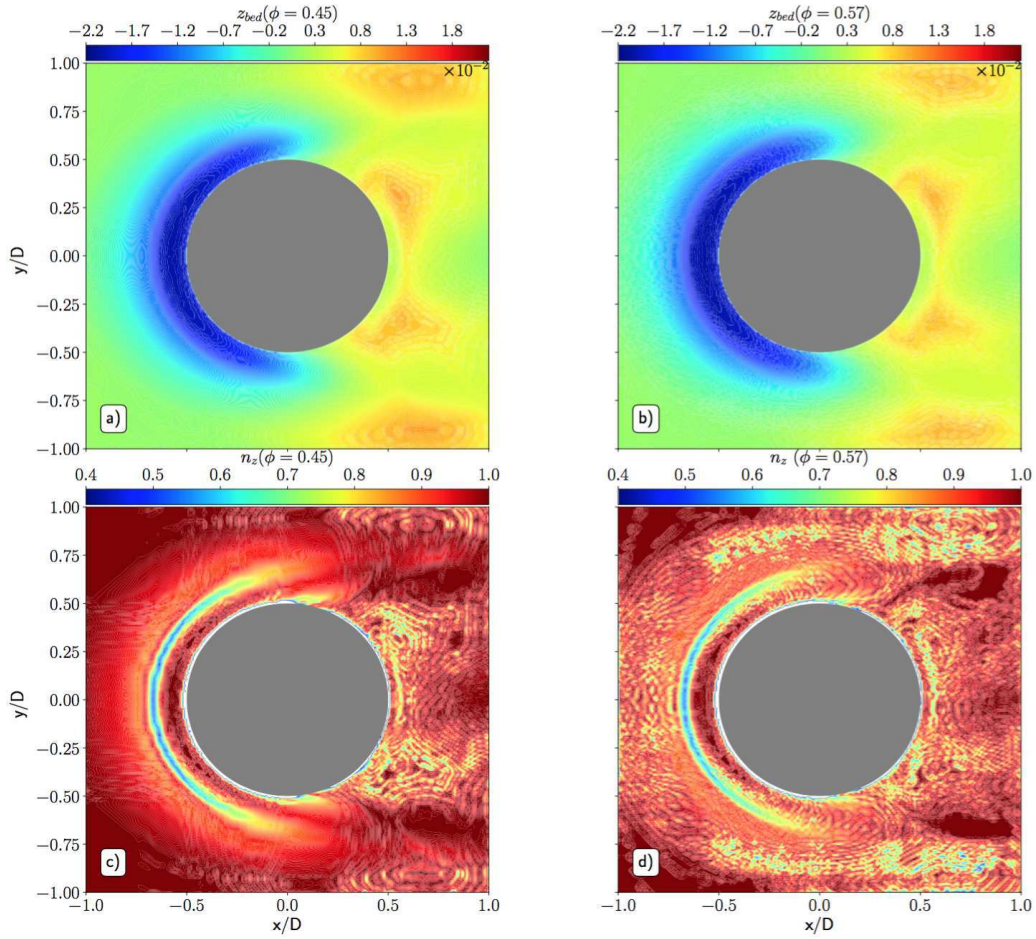

FIGURE B.2: Vertical elevation of iso-surface of concentration $\phi = 0.45$ (a), $\phi = 0.57$ (b), vertical component of the bed interface normal estimated at $\phi = 0.45$ (c) and at $\phi = 0.57$. t=10s.

Therefore, the iso-surface of concentration $\phi = 0.45$ has been chosen to calculate the normal and tangential vectors. The average values taken by the normal vector are not much impacted by this choice but the noise is clearly reduced.

In the uniform two-phase flow case presented in Chapter 4 it has been shown that taking the maximum fluid shear stress or the mixture one at any vertical level in the transport layer predicts similar results in term of Shields number. Here, for a multi-dimensional and non uniform two-phase flow case, the best way to compute the bed shear stress is determined by comparing the bed shear stress amplification at early time between the Rigid-Bed and the Live-Bed configurations.

Similarly to the one-directional flow configuration, the vertical position where the mixture or the fluid shear stress is computed has to be identified. This vertical position corresponds to a given iso-surface of concentration.

Several value of sediment concentration, corresponding to several vertical positions are tested : $\phi = 0.57$ (corresponding to the immobile bed interface), $\phi = 0.45$ (inside the bedload transport layer) or $\phi = 0.08$ (at the top of the bedload transport layer). The bedload transport layer is

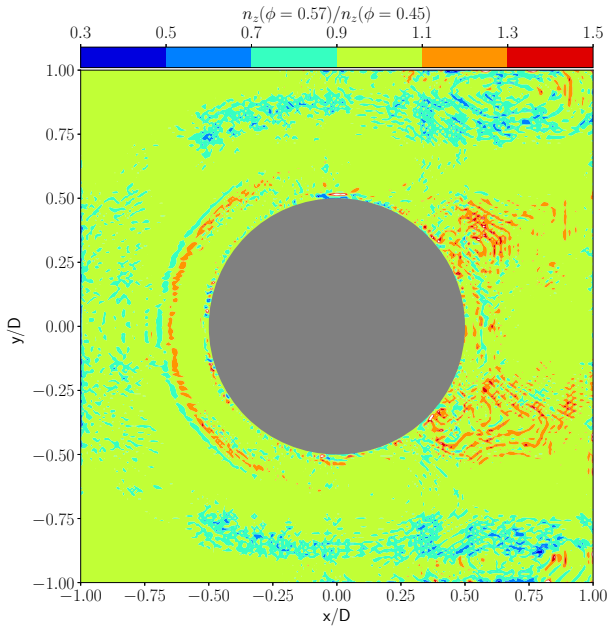

FIGURE B.3: Ratio between the vertical component of the bed interface normal estimated at $\phi = 0.57$ and $\phi = 0.45$. t=10s.

still defined as the vertical distance between the iso-surface of sediment concentration $\phi = 0.57$ and $\phi = 0.08$, the latter corresponding to the distinction between bedload and suspended load (*Dohmen-Janssen et al.*, 2001).

Figure B.4 shows the bed shear stress amplification for both the Rigid-Bed and the Live-Bed configuration at t=1s. At t=0s, the unidirectional case solution is imposed all over the computational domain. At early computational times, all the hydrodynamic field are impacted by the pile presence. As a consequence, two contra-rotatives vortices are generated downstream of the pile at t=1s. This phenomenon is clearly observable in bed shear stress amplification predicted with equation B.11 for the Rigid-Bed case (see figure B.4.a).
The other panels of figure B.4 (subfigures b) to e).) shows the bed shear stress amplification at t=1s in the Live-Bed case. The bed shear stress is projected on the plan tangential to the local slope as described by eq. B.16. First, in the subfigure B.4.b, the bed shear stress amplification is estimated following the maximum of the fluid shear stress. It clearly appears the bed shear stress amplification is overestimated, especially around and downstream of the cylinder.
In the subfigures B.4.e and B.4.f the projected bed shear stress amplification is estimated with the mixture approach (eq. B.12) at the sediment concentration level, ϕ=0.45 and ϕ=0.57. It can be seen that estimating the mixture shear stress close to the bed results in more noisy bed shear stress amplification. This is due to the fact that the iso-concentration levels are more noisy for high concentration values (see Appendix B). This is particularly visible for $\phi = 0.57$ (subfigure B.4.f). Therefore, using this criterion to determine the bed shear stress amplification may result in noisy and hardly exploitable results. In addition, for this concentration, the bed shear stress amplification is highly overestimated. It seems thus better to use a lower sediment concentration to calculate the mixture bed shear stress. The mixture bed shear stress estimation at ϕ=0.45

seems less noisy and in good agreement with the RB case. The subfigures B.4.c, B.4.d show the projected bed shear stress amplification estimated at the sediment concentration level, ϕ=0.08 using equations B.14 (subfigure B.4.c) and B.12 (subfigure B.4.d). The bed shear stress amplification is similar between the both methods. Even if the bed shear stress amplification prediction are overestimated compared with the Rigid-Bed reference (subfigure B.4.a), the localization of the remarkable bed shear stress amplification patterns around the cylinder (due to the streamlines contraction) and downstream of the cylinder (linked to the contra-rotatives vortices) are similar between subfigures B.4.a, B.4.c and B.4.d.

Figure B.5.a shows the bed interface elevation at t=1s for the Live-Bed case. The erosion pattern generated by the HSV, in front and around the cylinder is already noticeable. The HSV erosion pattern is approximatively 2cm wide and goes up to 4mm depth. The vertical component of the bed interface normal (figure B.5.b) takes values comprised between 0.7 and 1. It gives a indication of the bed slope, $n_z = 1$ meaning that the sediment bed interface is flat. In the erosion pattern generated by the HSV, the vertical component of the bed interface normal takes values down to 0.85 approximatively highlighting showing that, even at early time, the sediment bed present variations and local slopes may be non-negligible.
Figure B.5.c shows the angle of steepest descent or maximum slope of the bed β. It is determined from the magnitude of the horizontal gradient of the bed elevation :

$$\beta = arctan \mid \nabla_h z_{bed} \mid = arctan(\sqrt{\left(\frac{\partial z_{bed}}{\partial x_i}\right)^2 + \left(\frac{\partial z_{bed}}{\partial x_j}\right)^2}), \tag{B.17}$$

where $\nabla_h z_{bed}$ is the horizontal gradient of the bed elevation.
The noticeable elevations variations are found at the upstream part of the scour hole, in the cylinder vicinity at $\Gamma \approx \pm 90°$ (where the extension of the HSV legs mark ends) and at the contra-rotative vortices location. These locations correspond to those at which the vertical component of the bed interface normal deviation from the unity is maximum. In the scour hole, the slope can reach an angle up to 20°. The bed elevations variations are smooth and no slope break is observed.
Finally, the figure B.5.d shows the ratio between the bed shear stress obtained from equations B.16 and B.12, *i.e* with and without the projection on the plan tangential to the local slope. Away from the cylinder, this ratio is comprised between 0.9 and 1.1. The ratio deviates from the unity only where a slope presence has been previously identified : at the upstream part of the scour hole, where the extension of the HSV legs mark ends (around $\Gamma = \pm 90°$) and at the contra-rotative vortices location.

At t=1s, the slope is mild and considering it has only a small effect on the bed shear stress estimation and no clear conclusion can be draw concerning the best method for the bed shear stress determination. The fluid and mixture estimation at ϕ=0.08 and the mixture estimation at *phi*=0.45 result in different but overall good agreement with the Rigid-Bed case. It is necessary to perform a similar analysis at an longer time.

To this end, the figure B.6 shows the same quantities than figure B.5 for t=10s. The bed interface elevation plotted in subfigure B.6.a shows that the HSV erosion pattern is more important and extend further around the cylinder. The resulting bed elevations variations are different from those reported at t=1s. Both, the vertical component of the bed interface normal (subfigure B.6.b) and the slope angle of the bed interface (subfigure B.6.c) show similar variations, with a important slope located at $R/D \approx -0.7$. Here, R/D is the distance to the center of the cylinder

made dimensionless by the cylinder diameter, it is equivalent to x/D on the x-axis.
The ratio between the bed shear stress obtained with and without the projection on the plan tangential to the local slope (subfigure B.6.d) shows that the projected bed shear stress estimation is different where important slopes have been identified : in the semi-circular area where the slope is gently increasing and at the slope break localization, where the ratio can take values up to 2.5.
Downstream of the cylinder the projected bed shear stress is less than the one estimated over a flat bed. This may be due the sediment accumulation just downstream of the cylinder. As the results are noisy in that part of the domain no clear conclusion can be drawn.
At t=10s the erosion is important enough to significantly affect the bed elevation and induce strong bed slopes.

Figure B.7 shows the bed shear stress amplification for both the Rigid-Bed and the Live-Bed configuration at t=10s. For the Live-Bed configuration, (subfigures B.7.(b-e).) the bed shear stress is projected on the plan tangential to the local slope as described by eq. B.16. The vortex-shedding is not developed and the maximum of bed shear stress amplification is located around $\Gamma = \pm 65°$ in the Rigid-Bed case (subfigure B.7.a). Similarly to what has been observed for t=1s all results on the Live-Bed case are overestimating the bed shear stress amplification, particularly the mixture estimation at $\phi = 0.57$. Again, for high sediment concentration the bed shear stress amplification is extremely noisy, this can be seen for the mixture bed shear stress estimation at ϕ=0.57 but also at ϕ=0.45. As for t=1s, the bed shear stress amplification obtained from the fluid or the mixture shear stress at ϕ=0.08 are extremely similar but here, very different from the Rigid-Bed case. At t=10s the erosion hole depth and the slope are probably modifying the flow and the bed shear stress repartition too importantly to make the comparison with the Rigid-Bed case relevant. Therefore, as the bed shear stress estimation is too noisy using the mixture estimation at *phi*=0.57 or *phi*=0.45, in the following, the bed shear stress will be estimated via the mixture approach at $\phi = 0.08$.

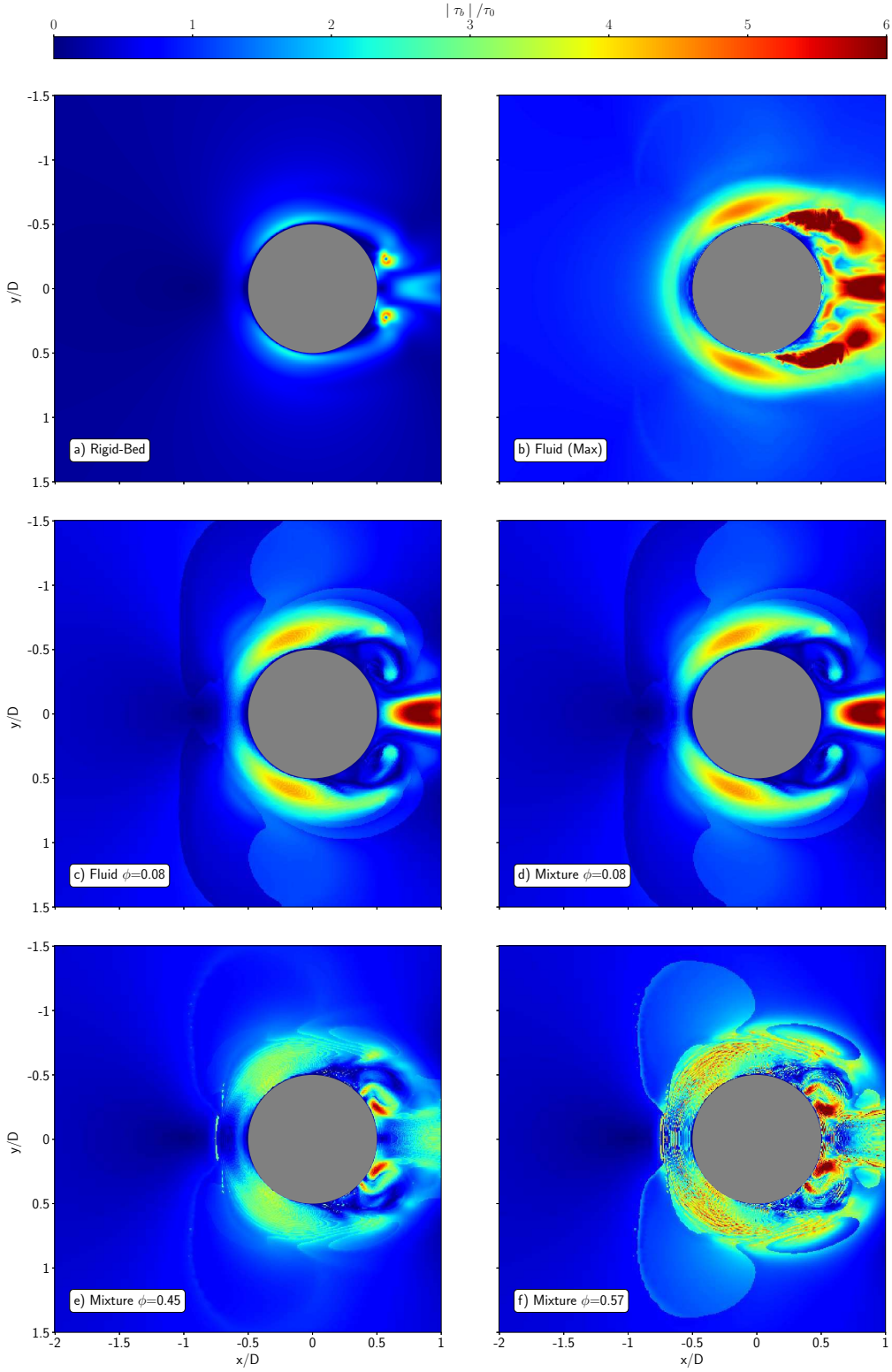

FIGURE B.4: Bed Shear Stress amplification at t=1s with MeshA and MeshILB for Rigid-Bed and Live-Bed cases, respectively. For the Live-Bed configuration, (subfigures B.4.(b-e).) the bed shear stress is projected on the plan tangential to the local slope as described by eq. B.16.

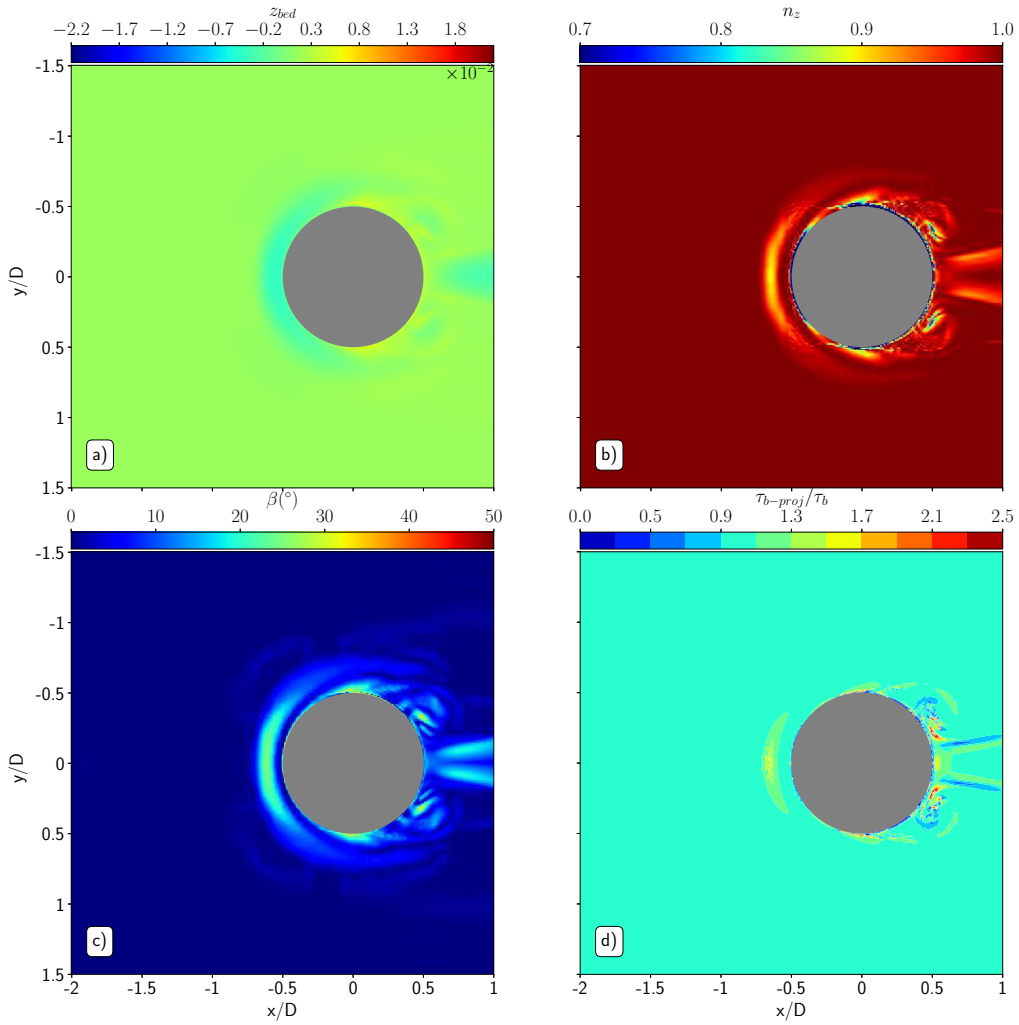

FIGURE B.5: Bed interface elevation (a), vertical component of the bed interface normal (b), angle of maximum slope of the bed (c) and ratio between the bed shear stress obtained with and without the projection on the plan tangential to the local slope (d). t=1s, MeshILB, Live-Bed case.

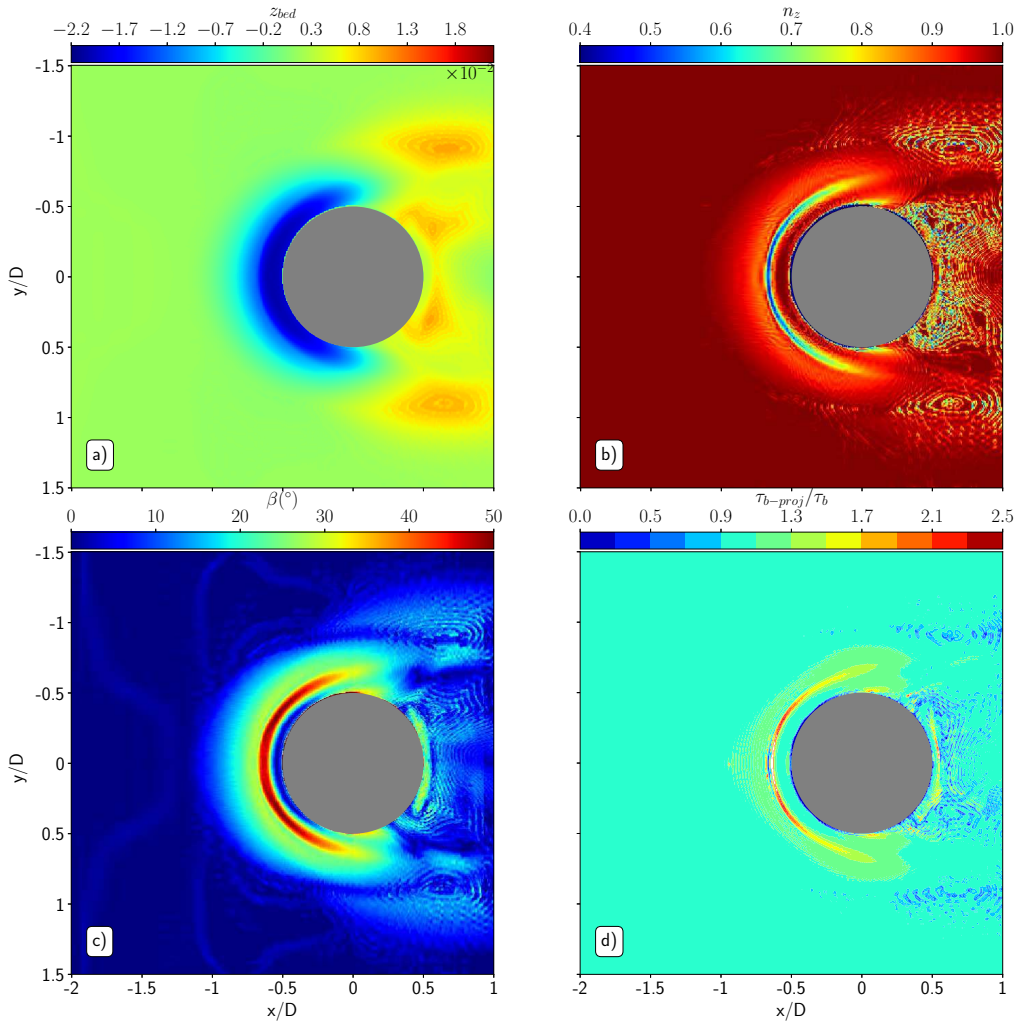

FIGURE B.6: Bed interface elevation (a), vertical component of the bed interface normal (b), angle of maximum slope of the bed (c) and ratio between the bed shear stress obtained with and without the projection on the plan tangential to the local slope (d). t=10s, MeshILB, Live-Bed case.

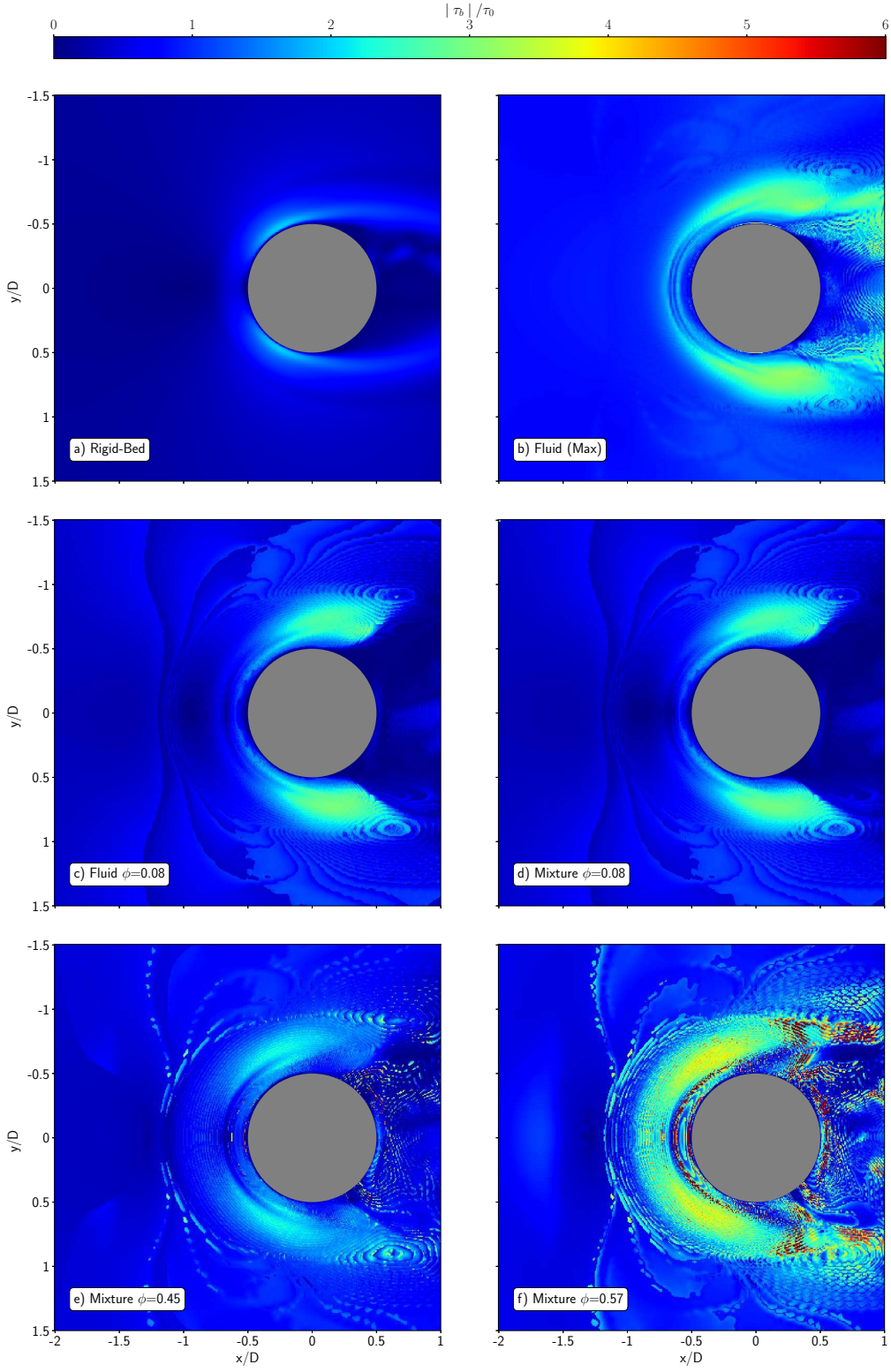

FIGURE B.7: Bed Shear Stress amplification at t=10s with MeshA and MeshILB for Rigid-Bed and Live-Bed cases, respectively. For the Live-Bed configuration, (.b to .e) the bed shear stress is projected on the plan tangential to the local slope as described by eq. B.16.

Annexe C

English translation of the introduction

Foreword

This Appendix is the translation of the introduction (Chapter 1).

C.1 Context of the Thesis

The world population growth is accompanied by a very strong littoralisation. It is estimated that about 60% of the world's population, nearly 4 billion people, is living within 60 kilometers of the coast. There is an increasing population pressure on the world's coasts. For instance, according to the Ministry of Ecology, Sustainable Development and Energy [1], in 2010, the population density of French metropolitan municipalities located on the coast was two and a half times higher than the average density in all metropolitan France.
Simultaneously with the strong urbanization of the coastline, the coastal areas underwent another major transformation for the last thirty years : the use of the natural environment for the production of renewable energy to meet the growing energy demand of our society. Extracting energy from the marine environment is possible using several methods : one can extract wave energy, currents energy (both marine and fluvial) or extract the kinetic energy from the wind using offshore wind turbines. Among these methods, it is the extraction of wind energy that has the most efficient and inexpensive technologies and also the most important energy potential. The latter being more important at sea than on the mainland, many countries plan or multiply the construction of offshore wind farms along their coasts. According to the 2013 annual report of the European Wind Energy Association (*EWEA*, 2013), the European offshore wind capacity was of 5GW in 2012. By 2030, this report estimates that this capacity could reach 150GW which would then correspond to 14% of current European electricity consumption.

This growth in offshore wind energy is worldwide ; China and the United States also want to develop this means of energy production (*Archer et al.*, 2014). However, at present, several major locks (ecological, technical and scientific) limit the capabilities of offshore wind energy.
The first lock is the ecological impact on coastal and marine ecosystems generated by the construction and the operation of offshore wind farms. For instance, the wind turbine blades

1. http: //www.geolittoral.developpement−durable.gouv.fr/IMG/pdf/etat_des_lieux_mer_et_littoral.pdf

can be a source of mortality for birds. Furthermore, the presence of wind farms can alter the migratory routes of some birds (*Gove et al.*, 2013). In the marine environment, the impacts on the wildlife are numerous, ranging from the local turbidity increase during the wind turbine piles construction to the electromagnetic disturbance of submarine cables. A non-exhaustive summary can be found on that subject in *Dai et al.* (2015).
In the atmosphere, the first effect of the wind turbine presence is the generation of a turbulent wake. The wake generates an increase of the atmospheric turbulent mixing close to the surface. This can lead to local temperature increase, at least for onshore farms (*Zhou et al.*, 2012). On a larger scale, the impact of wind farms on the regional climate (*Vautard et al.*, 2014) or the possible reduction of the power of hurricanes by the massive presence of wind farms (*Jacobson et al.*, 2014) have been studied recently, showing that the wind farms environmental impacts are an important question nowadays.
The regional ocean circulation can also be perturbed by the presence of large wind farms. The work of *Broström* (2008) shows that the generation of upwelling is possible downstream the wind farms. These upwellings could be a response of the ocean dynamics to the atmospheric disturbances generated by the wind farms.

The atmospheric and the oceanic flows are not the only ones to be disturbed by the presence of structures such as offshore wind turbines. The atmospheric perturbations are controlled by the turbines but the foundations have an impact on the morphodynamic and on the sediment transport. The foundations for offshore wind turbines can be of different types but all of them have a significant anchorage in the seabed (see figure 1.1). At the end of 2012, in Europe, over 1662 operating offshore wind turbines, only two experimental machines were "floating", *i.e* without significant fixations in the seabed (*EWEA*, 2013). Amongst the offshore wind turbines built on the European coast, 74% have a monopile-type foundation (*EWEA*, 2013).

The foundations impacts on the sediment can be spatially distinguished between the farm scale and the pile scale. At the farm scale, it was observed that the seabed elevation could be raised locally because of the piles density that is disrupting the flow, resulting in a local accumulation of sediment (*Van der Veen et al.*, 2007). At the pile scale, the structure disturbs the flow in several ways : there is a contraction of the streamlines around the pile, an acceleration of the flow, a plunging flow at the front of the structure, a generation of a coherent structure called "horseshoe vortex" (HSV) in front of and around the pile at the water/sediment interface and finally there is a vortex-shedding mechanism downstream of the structure. All of these disturbances contribute to the local increase of the sediment transport and of the erosion around the structure : a phenomenon known as scouring (see section C.2.4 for a complete description of the phenomenon). If the scour phenomenon is important, the sediment under the pile foundations can be eroded, resulting in a potential collapse of the structure. Solutions exist to reduce the scour, but they are not without cost or inconvenience. The scour also takes place around the armor stones that can be placed on the seabed to protect the piles. This only removes spatially the issue from the pile without totally resolving it (*Petersen et al.*, 2015). Another solution to reduce scour is to increase the depth of the foundations or the diameter of the pile (*Matutano et al.*, 2013) but this implies again significant additional costs.
The scour can also suspend the sediments around and downstream of the pile. The marine currents (mainly the tide) are advecting the suspended particles forming wakes of high turbidity that can measure between 30 to 150 meters in width and several kilometers in length (*Vanhellemont and Ruddick*, 2014). These turbid wakes are oriented in the direction of the cur-

rent as shown in figure 1.2, representing a satellite image of the Thanet wind farm in the Thames Estuary. It is very clear in figure 1.2 that the turbid wake generation point is the wind turbine pile. These turbid wakes are not without potential nuisance for the environment as a high turbidity affects marine life.

The development of offshore wind energy must be accompanied by concrete progress in several scientific domains to improve the production, reduce the costs and prevent the environmental impacts. According to *Archer et al.* (2014), the predictive numerical models used to determine the potential of a given site require the improvement and the multiplication of in-situ measurements for their calibration. They also need to better account for the turbulent wakes effects, so as their impacts on energy production. Simultaneously, the environmental and the structural risks generated by the scour phenomenon must be better understood and mastered. A better understanding of the complex interactions between the flow, the structure and the seabed is absolutely necessary (*Sumer*, 2014). It will undoubtedly reduce the costs associated with the piles foundations. They are currently corresponding to one-third of the total cost of an offshore wind turbine (*Sumer*, 2014). For comparison, on land, where scour is not present and where the building conditions are less difficult, the cost associated with the pile foundations of a wind turbine represents only about 10% of the total cost (*Petersen*, 2014).
More generally, the scour phenomenon encountered around offshore wind turbines piles is similar to the one observed around bridge piers in river (*Breusers and Raudkivi*, 1991; *Breusers et al.*, 1977). Incidentally, most of the scour literature is focused on rivers (see section C.2.4). Thus, an improvement in the scour understanding and predictions will also allow advances in fluvial or estuarine civil engineering. These advances are expected by the major actors in the field (engineers, operators, local authorities or government agency). Indeed, because of the increasing urbanization of the coastline, the number of structures interacting with the fluvial or coastal sedimentary dynamics is constantly increasing. The repair price of the damaged structures is also extremely important. Based on past examples (*Lillycrop and Hughes*, 1993), we can estimate that the repair price for structures damaged by scour varies between two million US$ for bridge piers to more than 10 million US Dollars for dykes. In the United States, the average cost of repairing motorway structures impacted by floods was approximatively of 50 million US$ in 1995 (*Lagasse et al.*, 1995). This significant cost is explained by the large number of civil engineering structures impacted by the scour phenomenon. For example, it is estimated that in the 1970-2000 period, 600 of the 600,000 existing bridges in the United States have collapsed due to the scour (*Briaud et al.*, 1999). This accounts for 60% of the causes of bridge destruction over this period. For engineers, there is currently no mathematical and numerical model capable of predicting with sufficient precision the scour in order to help design civil engineering structures. The use of small-scale physical models to correctly design these structures is still widespread in many engineering companies (*Harris et al.*, 2016) . The use of small-scale physical models has a significant cost because it is necessary to build a new model for each configuration studied. A better understanding of the scour phenomenon together with better predictions for the design of civil engineering structures could undoubtedly reduce the costs related to the dimensioning but also to the possible repairs.

This PhD thesis work focuses on two axes in order to better understand the multi-scale interactions between an offshore wind turbine and its environment : the environmental impact of the offshore wind wake on the oceanic and sedimentary dynamics on one hand and the two-phase simulation of the scour around a vertical cylindrical pile on the other hand.

C.2 State of the art

This part of the manuscript aims to describe the state of the art of sediment transport and its modeling. The basic principles and the different modes of sediment transport will be detailed at first. Then I will focus more specifically on how sediment transport is usually described when trying to model it numerically. Subsequently, a description of the two-phase flow approach of sediment transport will present the history of the approach chosen for most of the work presented in this manuscript. Finally, a physical description and a historical review of the numerical modeling work of the scouring phenomenon will be proposed.

C.2.1 Sediment transport - physical description

a) Sediment definition

Sediments are an ensemble of particles resulting from the alteration of continental geological formations. The sediment erosion, transport and deposition are controlled by physical processes such as wind, water or ice. The sediments chemical composition is varied because it is related to the nature of the rocks from which they originate. The sediments also have a great variety of particle size (size, shape, density). In the literature, many particle size classifications have been proposed. Generally, the different categories correspond to changes in the mechanical or physical properties of the grains.
The sediments have different behavior, dynamics and response to the stress generated by their environment according to their size and shape. Therefore, we will not find the same size of sediments near or far from the erosion zone. The coarsest sediments are the ones that move the least distance from their erosion zone to their deposition zone. In estuarine or coastal environments, the sediments are mainly sands and clays having a size smaller than a few millimeters. In the river environment, coarser sediments such as gravel (about ten millimeters) or large pebbles (several tens of millimeters) can be found.
The granulometry is not the only parameter that influences the sediment behavior. The finer the sediment, the more the knowledge of clay and organic matter amount is needed. It allows to distinguish between non-cohesive sediments and cohesive sediments. The particles constituting the first are independent of each other and their movements are individuals, this is the case of gravel or coarse to medium sands for instance. A small amount of clay (5 to 10%) is sufficient to make the sediment cohesive ; the particles will tend to agglomerate under the effect of attractive molecular forces and to form aggregates : a process called flocculation (*Chauchat*, 2007). The latter is reinforced by the presence of organic matter. The cohesive sediments respond in different ways from the non-cohesive ones to the stress of the environment (current, waves, etc.), this is the case of silt, for example. In this thesis, I will focus only on non-cohesive sediments of sand type.

b) The different sediment transport modes

When a fluid flows over a sediment bed composed of particles, it generates a shear stress τ. For or a given particle, if the shear stress exceeds a threshold value, the particle is destabilized, mobilized, and the sediment transport begins. The destabilizing force generated by the flow on the particle is proportional to τd^2, where d is the median diameter of the particles deposited on the bed. This destabilizing force can be compared with the stabilizing forces acting on the particle that correspond to the grains weight ($\propto (\rho^s - \rho^f) g d^3$) to construct the Shields number

Shields (1936) :

$$\theta = \frac{\tau}{(\rho^s - \rho^f)gd}, \tag{C.1}$$

where ρ^s and ρ^f are the particle and fluid density, respectively, and g is the gravitational acceleration. The Shields number is therefore the ratio between the destabilizing and stabilizing forces acting on a particle. The shear stress τ can be determined from the wall fluid friction velocity u_* according to :

$$\tau = \rho^f {u_*}^2 \tag{C.2}$$

For a given particle type, it threshold of motion is given by the critical Shields number, usually written as θ_c. This threshold of motion depends on the particulate Reynolds number Re_p (*Shields*, 1936; *Van Rijn*, 1984a). The latter depends on the particle median diameter's :

$$Re_p = \frac{\mid u^s - u^f \mid d}{\nu}, \tag{C.3}$$

with u^s and u^f being the solid and fluid velocity and ν the kinematic viscosity. In practice, for sands on a horizontal bed, the dependence of the critical Shields number on the particulate Reynolds number is rather small and one can consider that $\theta_c \approx 0.05$ (*Fredsøe and Deigaard*, 1992).
The grains mobilization is facilitated if they are placed on an inclined sediment bed. We can distinguish two cases where the critical Shields number is modified by the slope (*Fredsøe and Deigaard*, 1992) :

- On a slope transverse to the flow direction :

$$\theta_c = \theta_{c0} \ \cos\beta \sqrt{1 - \frac{\tan^2\beta}{\tan^2(\beta_s)}} \tag{C.4}$$

- On slope longitudinal to the flow direction :

$$\theta_c = \theta_{c0} \ \cos\beta \left(1 - \frac{\tan\beta}{\tan(\beta_s)}\right), \tag{C.5}$$

where θ_{c0} is the value of the Shields number over a flat bed, β is the angle between the horizontal and the sediment bed and β_s the static friction angle (also called the angle of repose) of the sediment. The latter is the angle with the horizontal beyond which a pile of grains become unstable. For $\beta > \beta_s$, avalanches mobilizing a few layers of grains at the bed surface is triggered. These avalanches will continue until the angle of the slope is again equal to or lower than β_s.

The value of the Shields number controls the way sediments are transported. Three modes of particle transport are usually distinguished : bedload, saltation and suspension.
The **bedload transport** corresponds to the grains motion in the upper layer of the sediment bed. The sediment grains are rolling discontinuously on the bed in the flow direction. According to the definition of *Fredsøe and Deigaard* (1992), during bedload, the particles are always more or less in contact with the bottom. This transport usually occurs when the shear stress acting on the bed is close to the critical motion constraint τ_c (*i.e* when the Shields number is close to the critical one).
For **saltation**, the particles motion is made of successive jumps in the flow direction. Unlike

bedload, the contact with the bed is not continuous but rather punctual. During a jump, the height reached by a grain does not generally exceed the order of magnitude of its diameter. This sediment transport mode is set up when the threshold of motion is exceeded.
The suspension (also called suspended load) corresponds to the particles transport by the fluid turbulence in the water column. Once lifted, the particles are not deposited again on the bottom. This occurs when the flow is intense enough to keep the particles in suspension. This phenomenon concerns only the smallest particles, light enough to be transported by flow turbulent velocity fluctuations. This phenomenon is usually described using a dimensionless suspension number giving the ratio between the gravitational forces and the turbulent fluid forces raising the particles in the vertical direction (*Van Rijn*, 1984b) :

$$S_u = \frac{w_{fall0}}{u_*}, \tag{C.6}$$

where w_s is the falling velocity of the particles in the motionless fluid. When the vertical velocities generated by the turbulent flow fluctuations near the bed are larger than the particle falling velocity, the latter remains in suspension.
Saltation is generally included in the bedload definition and these two modes of transport are usually considered as a single type of particle motion. The distinction is therefore only made between bedload (grains rolling and saltation) on one side and suspended load on the other side. Indeed, for the bedload, the fluid puts the grains into motion horizontally whereas the suspension of the particles is acting in the vertical direction.
Since the natural environments are polydisperse in terms of grain size, many types of transport are often encountered at the same space and time. For the same flow, the finest sediments are be transported in suspension while those of larger size are transported by bedload.

Focusing on bedload transport, the rate of particles transport changes according to the value of the Shields number. Indeed, for Shields number values below the critical Shields θ_c (≈ 0.05 for sands on a flat bottom), there is no particle motion and therefore no solid transport. When the Shields number increases, for $\theta \in [0.05 - 0.3]$, the solid transport is non-zero but remains rather low. The thickness of the transport layer is of the order of the grain diameter. Bedforms such as ripples or dunes may exist on the sediment bed. When $\theta \geq 0.3$, the bedload layer thickness reaches several particle diameters and is dense in terms of grains. As the flow is very intense, the sediment no longer reveals bedforms. In the latter case, the solid transport is in a regime of intense bedload, more commonly denoted as sheet-flow regime (*Graf*, 1984). The term "upper stage plane bed" can also be found in the literature.
The figure 1.3 shows a schematic view of the sheet-flow regime. Each of the four layers identified in figure 1.3 represents a vertical region where one type of particle interaction is dominant. The lowest layer is representative of the porous and immobile sediment bed. Above, there is a region of high particle concentration where the sediment transport is dominated by contact interactions between the particles. Higher on the vertical, the particle concentration is lower and the collisions between particles so as the suspension by turbulence are the main drivers of sediment transport. At the very top of the water column there is a region where the particle concentration is extremely low and in which the sediment transport is controlled by turbulence.
The transition between these four zones is rather progressive in reality. This particular case illustrates that sediment transport along the vertical is a continuous varying phenomenon.

C.2.2 State of the art of the "classic" modeling of sediment transport

The approach commonly used to model sediment transport is to divide the computational domain into two subfields, in which hydrodynamics and morphodynamics are solved distinctly. They are often linked by friction terms (see Chapter 2, more particularly the equations 2.7 and 2.8).
Depending on the case studied and of the complexity of the hydrodynamic model, the fluid dynamic can be solved using the Barré-de-Saint-Venant 1D or 2D equations (*de Saint-Venant*, 1871; *Vallis*, 2006) or the 3D Navier-Stokes (NS) equations (eq. C.7). The Barré-de-Saint-Venant equation are also know as Shallow Water (SW) equations. The Navier-Stokes equations are based on a momentum balance :

$$\rho^f \left(\frac{\partial \boldsymbol{u^f}}{\partial t} + (\boldsymbol{u^f} \cdot \nabla)\boldsymbol{u^f} \right) = -\nabla p^f + \nabla \cdot \boldsymbol{\tau^f} + \boldsymbol{f} + \rho^f \boldsymbol{g}, \tag{C.7}$$

where ∇ is the three-dimensional gradient operator, ρ^f and $\boldsymbol{u^f}$ are the density and velocity vector for the fluid, p^f is the pressure, $\boldsymbol{\tau^f}$ is the fluid Reynolds stress, $\boldsymbol{g}$ the gravitational acceleration in the $-\overrightarrow{z}$ direction and $\boldsymbol{f}$ the forces other than the gravity. The left-hand terms of eq. C.7 represent the time variations and the advection of the momentum while the right-hand terms are the forces that apply to the fluid. One can distinguish the pressure forces (∇p^f), the viscous forces ($\nabla \cdot \boldsymbol{\tau^f}$) or the gravity ($\rho^f \boldsymbol{g}$).

Depending on the spatial scale of the study, on the sediment type or on the flow conditions, the complete description of the morphodynamics requires a system of equations with several degrees of complexity. In this general description, we will focus on non-cohesive sediment dynamics, at a local or regional scale. At such scales, the sediment transport layer, which is not exceeding a thickness of ten centimeters, can not be solved explicitly (*Amoudry and Souza*, 2011).
The sediment transport distinction into suspended load and bedload requires two equations. The first one describes the evolution sediment concentration in the fluid phase and the second describes the sediment bed interface evolution. These two equations are based on the sediment mass conservation principle.

a) Suspended load

The sediment mass conservation applied to an elementary volume of fluid gives an equation for the sediment concentration ϕ in the water column. This equation can be written as an advection-diffusion equation for the concentration (*Amoudry and Souza*, 2011) :

$$\frac{\partial \phi}{\partial t} + \nabla \cdot (\boldsymbol{u^f} \phi) = \frac{\partial w_{\text{fall}} \phi}{\partial z} + \nabla \cdot (K_\phi \nabla \phi). \tag{C.8}$$

The left-hand side of eq. C.8 represents the time variations and the advection of the sediment concentration under the fluid flow effect. On the right-hand side of the equation, the first term represents the vertical variations in sediment concentration associated with their deposition, w_{fall} is the sediment fall velocity. The second term in the right-hand side of eq. C.8 represents the concentration diffusion under the effect of turbulent fluxes. K_ϕ is a sediment diffusivity term, following *Van Rijn* (1984b) definition it can be related to the turbulent viscosity ${\nu_t}^f$ by two parameters :

$$K_\phi = \frac{1}{S_c} \Phi {\nu_t}^f, \tag{C.9}$$

The first term is the inverse of the Schmidt number S_c (*Van Rijn*, 1984b). It is a function depending on the ratio between the grains falling velocity and the friction velocity. It expresses the importance of the particle inertia terms with respect to the flow turbulence. Based on *Coleman* (1970) data *Van Rijn* (1984b) has proposed the following expression :

$$\frac{1}{S_c} = 1 + 2\left(\frac{w_{fall}}{u_*}\right)^2. \tag{C.10}$$

The second parameter in eq. C.9 accounts for the turbulence attenuation effects induced by the particles presence. It is expressed as a function of the ratio between the concentration ϕ and the maximum concentration ϕ_{max}. It increases with the particle concentration (*Van Rijn*, 1984b) :

$$\Phi = 1 + \left(\frac{\phi}{\phi_{max}}\right)^{0.8} - 2\left(\frac{\phi}{\phi_{max}}\right)^{0.2}. \tag{C.11}$$

The sediments falling velocity depends on the particle concentration. *Van Rijn* (1984b) proposes a Richardson-Zaki type law to describe it :

$$w_{fall} = w_{fall0}(1-\phi)^4, \tag{C.12}$$

where w_{fall0} is the falling velocity of an isolated particle. The latter can be estimated via several relationships, *Van Rijn* (1984b) recommends to use the *Zanke* (1977) formula but nowadays one of the reference formulae is the one proposed by *Jiménez and Madsen* (2003) :

$$w_{fall0} = \frac{1}{A + \frac{B}{S_*}}\sqrt{(s-1)gd}, \tag{C.13}$$

with $S_* = \dfrac{d}{4\nu^f}\sqrt{(s-1)gd}$, $s = \dfrac{\rho^s}{\rho^f}$ and A and B are particles form-factors. For natural particles (non-spherical) the standard values are A=0.954 and B=5.12. For spherical particles, A = 0.79 and B = 4.61.

Let us assume a stationary and uniform flow with no vertical component for the fluid velocity. The equation C.8 can be transformed to describe the evolution of the concentration on a vertical profile :

$$K_\phi \frac{\partial \phi}{\partial z} + w_{fall}\phi = 0 \tag{C.14}$$

Equation C.14 shows that the vertical sediment concentration profile results from an equilibrium between the particles deposition under gravity and sediment suspension by the turbulent flow (*Rouse*, 1939).

It is necessary to determine the bottom boundary conditions to completely solve eq. C.8 or eq. C.14. The bottom sediment flow is usually divided into two vertical components. The first component is related to the erosion (E) and represents the sediment exchange between the bed and the fluid. It is directed upwards as shown in the figure **??**. The second component D is directed downward and is related to the sediment deposition under the effect of gravity. The bottom boundary condition for equation C.14 isu :

$$\left(K_\phi \frac{\partial \phi}{\partial z} + w_{fall}\phi\right)\Big|_{z=z_{bed}} = E - D, \tag{C.15}$$

where z_{bed} is the sediment bed interface vertical position. The sediment deposition under the effect of gravity is written as the falling flux :

$$D = w_{fall}\phi_{bed}, \tag{C.16}$$

where ϕ_{bed} is the local sediment concentration on the first layer above the bed interface.
There are many definitions for the erosion rate E. In the case of non-cohesive sediments, most of the formulas are dependent on the particles size and on the fluid bed shear stress (*Van Rijn*, 1984c). The formula proposed by *Van Rijn* (1984c) is the one with the smallest variability with particle size for $d \in [100 - 1000\mu m]$:

$$E = 0.00033\rho^s D^{*0.3} T^{1.5}((s-1)gd)^{0.5}, \tag{C.17}$$

where $T = \dfrac{u^{*2} - u_c^{*2}}{u_c^{*2}}$ is a parameter describing the transport with u_c^* being the friction velocity at the threshold of motion defined by *Shields* (1936). $D^* = d\left(\dfrac{(s-1)g}{\nu^2}\right)^{0.33}$ is the dimensionless particles diameter.

b) Bedload transport

The sediment mass conservation applied on an elementary bed surface allows to write an equation describing the morphodynamics evolution, also known as the Exner equation(*Exner*, 1920, 1925). Here, the Exner equation is presented in its simplest form, applied to a layer near the sedimentary bed :

$$\rho^s(1-p_b)\frac{\partial z_{bed}}{\partial t} + \nabla_{\mathbf{h}} \cdot \mathbf{q^s} = -E + D, \tag{C.18}$$

with p_b being the bed porosity, ∇_h the horizontal gradient operator and $\boldsymbol{q^s}$ the bedload transport rate. Exner's equation expresses that the local increase or the decrease of the bed level is proportional to the deposition or the erosion generated by the sediment transport rate.
The equations C.8 and C.18 are coupled through the erosion and deposition flux terms described by equation C.15.

Exner's equation resolution requires the determination of the bedload sediment transport $\mathbf{q^s}$. In the literature, there are many formulas for $\mathbf{q^s}$, most of them being empirical or semi-empirical. The most used are the transport formulas of *Meyer-Peter and Müller* (1948), *Wilson* (1966) or *Engelund and Fredsøe* (1976). Despite the variety of formulas estimating $\mathbf{q^s}$, most of them can be expressed by a power law between the non-dimensional transport rate $q^* = q^s/\sqrt{(s-1)gd^3}$ and the excess Shields number $\theta - \theta_c$:

$$q^* = m\theta^j(\theta - \theta_c)^k, \tag{C.19}$$

where m, j and k are different constants according to the transport formulas. Whatever the formula chosen, one usually finds $j + k \approx 1.5$, whereas the pre-factor m varies considerably. For *Meyer-Peter and Müller* (1948), m= 8 but in *Wilson* (1966), m= 12, for instance. A recent reanalysis of *Meyer-Peter and Müller* (1948) results performed by *Wong and Parker* (2006) recommends to use $m = 3.97$. This work is today considered as a reference.

The succinct above presentation is not intended to establish a complete state of the art of

the "classical" sediment transport modeling but rather to show its limits. It can be seen that with this approach, small-scale processes are totally ignored and that the transport layer is not directly resolved. Moreover, the assumptions of a transport divided into bedload and suspended load is a rather simplistic view and does not allow to describe many concrete application cases, like sheet-flow for instance (see section b)). The empirical formulations describing the relationship between the sediment transport rate and fluid bed shear stress are obtained under idealized uniform conditions and are used outside their validity range when flow is no longer uniform or when the slope of the bed is important. This is the case of scour around a cylindrical pile for instance.

C.2.3 State of the art of the two-phase flow modeling of sediment transport

The difficulties and inaccuracies associated with the traditional sediment transport modeling approach require the development of other, more complete, sediments transport modeling approaches. The latters have to integrate the complexity of the coupling phenomena between the different modes of sediment transport and the hydrodynamics, in particular at the grains scale. During the past two decades, the development of a two-phase approach for sediment transport has been a very active research topic. In the two-phase approach, the equations of the dynamics are solved for the two phases constitutive of the medium, the fluid phase (the water) and the particulate phase. Concerning the latter, the sediment is seen as a continuous phase dispersed in the fluid. Contrary to the so-called "classical" approach, this two-phase approach allows to take into account the majority of the physical processes of sediment transport, namely the interactions between the particles and the fluid, the effect of the fluid turbulence on the particles or the particle-particle interactions that are dominant near the sedimentary bed.

The two-phase approach is based on solving the mass and momentum conservation equations for both phases (fluid and sediment). The continuous medium approach is always used for the fluid phase, but there are several ways to describe the particle phase dynamics. The Lagrangian approach describes the behavior of each particle and their interactions. This approach can be found in the work of *Escauriaza and Sotiropoulos* (2011) for example. Describing the sediment in a lagrangian way is very expensive numerically. It is therefore restricted to a limited number of particles, of the order of several tens of millions in 2012 (*Capecelatro and Desjardins*, 2013). This Lagrangian approach will not be more detailed here. In the literature, two-phase flow models are more commonly using a continuous (or Eulerian) approach to describe the sediment. They are denoted as Eulerian-Eulerian two-phase models (for the fluid phase and the sedimentary phase). In this case, the momentum equations for the fluid (eq. C.20) and the sediment (eq. C.21) are very similar to one each other and based on the clear fluid Navier-Stokes equations. (eq. C.7) :

$$(1-\phi)\rho^f\left(\frac{\partial \boldsymbol{u^f}}{\partial t}+(\boldsymbol{u^f}\cdot\nabla)\boldsymbol{u^f}\right)=-(1-\phi)\nabla p^f+(1-\phi)\left(\boldsymbol{f}+\rho^f\boldsymbol{g}\right)+\nabla\cdot\boldsymbol{\tau^f}-n\boldsymbol{f_D}, \quad \text{(C.20)}$$

$$\phi\rho^s\left(\frac{\partial \boldsymbol{u^s}}{\partial t}+(\boldsymbol{u^s}\cdot\nabla)\boldsymbol{u^s}\right)=-\phi\nabla p^f-\nabla p^s+\nabla\cdot\boldsymbol{\tau^s}+\phi\left(\boldsymbol{f}+\rho^s\boldsymbol{g}\right)+n\boldsymbol{f_D}, \quad \text{(C.21)}$$

where ϕ is the sediment volume fraction, ρ^k and $\boldsymbol{u^k}$ the density and the velocity vector for the phase k, p^k and $\boldsymbol{\tau^k}$ the pressure and shear stresses of the k phase, $\boldsymbol{g}$ the gravitational acceleration, $\boldsymbol{f}$ the volume forces other than the gravity, $\boldsymbol{f_D}$ the forces exerted by the fluid on a single particle and n the number of particles per volume unit.

Tableau C.1: Summary of Eulerian-Eulerian two-phase flow models for sediment transport applications

Authors	Turbulence model	Particle stress	Application case
Jenkins and Hanes (1998)	mixing length	kinetic theory	1D Sheet-Flow (SF)
Revil-Baudard and Chauchat (2013)	mixing length	granular rheology	1D Sheet-Flow
Bakhtyar et al. (2009)	$k-\varepsilon$	Bagnold	2D oscillatory SF
Amoudry et al. (2008); *Chauchat and Guillou* (2008); *Cheng et al.* (2017); *Hsu et al.* (2004); *Yu et al.* (2010)	$k-\varepsilon$	kinetic theory	1D SF, 2D Scour
Amoudry (2014); *Jha and Bombardelli* (2009)	$k-\omega$	kinetic theory	1D oscillatory SF, 1D open channel
Lee et al. (2016)	$k-\varepsilon$	granular rheology	2D Scour
Cheng et al. (2018b)	LES	Kinetic theory	3D Sheet-FLow

Compared to the Navier-Stokes equations used for the single-phase approach (eq. C.7), the momentum conservation equations for the fluid (eq. 1.20) and solid phases (eq. 1.21) are coupled through $\boldsymbol{f_D}$. The latter is representing the interactions between fluid and particles. As detailed in Chapter 3, these interactions are mainly governed by the drag and are proportional to the particulate phase's volume. Closure models are needed to determine the granular stresses for the sediment ($\boldsymbol{p^s}\overline{\overline{I}}+\boldsymbol{\tau^s}$) as well as the fluid stress $\boldsymbol{p}\overline{\overline{I}}+\boldsymbol{\tau^f}$. We call them, respectively, granular stress closure models (particle-particle interactions) and turbulence closure models. The complete description of the closure models are provided in Chapter 3.

The different two-phase flow models for sediment transport present in the literature can be distinguished by their granular stress and turbulence closure models. A summary of the different two-phase flow models proposed in the literature together with the configuration cases on which they are applied to, is proposed in the table C.1.

Several families of turbulence closure models have been used for Eulerian-Eulerian two-phase flow solvers in the literature : "zero-equation" RANS (Reynolds Averaged Naval Stokes equations) models such as the mixture length approach, two-equation RANS models (k-ε, k-ω) and finally the LES (Large Eddy Simulation) approach (*Cheng et al.*, 2018b), it is very recent and will not be detailed here.

The first RANS turbulence closure developed for two-phase flow models is the mixing length approach (*Jenkins and Hanes*, 1998). This approach has been commonly used in the literature but it is limited to 1D cases, mainly sheet-flow (*Chauchat*, 2018; *Dong and Zhang*, 1999; *Revil-Baudard and Chauchat*, 2013). More recently, two-equation RANS closure models have been widely used, particularly the k-ε model (*Bakhtyar et al.*, 2009; *Hsu et al.*, 2004; *Longo*, 2005) and to a lesser extent the k-ω turbulence model (*Amoudry*, 2014; *Jha and Bombardelli*, 2009). The k-ε model, originally developed by *Hsu et al.* (2004), has been tested and validated in many configurations ranging from one-dimensional unidirectional sheet-flow (*Chauchat*,

2018; *Hsu et al.*, 2004), or oscillating sheet-flow (*Cheng et al.*, 2017) to 2D scour configurations downstream of an apron (*Amoudry and Liu*, 2009; *Cheng et al.*, 2017), plug-flow phenomenon (*Cheng et al.*, 2017) or the 2D scour formation under a pipeline (*Lee et al.*, 2016). The plug-flow phenomenon (*Sleath*, 1999) is a momentary cohesion loss of the sediment bed under a horizontal pressure gradient effect. The associated sediment transport is very intense and can not be solely solved by taking into account the fluid shear stress on the bed as in conventional models. This phenomenon can occur as a result of waves in coastal areas (*Foster et al.*, 2006).

For the granular stresses closure, a first approach based on Bagnold's rheology (*Bagnold*, 1954) has been proposed by *Hanes and Bowen* (1985) and used in the case of oscillating sheet-flow by *Bakhtyar et al.* (2009). Other approaches are much more used in the literature : the kinetic theory of granular flows (*Jenkins and Savage*, 1983) or the dense granular flows rheology $\mu(I)$ (*Forterre and Pouliquen*, 2008; *GDRmidi*, 2004; *Jop et al.*, 2006).
Inspired from the kinetic theory of gases, the kinetic theory of granular flows (KT) was first written for dry granular flows (in air). Its first adaptation for sediment transport was carried out by *Jenkins and Hanes* (1998). This approach is based on the idea that particle interactions are dominated by binary collisions. In this collisional granular system, the granular stress can be determined from the particle phase velocity fluctuations. These fluctuation measurement is also called the granular temperature (see Chapter 3). In addition to the momentum equation for the particle phase, the granular temperature determination requires the resolution of an transport equation. Widely used, especially for the study of the sheet-flow (*Hsu and Hanes*, 2004; *Hsu et al.*, 2004; *Jenkins and Hanes*, 1998), this KT is known to be unsuitable in the densest parts of the flow, that is to say in regions where particle-particle interactions are governed by quasi-permanent contacts rather than binary collisions (*Jenkins*, 2006). An improvement recently proposed by *Jenkins* (2006) consists in spliting the flow into a collisional layer where the kinetic theory is applied and a viscous layer describing the transition between this collisional regime and the quasi-static one of the non-mobile sedimentary bed. The description of this viscous layer can be done analytically. This semi-analytic approach and its successive improvements (*Berzi*, 2011; *Berzi and Fraccarollo*, 2013, 2015, 2016) can be found in the literature under the name Extended Kinetic Theory but will not be used in this thesis work.

The second major approach used for the granular stress determination is a phenomenological approach, denoted as the dense granular flows rheology (or $\mu(I)$ rheology). It results from the work initiated by the *GDRmidi* (2004) for the dry granular flows. This approach is based on a dimensional analysis of a simple shear configuration (*Forterre and Pouliquen*, 2008) and involves the inertial number I as control parameter. The latter can be interpreted as a ratio between the characteristic time scale for a vertical rearrangement of grains and a horizontal deformation time scale. The inertial number is the parameter controlling the $\mu(I)$ friction coefficient, linking the particulate pressure and the granular shear stresses necessary to close the momentum equation of the particle phase (see chapter 3, section b) for more details). The $\mu(I)$ rheology has been successfully applied for modeling sediment transport under laminar conditions (*Ouriemi et al.*, 2009) and turbulent (*Chauchat*, 2018; *Lee et al.*, 2016; *Revil-Baudard and Chauchat*, 2013).

As described in table 1.1 most of the two-phase approach application cases are one-dimensional and use RANS closure models for the turbulence. Some two-dimensional cases (*Amoudry et al.*, 2008; *Bakhtyar et al.*, 2009; *Chauchat and Guillou*, 2008; *Cheng et al.*, 2017; *Lee et al.*, 2016) and a very recent 3D case, using the LES approach for turbulence (*Cheng et al.*, 2018b) can be

found in the literature. The small number of multidimensional cases can be explained by the complexity of the models used in the two-phase flow approach as well as by their high computational cost. Nevertheless, the configurations for which the classical models are used outside of their validity domains are often complex, multidimensional and unstationnary. The application of the two-phase flow approach to various multidimensional study cases is therefore requiring the development of a multidimensional two-phase flow model integrating the different closure choices for both the turbulence and the granular stresses.

C.2.4 The scour phenomenon and its modeling

a) The scour around a cylindrical vertical structure

When a solid object such as an offshore wind turbine pile or a bridge pier is placed in a steady flow (in a river or a in a marine current for the coastal areas), the latter will be modified by the presence of the object. Several characteristic coherent structures appear (figure 1.5). There is a three-dimensional flow separation in front of the solid body, mainly due to the strong adverse pressure gradient induced by the structures presence. This flow separation generates streamlines contraction on each side of the object, leading to a flow acceleration around the solid body. There is formation of a boundary layer at the solid structure and generation of a lee-wake vortices (usually under vortex-shedding form) in the structure wake. In front of the pile a plunging flow impacts the sediment bed similar to a jet, generating the formation of a horseshoe vortex (HSV) near the bed, in front of and around the solid structure. The presence of the solid body also induces a deflection of the free surface and a generation of roller surface vortices. Being less important than the other coherent structures of the flow, this deflection can be neglected when the Froude number ($F_r = u^f/\sqrt{gh}$, with h the water height) is less than 0.2 (*Roulund et al.*, 2005), that is to say when the gravity effects are important as compared to the fluids inertia.

The lee-wake vortices and the HSV lead to a local increase of the fluid bed shear stress. In the fluvial or coastal environment, the bed is generally composed of sediments, the local solid transport is thus more important and a erosion hole arise around the structure (see figure 1.5). This is the scour. This phenomenon is difficult to measure and quantify in the field. Its understanding has first been built on an empirical approach in simple laboratory experiments.

According to *Chabert and Engeldinger* (1956), the flow conditions far from the structure allows to distinguish two scour types :

- If the upstream flow does not induce sediments transport ($\theta < \theta_c$), then it is called clear-water scouring. In this case the sediment is eroded by the flow and the scour hole is never filled up with sediment.
- If the upstream flow induces sediments transport, then it is called live-bed scour. In this case, the sediment is eroded by the flow to form the scour hole, but in the same time it is continually filled-up with sediments.

With time, the scour hole depth increases and the erosion capacity of the HSV gradually decreases until an equilibrium state is reached. In the case of a clear-water scour, the equilibrium state is reached when the stress on the bottom of the scour hole is of the order of the critical grains motion stress ($\theta \approx \theta_c$). In the case of a live-bed scour, it is reached when, over a given period, the average amount of sediment brought to the scour hole is equal to that extracted by the coherent structures (*Melville*, 1984). In both cases, the equilibrium depth corresponds

to the elevation difference between the deepest point of the scour hole and the interface of the undisturbed sedimentary bed. Its order of magnitude is that of the pile diameter.
The scour dynamics spin-up is also different depending on whether it is a clear water or live-bed type. For the live-bed case, the equilibrium is reached quickly and the equilibrium depth evolves periodically around an average value because of the bedforms passage in the scour hole. Figure 1.6, that can be found in *Melville and Chiew* (1999) shows that the time necessary to reach the equilibrium is longer in the clear-water than in live-bed case. It can also be seen that the equilibrium time increases rapidly with speed in the case of a clear-water scour whereas it is the opposite in the case of a live-bed scour.

The work presented in the literature have first sought to characterize the coherent structures around the pile and the maximum scour depth as a function of parameters such as flow velocity, flow depth, pile diameter, pile shape or the angle of incidence between the flow and the pile. A review of various works on the subject can be found in *Breusers et al.* (1977). Work estimating the over-stress generated by the vortex structures on the sediment bed can be found in *Hjorth* (1975) or *Melville et al.* (1975).

The detailed study of the interactions between the horseshoe vortex and the sedimentary bed was made by *Dargahi* (1990). The scour was in a clear-water regime, with a pile Reynolds number of $Re_D = 39000$. Its definition is :

$$Re_D = \frac{\overline{U^f} D}{\nu}, \tag{C.22}$$

where $\overline{U^f}$ is the average flow velocity and D is the pile diameter.
Initially, the scour generated by the HSV appears at $\pm 45°$ with respect to the longitudinal axis along the cylinder perimeter. The scour is triggered by the vortex named V1 by *Dargahi* (1990). V1 is located at the base of the pile (see figure 1.7). Very quickly the scour occurs simultaneously under the four other vortices composing the system. Subsequently, the erosion pits formed under V2 and V4 move towards the upstream face of the cylinder. The HSV behavior is described by *Dargahi* (1990) as follows : the sediment is eroded under the effect of V2 and V4, and suspended into V3 and V5. Part of the sediment is trapped in the vortex system and transported downstream whereas the other will tend to redeposit under V3 and V5 forming two bumps (see figure 1.7.c). If the position of V1 does not evolve over time, the vortices V2, V3, V4 and V5 are oscillating back and forth in the plane of symmetry. As a result, the erosion holes generated by V2 and V3 and the deposition zones vary spatially over time. As time increases, the erosion holes are deeper and steeper. The whole sediment becomes very unstable ; increasing the transport. The depth increase of the scour hole related to V2 has an influence on the hydrodynamics. The V1 and V2 vortices are merging (figure 1.7.f and g) and the slope of the associated erosion hole has a concave shape near the cylinder. The resulting vortex system has two main vortices and two associated erosion holes (figure 1.7.f and g). The eroded sediment within these two holes comes partly from their excavation and partly from the evacuation of the surplus brought by the avalanches occurring on their upstream slopes. In time, the system tends to a single erosion hole with two different slopes of similar length (figure 1.7.k). These two slopes are the result of the two main vortices of the system : V2 and V4. If V3 and V5 are still present, their intensity and their importance for long times are greatly reduced.

The figure 1.8 shows the resulting erosion profile along the plane of symmetry observed by *Dargahi* (1990). There is a partial symmetry between the upstream scour hole generated by the

HSV and the downstream one, mainly due to the vortex-shedding. In both cases, a slope break is found between an upper slope (between points 1 and 2) and lower one (between 2 and 3). These slopes are of similar length. The main differences are the formation of a dune in 1, downstream of the pile whereas the bed remains flat for upstream scour hole. The concave slope related to the interaction of the plunging flow and the HSV is only observable for the upstream erosion pit.
For a clear-water case, *Dargahi* (1990) describes the upstream erosion mechanism as the result of the combination of the action of the two main vortices V2 and V4 and the plunging flow at the front of the cylinder. Downstream, the formation of the erosion pit is due to the action of vortices detached from the cylinder. The downstream transport is periodic and governed by the vortex-shedding frequency. The formation of ripples downstream of the pile was also observed by *Dargahi* (1990). It is the HSV legs extending downstream of the pile which links the upstream and downstream erosion pits.
The scour study and the evolution of the scour hole shape proposed by *Dargahi* (1990) is mainly done in the symmetry plane. More recent experiments have shown that in the case of clear-water scour, erosion is maximum at the cylinder sides at the beginning of the scour process, and maximum in front of the obstacle at the equilibrium. This result is true for sediments ranging from sands (*Link et al.*, 2008) to gravel (*Diab et al.*, 2010).
Concerning the live-bed case, the scour dynamics is affected by the sediment transport upstream of the scour hole. The vortex structures responsible for scouring are also the HSV and the vortex-shedding, but the literature does not seem to show a thorough investigation of the interaction between these structures and the erosion dynamic such as that of *Dargahi* (1990) for the clear-water scour case.

The dynamics and the equilibrium states of each scour type present important differences. However, their effects on structures such as offshore wind turbines or bridges are similar. Indeed, if the scour is too important, the pile foundations can be bare, reducing its stability and potentially lead to its collapse, a consequence that has significant cost (see section C.1).
It is to reduce these risks that together with the scour knowledge improvement, the literature has produced a lot of works devoted the development of formulas estimating the maximum depth of erosion for precise configurations (pile shape, scour type...). Among the most used, we can mention the formulas of *Breusers et al.* (1977) or *Melville and Sutherland* (1988). However, most of these formulas are empirically derived and many show significant biases when compared to field data (*Johnson*, 1995).
The improvement of the scour knowledge has mainly been built on the river bridge pier case, *i.e* upstream steady flow configurations. Works like those of *Dargahi* (1982), *Breusers and Raudkivi* (1991) or *Melville and Coleman* (2000) provide a clear view of the research progress on scour.
In the coastal areas, the current in which the solid structures are placed is no longer constant but oscillating (tides, waves). This oscillating dynamics can be generated by the tide or local weather variations. These disturbances will make the scour dynamics more complex. For more details, a complete coastal scour state of the art can be found in the books of *Whitehouse* (1998) or *Sumer et al.* (2002).

The scour dynamics is also more complex when several structures are interacting. I will only mention here the case of a group of cylindrical piles in a steady flow. In this case, there are two spatial scales for the scour : the pile diameter and the pile group extension. The experimental results of *Sumer et al.* (2005) show that depending on the pile arrangement, the scour around the group can be much deeper that around an single pile.

Most of the more recent experimental scour configurations are complex configurations dealing with the study of particular scour regimes. One can mention here several current research topics such as the scour around riprap piles protection (*De Vos et al.*, 2011, 2012; *Petersen et al.*, 2015; *Whitehouse et al.*, 2011), the scour around tripod (*Stahlmann et al.*, 2013) or a better determination of the overall scour hole shape its formation by coherent structures (*Link et al.*, 2008, 2012).

If the current experimental research mainly focuses on the complex configurations mentioned above, the case of a scour around a cylindrical pile in a steady flow is still not fully understood. It has recently been observed that, in a clear-water case, the vortex-shedding erosion triggering condition is weaker than that for the HSV. As a result, for a small range of flows, the erosion is mainly related to the vortex-shedding downstream of the pile and not to the horseshoe vortex in front of it (*Lachaussée et al.*, 2018).

b) Numerical modeling of scour

The numerical description of scour is still in its infancy. Indeed, this approach was impossible for a long time because computer resources were not sufficient to solve complex three-dimensional problems over a sufficient range of non-linearly interacting scales in space and time. This section focuses on scour in a constant current and on numerical approaches using a coupling between an hydrodynamic code (resolution of the Navier-Stokes 3D equations) and a morphodynamic one (resolution of the Exner's equation, see section **??**). These are the state of the art models to perform numerical simulations of scour. The first 3D numerical simulation of scour around a pile in constant flow has been published in 1993 (*Olsen and Melaaen*, 1993). The case is in the clear water regime. In this work, the resolution of hydrodynamics is based on stationary Navier-Stokes (NS) equations with a k-ε turbulence mode. Knowing the bed shear stress, an advection-diffusion equation solves the evolution of the sediment concentration. The scour was not simulated until equilibrium, but comparisons with experimental measurements have shown that the transitory regime is well reproduced for the horseshoe vortex. Downstream of the cylinder, because the model k-ε does not predict vortex-shedding, the model of *Olsen and Melaaen* (1993) is not able to reproduce.
The computational capabilities improvement allowed *Olsen and Kjellesvig* (1998) to continue the work of *Olsen and Melaaen* (1993) until the equilibrium of the scour. They obtain scour depth prediction in good agreement with several empirical formulas of the literature for the upstream part of the scour hole (generated by the horseshoe vortex)

The work of *Roulund et al.* (2005) presents a major advance in the numerical simulation of scour. The stationary NS equations are solved and the k-ω SST (*Menter*, 1993), the RANS model presenting the best performance for adverse pressure gradient cases, is used to determine the Reynolds stress. The sediment transport (simplified to bedload transport only) is solved thanks to the formula of *Engelund and Fredsøe* (1976). An avalanche model avoiding slope angles greater than the repose angle of sediment in the scour hole is also used. For the first time, this is a Live-Bed case that is modeled. The bottom stress as well as the upstream and the downstream erosion depths are compared between numerical predictions and experimental data. *Roulund et al.* (2005) show that the agreement between the numerical predictions and the experimental observations is good in transient and equilibrium states for most of the observed quantities. The numerical

simulations presented in *Roulund et al.* (2005) are often considered as a reference case in many posterior studies (*Baykal et al.*, 2015; *Stahlmann et al.*, 2013).

With the RANS approaches for the turbulence quantities, accounting for the suspension load allows to significantly improve the erosion predictions compared to *Roulund et al.* (2005). For example, *Baykal et al.* (2015) numerical results present a very clear improvement over *Roulund et al.* (2005) predictions when an advection-diffusion equation for sediment concentration (*Fredsøe and Deigaard*, 1992) is added to the sediment transport model. This result can also be found in *Stahlmann et al.* (2013) work.
In addition, *Stahlmann et al.* (2013) and *Baykal et al.* (2015) show that the resolution of unsteady NS equations (URANS turbulence model) allows to improve the scour predictions downstream of the cylinder by predicting the vortex-shedding.

The studies previously mentioned have shown that improving the prediction of coherent structures such as the horseshoe vortex upstream and around the pile or the vortex-shedding downstream of the pile improve the agreement between the scour measurements and numerical predictions. However, the URANS turbulence closures, are generally too diffusive to resolve the small-scale dynamics of the flow (*Paik et al.*, 2004, 2007). It is better to use Large Eddy Simulations (LES) rather than URANS approaches to accurately capture this type of structure. There is currently no work on the application of an LES approach for turbulence coupled with a "classical" sedimentary transport model in the case of three-dimensional scour around a cylinder. However, the work of *Kirkil et al.* (2008) and *Link et al.* (2012) using the LES approach for hydrodynamics in "frozen" scour holes (the bottom of the computational domain has the shape of a scour hole but there is no sediment transport model) show that the LES allows to find a complex swirl dynamics in the HSV close to that described by *Dargahi* (1990) (bimodal oscillation, several vortices of different sizes).

The study of complex scour configurations around tripod structures (*Stahlmann et al.*, 2013), or the scour in the presence of riprap protections (*Nielsen et al.*, 2013) have also recently numerically been investigated. For tripods, the computational cost is extremely important and the interactions between the hydrodynamics and the solid structure are poorly mastered. Up to now, only a proof of concept of the applicability of numerical models to this kind of configuration has been provided by *Stahlmann et al.* (2013).

The "classical" approach for scour modeling involves the use of empirical sediment transport formulas (see section C.2.2) to solve the sediment dynamics. These formulas are mostly obtained in uniform and idealized configurations (*Engelund and Fredsøe*, 1976; *Meyer-Peter and Müller*, 1948). As a result, most formulas are used out of their validity range when applied for three-dimensional scour around a cylindrical pile. The complex interactions between the HSV, the sediments and the steep slope within the scour hole make the configuration far from the uniform conditions where the "classical" sediment transport formula have been obtained.
In a case of sour around a cylindrical pile, the agreements between the model predictions and the observations are conclusive from a research point of view (*Baykal et al.*, 2015). However, to design civil engineering structures, the conventional sediment transport models are not comprehensive enough. Therefore, engineers are still using small-scale physical models to parameterize them.
In the case of more complex scours processes (backfilling, waves, protections, tripods) numerical

simulation are nowadays a way to improve the scientific knowledge rather than an engineering tool.

To get rid of the traditional assumptions, such as the distinction between bedload and supended load local correlation, between the sediment flux and the fluid bed shear stress, seems necessary to improve the numerical predictions of scour. The development of Eulerian-Lagrangian two-phase models for sediment transport (*Escauriaza and Sotiropoulos*, 2011) can be quoted here to highlights the research effort for another scour modeling approach. However, the computational resources required by the Lagrangian approach for the description of the granular medium are so important that only a small number of particles can be modeled. This number is much less than necessary for a complete simulation of three-dimensional scour. For instance, the configuration presented in Chapter 5 would require 6.5 billion particles, much more than is currently possible. The use of the Lagrangian two-phase approach to perform a complete scour simulation is therefore impossible, even in a near future. Nevertheless, some aspects of scour can be studied thanks to the Lagrangian approach. In the work of *Link et al.* (2012) the model of *Escauriaza and Sotiropoulos* (2011) is used : 10,000 particles allow to study the sediment transport in an already formed scour hole.
The computational times associated with a two-phase Eulerian-Eulerian approach for sediment transport are also very important. They are nevertheless more compatible with a 3D scour configuration than a Lagrangian description of the sediments motion. In the past, only 2D configurations have been realized with two-phase Eulerian-Eulerian approach (*Amoudry and Liu*, 2009; *Cheng et al.*, 2017; *Lee et al.*, 2016), and the move to a 3D configuration represents a real challenge in terms of high performance numerical computations.

C.3 Objectives and organization of the thesis

Two major axes are followed in this manuscript. The first one deals with the interactions between a wind turbine-generated atmospheric wake and the local dynamics of the ocean and the sediment using a two-dimensional model following the classical approach of sediment transport. The second axe deals with numerical simulations of the scour phenomenon around a cylindrical pile using a three-dimensional Eulerian-Eulerian two-phase flow model : sedFoam.
The spatial scales and the numerical modeling approaches chosen differ between the two axes. Nevertheless, the overall objective is the same : contribute to the knowledge improvement of the interactions between an offshore wind turbine and its environment.

Chapter 2 focuses on the numerical modeling of multi-scale interactions between the atmosphere-ocean-sediment coupled system and the atmospheric wake generated by an offshore wind turbine. This work is motivated by the studies of *Broström* (2008), *Rivier et al.* (2016) and *Van der Veen et al.* (2007) showing the impacts of an offshore wind farm on the local ocean and sediment dynamics. Here, the purpose is to know if similar impacts can be found at the wake scale. The approach used for sediment transport is the "classical" approach presented in the C.2.2 section. Regarding ocean dynamics, *Moulin and Wirth* (2014) recently showed the importance of accounting for the oceanic velocity in the atmosphere-ocean interactions at the mesoscale (O(10km)). However, most wind turbine models consider the ocean as an inert boundary, which can affect their reliability.
The work presented in chapter 2 attempts to answer the following questions : (i) What is the

impact of an offshore wind turbine wake on the local ocean and sediment dynamics by taking into account account of the oceanic velocity in the atmosphere-ocean interactions ? (ii) Is it possible to parameterize them for future upscalling simulations ? (iii) Have the ocean and sediment dynamics a feedback on the atmospheric energetic budget around a turbine ?
These results are published in *Nagel et al.* (2018)

The scour phenomenon investigation using a two-phase approach is the subject of the following chapters. Chapter 3 describes the two-phase Eulerian-Eulerian model for sediment transport, sedFoam. Chapter 4 presents the validation of the model on 1D and 2D sediment transport cases. Finally, Chapter 5 describes the application to the three-dimensional scour around a cylindrical pile in a steady flow. The objectives of this part of the manuscript are : (i) to provide a proof of concept that the two-phase approach can be used in the case of complex three-dimensional simulations, including multiple interactions between the flow, the solid structure and the sedimentary bed. (ii) to characterize the contribution of small scale processes in the scour modeling. (iii) characterize the impact of traditional assumptions such as the local correlation between the sediment flow and the bed shear stress for sediment transport in the scour hole.
Some of the results presented in chapter 4 are published in (*Chauchat et al.*, 2017).
Finally, a general conclusion on the two main axes of this PhD thesis work as well as the perspectives is proposed in the chapter 6.

Résumé : Le travail réalisé dans cette thèse a consisté en le développement et l'utilisation des modèles numériques pour étudier les interactions multi-échelles entre une éolienne offshore et la dynamique locale océanique et sédimentaire. Dans une première partie, les interactions entre le système couplé océan-sédiment et le sillage atmosphérique généré par une turbine éolienne offshore sont étudiées à l'aide d'un modèle numérique 2D développé au cours de la thèse et écrit en fortran. Ce modèle résout les équations de Barré-De-Saint-Venant pour l'océan et l'équation d'Exner pour le sédiment. Dans un seconde partie, le phénomène d'affouillement 3D autour d'un cylindre vertical est étudié à l'aide d'un modèle diphasique eulérien-eulérien, *sedFoam*, implémenté dans la boîte à outils numériques OpenFOAM. L'approche diphasique permet de tenir compte des processus de petite échelle en s'affranchissant des hypothèses classiquement faites pour la modélisation du transport sédimentaire, notamment la corrélation locale entre le flux de sédiments et la contrainte de cisaillement fluide sur le fond.

Concernant l'impact du sillage atmosphérique généré par une turbine, nous avons montré que celui-ci peut générer des allées tourbillonnaires dans l'océan. La dynamique turbulente océanique est alors contrôlée par le paramètre de sillage $S = C_d D/H$, où D est le diamètre du sillage au point d'impact sur la surface de l'océan, C_d est le coefficient de la loi de friction quadratique entre l'océan et le fond et H la profondeur de l'océan. Une paramétrisation des flux turbulents basée sur S est proposée pour modéliser la dynamique océanique dans des modèles à plus grande échelle de type RANS (Reynolds Averaged Navier-Stokes). Les résultats montrent que la dynamique océanique a une rétro-action sur la puissance du vent disponible. Les résultats montrent également que la dynamique sédimentaire instantanée est couplée à la dynamique océanique. Cependant, les variations de l'élévation du fond marin sont faibles (mm/mois) et l'impact morpho-dynamique du sillage est négligeable.

Concernant la simulation diphasique de l'affouillement, après une validation du modèle sur des configurations 1D et 2D, des simulations tridimensionnelles autour d'une pile cylindrique sont présentées. Dans un premier temps, une configuration sans sédiments est réalisée afin de valider la capacité du modèle de turbulence URANS (Unsteady Reynolds Averaged Navier-Stokes) développé dans ce travail de thèse à reproduire les structures tourbillonnaires responsables de l'affouillement comme le tourbillon en fer à cheval et le lâché tourbillonnaire à l'aval du cylindre. Ensuite, les premières simulations diphasiques 3D de l'affouillement autour du cylindre ont été réalisées en régime de transport de type lit-mobile. Ces simulations constitue un véritable challenge en terme calcul numérique à haute performance. La comparaison favorable des résultats de simulations avec les résultats expérimentaux de la littérature apporte la preuve de concept que l'approche diphasique est pertinente pour étudier des configurations d'écoulements complexes instationnaire et tridimensionnelle. Les résultats de simulation sont ensuite analysés pour étudier la relation entre le flux local de transport de sédiments, la valeur de la contrainte fluide sur le fond et la pente locale du lit sédimentaire. La déviation par rapport aux résultats obtenus en écoulement uniforme permet d'identifier les mécanismes prépondérant de transport associées au tourbillon en fer à cheval, à la pente de fond et aux tourbillons lâchés dans le sillage du cylindre. Les résultats obtenus montrent une sensibilité à la résolution numérique en particulier à l'aval du cylindre illustrant le besoin de réaliser des simulations des grandes échelles turbulentes diphasiques.

Mots-clés : Affouillement, transport de sédiments, écoulement diphasique, simulation numérique, turbulence.

Abstract : The work undertaken in this PhD thesis was to develop and use numerical models to investigate the multi-scale interactions between an offshore wind turbine and the local ocean and sediment dynamics. First, the interactions between the coupled ocean-sediment system and the atmospheric wake generated by an offshore wind turbine are investigated using an idealized two-dimensional model developed during this Phd thesis and written in fortran. The model integrates the shallow water equations for the ocean together with the Exner equation for the sediment bed. In a second part, the 3D scour phenomenon around a vertical cylinder in a steady current is studied using a two-phase flow eulerian-eulerian solver, sedFoam, written within the framework of the numerical toolbox OpenFOAM. The two-phase flow approach accounts for small-scale processes by avoiding the traditional assumptions made for sediment transport modeling, such as a local correlation between the sediment flux and the fluid bed shear stress.

Regarding the atmospheric wake generated by a turbine, the results shows that its impact on the ocean's surface can generate vortices. The resulting turbulent ocean dynamics is controlled by the wake parameter $S = C_d D/H$, where D is the wake diameter at the impact location on the ocean surface, C_d is the quadratic friction coefficient between the ocean and the sediment and H is the oceanic layer depth. A turbulence parameterization based on S is proposed, allowing for upscaling simulations in larger scales Reynolds Averaged Navier-Stokes (RANS) models. It is shown that the ocean dynamics has an effect on the available wind power. The results also show that the instantaneous sediment dynamics is strongly coupled with the ocean one but that the overall seabed elevation variations remain small (a few millimeters/month). The morphodynamic impact of the wake is thus negligible.

Concerning the two-phase flow simulation of scour, sedFoam is first validated on 1D and 2D configurations. Then, 3D simulations around a vertical cylindrical pile are presented. At first, a validation of the Unsteady Reynolds Averaged Navier-Stokes (URANS) turbulence model developed in this work is performed on a configuration without sediment. The results show that the vortices structures responsible for scouring, the Horse Shoe Vortex (HSV) and the vortex-shedding in the lee of the cylinder are correctly reproduced. Then, 3D two-phase flow simulations of the scour around a cylindrical pile have been carried out in a live-bed configuration. This work is the first attempt to model 3D scour phenomenon using the two-phase flow approach. Such simulations represent a real challenge in terms of high performance computing. The good agreement between the numerical predictions and the literature experimental results provide the proof of concept that the two-phase flow approach can be used to study complex 3D and unsteady flow configurations. The relationship between the local bed shear stress, the sediment flux and the local sediment bed slope is further investigated. The deviation of the results from a uniform flow configuration is further analyzed to identify the relevant sediment transport mechanisms associated with the HSV, the slope in the scour mark and the vortex-shedding downstream of the cylinder. Finally, the numerical results show a grid sensitivity of the morphological predictions in the lee of the cylinder that are most probably related to small-scale resolved vortical structures. This highlights the need for two-phase flow Large Eddy Simulations on this configuration in the future.

Keywords : Sour, sediments transport, two-phase flow, numerical simulation, turbulence.